Simulations for
LISA & GRACE-Follow-On:

Satellite constellations at Lagrangian points for LISA-like missions

Interferometer simulations for the GRACE Follow-On mission

Master of Science Degree Thesis
by
Vitali Müller

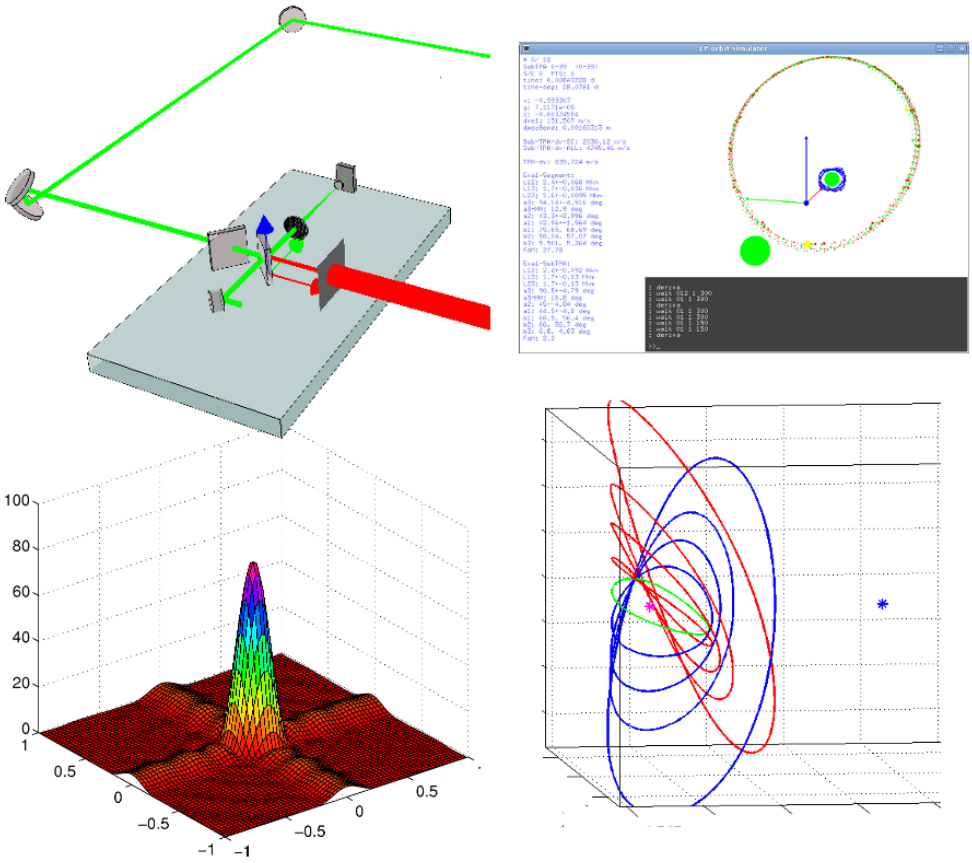

April 2nd, 2013

Max-Planck-Institute for Gravitational Physics
(Albert-Einstein-Institute)
Gottfried Wilhelm Leibniz Universität Hannover

Simulations for
LISA & GRACE-Follow-On:

Satellite constellations at Lagrangian points for LISA-like missions

Interferometer simulations for the GRACE Follow-On mission

1st Examiner:	Prof. Dr. Karsten Danzmann Albert-Einstein-Institute, Hannover
2nd Examiner:	Priv.-Doz. Dr. Gerhard Heinzel Albert-Einstein-Institute, Hannover
Supervisor:	Dr. Benjamin Sheard Albert-Einstein-Institute, Hannover

Kurzzusammenfassung

Diese Arbeit ist zweigeteilt. Der erste Teil beschäftigt sich mit Satellitenorbits für eine Weltraummission zur Detektion von Gravitationswellen. Gravitationswellen sind von Albert Einstein erstmals vorhergesagte Vibrationen der vierdimensionalen Raum-Zeit, die durch astrophysikalische Ereignisse (z.B. Verschmelzung von Schwarzen Löchern, Explosion von Sternen) ausgelöst werden können und sich als Längenänderungen zwischen Objekten, z.B. Satelliten, manifestieren. Mit Hilfe von Laserlicht, interferometrisch, ist es möglich diese relativen Längenänderungen zu messen, die etwa dem Verhältnis eines Atomdurchmessers zu der Entfernung zwischen Sonne-Erde entsprechen. Es wird in dieser Arbeit untersucht, ob drei Satelliten in der Nähe der sog. Librationspunkte (Lagrangepunkte) so fliegen können, dass sie eine Konstellation bilden, die sich nur geringfügig über die Missionslaufzeit verändert und somit zwischen den Satelliten interferometrische Messungen ermöglicht. Dazu werden die Besonderheiten der Librationspunkte erläutert und die grundlegende Dynamik einzelner Objekte in ihrer Umgebung hergeleitet. Im Anschluss wird die Kombination von mehreren Trajektorien zu einer Konstellation untersucht und numerisch optimiert.

Im zweiten Teil der Arbeit wird auf die Satellitenmission GRACE Follow-On eingegangen, die aus zwei Satelliten besteht und das Schwerefeld der Erde vermessen soll. Dazu müssen Entfernungänderungen zwischen den Satelliten präzise in einem Frequenzbereich von 2 mHz bis zu 100 mHz bestimmt werden. Dafür wird am Albert-Einstein-Institut in Zusammenarbeit mit Industrie und internationalen Partnern ein Instrument entwickelt, welches mit Hilfe von Laserlicht, interferometrisch, Entfernungsänderungen mit einer Auflösung von unter 0.001 Millimeter detektieren kann. Die allgemeine Funktionsweise und die einzelnen Komponenten dieses sog. Laser Ranging Interferometer werden erläutert, sowie verschiedenste Effekte, welche die Messung verfälschen können, analysiert. Die Simulationsergnisse zeigen zudem wie Ungenauigkeiten in der Positionierung von einzelnen Komponenten die Messungen beeinflussen.

Abstract

This thesis is separated into two parts. The first part is about satellite orbits for space-based gravitational wave detectors. Gravitational waves are ripples in the four-dimensional spacetime and were firstly predicted by Albert Einstein. They can be caused by astrophysical events (e.g. merging black holes, stellar explosions) and manifest as length changes between objects, for example, satellites. The order of magnitude of the relative length changes corresponds approximately to the size of an atom over a measurement distance between Sun and Earth. However, even this tiny effect can be measured with laser light, interferometrically. In this thesis the construction of satellite constellations in the vicinity of the so-called Lagrangian points is investigated, which might be stable enough over the mission duration to allow interferometric measurements between the spacecrafts. Therefore, the fundamental dynamics of single objects in the proximity of Lagrangian points are studied, followed by attempts to construct constellations by combining different trajectories. Finally, numerical optimization techniques are applied to further improve the constellations.

The second part of this thesis is concerned with an instrument for the GRACE Follow-On mission. This planned mission consists of two satellites in a low Earth orbit, which shall measure Earth's gravity field. Therefore, the inter-satellite distance fluctuations need to be determined very precisely in the frequency range from 2 mHz to 100 mHz. For this purpose the Albert-Einstein-Institute develops in cooperation with industry and international partners a Laser Ranging Interferometer with a target precision better than 0.001 millimeter. An overview about the working principle of the instrument as well as the purpose of single components is presented. The contribution of various perturbations like spacecraft attitude jitter on the performance is computed. Finally, simulation results show how various misadjustments of components influence the measurements.

Selbstständigkeitserklärung

Ich versichere, die vorliegende Arbeit selbstständig und nur mit den angegebenen Quellen und Hilfsmitteln angefertig zu haben, sowie die Zitate deutlich kenntlich gemacht zu haben.

Vitali Müller
Hannover, den 2. April 2013

Contents

Abbreviations and Nomenclature

$\sim$	a tilde denotes the Fourier transform of a quantity e.g. $\tilde{\Phi} = \mathcal{F}(\Phi)$
$\hat{}$	a hat denotes always a matrix
$\widetilde{\delta\Phi}$	a tilde with delta denotes the linear spectral density with units $[\widetilde{\delta\Phi}] = [\Phi]/\sqrt{\text{Hz}}$
CoM	Center of Mass
CR3BP	Circular Restricted Three Body Problem
DPS	Differential Power Signal
DWS	Differential Wavefront Sensing
ESA	European Space Agency
GFO	GRACE Follow-On
GFZ	German Research Centre for Geoscience (GeoForschungsZentrum), Potsdam
IC	Initial Configuration
KBR	K/Ka band microwave ranging system
LEO	Low Earth Orbit
LISA	Laser Interferometer Space Antenna
LOS	Line of Sight, connection line between CoM and CoM
LRI	Laser Ranging Interferometer
PLL	Phase Lock Loop
POMC	Point Of Minimal Coupling
QPD	Quadrant photodiode
RX	Received / Receiver
S/C	Spacecraft
SEZ	Solar Exclusion Zone
SM	Steering Mirror
SSB	Solar System Barycentric (frame)

TMA	Triple Mirror Assembly
TX	Transmitted / Transmitter

Chapter 1

Introduction

1.1 Satellite orbit constellations at Lagrangian points

The first part of this thesis is concerned with satellite orbits in the proximity of the Sun-Earth Lagrangian points, in particular with reference to space-borne gravitational wave detectors. Therefore, the chapter starts with a short introduction to the LISA and LISA-like missions and points out some constraints and key parameters for the constellations of such missions.
Then the fundamental dynamics in the vicinity of the Lagrangian points are studied in a simplified dynamical model called the *circular restricted three body problem*. This approximation reduces the complexity, which is apparent in an full ephemeris model[1], and allows analytical and semi-analytical approaches, which yields a better understanding of the system. In this context the determination of reference trajectories, analytically and numerically, is treated and provides a brief historical survey of this field.
Afterwards a combination of these natural trajectories to a detector constellation is discussed. Three exemplary constellations are chosen and the constellation deformations and key figures are computed. Then a numerical optimization method is introduced and the results of the optimized constellations are given.
In the end also an alternative optimization approach is sketched, which was developed in an early stage of the research and was a first attempt to optimize trajectories in a full ephemeris model.
The focus of this thesis was to study the dynamics and constellations in general, even if the results might not fulfill the required constraints, yet, e.g. on constellation stability.

The analytical expressions were derived using `Mathematica`. The numerical studies including orbit integration and optimization were written in `C/C++`. In fig. 1.1 the graphical front-end is shown, which was used to visualize the orbit trajectories and important constellation figures during the optimization. It was also used to control and adjust the optimization parameters. `Matlab` was mainly used to produce the plots.

1.2 Interferometer simulations for GRACE Follow-On

The second part of this thesis is about the Laser Ranging Interferometer for the GRACE Follow-On mission. A short introduction to the mission as well as an overview about the working principle of the instrument is given, where basic knowledge about laser interferometers is presupposed. However, the equations for the

[1] accounting for the precise position of all planets and corresponding forces

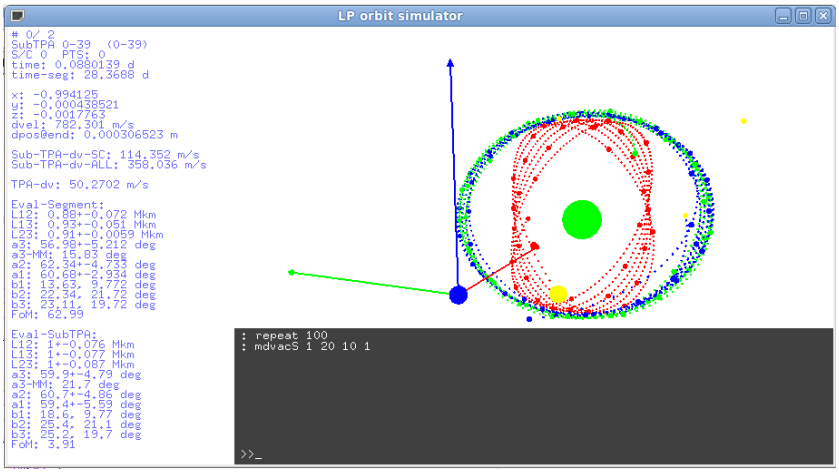

Figure 1.1: Graphical front-end of the orbit simulator used to optimize the spacecraft constellations.

signals of an heterodyne interferometer and the contribution of some expected noise sources are derived or provided. The subunits of the optical part of the Laser Ranging Interferometer are discussed, whereby it was tried to derive parameter, which are also useful for the design process and for the laboratory experiments. Various aspects are covered, which are necessary for the understanding of later simulation results. Furthermore, two simplified models are presented for the influence of spacecraft rotations on the phase measurement between two spacecrafts and for the measurements of the optical bench on a single spacecraft. In the end the previously derived equations and models are applied in simulations on a particular optical bench setup. The coupling of various setup parameters into the final length measurement is studied, trying to reveal important factors for the design process and for the final performance.

For the simulations a tool called IfoCad was used, which was initially developed by Gerhard Heinzel (AEI Hannover). It is a framework of C subroutines to plan and optimize the geometry of laser interferometers[2]. Recently the development of a C++ version including general astigmatic Gaussian beams [Kochkina *et al.* , 2013], polarization tracing and full 3-d support was expedited. During this thesis the software was extended to meet the required functionality.

[2]Download: http://www.lisa.aei-hannover.de/ifocad/

Chapter 2

Satellite constellations at Lagrangian points for LISA-like missions

2.1 Laser Interferometer Space Antenna (LISA)

The Laser Interferometer Space Antenna is a satellite mission to detect and measure gravitational waves. It was firstly proposed to ESA in 1993 for the M3 slot of ESA's *Horizon 2000* program [LISA, 1993]. In the subsequent years the proposal evolved to a mission concept with three identical spacecraft (S/C) in a heliocentric orbit [LISA, 2011]. The satellites are arranged in a rotating equilateral triangle with 5 million km armlength, trailing the Earth by about 20° (see fig. 2.1). The constellation plane is thereby inclined by 60° w.r.t. the ecliptic plane.

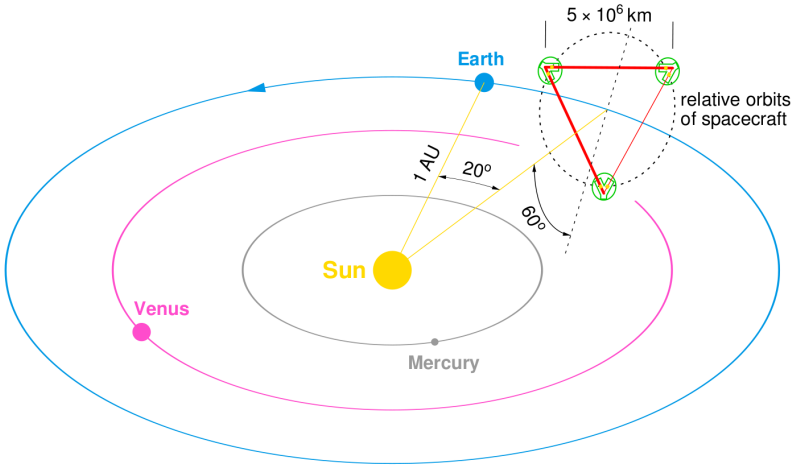

Figure 2.1: The LISA constellations constisting of 3 identical S/C in a heliocentric orbit [LISA, 2000, p. 64].

The scientific measurement of space-based gravitational wave detectors is the inter-satellite distance variation, which contains the signature of a gravitational wave. A gravitational wave distorts the space-time, in the context of general relativity it is expressed as a variation in the metric tensor h_{ij}. The relative length change, the so-called strain, due to gravitational waves is expected to be $< 10^{-21}$, requiring picometer (10^{-12} m) precision for a 5 million km long section of measurement at least in the interesting frequency band of the gravitational wave oscillation. Therefore, each spacecraft will have free-falling (and free-floating) testmasses, which serve as

reference points for the distance measurement. The spacecrafts are operated in a drag-free mode, shielding the testmasses from perturbations and compensating external disturbances (e.g. solar radiation pressure), allowing to reach the required picometer sensitivity between the testmasses.
In the end of 2011 the mission was reformulated and proposed to ESA as Next Generation Observatory [NGO-Yellowbook, 2011], sometimes also called eLISA, where an armlength of 1 million km and only two arms (sides of the triangle) were foreseen. These changes were mainly driven by attempts of cost reduction and to the detriment of scientific output.

2.1.1 LISA orbits and constellation

LISA as well as NGO utilize the same satellite constellation, which differs only by the armlength L and the amount of used arms. The equilateral constellation triangle rotates with a period of one year around the constellation center (fig. 2.2) and does not require orbit corrections during the 5 year science mission time.
The constellation can be obtained (up to first order) by slightly increasing the inclination ϵ w.r.t. the ecliptic plane and the eccentricity e of each S/C orbit according to [Dhurandhar *et al.* , 2005, eq. (3)+(4)]

$$\tan(\epsilon) = \frac{L/(2 \cdot 1\,\mathrm{AU})}{1 + L/(2 \cdot \sqrt{3} \cdot 1\,\mathrm{AU})}, \tag{2.1}$$

$$e = \left(1 + \frac{L}{\sqrt{3} \cdot 1\,\mathrm{AU}} + \frac{2L}{3 \cdot 1\,\mathrm{AU}}\right)^{1/2} - 1 \tag{2.2}$$

which can be seen at the light green line in fig. 2.2. The other orbital elements need to be adjusted for each spacecraft, individually. Changing the inclination of an orbit is expensive in terms of energy and fuel ([Vallado & McClain, 2007, p. 353], [Wertz & Larson, 1999, p. 148]), hence constellations with smaller armlength (and therefore smaller required inclination change) are easier to realize.

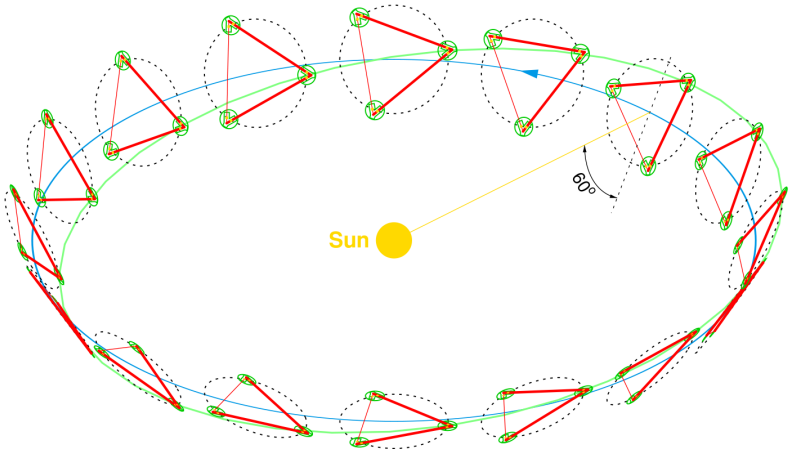

Figure 2.2: LISA orbit evolution for one year from [LISA, 2000, p. 65]

The LISA formation has been studied extensively ([Li *et al.* , 2008], [Bik *et al.* , 2007], [Dhurandhar *et al.* , 2005], [Hughes, 2002]) and was optimized in a full ephemeris model accounting for accelerations due to all planets and relativistic post-Newtonian corrections. Some key parameters and their consequences are:

- **Arms**: 3 (= 6 links)
  The measured amplitude of a gravitational wave in a Michelson detector depends on the polarization of the gravitational wave, on the distance to the

source and on the sky location. With a LISA-like configuration with three arms (between the three S/C) one can instantaneously determine the polarization and the distance to the source. In a two arm configuration the polarization and distance to the source are entangled and one needs the rotation of the constellation (due to the orbital evolution) to distinguish these effects.

- **Armlength**: 5 million km with variations $< 1\%$
  The armlength of the interferometer determines the measurement band of the detector. The advantage of space-based detectors over ground-based detectors is the lack of seismic noise in space, which yields in combination with longer armlengths a better sensitivity at low frequencies. The measurement band for a detector with armlengths of the order 1 million km is approximately between 0.1 mHz and 1 Hz [LISA, 2000].

- **Doppler rate**: The first time derivative of the armlength, also called the line-of-sight velocity, is below 20 m/s, which corresponds to a Doppler shift in frequency of below approximately 20 MHz for 1064 nm light. The current hardware development for LISA assumes signals below 20 MHz, however, there might be schemes to handle even larger relative velocities (e.g. by adjusting the offset frequencies).

- **Inner constellation angles**: 60.0° on each S/C with variations $< 0.81^\circ$
  Each spacecraft emits (and receives) two laser beams. The variations of the relative angle between the beams is a critical parameter, since large variations require the rotation of the telescopes on each S/C or some other beam steering mechanism. The best sensitivity on gravitational waves is obtained for a Michelson detector topology with 90.0° angle between the arms [1].

- **Constellation revolution frequency** in SSB: once per year
  The rotation of the constellation in the solar-system barycentric (SSB) frame modulates the signal of the gravitational waves. A higher revolution rate allows better distinction and parameter estimation of the gravitational wave sources.[2]

- **Orbit correction and stationkeeping** during science mission time: None
  Stationkeeping maneuvers would require an interruption of the measurements, since the testmasses would be non free-falling. The orbit corrections should be kept as small and rare as possible to reduce the costs, amount of fuel and measurement gaps.

A drawback of the constellation is the expensive orbit injection in terms of fuel, which requires approximately $\Delta V = 1$ km/s for each S/C after reaching an escape orbit ($\Delta V \approx 10.9$ km/s from LEO [Turner, 2009, p. 23]), and a transfer time of 14 months [LISA, 2011].
Satellite orbits in the vicinity of the Lagrangian points can be reached usually with less fuel and costs (e.g. $\Delta V \approx 3.3$ km/s from LEO to L_1 Halo orbits [Rausch, 2005, p. 86]), which also motivated the research on LISA-like constellations in the vicinity of Lagrangian points.

2.1.2 Other LISA-like concepts

The LISA concept has been studied for the recent two decades by a worldwide gravitational wave community. Over the years the concept evolved from a mission with

[1] Gravitational waves are transverse waves, stretching and squeezing space in two orthogonal directions [Misner *et al.* , 1973, ch. 35, propagation of gravitational waves]

[2] private communication with Stanislav Babak, Albert-Einstein-Institute, Golm

six S/C to a mission with three S/C. The idea of LISA, measuring gravitational waves interferometrically with laser links between S/C withstood, although the concrete implementation evolved and changed. Especially due to the introduction of the new name NGO in 2011/2012, the term *LISA-like* is used here as a synonym for space-based gravitational wave detector utilizing laser interferometric measurements.
There have been other LISA-like mission proposals, which should be mentioned for the sake of completeness:

LAGOS

The predecessor of LISA was already proposed in 1984/1985 [Faller *et al.* , 1985]. The concept was based on a V-shaped constellation in heliocentric orbit with 120° angle between the 1 million km long arms. The three S/C should head the Earth by 15°.

OMEGA / SAGITTARIUS

An mission utilizing retro-grade geocentric orbits with 600 000 km radius is OMEGA [Hellings, 1996] (predecessor SAGITTARIUS in 1993). The vertices of the equilateral triangle are distributed evenly on the orbit and host two probes, such that the total constellation consists of six S/C. The baseline armlength is 1.04 million km.

LAGRANGE

The LAGRANGE [Conklin *et al.* , 2011] proposal foresees three S/C located at the Earth-Moon Lagrange points L_3, L_4 and L_5 forming an equilateral triangle with baseline armlength of 0.67 million km. The armlength variation is specified with $< 5\%$, which yields Doppler rates < 150 m/s, while the inner angle varies by $\pm < 5°$.

DECIGO

The Japanese proposal DECIGO [DECIGO-Team, 2009, DECI-Hertz Interferometer Gravitational wave Observatory] consists in the final stage out of 3-4 clusters of 3 S/C in heliocentric orbits. The S/C in each cluster are controlled with formation flying techniques and form an equilateral triangle with 1000 km baseline armlength.

For a more detailed comparison of different mission schemes refer to [NASA, 2012].

2.2 Circular Restricted Three Body Problem

In this thesis the circular restricted three-body problem (CR3BP) is used as an approximation for the Sun-(Earth+Moon) system. All objects are treated as point masses. The primary body is the Sun with mass $m_\odot$, while the secondary body has a mass $m_{\oplus\leftmoon}$, which is the sum of Earth mass and Moon mass. We are interested in the motion of a satellite with mass m_{sat}. In the *restricted* problem the satellite does not influence the motion of both bodies, such that

$$m_\odot \gg m_{\text{sat}} \quad \wedge \quad m_{\oplus\leftmoon} \gg m_{\text{sat}}, \tag{2.3}$$

while the *circular* indicates a circular orbit of the secondary body around the primary body. The radius of the circular orbit is $r = 1\,\text{AU} = 149.598 \cdot 10^6$ km and the angular velocity of the secondary body is

$$\omega = \sqrt{\frac{G \cdot (m_\odot + m_{\oplus\leftmoon})}{r^3}} = 1.99098 \cdot 10^{-7}\,\text{rad/sec}, \tag{2.4}$$

which is well known from the circular restricted two-body (Kepler) problem [Montenbruck & Gill, 2000, eq. 2.27].
Usually a co-rotating (synodic) normalized frame is chosen (Howell & Pernicka [1988], Richardson [1980]). The time is normalized to

$$T = \frac{1}{\omega}, \tag{2.5}$$

which yields $\omega = 1$ and a simplification of the equations of motion in the synodic normalized frame. The spatial coordinates are unitless and normalized to $r = 1\,\mathrm{AU}$, the origin of the coordinate frame is co-located with the barycenter of primary and secondary body and the x-direction is co-aligned with the connection line of primary and secondary. The z-direction is co-aligned with the angular momentum vector of $m_{\oplus\mathbb{C}}$ (see fig. 2.3). Using the reduced mass for the secondary object

$$\mu = \frac{m_{\oplus\mathbb{C}}}{m_{\odot} + m_{\oplus\mathbb{C}}} \approx 3.0404 \cdot 10^{-6}, \tag{2.6}$$

one can write the position of the primary body as $\vec{p}_{\odot} = (\mu, 0, 0)^{\mathsf{T}}$ and of the secondary body as $\vec{p}_{\oplus\mathbb{C}} = (\mu - 1, 0, 0)^{\mathsf{T}}$ [Gómez *et al.* , 1998].
Then, the potential at a point $\vec{p}_{\mathrm{sat}} = (x, y, z)^{\mathsf{T}}$ is [Zazzera *et al.* , 2004, eq. 1.7]

$$U(\vec{p}_{\mathrm{sat}}) = \frac{1}{2}(x^2 + y^2) + \frac{1}{2}\mu(1-\mu) + \frac{1-\mu}{|\vec{p}_{\mathrm{sat}} - \vec{p}_{\odot}|} + \frac{\mu}{|\vec{p}_{\mathrm{sat}} - \vec{p}_{\oplus\mathbb{C}}|} \tag{2.7}$$

$$= \frac{1}{2}(x^2 + y^2) + \frac{1}{2}\mu(1-\mu) + \sum_{n=2}^{\infty} c_n \cdot \rho^n \cdot P_n\left(\frac{x}{\rho}\right), \tag{2.8}$$

where the last two terms of the first line have been expanded in a series of Legendre polynomials[3] $P_n(x)$ with $\rho = \sqrt{x^2 + y^2 + z^2}$ and constant coefficients c_n [Richardson, 1980].
Then the equations of motion can be written as [Zazzera *et al.* , 2004, eq. 1.6]

$$\ddot{x} - 2\dot{y} = \frac{\partial U}{\partial x}, \tag{2.9}$$

$$\ddot{y} + 2\dot{x} = \frac{\partial U}{\partial y}, \tag{2.10}$$

$$\ddot{z} = \frac{\partial U}{\partial z}. \tag{2.11}$$

These equations have a first integral, called *Jacobi's integral*, given by [Zazzera *et al.* , 2004, eq. 1.9]

$$C = 2 \cdot U(x, y, z) - (\dot{x}^2 + \dot{y}^2 + \dot{z}^2), \tag{2.12}$$

where C is the so-called *Jacobi constant*. The Jacobi constant for a particular orbit can be used to determine forbidden areas in the phase space for the trajectory [Zazzera *et al.* , 2004, p.11] or is often used as a parameter for the characterization of orbit families.

2.2.1 Symmetries

It is easy to show (see e.g. [James, 2006], [Thurman & Worfolk, 1996]), that the CR3BP has symmetries, which can be exploited to simplify the computation or reduce the computational effort. Assume an orbit $(x(t), y(t), z(t))$ fulfilling the equations of motion of the CR3BP, then the following two orbits also fulfill the equations of motion:

[3] Such an expansion is sometimes used in orbit simulations to compute the acceleration due to celestial bodies [Vallado & McClain, 2007, p.571, Third-Body Perturbations]

1. $(x(t), y(t), -z(t))$: corresponds to a reflection across the xy-plane.

2. $(x(-t), -y(-t), z(-t))$: corresponds to a reflection across the xz-plane and time-reversal.

From the first point one can conclude that for an orbit located in the half space $z > 0$, there exists a counter-part in the half-space $z < 0$.

2.2.2 Lagrangian Points

The equilibrium points of the CR3BP are the points, where the gravitational force and the centrifugal force acting on the spacecraft, cancel each other. These points are denoted as *Lagrangian*, *Lagrange* or *Libration points*. They can be found by solving

$$\nabla U(x, y, z) = 0. \tag{2.13}$$

The solution consists of three co-linear points (L_1, L_2, L_3), which are on the x-axis, and two triangular points (L_4, L_5), as depicted in fig. 2.3. The co-linear points can be found by solving a polynomial equation of degree five [Zazzera *et al.* , 2004], while the triangular points are the vertices of two equilateral triangles, where the other two vertices are the primary and secondary body. All five points are in the xy-plane, which is the ecliptic plane. It is known that the co-linear equilibrium points are unstable, whereas the triangular points are stable for particular values of μ [Wie, 1998, sec. 3.7.3]. The numerical values for the Sun-(Earth+Moon) system are:

$$\vec{L}_1 = \begin{pmatrix} -0.9900 \\ 0 \\ 0 \end{pmatrix}, \quad \vec{L}_2 = \begin{pmatrix} -1.0101 \\ 0 \\ 0 \end{pmatrix}, \quad \vec{L}_3 = \begin{pmatrix} 1.0 \\ 0 \\ 0 \end{pmatrix},$$
$$\vec{L}_4 = \begin{pmatrix} -0.4999 \\ 0.8661 \\ 0 \end{pmatrix}, \quad \vec{L}_5 = \begin{pmatrix} -0.4999 \\ -0.8661 \\ 0 \end{pmatrix}. \tag{2.14}$$

The distance between Earth+Moon and the L_1 or L_2 point is approximately 1.5 million km.

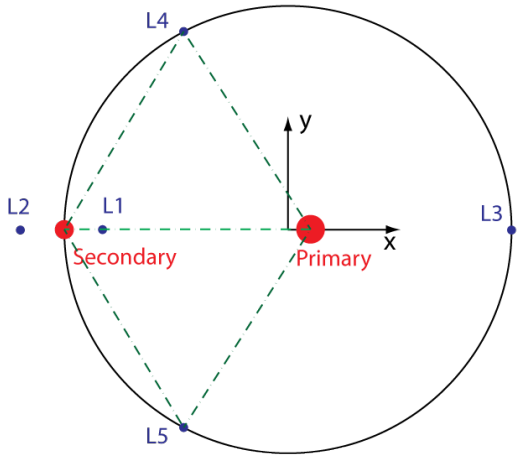

Figure 2.3: CR3BP frame and Lagrangian points

2.2.3 Dynamics near Lagrangian Points L_1 and L_2

To study the dynamics we expand the equations of motion (eq. (2.9)-(2.11)) up to third order in x,y,z

$$\begin{aligned}\ddot{x} - 2\dot{y} - (1 + 2c_2)x &= \frac{\partial}{\partial x}\sum_{n=3}^{\infty} c_n \cdot \rho^n \cdot P_n\left(\frac{x}{\rho}\right) \\ &= +\frac{3}{2}c_3(2x^2 - y^2 - z^2) + 2c_4x(2x^2 - 3y^2 - 3z^2) + \mathcal{O}(4),\end{aligned} \tag{2.15}$$

$$\begin{aligned}\ddot{y} + 2\dot{x} - (1 - c_2)y &= \frac{\partial}{\partial y}\sum_{n=3}^{\infty} c_n \cdot \rho^n \cdot P_n\left(\frac{x}{\rho}\right) \\ &= -3c_3xy - \frac{3}{2}c_4y(4x^2 - y^2 - z^2) + \mathcal{O}(4),\end{aligned} \tag{2.16}$$

$$\begin{aligned}\ddot{z} + c_2z &= \frac{\partial}{\partial x}\sum_{n=3}^{\infty} c_n \cdot \rho^n \cdot P_n\left(\frac{x}{\rho}\right) \\ &= -3c_3xz - \frac{3}{2}c_4z(4x^2 - y^2 - z^2) + \mathcal{O}(4),\end{aligned} \tag{2.17}$$

and we shift the coordinate system origin to the L_1 or L_2 point $(x_0, 0, 0)$ by substituting

$$x \to x + x_0. \tag{2.18}$$

The constants c_n can then be computed using the expression

$$c_n = |\gamma|\frac{\mu}{\gamma^{n+2}} - \frac{\mu - 1}{(1 + \gamma)^{n+1}}, \tag{2.19}$$

with

$$\gamma = \mu - 1 - L_{i,x} \qquad (i = 1, 2), \tag{2.20}$$

being the signed distance in x-direction between Earth+Moon and Lagrangian point under investigation. In the literature (Richardson [1980] and Gómez [2001]) usually an additional spatial normalization is introduced[4], which yields a different expression for the c_n constants:

$$\tilde{c}_n = \frac{1}{\gamma^3}\left((\pm 1)^n\mu + (-1)^n\frac{(1 - \mu)\gamma^{n+1}}{(1 \mp \gamma)^{n+1}}\right), \tag{2.21}$$

with upper sign for L_1 and lower sign for L_2 and with unsigned distance $\gamma = |\mu - 1 - L_{i,x}|$. The numerical values for both formulas are tabulated in table 2.1 and deviate for $n > 2$.

	L_1		L_2	
n	c_n	$\tilde{c}_n$	c_n	$\tilde{c}_n$
2	4.06107	4.06107	3.94052	3.94052
3	-301.670	3.02001	295.671	-2.97984
4	30239.0	3.03054	29243.2	2.97026

Table 2.1: Coefficients c_n and $\tilde{c}_n$ at the L_1 and L_2 point.

[4] the spatial coordinates are normalized to the distance $|\gamma|$ between secondary body and Lagrangian point under investigation

If a satellite is at rest at the Lagrangian point ($x = y = z = \dot{x} = \dot{y} = \dot{z} = 0$), it will experience no acceleration ($\ddot{x} = \ddot{y} = \ddot{z} = 0$) in the synodic frame of the CR3BP. The S/C remains fixed w.r.t. the primary and secondary body. However, small deviations increase exponentially due to the unstable character of the collinear Libration points.
The dynamics consisting of periodic and quasi-periodic orbits near the Lagrangian point are often visualized in a Poincaré map, which consists of intersection points of the ecliptic plane with orbits of a particular energy value (see fig. 2.4). A periodic orbit, which is located completely in the ecliptic plane, is directly visible in the Poincare map (horizontal Lyapunov orbit, black line in fig. 2.4). Other periodic orbits, which are not completely in the ecliptic plane, intersect with the ecliptic plane always at the same points, hence these orbits are single points on the Poincaré map. Quasi-periodic orbits intersect after each orbit revolution at another point with the ecliptic plane. Thus, these orbits are shown as lines on a Poincaré map (blue lines in fig. 2.4).
Such maps can be derived from the Hamiltonian of the system in a systematic semi-analytical approach using *Dynamical System Theory*. For further details refer to Jorba & Masdemont [1999].

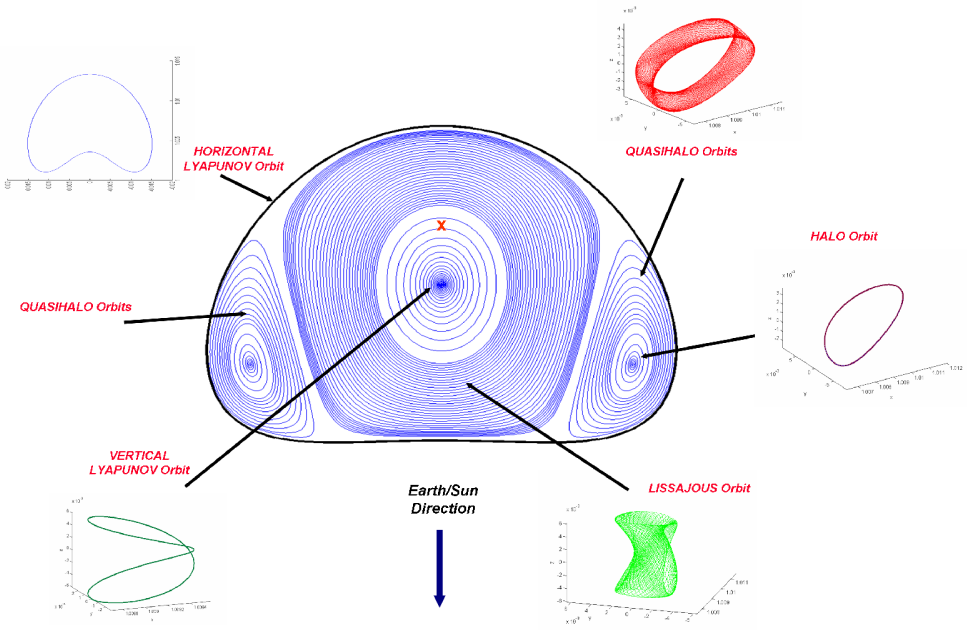

Figure 2.4: The perodic and quasi-periodic orbits around L2 shown on a Poincaré section of the ecliptic plane (from [Kolemen *et al.* , 2007]). The red cross indicates the Lagrange point.

In the next subsections we discuss the aforementioned orbits in more detail.

2.2.4 Lissajous Orbits

The Lissajous orbits arise as a solution of the linearized equations of motion. The linearized equations of motion are obtained, if the right-hand-side of eq. (2.15)-(2.17) is set to zero. Then the z-component is the differential equation of an harmonic oscillator, while the xy-components are coupled ordinary differential equations. A bounded solution for the linearized equations, when only the oscillatory modes are

excited, is derived in detail in [Wie, 1998, sec. 3.7.4] and can be transformed to

$$x(t) = -\frac{A_y}{k}\cos(\lambda t + \phi), \tag{2.22}$$

$$y(t) = A_y \sin(\lambda t + \phi), \tag{2.23}$$

$$z(t) = A_z \cos(\nu t + \psi), \tag{2.24}$$

where $\nu = \sqrt{c_2}$ is the oscillation frequency of the out-of-plane motion. The in-plane frequency λ is a solution of the characteristic equation [Richardson, 1980]

$$x^4 - (c_2 - 2)x^2 - (c_2 - 1)(1 + 2c_2) = 0, \tag{2.25}$$

whereby two roots are purely imaginary and denote the oscillatory (stable) modes

$$x_{1,2} = \pm i\lambda, \tag{2.26}$$

while the other two real roots yield the unstable modes. The factor k is given by [Richardson, 1980]

$$k = \frac{1}{2\lambda}(\lambda^2 + 1 + 2c_2). \tag{2.27}$$

In general the frequencies ν and λ are unequal. For the L_1 point of the Sun-(Earth+Moon) system the numerical dimensionless values are $\nu \approx 2.015$ and $\lambda \approx 2.086$, which correspond to orbital periods of 181 days and 175 days, respectively. For the L_2 point the in-plane period is 177.5 days, while the out-of-plane oscillation has a period of 184 days. Thus, eq. (2.22)-(2.24) parameterize in general Lissajous trajectories around the Libration points, as depicted in fig. 2.6. The amplitudes A_y and A_z as well as two phase angles ϕ and ψ are the parameters defining the trajectory.
The Lissajous solution (eq. (2.22)-(2.24)) for the linearized equations of motion can be successively extended to fulfill the equations of motion of higher orders (eq. (2.15)-(2.17)) using a Lindstedt-Poincaré approach (see sec. 2.3).

2.2.5 (Solar) Exclusion Zone

Already in [Clarke, 1947] orbits in the vicinity of the Lagrangian points of the Earth-Moon system were suggested for communication with the surface of the Moon. In [Farquhar, 1968] Lissajous trajectories at the L_2 point were discussed to establish a communication link between the far side of the Moon and the Earth.
A Lissajous trajectory for the communication with the far side of the Moon needs to be designed to minimize the time in the occulted zone, where the satellite is occluded by the Moon when observed from Earth. For the L_1 point of the Sun-(Earth+Moon) system the so-called Solar Exclusion Zone (SEZ) should be avoided, where a communication downlink is disturbed by interference with solar radiation. The SEZ is defined by an enlarged solar disk as viewed from Earth (fig. 2.5). For the S-band link of the ISEE-3 mission a cone with half opening angle 3° was assumed [Dunham & Farquhar, 2002]. In [Davis *et al.* , 2004] a conservative exclusion zone with 4.75° is defined for the ACE mission. In this thesis a SEZ half opening angle of 4.5° is used, which corresponds to a disk perpendicular to the ecliptic plane with 118 000 km radius at the L_1 point.

2.2.6 Lyapunov Orbits

Assuming a motion only in the ecliptic plane (in-plane), the so-called horizontal Lyapunov orbits are obtained. They have in case of the linearized equations of

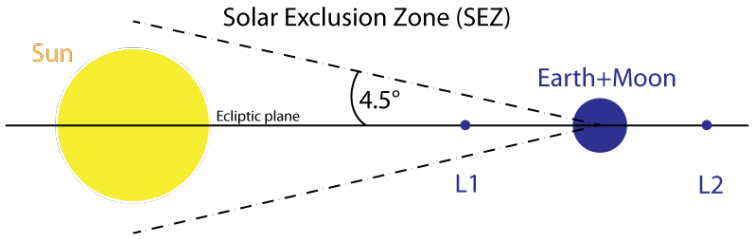

Figure 2.5: Solar Exclusion Zone

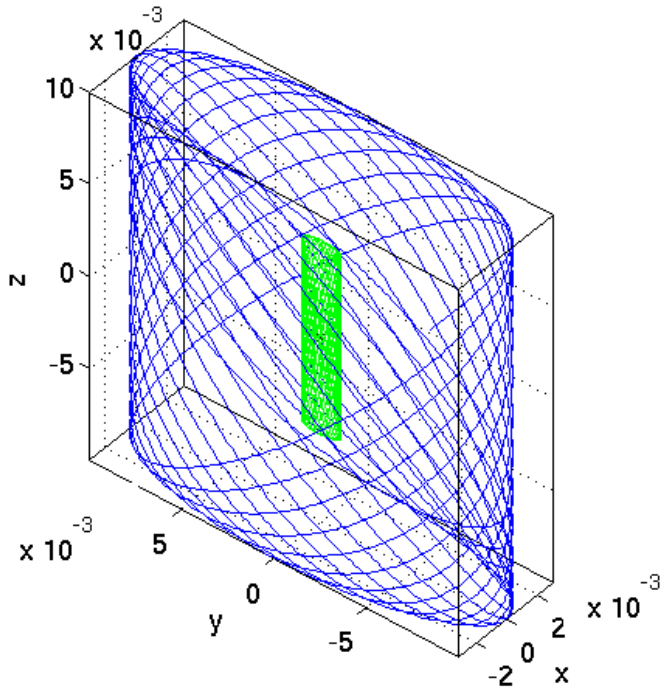

Figure 2.6: Large (blue) and small (green) Lissajous orbits around the Langrange point (located at $(0, 0, 0)$) solving the linearized equations of motion.

motion an elliptical shape with amplitudes A_y/k and A_y. For higher orders and large amplitudes the shape is distorted due to non-linear contributions to a bean-like orbit (see fig. 2.4, top-left).
A pure vertical excursion yields the vertical Lyapunov orbits, which are simple oscillations in the z-direction for the linearized equations of motion. Non-linear contributions result also in xy-motion yielding orbits shown in fig. 2.4 (bottom-left).

2.2.7 Halo Orbits

Already in [Farquhar, 1968] the Halo orbit concept is mentioned, where the in-plane frequency λ and the out-of-plane frequency ν are equalized by S/C thrusters (so-called "frequency-control"). This three-dimensional periodic orbit does not enter the occulted zone. Later Farquhar & Kamel [1973] derived analytical expressions for "natural" Halo orbits for the translunar L_2 point in the Earth-Moon system in a third-order approximation. Richardson [1980] derived the equations for the Halo orbits in the CR3BP of the Sun-(Earth+Moon) system in a compact form. For large amplitudes A_x and A_z the frequencies λ and ν can be matched due to non-linear contributions on the right-hand-side of eq. (2.15)-(2.17), if both amplitudes fulfill an

equation of the form [Richardson, 1980, eq. (18)]

$$\alpha \cdot A_x^2 + \beta \cdot A_z^2 = \delta, \tag{2.28}$$

which is often denoted as *amplitude relationship* for Halo orbits. α, β and δ are constants, which depend on the Lagrangian point under investigation and on the reduced mass μ of the system. From the functional dependency shown in fig. 2.7 for the Sun-(Earth+Moon) system one can determine a minimum A_x amplitude of approximately 200.000 km for Halo orbits.
In addition the *phase relationship* [Richardson, 1980, eq. (19)]

$$\psi = n \cdot \frac{\pi}{2} + \phi, \qquad n = 1, 3 \tag{2.29}$$

between the in-plane and out-of-plane components emerges during the development of the solution. The switch variable n indicates two families of Halo orbits, often denoted as type/class I and II or northern and southern Halo orbits, which are caused by symmetries in the equations of motion (symmetry 1 in sec. 2.2.1). The conversion from a northern to a southern Halo orbit is given by a reflection of the trajectory at the ecliptic plane. A spacecraft on a northern Halo orbit is visible most of the time from Earth's northern hemisphere (see fig. 2.8). This usually also requires the communication infrastructure to be located and available on the northern hemisphere, when communication with the S/C is desired.
The periodic Halo orbits of the CR3BP, which bifurcate from the horizontal Lyapunov orbits [Gómez, 2001, p.434], are only an approximation to the real problem, where the primary and secondary body are not on a perfect circular orbit and where the Halo orbits are perturbed by the gravitational attraction of other planets and solar radiation pressure. In Gómez [2001] and Farquhar & Kamel [1973] the solutions for the equations of motion including perturbations are called *quasi-periodic* orbits, since the trajectories are not closed in the general perturbed case.

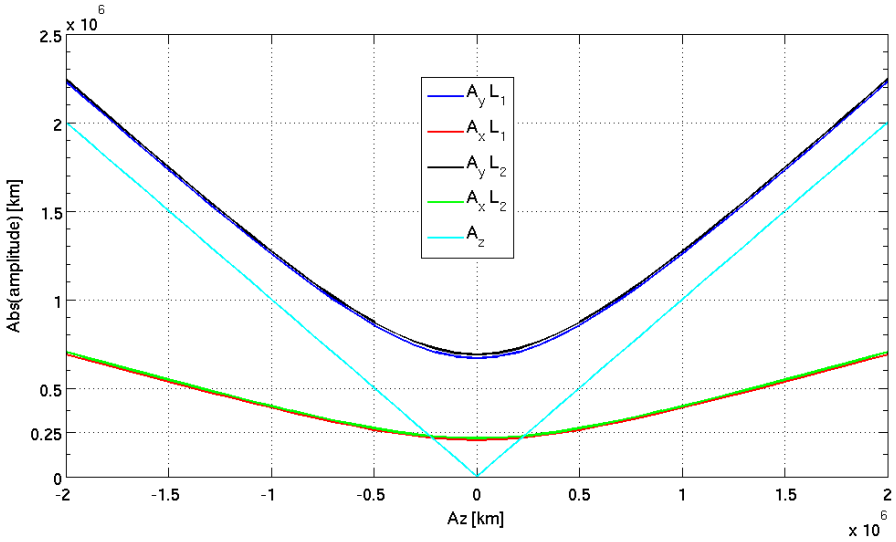

Figure 2.7: Amplitude relationship between A_z and A_y and between A_Z and $A_x = -A_y/k$ for the Halo orbits around Lagrange points L_1 and L_2 obtained from a third order solution (sec. 2.3.3).

2.2.8 Quasi-Halo Orbits

Another type of quasi-periodic orbits are so-called Quasi-Halo orbits, which are Lissajous orbits around the Halo orbits [Gómez *et al.* , 1997] (see fig. 2.4, top-right).

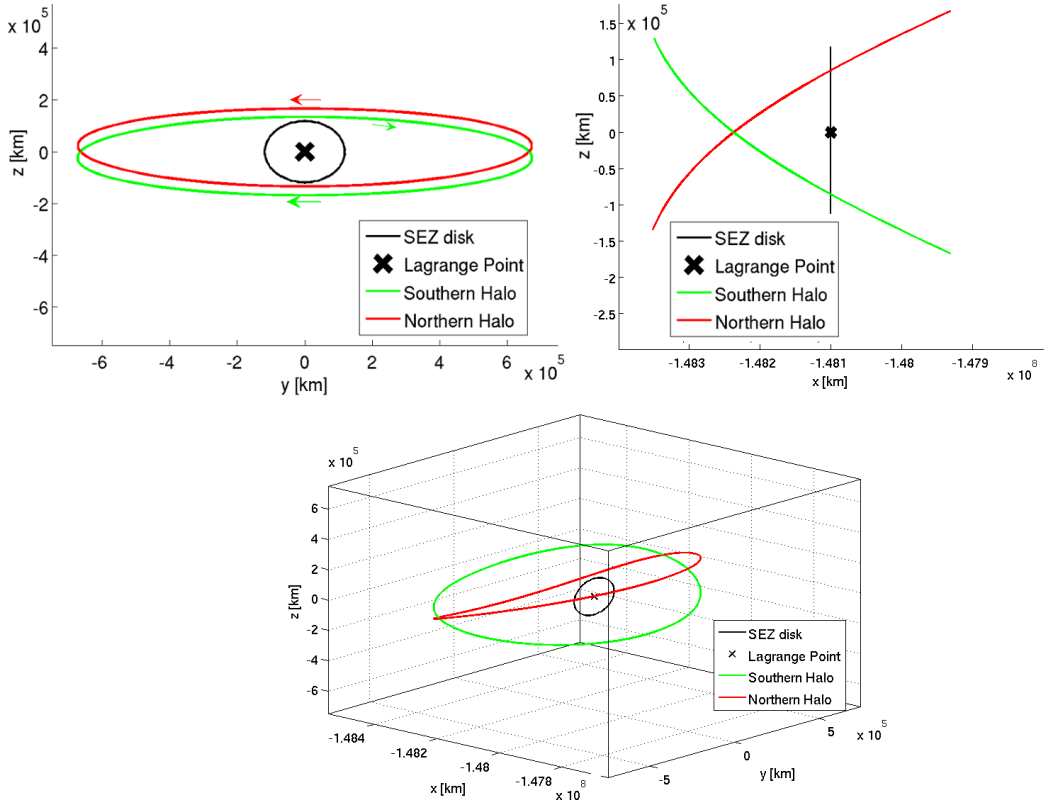

Figure 2.8: top-left: Northern and southern Halo orbits in yz-plane with flight direction (arrows) **top-right:** Northern and southern Halo orbit in xz-plane **bottom:** Isometric plot

These orbits form a torus around the Halo, such that spacecrafts on a Quasi-Halo orbit can circle around a spacecraft on an inner Halo orbit. A detailed analytical and numerical treatment of Quasi-Halo orbits can be found in [Gómez *et al.* , 1997] and [Gómez *et al.* , 1998]. These trajectories are of special interested for formation flying. For example Howell & Barden [1999] made numerical studies on a constellation consisting of 6 spacecraft distributed evenly on a circle with radii of 100 km and 1000 km (see fig. 2.9). The constellation experiences distortions during an orbital period, but can be maintained with low costs in terms of ΔV. Since the required ΔV increases approximately linearly with the radius size [Howell & Barden, 1999], this scheme seems unfeasible for LISA-like applications with armlengths of $\approx 10^6$ km. However, these trajectories might be of interest for smaller space-based gravitational wave detectors.

During a lecture week[5] *in 2011 a combination of Halo and Quasi-Halo orbits was suggested to host an octahedral gravitational wave detector consisting of six S/C. However, the deformation of the constellation and formation control possibilities were not investigated. A paper describing the detector concept is being prepared.*

2.3 Analytical Determination of Reference Orbits

We would like now to compute analytical expressions for the trajectories from previous section, so we can search for constellations of three spacecrafts on these orbits. Since the solution for the linearized equations of motion (up to first order in x,y,z) is known (eq. (2.22)-(2.24)), it will serve as the initial point to develop a series solv-

[5] IMPRS Lecture Week in Palma de Mallorca, Spain, November 2011, organized for PhD students of the Albert-Einstein-Institute

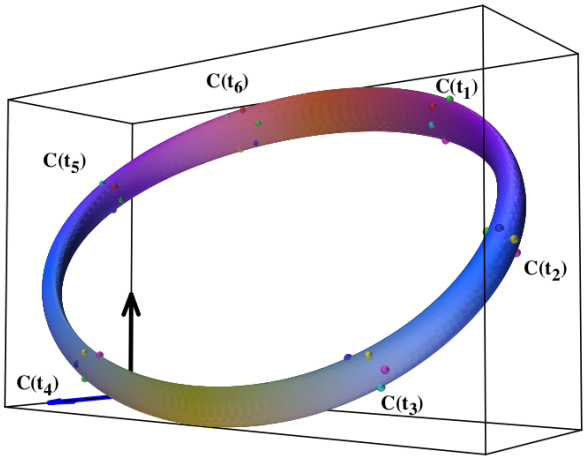

Figure 2.9: Quasi-Halo orbits: six spacecrafts (dots with different colors) on a natural torus enveloping a periodic Halo orbit (from Howell & Barden [1999])

ing higher orders of the equations of motion using the so-called Lindstedt-Poincaré method from perturbation theory. Farquhar & Kamel [1973] and Richardson [1980] used this approach to obtain results up to third order in x,y,z. However, it is a lengthy and tedious work [Richardson, 1980] and requires an algebraic manipulation software for high orders. As shown in the books by Gómez [2001] this approach can be automatized to derive solutions even up to orders > 20.

2.3.1 Lindstedt-Poincaré Method

The Lindstedt-Poincaré method can be used to obtain a solution to a non-linear differential equation of the form [Mickens, 1981]

$$\ddot{u} + \omega_0^2 \cdot u + \epsilon \cdot f(u, \dot{u}) = 0, \tag{2.30}$$

where ϵ is a small parameter and f is an arbitrary function of two parameters. The zeroth order in ϵ yields a harmonic oscillation with fundamental frequency ω_0. A common approach to obtain a solution for the non-linear differential equation is to use a perturbation series ansatz

$$u = y_0 + \epsilon y_1 + \epsilon^2 y_2 + ... = \sum_{n=0}^{\infty} \epsilon^n \cdot y_n, \tag{2.31}$$

and then to solve the differential equations for each order of ϵ recursively, e.g. the solution for the zeroth order in ϵ has to be used in the equation of first order in ϵ and so on. However, it turns out that the solution can contain unphysical secular terms[6], because the series expansion retains only a finite number of terms [Mickens, 1981]. Therefore, the astronomer Lindstedt introduced a new time variable τ, which is given by

$$\tau = t \cdot \omega = t \cdot (1 + \epsilon \cdot \omega_1 + \epsilon^2 \cdot \omega_2 + ...), \tag{2.32}$$

to suppress the secular terms by choosing properly ω_i $(i > 0)$ and to take into account the fact that non-linearities can also alter the fundamental frequency.

[6] terms of the form $t^n \cdot \cos(t)$ or $t^n \cdot \sin(t)$ are called secular terms [Mickens, 1981]

As an example we take the so-called *Duffing* equation [Nayfeh, 2008, p.58]

$$\frac{d^2u}{dt^2} + u + \epsilon \cdot u^3 = 0, \tag{2.33}$$

and rescale the time according to eq. (2.32)

$$\frac{d^2u}{d\tau^2} + (1 + \epsilon \cdot \omega_1 + ...)^2 \cdot (u + \epsilon \cdot u^3) = 0. \tag{2.34}$$

Then we substitute eq. (2.31) into eq. (2.34) and obtain the sum

$$\left(\frac{d^2y_0}{d\tau^2} + y_0\right) \tag{2.35}$$

$$+ \epsilon \cdot \left(\frac{d^2y_1}{d\tau^2} + y_1 + y_0^3 + 2 \cdot \omega_1 \cdot y_0\right) \tag{2.36}$$

$$+ \epsilon^2 \cdot \left(\frac{d^2y_2}{d\tau^2} + y_2 + \omega_1^2 \cdot y_0 + 2 \cdot \omega_2 \cdot y_0 + 2 \cdot \omega_1 \cdot y_0^3 + 2 \cdot \omega_1 \cdot y_1 + 3 \cdot y_0^2 \cdot y_1\right) \tag{2.37}$$

$$+ \mathcal{O}\left(\epsilon^3\right) = 0. \tag{2.38}$$

One can now solve each order of ϵ separately. The first line (2.35) is of order ϵ^0 and leads to the fundamental solution y_0:

$$y_0(\tau) = a \cdot \sin(\tau + \phi), \tag{2.39}$$

while the second line (order ϵ^1) can be transformed using y_0 and trigonometric identities to

$$\left(\frac{d^2y_1}{d\tau^2} + y_1 + y_0^3 + 2 \cdot \omega_1 \cdot y_0\right) = 0 \tag{2.40}$$

$$\Leftrightarrow \quad \frac{d^2y_1}{d\tau^2} + y_1 = \frac{a^3}{4} \cdot \sin(3 \cdot (\tau + \phi)) + \sin(\tau + \phi) \cdot \frac{3a^3 + 8a\omega_1}{4}. \tag{2.41}$$

Terms on the right hand side proportional to $\sin(\tau)$ or $\cos(\tau)$ will yield secular terms in the final solution and can be avoided here by choosing

$$\omega_1 = -\frac{3}{8}a^2. \tag{2.42}$$

We can prove this by solving the differential equation directly (e.g. with `Mathematica`):

$$y_1(\tau) = \frac{-a^3}{32}\sin(3 \cdot (\tau + \phi)) - \frac{3 \cdot a^3 + 8 \cdot a \cdot \omega_1}{16}\sin(\tau + \phi) + \tau\frac{3 \cdot a^3 + 8 \cdot a \cdot \omega_1}{8}\cos(\tau + \phi). \tag{2.43}$$

We note that the (last) secular term proportional to τ vanishes, if eq. (2.42) is fulfilled. The solution of y_0 and y_1 could now be used to solve the differential equation for y_2 and so on. However, we give the final solution for eq. (2.33) only up to first order in ϵ as

$$u(t) = y_0(t) + \epsilon \cdot y_1(t) = a \cdot \sin(\omega t + \phi) - \epsilon\frac{a^3}{32}\sin(3 \cdot (\omega t + \phi)) \tag{2.44}$$

with $\omega = 1 - \epsilon \cdot 3/8 \cdot a^3$.

2.3.2 Lissajous orbits up to 3rd order

We will now sketch the Lindstedt-Poincaré procedure to develop an analytical expressions of the Lissajous trajectories for the equations of motion up to third order in x,y,z (eq. (2.15)-(2.17)). Thus, recall the equations of motion

$$\begin{pmatrix} \ddot{x} - 2\dot{y} - (1+2c_2)x \\ \ddot{y} + 2\dot{x} - (1-c_2)y \\ \ddot{z} + c_2 z \end{pmatrix} = \begin{pmatrix} +\frac{3}{2}c_3(2x^2 - y^2 - z^2) + 2c_4 x(2x^2 - 3y^2 - 3z^2) \\ -3c_3 xy - \frac{3}{2}c_4 y(4x^2 - y^2 - z^2) \\ -3c_3 xz - \frac{3}{2}c_4 z(4x^2 - y^2 - z^2) \end{pmatrix}, \tag{2.45}$$

and note that the terms containing c_3 are of second order in the amplitudes, and c_4 terms are of third order in x, y, z. Then we can use the following perturbation series ansatz for the orbit

$$\vec{q}(t, \omega_{xy}, \omega_z) = \begin{pmatrix} q_x^{(0)}(\omega_{xy} t) \\ q_y^{(0)}(\omega_{xy} t) \\ q_z^{(0)}(\omega_z t) \end{pmatrix} + \epsilon \begin{pmatrix} q_x^{(1)}(\omega_{xy} t) \\ q_y^{(1)}(\omega_{xy} t) \\ q_z^{(1)}(\omega_z t) \end{pmatrix} + \epsilon^2 \begin{pmatrix} q_x^{(2)}(\omega_{xy} t) \\ q_y^{(2)}(\omega_{xy} t) \\ q_z^{(2)}(\omega_z t) \end{pmatrix}, \tag{2.46}$$

where the subscript indicates the component (x,y, or z), while the superscript indicates the order. Since we already know that the solution of the linearized equations of motion are Lissajous orbits with in-plane frequency λ and out-of-plane frequency ν, two separate frequencies are used in the Lindstedt-Poincaré method:

$$\omega_{xy} = \omega_{xy}^{(0)} + \epsilon \cdot \omega_{xy}^{(1)} + \epsilon^2 \cdot \omega_{xy}^{(2)}, \tag{2.47}$$

$$\omega_z = \omega_z^{(0)} + \epsilon \cdot \omega_z^{(1)} + \epsilon^2 \cdot \omega_z^{(2)}. \tag{2.48}$$

We substitute the ansatz eq. (2.46) into eq. (2.45) and perform a series expansion in ϵ on both sides. For each power of ϵ we obtain differential equations, which we can solve recurrently. This *classical* approach is a tedious process with lengthy expressions and requires solving differential equations in each step.
However, one notices during the development of the solution, that the final trajectory can be written as a power series in the amplitudes A_y and A_z. Using the ansatz [Canalias *et al.* , 2004, p. 85]

$$\vec{q}_{\mathrm{LJ}} = \begin{pmatrix} x(t) \\ y(t) \\ z(t) \end{pmatrix} = \sum_{i,j=1}^{\infty} \left(\sum_{|k|<i, |m|<j} \begin{pmatrix} x_{ijkm} \cdot \cos(k\theta_1 + m\theta_2) \\ y_{ijkm} \cdot \sin(k\theta_1 + m\theta_2) \\ z_{ijkm} \cdot \cos(k\theta_1 + m\theta_2) \end{pmatrix} \cdot A_y^i A_z^j \right), \tag{2.49}$$

with

$$\theta_1 = \omega_{xy} t + \phi \tag{2.50}$$

$$\theta_2 = \omega_z t + \psi \tag{2.51}$$

$$\omega_{xy} = \sum_{i,j=0}^{\infty} \omega_{xy,ij} A_y^i A_z^j \tag{2.52}$$

$$\omega_z = \sum_{i,j=0}^{\infty} \omega_{z,ij} A_y^i A_z^j, \tag{2.53}$$

we can directly determine the coefficients x_{ijkm}, y_{ijkm}, z_{ijkm}, $\omega_{xy,ij}$ and $\omega_{z,ij}$ recurrently up to a particular order $N = i + j$ without solving differential equations.

First order: $N = 1$

From the solution of the linearized equations of motion (eq. (2.24)) we can directly deduce the first non-zero constants:

$$\omega_{xy,00} = \lambda, \qquad \omega_{z,00} = \nu, \qquad x_{1010} = -1/k, \qquad y_{1010} = 1, \qquad z_{0101} = 1. \tag{2.54}$$

Second order: $N = 2$

To obtain the coefficients of the second order we substitute eq. (2.49) into eq. (2.45). Then we dismiss all terms with larger or smaller amplitude order than $N = 2$ (keep terms with $i + j = 2$ in $A_y^i A_z^j$). The smaller orders have been solved already, while the larger orders will be solved subsequently. The right-hand-side contains only known terms and variables. The left-hand-side has also the unknown coefficients of order $N = 2$. We can bring all terms on one side and zero each prefactor of the sine and cosine terms by solving a linear system, which yields the unknown coefficients:

$$x_{0200} = \frac{3c_3}{8c_2 + 4}, \qquad x_{2000} = \frac{3c_3\left(k^2 - 2\right)}{4(2c_2 + 1)k^2}, \tag{2.55}$$

$$x_{2020} = -\frac{c_3\left(9\left(3c_2^2 - 4\right)k + 2(9c_2 + 32)\lambda\right)}{4\left(2\left(18c_2^2 + 23c_2 + 32\right)\lambda + \left(54c_2^3 + 21c_2^2 - 32c_2 - 52\right)k\right)}, \tag{2.56}$$

$$x_{0202} = \frac{3(3c_2c_3 + c_3)}{72c_2^2 - 28c_2 + 4}, \qquad y_{0202} = -\frac{3c_3\nu}{18c_2^2 - 7c_2 + 1}, \tag{2.57}$$

$$y_{2020} = -\frac{c_3\left(18c_2^2 + 9c_2\lambda^2 - 7c_2 + 4\lambda^2 - 8\right)}{2\left(2\left(18c_2^2 + 23c_2 + 32\right)\lambda + \left(54c_2^3 + 21c_2^2 - 32c_2 - 52\right)k\right)}, \tag{2.58}$$

$$z_{1111} = -\frac{3c_3}{2k\lambda^2 + 4k\lambda\nu}, \qquad z_{111(-1)} = -\frac{3c_3}{2k\lambda^2 - 4k\lambda\nu} \tag{2.59}$$

Third order: $N = 3$

The coefficients of third order are obtained in the same way as for the second order. They can be found in Appendix A.

Evaluation and Validation

The Lissajous orbits obtained here depend on two amplitudes and two phase angles

$$\vec{q}_{\mathrm{LJ}}(t) = \vec{q}_{\mathrm{LJ}}(t, A_y, A_z, \phi, \psi), \tag{2.60}$$

where the special case of $A_z = 0, A_y \neq 0$ provides the planar (horizontal) Lyapunov orbits and $A_z \neq 0, A_y = 0$ yields vertical Lyapunov orbits (see fig. 2.10). A variety of orbit shapes and sizes can be adjusted with the four parameters, but they usually enter the SEZ after some time, since the trajectories are not periodic.
The frequency of the in-plane and out-of-plane component is depicted in fig. 2.11. For large A_y ($\approx 10^6$ km) both frequencies can be matched due to non-linear contributions, which results in the Halo orbits. One should keep in mind that the actual size of the orbit may differ from the amplitudes A_y and A_z (for orders > 1), because the higher-order terms also influence the size of the orbit.
A method to validate the expressions is to compute the amount of ΔV required to stay on the trajectory when a continuous (perfect) thruster compensates the residual acceleration, which tries to pull the spacecraft from the trajectory. The acceleration in the CR3BP without any approximation can be written as (eq. (2.9)-(2.11))

$$\vec{f}(\vec{q}) = \begin{pmatrix} 2\dot{y} + \frac{\partial U}{\partial x}(x, y, z) \\ -2\dot{x} + \frac{\partial U}{\partial y}(x, y, z) \\ \frac{\partial U}{\partial z}(x, y, z) \end{pmatrix} \tag{2.61}$$

for a trajectory $\vec{q}(t) = (x(t), y(t), z(t))^{\mathsf{T}}$ and at a time t. The integrated difference between the acceleration of a free-falling satellite and the second derivative of the

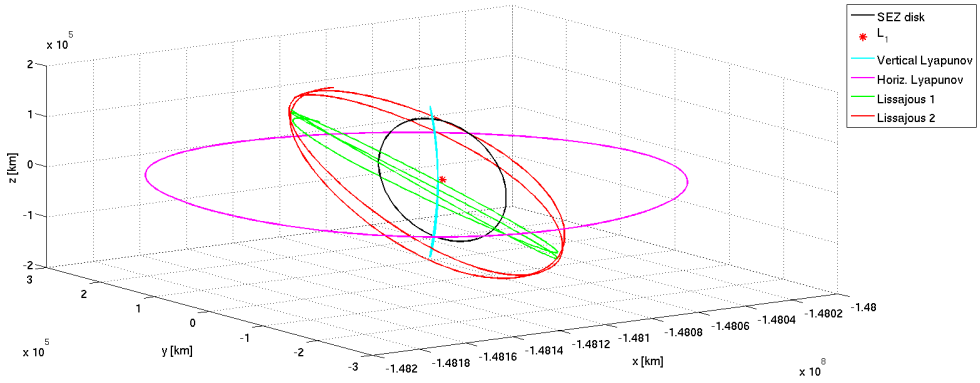

Figure 2.10: Different Lissajous orbits obtained from the third order solution.

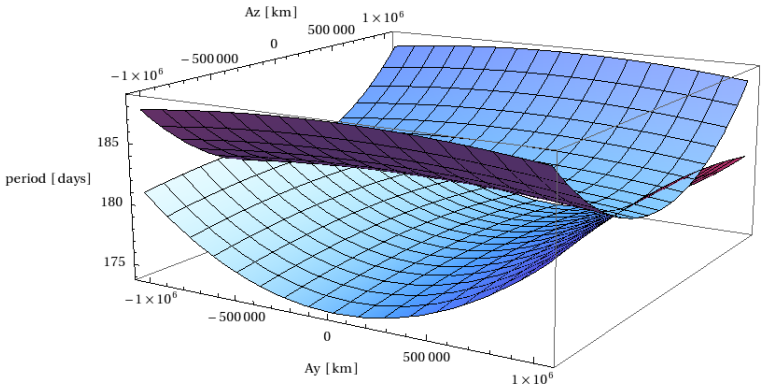

Figure 2.11: Frequencies of Lissajous orbits around L_1 v.s. the amplitudes A_y and A_z in the third order solution. The upper surface shows the dependency of the out-of-plane frequency $(\omega_{z,00} + \omega_{z,20} \cdot A_y^2 + \omega_{z,02} \cdot A_z^2)$, while the lower one the in-plane frequency $(\omega_{xy,00} + \omega_{xy,20} \cdot A_y^2 + \omega_{xy,02} \cdot A_z^2)$.

orbit trajectory yields the ΔV value:

$$\Delta V = \int_{t_0}^{t_e} \left| \ddot{\vec{q}}_{\mathrm{LJ}}(t) - \vec{f}(t, \vec{q}_{\mathrm{LJ}}) \right| \mathrm{d}t. \tag{2.62}$$

Some numerical examples can be found in table 2.2. The amount of ΔV decreases with higher orders of the solution, showing that the trajectory is becoming more accurate. However, the ΔV increases with the orbit size and even higher orders would be beneficial to model correctly large Lissajous orbits.

Amplitude in km		Phase in rad		ΔV in m/s		
A_y	A_z	ϕ	ψ	Order 1	Order 2	Order 3
1 000 000	0	0.0	0.0	932.8	847.1	204.5
600 000	600 000	0.0	0.0	620.4	473.5	219.7
600 000	600 000	0.6	0.0	618.9	478.9	196.9
60 000	60 000	0.0	0.0	6.7	0.31	0.023

Table 2.2: ΔV values for some Lissajous orbits around L_1 with integration time $t_e - t_0 = 1/2\,\mathrm{yr}$ and for different orders of the solution. The initial conditions are the four columns on the left side.

2.3.3 Halo orbits up to 3rd order

The classical Lindstedt-Poincaré approach can also be used to compute an analytical expression for Halo orbits. Therefore, one usually starts with re-arranged equations of motion

$$\begin{pmatrix} \ddot{x} - 2\dot{y} - (1+2c_2)x \\ \ddot{y} + 2\dot{x} - (1-c_2)y \\ \ddot{z} + \lambda^2 z \end{pmatrix} = \begin{pmatrix} +\frac{3}{2}c_3(2x^2 - y^2 - z^2) + 2c_4 x(2x^2 - 3y^2 - 3z^2) \\ -3c_3 xy - \frac{3}{2}c_4 y(4x^2 - y^2 - z^2) \\ -3c_3 xz - \frac{3}{2}c_4 z(4x^2 - y^2 - z^2) + z \cdot \Delta \end{pmatrix}, \tag{2.63}$$

where the c_2 coefficient in the z-component on the left-hand side has been replaced by λ^2 and on the right-hand-side a term with $\Delta = \lambda^2 - c^2$ was introduced. One needs to assume that Δ is of the same order as c_4, meaning that this term is only treated in orders $\geqslant 3$.
The solution of the linear order in x,y,z is now the periodic trajectory given by

$$\vec{q}^{(0)} = \begin{pmatrix} x(t) \\ y(t) \\ z(t) \end{pmatrix} = \begin{pmatrix} -\frac{A_y}{k}\cos(\lambda t + \phi) \\ A_y \sin(\lambda t + \phi) \\ A_z \cos(\lambda t + \psi) \end{pmatrix} \tag{2.64}$$

with single frequency λ. Using a perturbation series ansatz

$$\vec{q}(t) = \vec{q}^{\,(0)}(\omega t) + \epsilon \cdot \vec{q}^{\,(1)}(\omega t) + \epsilon \cdot \vec{q}^{\,(2)}(\omega t) \tag{2.65}$$

with $\omega = 1 + \epsilon \cdot \omega^{(1)} + \epsilon^2 \cdot \omega^{(2)}$ one can determine recurrently the higher orders. One needs to constrain the amplitudes A_y, A_z as well as the phases ϕ, ψ to remove all secular terms. Since solving the differential equations in each step is a tedious process with lengthy expressions, we assume a formal expansion in powers of the amplitude as ansatz [Canalias *et al.* , 2004, p. 86]

$$\begin{pmatrix} x(t) \\ y(t) \\ z(t) \end{pmatrix} = \sum_{i,j=1}^{\infty} \left(\sum_{|k|,|m|<i+j} \begin{pmatrix} x_{ijkm} \cdot \cos(k\theta_1 + m\theta_2) \\ y_{ijkm} \cdot \sin(k\theta_1 + m\theta_2) \\ z_{ijkm} \cdot \cos(k\theta_1 + m\theta_2) \end{pmatrix} \cdot A_y^i A_z^j \right), \tag{2.66}$$

with

$$\theta_1 = \omega t + \phi, \tag{2.67}$$

$$\theta_2 = \omega t + \psi, \tag{2.68}$$

$$\omega = \sum_{i,j=0}^{\infty} \omega_{ij} A_y^i A_z^j. \tag{2.69}$$

One should note that these equations provide periodic orbits, because only one frequency appears in the ansatz. To simplify the computation of the amplitude relationship, we use the following slightly modified equations of motion:

$$\begin{pmatrix} \ddot{x} - 2\dot{y} - (1+2c_2)x \\ \ddot{y} + 2\dot{x} - (1-c_2)y \\ \ddot{z} + c_2 z \end{pmatrix} = \begin{pmatrix} +\frac{3}{2}c_3(2x^2 - y^2 - z^2) + \cdot 2c_4 x(2x^2 - 3y^2 - 3z^2) + \mathcal{O}(A^4) \\ -3c_3 xy - \frac{3}{2}c_4 y(4x^2 - y^2 - z^2) + \mathcal{O}(A^4) \\ -3c_3 xz - \frac{3}{2}c_4 z(4x^2 - y^2 - z^2) + z \cdot \Delta(A_y, A_z) + \mathcal{O}(A^4) \end{pmatrix}, \tag{2.70}$$

with

$$\Delta(A_y, A_z) = \sum_{i,j=0} d_{ij} A_y^i A_z^j. \tag{2.71}$$

If the amplitude relationship $\Delta(A_y, A_z) = 0$ is fulfilled, the term $z \cdot \Delta(A_y, A_z)$ on the right-hand-side vanishes and eq. (2.70) is equal to the unmodified equations of motion (eq. (2.15)-(2.17)).

First Order: $N = 1$

From eq. (2.64) we deduce the first non-zero coefficients

$$\omega_{00} = \lambda \qquad x_{1010} = -1/k, \qquad y_{1010} = 1, \qquad z_{0101} = 1 \tag{2.72}$$

and substitute the first order trajectory into the equations of motion (eq. 2.70). Taking the first amplitude order on both sides yields

$$\begin{pmatrix} 0 \\ 0 \\ A_z(c_2 - \lambda^2) \cdot \cos(\lambda t + \psi) \end{pmatrix} = \begin{pmatrix} 0 \\ 0 \\ A_z d_{00} \cdot \cos(\lambda t + \psi) \end{pmatrix} \tag{2.73}$$

and hence the first coefficient of the amplitude relationship:

$$d_{00} = c_2 - \lambda^2. \tag{2.74}$$

Second Order: $N = 2$

Using the second amplitude order (on both sides) we can determine a linear system, which zeros each term. This yields the (non-zero) coefficients:

$$x_{0200} = \frac{3c_3}{8c_2 + 4}, \qquad x_{2000} \frac{3c_3\left(k^2 - 2\right)}{4(2c_2 + 1)k^2}, \tag{2.75}$$

$$x_{2020} = \frac{c_3\left(18c_2^2 + c_2\left(9\lambda^2 - 23\right) + 32\lambda^2 - 4\right)}{16k^2\left(-10c_2^2 + c_2\left(4\lambda^2 + 5\right) - 8\lambda^2 + 5\right)}, \tag{2.76}$$

$$x_{0202} = -\frac{3c_3\left(c_2 - 4\lambda^2 - 1\right)}{4\left(-2c_2^2 + 4c_2\lambda^2 + c_2 + \left(1 - 4\lambda^2\right)^2\right)}, \tag{2.77}$$

$$y_{2020} = \frac{c_3(3(c_2 - 1)k + 2\lambda)}{2k^2\left(-10c_2^2 + c_2\left(4\lambda^2 + 5\right) - 8\lambda^2 + 5\right)}, \tag{2.78}$$

$$y_{0202} = -\frac{3c_3\lambda}{-2c_2^2 + 4c_2\lambda^2 + c_2 + \left(1 - 4\lambda^2\right)^2}, \tag{2.79}$$

$$z_{1111} = -\frac{3c_3}{6c_2k - 8k + 16\lambda}, \qquad z_{111(-1)} = \frac{3c_3}{2c_2k} \tag{2.80}$$

Third Order: $N = 3$

Substituting the trajectory of second order into the eq. (2.70) and taking only the third order terms into account yields a system of equations, which can not be solved without further assumptions. To obtain the Halo orbits we have to constrain the phases to obey

$$\cos(\phi - \psi) = \pm 1 \quad \Leftrightarrow \quad \psi = \phi + n\pi, \quad n \in \{0, 1\}. \tag{2.81}$$

This phase-relationship has a $\pi/2$ offset compared to the phase relationship in eq. (2.29) [Richardson, 1980], since we used a cosine in the z-component of the ansatz (eq. (2.66)) instead of a sine.
With this phase constraint one can solve the linear system and obtains the coefficients given in appendix B. We note that the coefficients do not depend on the phase-angle switch n. In [Richardson, 1980] the assumption $A_z \geqslant 0, A_x \geqslant 0$ was made and n was used as a switch for the two types of Halo orbits. We can omit the n, when we allow also negative amplitude values. The type of the orbit (northern/southern) depends then on $\operatorname{sgn}(A_y) \cdot \operatorname{sgn}(A_z)$ and on the Libration point under investigation.

Finally, the Halo orbits can be written in the compact form

$$\begin{aligned}
x &= -A_y/k \cdot \cos(\tau_1) + A_y^2 \cdot x_{2000} + A_z^2 \cdot x_{0200} + (A_y^2 \cdot x_{2020} + A_z^2 \cdot \cdot x_{0202}) \cdot \cos(2\tau_1) \\
&\quad + (A_y^3 \cdot x_{3030} + A_y \cdot A_z^2 x_{1212}) \cdot \cos(3\tau_1) \\
y &= (A_y + A_y \cdot A_z^2 \cdot y_{1210} + A_y^3 \cdot y_{3010}) \cdot \sin(\tau_1) + (A_y^2 \cdot y_{2020} + A_z^2 \cdot y_{0202}) \cdot \sin(2\tau_1) \\
&\quad + (A_y^3 \cdot y_{3030} + A_y \cdot A_z^2 \cdot y_{1212}) \cdot \sin(3\tau_1) \\
z &= A_z \cdot \cos(\tau_1) + A_y \cdot A_z \cdot z_{111(-1)} + A_y \cdot A_z \cdot z_{1111} \cdot \cos(2\tau_1) \\
&\quad + (A_z^3 \cdot z_{3030} + A_y^2 \cdot A_z \cdot z_{2121}) \cdot \cos(3\tau_1)
\end{aligned} \tag{2.82}$$

with time and frequency dependency

$$\tau_1 = \omega \cdot t + \phi = (\lambda + A_y^2 \cdot \omega_{20} + A_z^2 \cdot \omega_{02}) \cdot t + \phi \tag{2.83}$$

and amplitude constraint

$$d_{0,0} + A_y^2 \cdot d_{20} + A_z^2 \cdot d_{02} = 0. \tag{2.84}$$

As pointed out in [Gómez, 2001, p. 56] the term $A_y \cdot A_z^2 \cdot y_{1210} + A_y^3 \cdot y_{3010}$ in the y-component of eq. (2.82) is missing in [Richardson, 1980] (and [Richardson, 1980b]).

Evaluation and Validation

The Halo families around the L_1 and L_2 point bifurcate from the horizontal Lyapunov orbit. They form a kind of *funnel* (see fig. 2.12) originating at the Lyapunov orbit (green traces) and opening towards the Earth+Moon.
A Halo orbit in the third order approximation is fully characterized with the A_z amplitude, since the amplitude relationship provides A_y (fig. 2.7). Orbits around L_1 have almost the same size as orbits around L_2. However, the orbit period is slightly different for Halos around L_1 than around L_2, as one can see on fig. 2.13.
The accuracy of the obtained analytical expression is assessed again with the amount of ΔV required to stay on the orbits (eq. 2.62), which is tabulated for some orbits in table 2.3.

Amplitude in km	ΔV in m/s		
A_z	Order 1	Order 2	Order 3
1 000 000	2024.4	4822.1	447.26
600 000	1014.45	1063.43	114.51
60 000	420.35	191.70	36.42
0*	414.79	186.32	35.93

Table 2.3: ΔV values for some Halo orbits around L_1 with integration time $t_e - t_0 = 1/2\,\mathrm{yr}$ and for different orders. The amplitude relationship of the third order was also used for the second and first order. *: corresponds to a horizontal Lyapunov orbit.

2.4 Numerical Determination of Periodic Reference Orbits

The analytical expressions obtained in the previous section are only valid for small amplitudes, since only the first three amplitude orders have been considered in the series expansion of the equations of motion. However, the analytical solutions can be used to derive numerically trajectories in the full CR3BP. Therefore, we will utilize the differential correction method, which is explained in the next section.

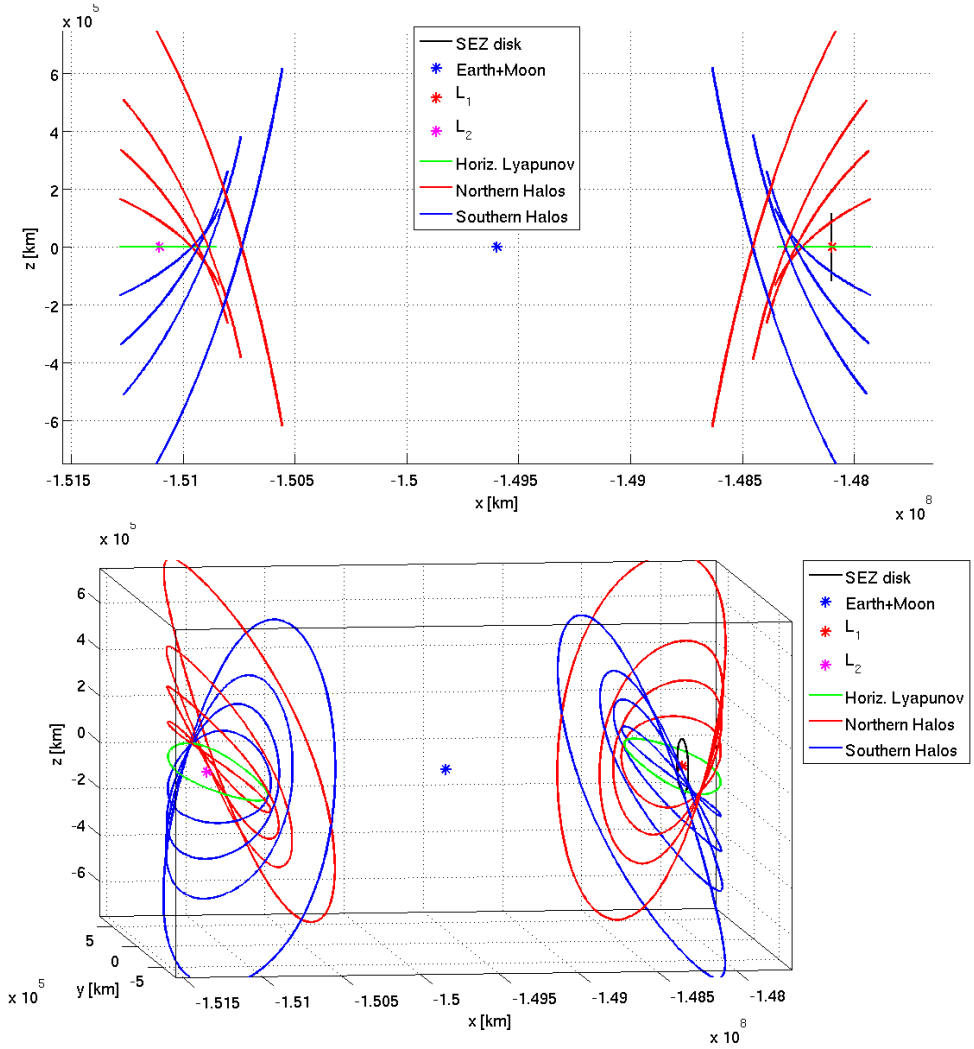

Figure 2.12: The two families of Halo orbits around L_1 and L_2 in xz (top) and isometric (bottom) view.

2.4.1 Differential Correction method

The differential correction method is based on the Newton's method and is a powerful tool for targeting problems. Assume a spacecraft with initial state $\vec{s}_0^{\,(0)} = (\vec{r}_0, \dot{\vec{r}}_0)^\mathsf{T}$ at time t_0 propagating in the CR3BP to the final state $\vec{s}_f^{\,(0)} = (\vec{r}_f, \dot{\vec{r}}_f)^\mathsf{T}$ at time t_f, which we will also write as

$$\vec{s}_f^{\,(0)} = \mathcal{P}(\vec{s}_0^{\,(0)}, t_0, t_f, \text{CR3BP}). \tag{2.85}$$

The propagation is obtained by a numerical integration, for example, with a Runge-Kutta method. Let $\vec{s}_t$ be the target state at the time t_f. We wish to compute a variation in initial state $\delta\vec{s}_0$, which yields a new initial state $\vec{s}_{0t} = \vec{s}_0 + \delta\vec{s}_0$. This new initial state shall propagate to the target state:

$$\vec{s}_t(t_f) = (\vec{r}_t, \dot{\vec{r}}_t)^\mathsf{T} = \mathcal{P}(\vec{s}_{0t}, t_0, t_f, \text{CR3BP})_{|t_f}. \tag{2.86}$$

Subtracting eq. (2.85) from eq. (2.86) and linearization of $\mathcal{P}$ in the first argument around $\vec{s}_0^{\,(0)}$ provides

$$\delta\vec{s}_{tf}^{\,(0)} = \vec{s}_t - \vec{s}_f^{\,(0)} \approx \hat{\Phi}_{(0)} \cdot \delta\vec{s}_0^{\,(0)}, \tag{2.87}$$

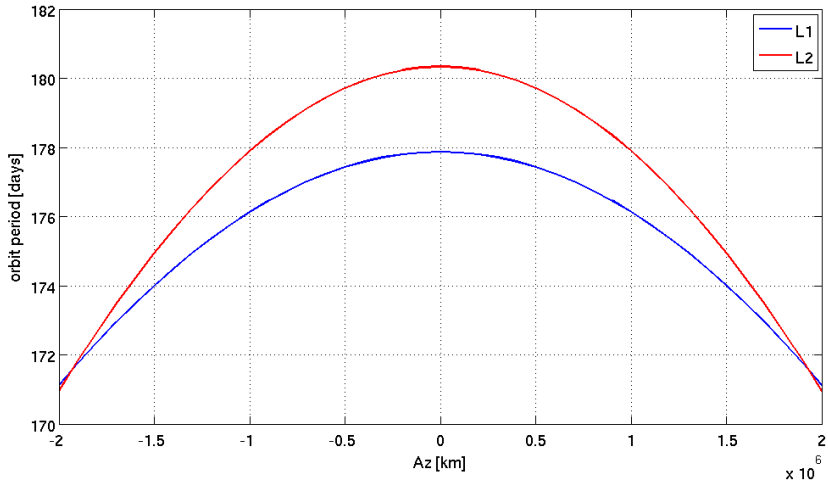

Figure 2.13: Orbit periods for Halo orbits around L_1 and L_2 in the third order solution.

where $\widehat{\Phi}$ is the state transition matrix relating a variation of the input parameter to a variation of the output parameter. If $\widehat{\Phi}$ is invertible, the sought initial state can be computed iteratively (like in Newton's method) with

$$\vec{s}_0^{\,(n+1)} = \vec{s}_0^{\,(n)} + \delta\vec{s}_0^{\,(n)} = \vec{s}_0^{\,(n)} + \widehat{\Phi}_{(n)}^{-1} \cdot \delta\vec{s}_{tf}^{\,(n)}, \tag{2.88}$$

whereas for convergence

$$\lim_{n\to\infty} \vec{s}_0^{\,(n+1)} = \vec{s}_{0t} \tag{2.89}$$

a good initial guess is required ($||\vec{s}_0^{\,(0)} - \vec{s}_t|| < \epsilon$) in general. The state transition matrix consists of partial derivatives of the output parameters (final state) w.r.t. the input parameters (initial state),

$$(\widehat{\Phi})_{ij} = \frac{\partial(\vec{s}_f)_j}{\partial(\vec{s}_0)_i}, \tag{2.90}$$

and can be computed in general with a numerical differentiation scheme,

$$(\widehat{\Phi})_{ij} = \frac{(\mathcal{P}(\vec{s}_0 + \delta\vec{\epsilon}_j, t_0, t_f, \text{CR3BP}) - \mathcal{P}(\vec{s}_0 - \delta\vec{\epsilon}_j, t_0, t_f, \text{CR3BP}))_i}{2 \cdot \epsilon}, \tag{2.91}$$

where the vector $\delta\vec{\epsilon}_j$ has only a single non-zero component at the j-th position with some small value ϵ. This method is very general and can be used even if the dynamical model (here CR3BP) is unknown or not well understood. Since the state transition matrix is a 6x6 matrix in case of a spacecraft with a state vector of 6 components (3 position and 3 velocity components), it requires multiple evaluations of trajectories, which might become very time consuming.
Another method to compute the state transition matrix, which requires only a single integration, exploits the fact that the state transition matrix is equal to the spatial differential of the flow generated by the differential equations of the dynamical model (see for example the excellent lecture notes on numerical celestial mechanics by J.D. Mireles James [James, 2006, Set 2, p. 3]). One can show [James, 2006] that the time derivative of the state transition matrix for the CR3BP can be written as

$$\frac{\mathrm{d}\widehat{\phi}}{\mathrm{d}t} = \widehat{A}(t) \cdot \widehat{\Phi}(t, t_0) \tag{2.92}$$

with

$$\widehat{A}(t)_{6x6} = \begin{pmatrix} 0_{3x3} & \mathbb{1}_{3x3} \\ (U_{xx})_{3x3} & \Omega_{3x3} \end{pmatrix}, \qquad \Omega_{3x3} = \begin{pmatrix} 0 & 2 & 0 \\ -2 & 0 & 0 \\ 0 & 0 & 0 \end{pmatrix} \tag{2.93}$$

and U_{xx} being the second derivatives of the CR3BP potential (eq. 2.8). Since the initial value

$$\widehat{\Phi}(t_0, t_0) = \mathbb{1}_{6x6} \tag{2.94}$$

is known, one can integrate numerically the 36 components of eq. (2.92), for example, together with the spacecraft state to obtain the state transition matrix for the final state.

So far we considered a targeting problem, where the arrival time t_f and all parameters of the final state are specified, while all six input parameters (position and velocity) are free. We assume now a more open problem, where we want to target only a position $\vec{p}_t$, but the final velocity and the arrival time are not specified. In addition only the initial velocity is a free parameter. To solve this problem, we use in an intermediate step an extended transition state matrix $\widehat{\Phi}_e$, which accounts also for a variation in the arrival time:

$$(\widehat{\Phi}_e)_{7x7} = \begin{pmatrix} & & & & & & v_x \\ & & & & & & v_y \\ & & \widehat{\Phi}_{6x6} & & & & v_z \\ & & & & & & a_x \\ & & & & & & a_y \\ & & & & & & a_z \\ v_x^{-1} & v_y^{-1} & v_z^{-1} & a_x^{-1} & a_y^{-1} & a_z^{-1} & 1 \end{pmatrix}, \tag{2.95}$$

with velocity $\dot{\vec{r}}(t_f) = (v_x, v_y, v_z)^\mathsf{T}$ and acceleration $\ddot{\vec{r}}(t_f) = (a_x, a_y, a_z)^\mathsf{T}$ at the arrival time t_f. The variational equation is

$$\begin{pmatrix} \delta\vec{p}_t \\ \delta\dot{\vec{p}}_t \\ \delta t_f \end{pmatrix}_{7x1} = (\widehat{\Phi}_e)_{7x7} \cdot \begin{pmatrix} \delta\vec{p}_0 \\ \delta\dot{\vec{p}}_0 \\ \delta t_f \end{pmatrix}_{7x1}, \tag{2.96}$$

where we note that δt_f is on the left and on the right hand side. Then, we use the extended matrix to derive a reduced matrix $\widehat{\Phi}_r$, which accounts only for the free parameters $(\dot{\vec{p}}_0, \delta t_f)$ and for the target parameters $(\vec{p}_t)$, by choosing the corresponding rows and columns. In this example we obtain:

$$\left(\delta\vec{p}_t\right)_{3x1} = (\widehat{\Phi}_r)_{3x4} \cdot \begin{pmatrix} \delta\dot{\vec{p}}_0 \\ \delta t_f \end{pmatrix}_{4x1} \tag{2.97}$$

with

$$(\widehat{\Phi}_r)_{3x4} = \begin{pmatrix} \widehat{\Phi}_{14} & \widehat{\Phi}_{15} & \widehat{\Phi}_{16} & v_x \\ \widehat{\Phi}_{24} & \widehat{\Phi}_{25} & \widehat{\Phi}_{26} & v_y \\ \widehat{\Phi}_{34} & \widehat{\Phi}_{35} & \widehat{\Phi}_{36} & v_z \end{pmatrix}. \tag{2.98}$$

We note that eq. (2.97) has an infinite number of solutions, since there are more free than target parameters (in other words: more free variables than equations). In this case we seek for a least-norm solution, which minimizes $||(\delta\dot{\vec{p}}_0, \delta t_f)^\mathsf{T}||_2$ in this example. This ensures that the imposed variations will be as small as possible.

In general the variational equation:

$$\delta(\vec{x}_f)_{m\times 1} = (\widehat{\Phi}_{m\times n}) \cdot \delta(\vec{x}_0)_{n\times 1} \tag{2.99}$$

can be solved using the following three different methods (as long as $\widehat{\Phi}$ has full rank and is well-conditioned)

- $m = n$: exact solution using the matrix inverse

$$\delta(\vec{x}_0) = \widehat{\Phi}^{-1} \cdot \delta(\vec{x}_f), \tag{2.100}$$

- $m > n$: over-determined system using the least-squares method

$$\delta(\vec{x}_0) = (\widehat{\Phi}^{\mathsf{T}}\widehat{\Phi})^{-1}\widehat{\Phi}^{\mathsf{T}} \cdot \delta(\vec{x}_f), \tag{2.101}$$

  which minimizes the residual norm $||(\widehat{\Phi}) \cdot \delta(\vec{x}_0) - \delta(\vec{x}_f)||_2$,

- $m < n$: under-determined system using the least-norm solution

$$\delta(\vec{x}_0) = \widehat{\Phi}^{\mathsf{T}}(\widehat{\Phi}\widehat{\Phi}^{\mathsf{T}})^{-1} \cdot \delta(\vec{x}_f), \tag{2.102}$$

  which minimizes the solution norm $||\delta(\vec{x}_0)||_2$.

These three solutions should be obtained using a QR or singular value decomposition (SVD), since these methods provide a better numerical stability than a direct implementation of eq. (2.101)-(2.102).[7]
With the above methods we solve eq. (2.97) and obtain an updated initial state:

$$\begin{pmatrix} \dot{\vec{p}}_0 \\ t_f \end{pmatrix} + \begin{pmatrix} \delta\dot{\vec{p}}_0 \\ \delta t_f \end{pmatrix}. \tag{2.103}$$

One can iteratively repeat the procedure, until the computed final position $\vec{p}_f$ reaches the target position $\vec{p}_t$ up to a certain precision ϵ. We use a short notation for the differential correction procedure

$$\vec{p}_f = \mathcal{D}(\vec{s}_0, t_0, t_f, \{\vec{p}_t\}, \{\dot{\vec{p}}_0, t_f\}, \epsilon), \tag{2.104}$$

where the first three parameters of $\mathcal{D}$ are the initial-guess parameters, the fourth parameter provides the target variables, the fifth the free variables, while the sixth parameter indicates that the final solution is only equal to the target solution within some defined precision ϵ.

2.4.2 Halo Orbits

The numerical determination of Halo orbits can be accomplished efficiently by exploiting the symmetries across the xz-plane. We can verify at the analytical expressions that the x and z component of the velocity vanishes on intersection of Halo orbit with the xz-plane. In case of a trajectory

$$\begin{pmatrix} x(t=t_0) \\ y(t=t_0) \\ z(t=t_0) \\ \dot{x}(t=t_0) \\ \dot{y}(t=t_0) \\ \dot{z}(t=t_0) \end{pmatrix} = \begin{pmatrix} x_0 \\ 0 \\ z_0 \\ 0 \\ \dot{y}_0 \\ 0 \end{pmatrix} \rightarrow \begin{pmatrix} x(t=t_1) \\ y(t=t_1) \\ z(t=t_1) \\ \dot{x}(t=t_1) \\ \dot{y}(t=t_1) \\ \dot{z}(t=t_1) \end{pmatrix} = \begin{pmatrix} x_1 \\ 0 \\ z_1 \\ 0 \\ \dot{y}_1 \\ 0 \end{pmatrix} \tag{2.105}$$

[7] It is well known that inverting the normal equations $((\widehat{\Phi}_r\widehat{\Phi}_r^{\mathsf{T}})^{-1})$ might lead to numerical problems. In this thesis a singular value decomposition was used, which was provided by the *Eigen C++ matrix library* (http://eigen.tuxfamily.org/) and directly computed the three different solution types.

the symmetry 2 in sec. 2.2.1 yields a periodic orbit, because backward integration provides

$$\begin{pmatrix} x(t=t_0) \\ y(t=t_0) \\ z(t=t_0) \\ \dot{x}(t=t_0) \\ \dot{y}(t=t_0) \\ \dot{z}(t=t_0) \end{pmatrix} = \begin{pmatrix} x_0 \\ 0 \\ z_0 \\ 0 \\ \dot{y}_0 \\ 0 \end{pmatrix} \rightarrow \begin{pmatrix} x(t=-t_1) \\ y(t=-t_1) \\ z(t=-t_1) \\ \dot{x}(t=-t_1) \\ \dot{y}(t=-t_1) \\ \dot{z}(t=-t_1) \end{pmatrix} = \begin{pmatrix} x_1 \\ 0 \\ z_1 \\ 0 \\ \dot{y}_1 \\ 0 \end{pmatrix}. \tag{2.106}$$

In other words, it is sufficient to compute only half of the Halo orbit, since the second half is symmetric. One can now use a differential corrector to aim for the above conditions:

$$\{\vec{s}_f\} = \mathcal{D}(\vec{s}_0, t_0, t_1, \{y_t = 0, \dot{x}_t = 0, \dot{z}_t = 0\}, \{z_0, \dot{y}_0, t_1\}, \epsilon), \tag{2.107}$$

where the initial position and velocity $\vec{s}_0 = (x_0, 0, z_0, 0, \dot{y}_0, 0)^\mathsf{T}$ and the guessed half period time $t_1 = T/2$ are used from an analytical orbit with small orbit amplitude, since large orbits are not modeled correctly by the analytical expressions. The target parameters are $\{y_t = 0, \dot{x}_t = 0, \dot{z}_t = 0\}$ and the free parameters are $\{z_0, \dot{y}_0, t_1\}$. With this method we obtain the first initial conditions for a Halo orbit $\vec{s}^{\,(1)}_{\text{halo}} = \left(x_0, 0, z_0^{(1,\,\text{fit})}, 0, \dot{y}_0^{(1,\,\text{fit})}, 0\right)^\mathsf{T}$ for a particular x_0 value and with the half period time $t_1^{(1,\,\text{fit})}$, which are valid in the non-approximated (fully non-linear) CR3BP.
The idea then is to continue this orbit by increasing (respectively decreasing) x_0 by a small amount Δx_0, such that the differential correction method with initial guess $\vec{s}_0 = \left(x_0 + \Delta x_0, 0, z_0^{(1,\,\text{fit})}, 0, \dot{y}_0^{(1,\,\text{fit})}, 0\right)^\mathsf{T}$ yields the initial conditions for the second slightly larger (or smaller) Halo $\vec{s}^{\,(2)}_{\text{halo}}$ with half orbit period time $t_1^{(2,\,\text{fit})}$.
This method is repeated until the whole family of Halo orbits is obtained (see fig. 2.14). For decreasing orbit size the differential corrector method converges at some point to the planar Lyapunov orbits, which serves as a stop criterion for the differential corrector loop. For increasing orbit sizes, where the orbits get closer to the Earth+Moon, the funnel of Halo orbits starts to close after reaching a maximum diameter. Therefore, the z-amplitude of the Halo is not a good choice to parameterize the orbits and we use the x value, when the northern Halo orbit intersects the xz-plane in the lower half space ($z < 0$)[8].
For even larger orbits the corrector looses track and is not able to find suited initial conditions. Using the differential corrector to find directly full periodic orbits (not half of the orbit) is possible, but decreases the maximum orbit size since the corrector looses track earlier due to the limited numerical precision of the initial conditions.
The orbit period for large Halo orbits is significantly smaller than for small Halos, since the large orbits are closer to the Earth+Moon (see fig. 2.15).
The state transition matrix $\widehat{\Phi}$ for a periodic orbit, evaluated for one orbit cycle $\widehat{\Phi}(t_0 + T, t_0)$, is called the monodromy matrix and has some interesting properties. Making use of the symmetries of the CR3BP, the monodromy matrix can be computed from the state transition matrix for a half cycle $\widehat{\Phi}(t_1, t_0) = \widehat{\Phi}(t_0 + T/2, t_0)$ [Thurman & Worfolk, 1996]:

$$\widehat{\Phi}(t_0 + T, t_0) = \widehat{S} \cdot \widehat{K}_1 \cdot \widehat{\Phi}(t_1, t_0)^\mathsf{T} \cdot \widehat{K}_2 \cdot \widehat{S} \cdot \widehat{\Phi}(t_1, t_0) \tag{2.108}$$

with symmetry matrix $\widehat{S} = \widehat{S}_{6\text{x}6} = \text{diag}(1, -1, 1, -1, 1, -1)$, which follows from symmetry 2 in sec. 2.2.1, and matrices $\widehat{K}_1$ and $\widehat{K}_2$:

$$\widehat{K}_1 = \begin{pmatrix} 0_{3\text{x}3} & \mathbb{1}_{3\text{x}3} \\ -\mathbb{1}_{3\text{x}3} & \Omega_{3\text{x}3} \end{pmatrix}, \qquad \widehat{K}_2 = \begin{pmatrix} \Omega_{3\text{x}3} & -\mathbb{1}_{3\text{x}3} \\ \mathbb{1}_{3\text{x}3} & 0_{3\text{x}3} \end{pmatrix}, \tag{2.109}$$

[8] It is the most southern point on a northern Halo, where z reaches its minimum.

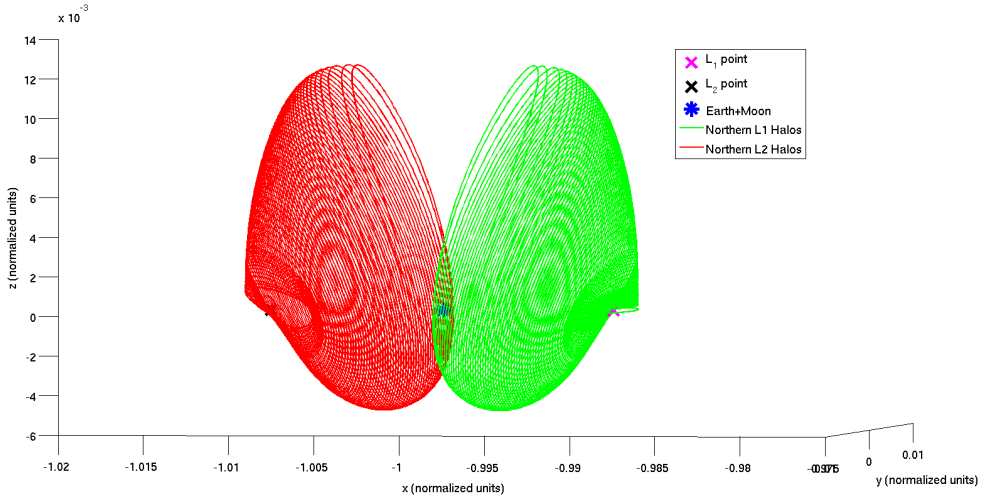

Figure 2.14: Northern Halo orbits around L_1 and L_2 obtained by the continuation method in the full CR3BP.

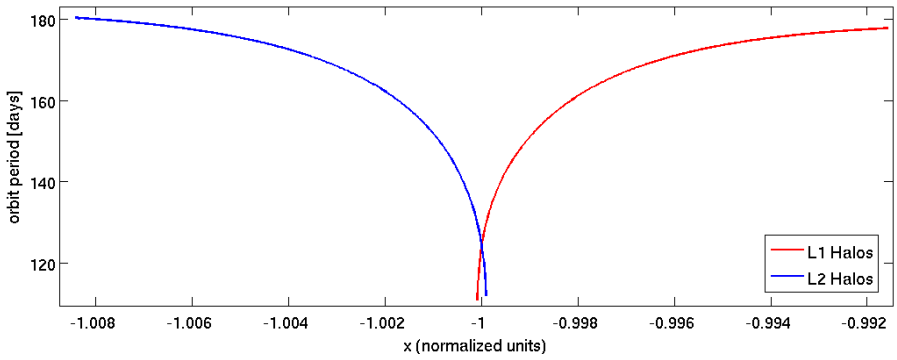

Figure 2.15: Orbit periods for Halo orbits around L_1 and L_2 obtained by the continuation method in the full CR3BP. The Earth+Moon is located approximately at $x = -1$.

where Ω_{3x3} was given in eq. (2.93). Although the monodromy matrix depends on the start point on the Halo orbit, the eigenvalues, which are also called *multipliers*, are invariant and describe the dynamics near the nominal Halo orbit. Since the CR3BP is a phase-space volume preserving Hamiltonian system [Thurman & Worfolk, 1996], the monodromy matrix $\widehat{M}$ is symplectic and has the following properties [Thurman & Worfolk, 1996]:

1. $\det(\widehat{M}) = 1$,
2. If λ is an eigenvalue of $\widehat{M}$, then so is $1/\lambda$,
3. Since the CR3BP is time invariant, two eigenvalues are one [James, 2006].

Moreover, the associated eigenvectors, which are not invariant along the orbit, have some geometrical meaning [Gómez, 2001, p. 145]:

1. $\lambda_1 = \lambda_2 = 1$: One eigenvector of the unity eigenvalue points along the flow, so it is tangent to the Halo orbit. The eigenvector of the second unity eigenvalue points in the direction of change in energy (Jacobi constant C).
2. $\lambda_3 = \bar{\lambda}_4 = 1$: These eigenvalues lie on the complex unit circle and allow oscillating orbits around the Halo orbits (Quasi-Halo orbits, sec. 2.2.3).

3. $\lambda_5 = 1/\lambda_6 > 1$: The eigenvector to the eigenvalue > 1 is a local approximation (tangent) to the unstable manifold of the orbit, while the other eigenvector is a local approximation (tangent) to the stable manifold of the Halo. The stable (respectively unstable) manifold of a Halo orbit can be defined as the subset of points in the phase-space, which converge to the Halo orbit when propagating forward (respectively backward) in time. These manifolds are interesting for mission design, especially for entering or leaving the orbits, since the manifolds extend partly towards the Earth [James, 2006].

In fig. 2.16 the numerical values of the eigenvalues for L_1 Halos are shown. The eigenvalue > 1 causes the instability of Halo orbits. However, there is a small region, where Halo orbits are stable.

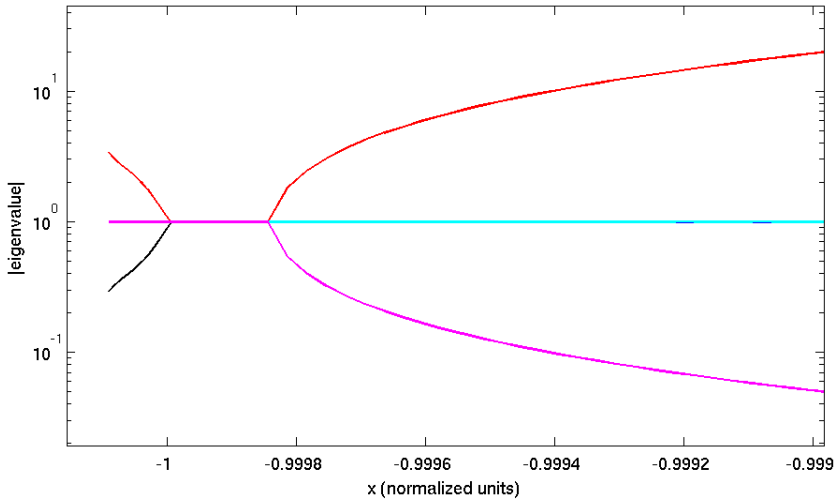

Figure 2.16: Modulus (absolute value) of the monodromy eigenvalues for L_1 Halos close to the Earth. A region where all eigenvalues have modulus one marks stable Halo orbits.

The numerical trajectory for the j-th orbit with period T_j obtained in this section can be stored as a Fourier series, since each vector component is periodic:

$$\vec{q}(t) = \sum_{n=0}^{N} \begin{pmatrix} c_{x,n,j} \cdot \cos(n\omega_j t) \\ c_{y,n,j} \cdot \sin(n\omega_j t) \\ c_{z,n,j} \cdot \cos(n\omega_j t) \end{pmatrix}, \tag{2.110}$$

with $\omega_j = 2\pi/T_j$. To reduce the amount of data, the Fourier series is truncated at an appropriate order N. In fig. 2.14 approximately 350 orbits for the L_1 and L_2 branch are shown. Another reduction can be obtained by choosing about 10 to 20 orbits and interpolating the Fourier coefficients and orbit period, such that the trajectories become

$$\vec{q}_{\text{halo}}(x_0, t, \varphi) = \sum_{n=0}^{N} \begin{pmatrix} c_{x,n}(x_0) \cdot \cos(n \cdot \omega(x_0) \cdot t + n \cdot \varphi) \\ c_{y,n}(x_0) \cdot \sin(n \cdot \omega(x_0) \cdot t + n \cdot \varphi) \\ c_{z,n}(x_0) \cdot \cos(n \cdot \omega(x_0) \cdot t + n \cdot \varphi) \end{pmatrix}, \tag{2.111}$$

where x_0 was used again to parameterize the Halos. In addition an initial phase φ was incorporated, so the starting point on the Halo orbit can be specified. The eq. (2.111) is now an analytical expression for Halo orbits in the CR3BP, which is also valid for large amplitudes.
The Fourier coefficients $c_{x,1}$, $c_{y,1}, c_{z,1}$ associated to the oscillations with the full orbit period $T(x_0)$ are shown in fig. 2.17. The orbit size is dominated by these

coefficients, because higher harmonics have smaller amplitudes. Hence, fig. 2.17 provides the amplitude relationship for the Halos in the full CR3BP.
The minimal amplitude for a Halo orbit, when $|c_{z,1}| \approx 0$, is in the y-direction approximately 650 000 km and in the x-direction approximately 200 000 km, which is in accordance to the previous results (see fig. 2.7). However, for a particular orbit size the y and z amplitudes intersect, meaning that the Halo has a circular shape in a yz-projection, which was not modeled by the third order approximation (fig. 2.7).

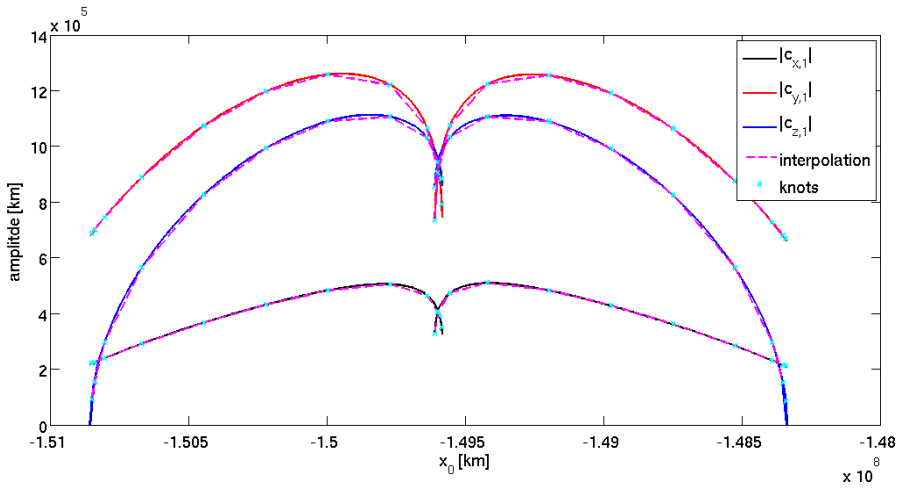

Figure 2.17: The absolute value of the Fourier coefficients for L_2 Halos (left side) and L_1 Halos (right side). The Earth is located at $x_0 = -1.496 \cdot 10^8$ km.

2.4.3 Targeting a Nominal Trajectory: Lissajous Orbits

The numerical determination of Lissajous orbits in the full CR3BP was treated by Howell & Pernicka [1988]. Assuming a given nominal trajectory $\vec{r}_{\text{nom}}(t)$, there are several reasons why the *true* trajectory of a spacecraft will deviate in general from the nominal path:

- Perturbations of the spacecraft,
- The nominal trajectory does not fulfill the equations of motions (completely),
- Instability of the orbit and errors due to numerical integration.

Thus, it is in general required to apply orbit corrections for stationkeeping from time to time, which we assume to be instantaneous changes in the spacecraft velocity, so-called ΔV maneuvers[9]. We wish now to compute a (true) trajectory, which is close to the nominal trajectory and requires only small ΔV corrections. The nominal trajectory does not have to be a Lissajous trajectory, hence the method presented in [Howell & Pernicka, 1988] is applicable to various other problems. In the beginning the nominal trajectory is divided into $N-1$ segments, so we obtain N target points $\vec{T}_i$

$$\vec{T}_i^{(0)} = \vec{r}_{\text{nom}}(t_i), \qquad i = 0, .., N-1, \tag{2.112}$$

where the time intervals $\Delta t_i^{(0)} = t_{i+1}^{(0)} - t_i^{(0)}$ do not have to be of the same length. The method works iteratively, therefore the superscript indicates the iteration step.

[9] It is advisable, especially in early space mission design studies, to use velocity changes with units of m/s to specify spacecraft maneuvers, since this quantity is independent of the spacecraft mass, which might be subject to changes. The actual thrust in units of Newton requires the knowledge of the S/C mass.

For each segment one can use the initial conditions $(\vec{r}_{\text{nom}}(t_i), \dot{\vec{r}}_{\text{nom}}(t_i))$ to compute the true trajectory $\vec{r}_i^{\,(0)}(t)$ from time $t_i^{(0)}$ to time $t_{i+1}^{(0)}$ using numerical integration techniques.
As illustrated in 1) at fig. 2.18 the true trajectory is in general discontinuous in the position due to the aforementioned reasons.
With a differential correction scheme one can adjust the initial velocities and travel times Δt_i for each segment independently, such that the discontinuities in position vanish up to some precision ϵ:

$$\{\vec{r}_i^{\,(1)}(t), \dot{\vec{r}}_i^{\,(1)}(t), t_{i+1}^{(1)}\} = \mathcal{D}(\{\vec{r}_i^{\,(0}, \dot{\vec{r}}_i^{\,(0)}\}, t_i, t_{i+1}, \{\vec{r} = \vec{T}_{i+1}^{\,(0)}\}, \{\dot{\vec{r}}_i, t_{i+1}^{(0)}\}, \epsilon). \tag{2.113}$$

This means the new segment trajectory $\vec{r}_i^{\,(1)}(t)$ fulfills

$$\vec{r}_i^{\,(1)}(t_i) = T_i^{(0)} = \vec{r}_{\text{nom}}(t_i),, \qquad i = 0, .., N-1, \tag{2.114}$$

$$\vec{r}_i^{\,(1)}(t_{i+1}) = T_{i+1}^{(0)} = \vec{r}_{\text{nom}}(t_{i+1}),, \qquad i = 0, .., N-1, \tag{2.115}$$

hence, it is continuous in position, but not in velocity (see the second line in fig. 2.18). The $\Delta\vec{V}_i$ at each target point can be computed with:

$$\Delta\vec{V}_i^{\,(1)} = \dot{\vec{r}}_i^{\,(1)}(t_i) - \dot{\vec{r}}_i^{\,(0)}(t_i), \qquad i = 0, .., N-1, \tag{2.116}$$

where the total $\Delta V^{(1)}$ is given by the sum:

$$\Delta V^{(1)} = \sum_{i=0}^{N} |\Delta\vec{V}_i^{\,(1)}|. \tag{2.117}$$

The total ΔV in the first iteration step can be quite large and depends on the correctness and stability of the nominal trajectory. The reduction of the total $\Delta V^{(1)}$ can be achieved with a modified differential corrector method, which we will discuss in detail subsequently. The idea of the method is to compute a variation in the travel times and in the position of the target points (= the initial position of each segment), which in turn produces a variation in the velocity discontinuity of

$$\delta\Delta\vec{V}_i^{\,(1)} = -\vec{\Delta}V_i^{\,(1)}, \tag{2.118}$$

yielding a net $\Delta\vec{V}_i^{\,(2)} = \delta\vec{V}_i^{\,(1)} + \Delta\vec{V}_i^{\,(1)}$ of approximately zero. Since a variation of the ith target point influences the trajectories $\vec{r}_{i-1}$ and $\vec{r}_i$, all target points need to be adjusted at the same time. The variational equation can be written in the form

$$\begin{pmatrix} \delta\Delta\vec{V}_1^{\,(1)} \\ \delta\Delta\vec{V}_2^{\,(1)} \\ \cdots \\ \delta\Delta\vec{V}_{N-2}^{\,(1)} \end{pmatrix}_{\text{3N-6x1}} = \widehat{Q}_{\text{3N-6x4N}} \cdot \begin{pmatrix} \delta\vec{T}_0^{\,(0)} \\ \delta t_0^{\,(1)} \\ \delta\vec{T}_1^{\,(0)} \\ \delta t_1^{\,(1)} \\ \cdots \\ \delta\vec{T}_{N-1}^{\,(1)} \\ \delta t_{N-1}^{\,(1)} \end{pmatrix}_{\text{4Nx1}}, \tag{2.119}$$

and can be solved by using eq. (2.102):

$$\begin{pmatrix} \delta\vec{T}_0^{\,(0)} \\ \delta t_0^{\,(1)} \\ \delta\vec{T}_1^{\,(0)} \\ \delta t_1^{\,(1)} \\ \cdots \\ \delta\vec{T}_{N-1}^{\,(0)} \\ \delta t_{N-1}^{\,(1)} \end{pmatrix}_{\text{4Nx1}} = \widehat{Q}^{\mathsf{T}} \cdot (\widehat{Q} \cdot \widehat{Q}^{\mathsf{T}})^{-1} \begin{pmatrix} \delta\Delta\vec{V}_1^{\,(1)} \\ \delta\Delta\vec{V}_2^{\,(1)} \\ \cdots \\ \delta\Delta\vec{V}_{N-2}^{\,(1)} \end{pmatrix}_{\text{3N-6x1}}, \tag{2.120}$$

such that the solution (the vector on the left-hand-side) has a minimal l^2-norm. This ensures that the variations of the target points are small and that the new trajectory will be close to the nominal path (see 3a and 3b in fig. 2.18). We note that $\Delta\vec{V}_0^{\,(0)}$ is not modified by eq. (2.120), since this quantity is an orbit insertion parameter, which is not included in the stationkeeping costs to be minimized.
The new trajectories $\vec{r}_i^{\,(2)}(t)$ given by the initial conditions

$$\vec{r}_i^{\,(2)}(t_i) = \vec{T}_i^{\,(1)} = \vec{T}_i^{\,(0)} + \delta\vec{T}_1^{\,(0)}, \qquad i = 0, ..., N-1, \tag{2.121}$$

$$\dot{\vec{r}}_i^{\,(2)}(t_i) = \dot{\vec{r}}_i^{\,(1)}(t_i), \qquad i = 0, \tag{2.122}$$

$$\dot{\vec{r}}_i^{\,(2)}(t_i) = \dot{\vec{r}}_i^{\,(1)}(t_i) + \delta\Delta\vec{V}_i^{\,(1)}, \qquad i = 1, ..., N-2, \tag{2.123}$$

are now continuous in the velocity, but slightly discontinuous in the position, since the differential correction is based on a linear approximation (see 3b in fig. 2.18). However, these discontinuities can be fixed again by introducing $\Delta\vec{V}_i^{\,(3)}$ steps with the differential correction scheme (eq. (2.113)) with smaller costs in terms of total ΔV than before (cf. plot 2 and 4 in fig. 2.18). The procedure of alternately varying the target point position and introducing $\Delta\vec{V}_i$ corrections can be repeated until a threshold ϵ for the total ΔV_i is reached.

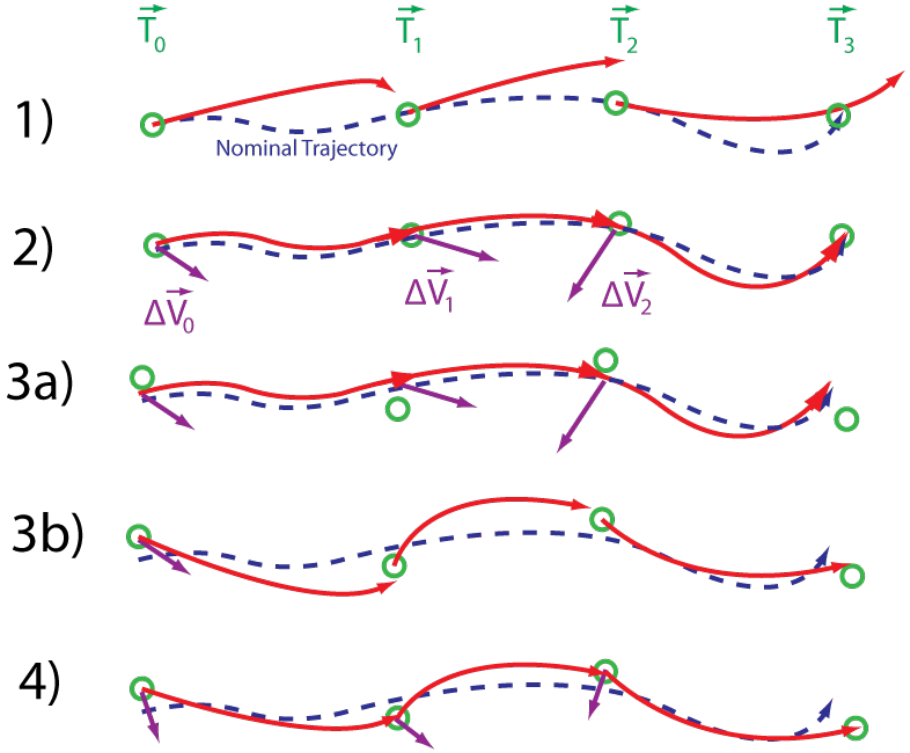

Figure 2.18: Working principle of the method described in [Howell & Pernicka, 1988] to obtain a trajectory with low ΔV consumption close to a nominal trajectory. The green circles mark the target points $\vec{T}_i$. The blue-dashed line is the nominal trajectory. The red lines are the trajectory segments obtained from integrating the equations of motion. The purple vectors indicate instantaneous corrections in the velocity ($\Delta\vec{V}$). The shorter arrows in 4) indicate a smaller total ΔV consumption than in 2). The steps 3a, 3b, and 4 are repeated until the total ΔV is below some threshold. See text for further description.

It will be investigated in subsequent sections, if the least-norm approach used to invert eq. (2.119) can be replaced by methods, which solve the equation under some other (more important) constraints than a minimum norm. These constraints on the

variations of the target points might be imposed, for example, by some constellation requirements.

Derivation of the correction matrix $\widehat{Q}$

To understand the derivation of the correction matrix $\widehat{Q}$ we assume at first only three target points $\vec{T}_0, \vec{T}_1, \vec{T}_2$ and a continuous trajectory in position (which means $\vec{r}_i(t_i) = \vec{T}_i$), but discontinuous in the velocity. We wish to reduce ΔV_1, which occurs at time t_1. We recall that the variational equation for the propagation from t_0 to t_1 can be written as

$$\begin{pmatrix} \delta\vec{r}_{1\leftarrow 0} \\ \delta\vec{v}_{1\leftarrow 0} \end{pmatrix}_{6\text{x}1} = \begin{pmatrix} \widehat{A}_{1\leftarrow 0} & \widehat{B}_{1\leftarrow 0} & \vec{v}_{1\leftarrow 0} \\ \widehat{C}_{1\leftarrow 0} & \widehat{D}_{1\leftarrow 0} & \vec{a}_{1\leftarrow 0} \end{pmatrix}_{6\text{x}7} \cdot \begin{pmatrix} \delta\vec{r}_0 \\ \delta\vec{v}_0 \\ \delta t_{1\leftarrow 0} - \delta t_0 \end{pmatrix}_{7\text{x}1}, \tag{2.124}$$

with 3-by-3 submatrices $\widehat{A}, \widehat{B}, \widehat{C}$ and $\widehat{D}$ such that

$$\widehat{\Phi}_r(t_1, t_0) = \begin{pmatrix} \widehat{A}_{1\leftarrow 0} & \widehat{B}_{1\leftarrow 0} \\ \widehat{C}_{1\leftarrow 0} & \widehat{D}_{1\leftarrow 0} \end{pmatrix}. \tag{2.125}$$

The position, velocity and acceleration of the satellite at time t_1, when propagating from t_0, is denoted as $\vec{r}_{1\leftarrow 0}$, $\vec{v}_{1\leftarrow 0}$ and $\vec{a}_{1\leftarrow 0}$, respectively. In the same way we derive the variational equations for the propagation from t_2 to t_1, which is backward in time [Howell & Pernicka, 1988, eq. 11]:

$$\begin{pmatrix} \delta\vec{r}_{1\leftarrow 2} \\ \delta\vec{v}_{1\leftarrow 2} \end{pmatrix} = \begin{pmatrix} \widehat{A}_{1\leftarrow 2} & \widehat{B}_{1\leftarrow 2} & \vec{v}_{1\leftarrow 2} \\ \widehat{C}_{1\leftarrow 2} & \widehat{D}_{1\leftarrow 2} & \vec{a}_{1\leftarrow 2} \end{pmatrix} \cdot \begin{pmatrix} \delta\vec{r}_2 \\ \delta\vec{v}_2 \\ \delta t_{1\leftarrow 2} - \delta t_2 \end{pmatrix}. \tag{2.126}$$

In the next step we solve the first vector equation in eq. (2.124) and eq. (2.126) for $\delta\vec{v}_0$ and $\delta\vec{v}_2$, respectively. This requires the inverse of the corresponding $\widehat{B}$ matrix. Then we use the second vector equation of eq. (2.124) and eq. (2.126) and substitute the results for $\delta\vec{v}_0$ and $\delta\vec{v}_2$. This yields

$$\begin{aligned} \delta\vec{v}_{1\leftarrow 0} =& (\widehat{C}_{1\leftarrow 0} - \widehat{D}_{1\leftarrow 0}\widehat{B}^{-1}_{1\leftarrow 0}\widehat{A}_{1\leftarrow 0})\delta\vec{r}_0 + \widehat{D}_{1\leftarrow 0}\widehat{B}^{-1}_{1\leftarrow 0}\delta\vec{r}_{1\leftarrow 0} \\ & - (\widehat{D}_{1\leftarrow 0}\widehat{B}^{-1}_{1\leftarrow 0}\vec{v}_{1\leftarrow 0} - \vec{a}_{1\leftarrow 0})(\delta t_{1\leftarrow 0} - \delta t_0), \end{aligned} \tag{2.127}$$

$$\begin{aligned} \delta\vec{v}_{1\leftarrow 2} =& (\widehat{C}_{1\leftarrow 2} - \widehat{D}_{1\leftarrow 2}\widehat{B}^{-1}_{1\leftarrow 2}\widehat{A}_{1\leftarrow 2})\delta\vec{r}_2 + \widehat{D}_{1\leftarrow 2}\widehat{B}^{-1}_{1\leftarrow 2}\delta\vec{r}_{1\leftarrow 2} \\ & - (\widehat{D}_{1\leftarrow 2}\widehat{B}^{-1}_{1\leftarrow 2}\vec{v}_{1\leftarrow 2} - \vec{a}_{1\leftarrow 2})(\delta t_{1\leftarrow 2} - \delta t_2), \end{aligned} \tag{2.128}$$

where we note that

$$\vec{v}_{1\leftarrow 2} - \vec{v}_{1\leftarrow 0} = \Delta\vec{V}_1, \tag{2.129}$$

$$\delta\vec{v}_{1\leftarrow 2} - \delta\vec{v}_{1\leftarrow 0} = \delta\Delta\vec{V}_1. \tag{2.130}$$

Thus, we obtain a functional dependency between $\delta\Delta\vec{V}_1$ and, for example, variations in the points $\vec{r}_0$ and $\vec{r}_2$. In addition we require that any variation produces a self-consistent and continuous trajectory in position:

$$\delta t_{1\leftarrow 2} = \delta t_{1\leftarrow 0} = \delta t_1, \tag{2.131}$$

$$\delta\vec{r}_{1\leftarrow 2} = \delta\vec{r}_{1\leftarrow 0} = \delta\vec{r}_1, \tag{2.132}$$

which simplifies the expressions. The velocity-dependent coriolis force term in the equations of motion of the CR3BP causes an inequality between $\vec{a}_{1\leftarrow 0}$ and $\vec{a}_{1\leftarrow 2}$, although both accelerations are evaluated at the same position, but with different velocities due to the ΔV maneuver.

The final variational equation can be written in linear form:

$$\delta\Delta\vec{V}_1 = (\widehat{Q}_{0,1,2})_{3\text{x}12} \cdot \begin{pmatrix} \delta\vec{r}_0 \\ \delta t_0 \\ \delta\vec{r}_1 \\ \delta t_1 \\ \delta\vec{r}_2 \\ \delta t_2 \end{pmatrix}_{3\text{x}12} = \begin{pmatrix} \widehat{Q}_a & \widehat{Q}_b & \widehat{Q}_c & \widehat{Q}_d & \widehat{Q}_e & \widehat{Q}_f \end{pmatrix}_{3\text{x}12} \cdot \begin{pmatrix} \delta\vec{r}_0 \\ \delta t_0 \\ \delta\vec{r}_1 \\ \delta t_1 \\ \delta\vec{r}_2 \\ \delta t_2 \end{pmatrix}_{12\text{x}1}, \tag{2.133}$$

where the right-hand-side contains the variations in the target point position $\delta\vec{T}_i = \delta\vec{r}_i$ and where the sub-matrices are [Howell & Pernicka, 1988, eq. 15]:

$$\begin{aligned}
\widehat{Q}_a &= \widehat{D}_{1\leftarrow 0}\widehat{B}^{-1}_{1\leftarrow 0}\widehat{A}_{1\leftarrow 0} - \widehat{C}_{1\leftarrow 0}, \\
\widehat{Q}_b &= \vec{a}_{1\leftarrow 0} - \widehat{D}_{1\leftarrow 0}\widehat{B}^{-1}_{1\leftarrow 0}\vec{a}_{1\leftarrow 0}, \\
\widehat{Q}_c &= \widehat{D}_{1\leftarrow 2}\widehat{B}^{-1}_{1\leftarrow 2} - \widehat{D}_{1\leftarrow 0}\widehat{B}^{-1}_{1\leftarrow 0}, \\
\widehat{Q}_d &= \widehat{D}_{1\leftarrow 0}\widehat{B}^{-1}_{1\leftarrow 0}\vec{v}_{1\leftarrow 0} - \widehat{D}_{1\leftarrow 2}\widehat{B}^{-1}_{1\leftarrow 2}\vec{v}_{1\leftarrow 2} + \vec{a}_{1\leftarrow 2} - \vec{a}_{1\leftarrow 0}, \\
\widehat{Q}_e &= \widehat{C}_{1\leftarrow 2} - \widehat{D}_{1\leftarrow 2}\widehat{B}^{-1}_{1\leftarrow 2}\widehat{A}_{1\leftarrow 2}, \\
\widehat{Q}_f &= \widehat{D}_{1\leftarrow 2}\widehat{B}^{-1}_{1\leftarrow 2}\vec{a}_{1\leftarrow 2} - \vec{a}_{1\leftarrow 2}.
\end{aligned} \tag{2.134}$$

A trajectory with $N \geqslant 3$ target points can be processed with this matrix equation:

$$\begin{pmatrix} \delta\Delta\vec{V}_1 \\ \delta\Delta\vec{V}_2 \\ \delta\Delta\vec{V}_3 \\ \dots \\ \delta\Delta\vec{V}_{N-2} \end{pmatrix}_{3\text{N-6x1}} = \begin{pmatrix} \widehat{Q}_{0,1,2} & \widehat{0}_{3\text{x}4} & \widehat{0}_{3\text{x}4} & \cdots & \widehat{0}_{3\text{x}4} \\ \widehat{0}_{3\text{x}4} & \widehat{Q}_{1,2,3} & \widehat{0}_{3\text{x}4} & \cdots & \widehat{0}_{3\text{x}4} \\ \widehat{0}_{3\text{x}4} & \widehat{0}_{3\text{x}4} & \widehat{Q}_{2,3,4} & \cdots & \widehat{0}_{3\text{x}4} \\ \vdots & \ddots & \ddots & \ddots & \vdots \\ \widehat{0}_{3\text{x}4} & \cdots & \cdots & \widehat{0}_{3\text{x}4} & \widehat{Q}_{N-3,N-2,N-1} \end{pmatrix} \cdot \begin{pmatrix} \delta\vec{r}_0 \\ \delta t_0 \\ \delta\vec{r}_1 \\ \delta t_1 \\ \delta\vec{r}_2 \\ \delta t_2 \\ \delta\vec{r}_3 \\ \delta t_3 \\ \dots \\ \delta\vec{r}_{N-1} \\ \delta t_{N-1} \end{pmatrix}_{4\text{Nx1}}, \tag{2.135}$$

where the large matrix is the sought $\widehat{Q}$.

Results for Lissajous Orbits

We examine the described method by choosing two Lissajous paths from the third-order approximation (eq. (2.49)) as the nominal trajectories with the following initial conditions

- **small**: $A_y = A_z \approx 300\ 000\,\text{km},\ \varphi = 0.6\,\text{rad},\ \psi = 0.0\,\text{rad},$
- **large**: $A_y = A_z \approx 600\ 000\,\text{km},\ \varphi = 0.6\,\text{rad},\ \psi = 0.0\,\text{rad},$

and an integration time of approximately 320 days. The trajectories are divided into 5 segments (equidistant in time) yielding 6 target points. The integration of the initial conditions at each target point yields segment trajectories, which are combined neither continuous in position nor in velocity (see red and blue traces in fig. 2.19). Using the differential corrector one obtains continuous trajectories in position (green traces in fig. 2.19), which intersect with the initial target points on the nominal path (blue crosses). The initial total ΔV is shown in table 2.4.

	total ΔV in m/s	
Iteration	small	large
initial	18.37	139.64
1	0.0283	1.744
2	< 0.0001	0.0287
3		< 0.0001

Table 2.4: Reduction of total ΔV for the large and small Lissajous orbit.

Iteratively the target point position is adjusted and a continuous track in position is maintained with the differential corrector until the total ΔV reached 1 mm/s. For the small trajectory 2 iterations were required, for the large trajectory 3 iterations, to converge to the final orbit (magenta traces in fig. 2.19). Since the nominal trajectory is only an approximation valid for small amplitudes, the large final trajectory deviates spatially more than the small trajectory from the nominal track, as apparent on the plot.

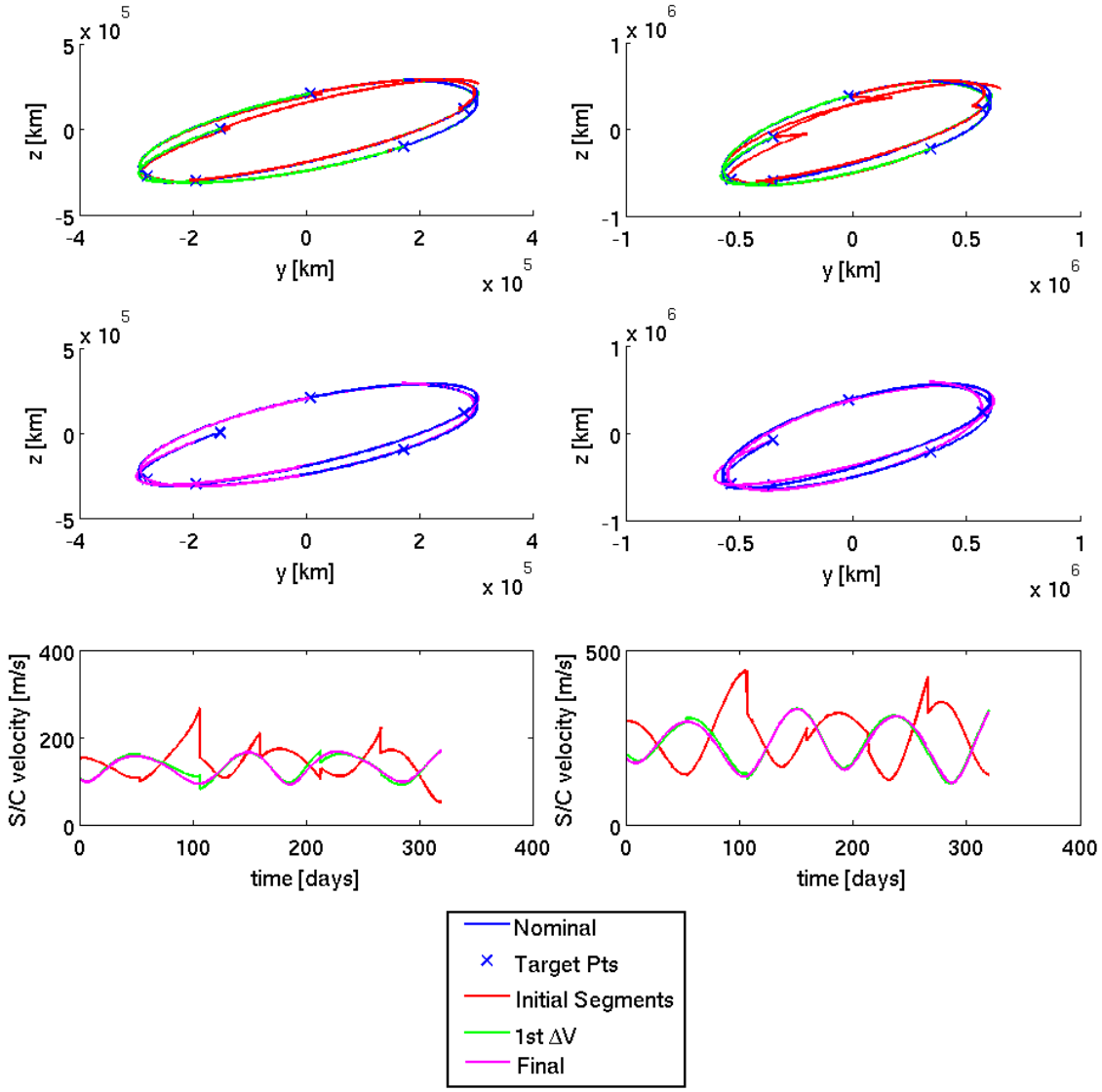

Figure 2.19: Small (left side) and large (right side) Lissajous orbits in yz-projection (top and middle) and the magnitude of the spacecraft velocity (bottom).

2.5 Search for Constellations

In this section we investigate the possibility of combining three reference orbits ($\vec{r}_0(t),\ \vec{r}_1(t),\ \vec{r}_2(t)$) of the CR3BP, which analytical expressions were derived in the previous sections, to obtain a spacecraft constellation, which might be applicable for space-based gravitational wave detectors. These results will also serve as starting point for further optimization attempts.
Recall that a halo orbit (eq. (2.111))

$$\vec{q}_{\text{halo}}(x_0, t, \phi)$$

has two free parameters (the amplitude and phase), while a Lissajous orbit (eq. (2.49))

$$\vec{q}_{\text{LJ}}(t) = \vec{q}_{\text{LJ}}(t, A_y, A_z, \phi, \psi)$$

has four parameters, where we restricted the problem, for example, to orbits around L_1. If all three spacecrafts are on Lissajous orbits, we wish to find *good* constellations in a 12 dimensional parameter space. Where we define a *good* constellation as a configuration where

- all S/C avoid the SEZ cone,
- the inner constellation angle, which is the angle between the two arms, is between 50° and 130° and the angle variations are small,
- the detector armlength is larger than 1 Mkm and the difference between both arms is small.

Since the parameter space is not very large, one can use e.g. `Mathematica` to interactively vary the parameters for each S/C orbit and directly observe the changes in quantities like inner constellation angle and armlength. One can also use numerical algorithms to obtain initial orbit parameter sets for *good* constellations. However, this usually depends on the definition of a figure of merit (see subsequent sec. 2.6.1) and does not provide a deep understanding of the problem under investigation. Therefore, the manual approach was used in this thesis.
After choosing a set of orbit parameters with the support of the analytical expressions, we transform the initial configurations to trajectories in the full CR3BP with minimal ΔV according to the method described in sec. 2.4.3. This eliminates a falsification due to the fact, that the analytical orbits are only approximations.
In this thesis the following initial configurations (IC) have been selected for further analysis:

2.5.1 Constellation: HHL120

This Halo-Halo-Lissajous (HHL) constellation consists of two daughter S/C on the same large Halo orbit (phase shifted by approximately 180°) and a center S/C on a Lissajous orbit close to the SEZ (see fig. 2.20). The angle between the arms is approximately 120°, whereas the angle variation (peak-peak) for a three year period is about 18° (first plot of the bottom fig. 2.21). The two arms of the detector have an average length of 1.4 Mkm and 1.3 Mkm with a Doppler rate up to ±200 m/s. The center S/C is only for short periods within the SEZ, where the SEZ angle is below 4.5° (second plot in the bottom fig. 2.21).
A secular drift is apparent in the armlength. It is caused by the dependency of orbital period on the orbit size (see fig. 2.13). For some configurations the effect can be minimized by adjusting the orbit parameters, however, not in general for arbitrary long periods.

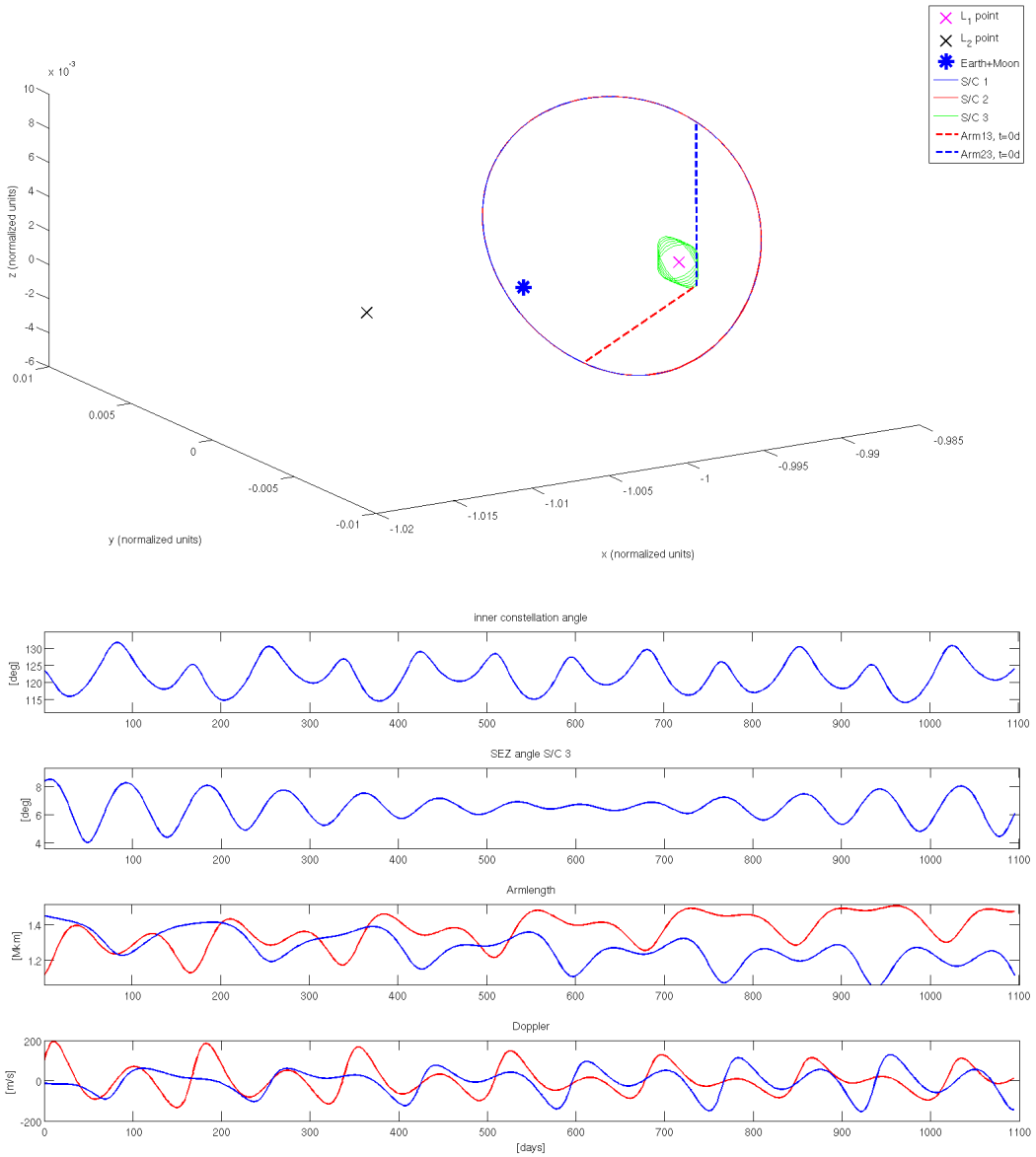

Figure 2.20: 3-d plot of the constellation HHL120 and orbits (top) and constellation information (bottom) for a three year period of the natural orbits.

2.5.2 Constellation: HHL90

There are two straight forward methods to achieve a constellation with 90° angle between the two interferometer arms, when the constellation HHL120 is taken as starting point. On the one hand, one can decrease the phase angle difference of the S/C on the large Halo orbit, such that the daughter S/C are closer together. However, this approach leads to large peak-peak angle variations of approximately 40°. On the other hand, one can leave the S/C on the large Halo separated by 180°, but increase the Halo orbit amplitude. With this approach, we obtain the constellation denoted here as **HHL90**. The average armlength is 1.7 Mkm and the peak-peak inner angle variation is approximately 27° (see fig. 2.21).

2.5.3 Constellation: HHH60

In this configuration all S/C are on the same large Halo orbit, separated by 120° orbital phase (see fig. 2.22). This configuration is an attempt to obtain an equilateral triangle constellation with three arms and 60° inner angle at each S/C. The (peak-

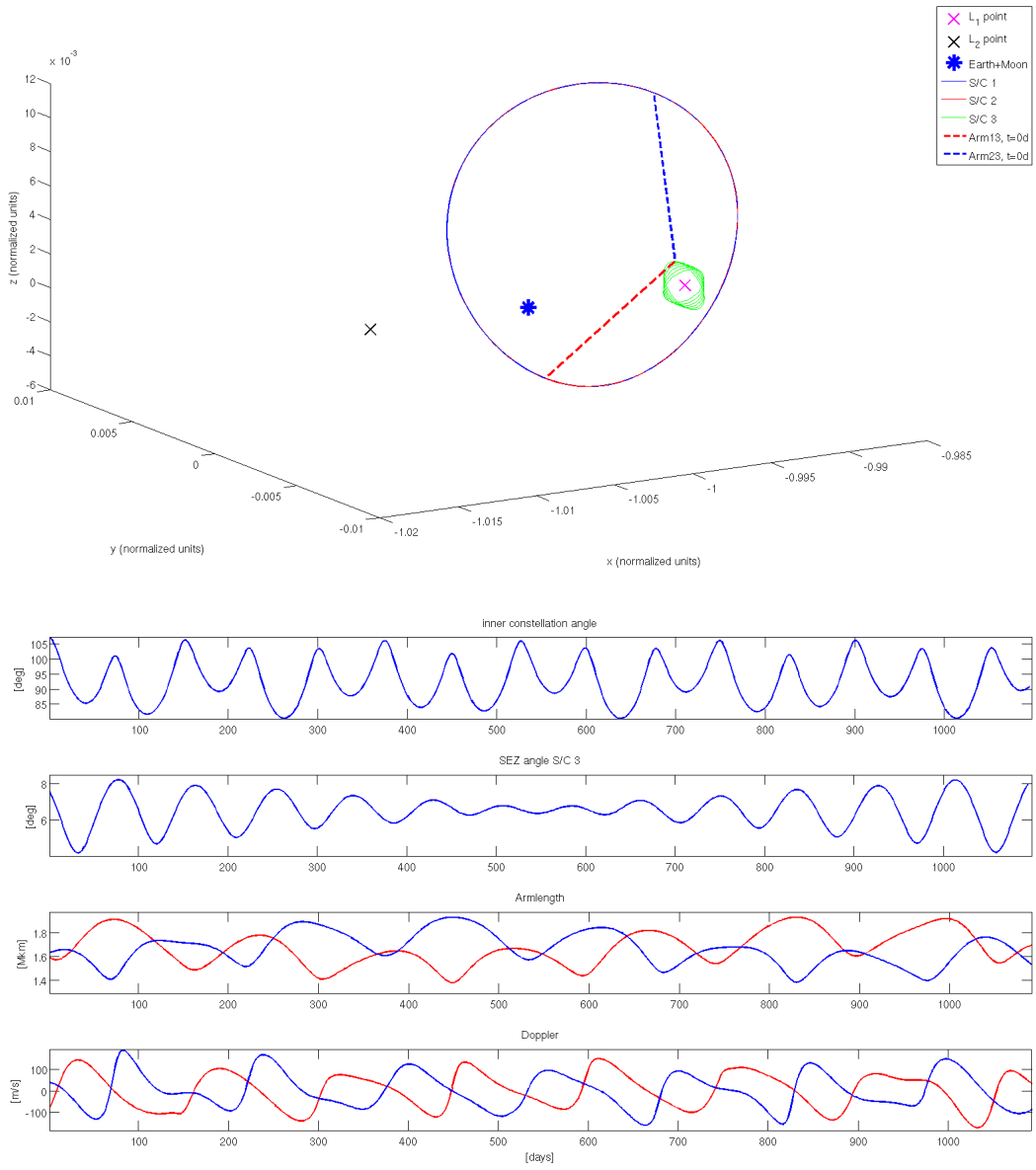

Figure 2.21: 3-d plot of the constellation HHL90 and orbits (top) and constellation information (bottom) for a three year period of the natural orbits.

peak) inner angle variation is approximately 24°. The baseline armlength is 2.0 Mkm.

The initial configurations presented in this section are formed by the natural orbits. They have some disadvantages for an application for a space-based gravitational wave detector. A major drawback is the large variation in the inner constellation angle, which definitely requires actuation of the outgoing beam direction on each S/C. Also the center S/C enters the SEZ zone in some constellations, causing potential communication problems with the S/C.
Therefore, the next section is dedicated to the optimization of these constellations by introducing orbit corrections.

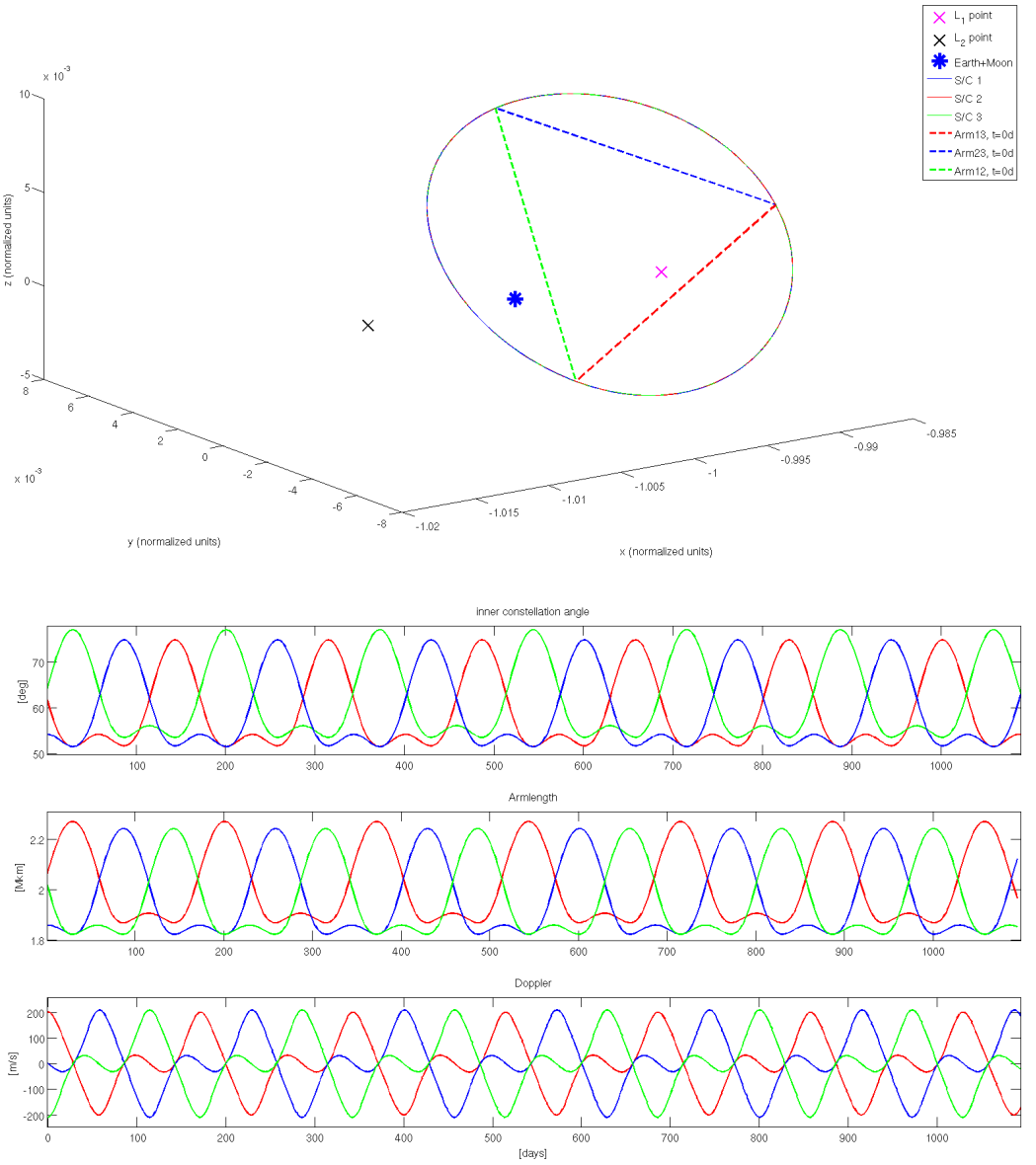

Figure 2.22: 3-d plot of the constellation HHH60 and orbits (top) and constellation information (bottom) for a three year period of the natural orbits.

2.6 Optimization

The initial configurations (IC) derived in the previous section are natural orbits, which require only small orbit corrections below 1 m/s/yr to compensate the orbit instability. We take N points spaced equally over the mission period (e.g. T_m = 3 years). For the i-th spacecraft we obtain for each point in time a target point (or waypoint) $\vec{T}^{\,(IC)}$:

$$\vec{T}^{(IC)}_{j,i} := \vec{r}_i^{\,(IC)}(t_{j,i}), \qquad j = 0, ..., N-1, \quad i = 0, 1, 2, \tag{2.136}$$

where we note that the target points are evaluated at the same time on all S/C

$$t^{(IC)}_{j,i} := j \cdot \frac{T_m}{N-1}, \qquad j = 0, ..., N-1, \quad i = 0, 1, 2. \tag{2.137}$$

Furthermore, we assume that S/C i applies a $\Delta\vec{V}_{j,i}$ thrust at time $t_{j,i}$. We wish now to compute a position of target points and times, such that

- the amount of total thrust ΔV required to fly through all target points is small,
- the constellation figure of merit F, describing the goodness of the orbits for a space-based GW detector, is good.

The figure of merit is an objective function, which maps the trajectories, or equivalently the initial conditions, onto a single positive real number. If we consider orbit corrections, each trajectory can be described by N target points (per S/C) and the dimension of the parameter space is

$$d = 3 \cdot N \cdot 3, \tag{2.138}$$

where we assumed fixed times $t_{j,i}$.
The figure of merit is then the following map:

$$F : X \subset \mathbb{R}^d \to \mathbb{R}_{\geqslant 0}, \tag{2.139}$$

where a smaller figure of merit value (usually) denotes a better constellation.
The here required optimization can be formulated as a non-linear multidimensional minimization problem. Various methods exist to tackle such problems (e.g. Particle Swarm Optimization, Evolutionary algorithms, Simplex). The main difficulty is to find a global (and not a local) minimum in a large parameter space for an objective function with several local minima. The results of the numerical methods usually will depend on an initial guess for the solution. In addition for problems with such a high dimension of the parameter space (here: $d > 100$), the search might take long since various evaluations of the objective function are required.
Another problem may arise from a practical point of view: The evaluation of the figure of merit with a set of target points requires a fit (optimization) of a trajectory through these points, as described in sec. 2.4.3. Since this (inner) method utilizes linear approximations and the knowledge of the previous trajectory (which should be close to the new solution), a large variation in the target point positions would cause problems. This complicates the search for a global solution.
Due to this problem and the high dimension number, we will use here a simple minimization method based on linearizations, which will be introduced in the next sections.

2.6.1 Definition of the Figure of Merit

The definition of a figure of merit is a subjective topic and requires often weighting and iterative adjustments to yield reasonable results, which usually also depend on the chosen numerical optimization method. For a given set of target points $\vec{T}_{j,i}$ and arrival times $t_{j,i}$ we compute the trajectory of each satellite $(\vec{r}_0(t), \vec{r}_1(t), \vec{r}_2(t))$ through the points and some evaluation data, which we will use for the figure of merit:

- Armlengths of the detector

$$L_{01}(t) = |\vec{r}_0(t) - \vec{r}_1(t)|, \quad L_{02}(t) = |\vec{r}_0(t) - \vec{r}_2(t)|, \quad L_{12}(t) = |\vec{r}_1(t) - \vec{r}_2(t)|, \tag{2.140}$$

- Inner constellation angles α_i at S/C i

$$\alpha_0(t) = \measuredangle(\vec{n}_{01}, \vec{n}_{02}), \quad \alpha_1(t) = \measuredangle(\vec{n}_{01}, \vec{n}_{12}), \quad \alpha_2(t) = \measuredangle(\vec{n}_{12}, \vec{n}_{02}), \tag{2.141}$$

with normalized arm directions

$$\vec{n}_{01}(t) = \frac{\vec{r}_0(t) - \vec{r}_1(t)}{L_{01}(t)}, \quad \vec{n}_{02}(t) = \frac{\vec{r}_0(t) - \vec{r}_2(t)}{L_{02}(t)}, \quad \vec{n}_{12}(t) = \frac{\vec{r}_1(t) - \vec{r}_2(t)}{L_{12}(t)}, \tag{2.142}$$

- Solar Exclusion Zone angles β_i at S/C i

$$\beta_i(t) = \measuredangle\left(\vec{r}_i - (\mu-1,0,0)^\mathsf{T},\ (1,0,0)^\mathsf{T}\right), \qquad i = 0,1,2, \tag{2.143}$$

  which are zero, if the spacecraft is on the connection line between Sun and Earth+Moon (x-axis). In the CR3BP the Earth+Moon is located at $(\mu - 1,0,0)^\mathsf{T}$,

- Armlength mismatch $S_i(t)$ at each spacecraft

$$\begin{aligned} S_0(t) &= L_{01}(t) - L_{02}(t), \quad S_1(t) = L_{01}(t) - L_{12}(t), \\ S_2(t) &= L_{12}(t) - L_{02}(t). \end{aligned} \tag{2.144}$$

Considering that the trajectories are computed numerically in a discrete time domain, we should also use discrete time steps:

$$t \to t_k := k\frac{T_m}{N_m - 1}, \qquad k = 0,..,N_m - 1, \tag{2.145}$$

where T_m is the mission duration and N_m the number of sample points.
Then we can define the figure of merit F according to

$$\begin{aligned} \sqrt{F} = &(S_2^{\text{avg}}/k_1)^2 + \delta\cdot(S_1^{\text{avg}}/k_1)^2 + \delta\cdot(S_0^{\text{avg}}/k_1)^2 \\ &+ (\alpha_2^{\text{avg}} - \alpha_{\text{nom}})^2/k_2 + \delta\cdot(\alpha_1^{\text{avg}} - \alpha_{\text{nom}})^2/k_2 + \delta\cdot(\alpha_0^{\text{avg}} - \alpha_{\text{nom}})^2/k_2 \\ &+ (\alpha_2^{\text{std}}/k_3)^2 + \delta\cdot(\alpha_1^{\text{std}}/k_3)^2 + \delta\cdot(\alpha_0^{\text{std}}/k_3)^2 \\ &+ \frac{1-\delta}{k_3}\cdot\sum_{k=0}^{N_m-1}\exp(-(\beta_2(t_k)/k_4)^4), \end{aligned} \tag{2.146}$$

where the superscript 'avg' and 'std' denotes the average and the standard deviation, respectively, of the corresponding time series. The constants $k_1,..,k_4$ are normalization constants and allow some tuning of the figure of merit. δ is used as a switch to distinguish between a two arm or three arm constellation:

$$\delta = \begin{cases} 0 & \text{2 arm constellation,} \\ 1 & \text{3 arm constellation.} \end{cases} \tag{2.147}$$

The first line of eq. (2.146) suppresses the inequality in the armlengths of the detector, the second line should ensure that the inner constellation angles are close to a nominal value α_{nom}, the third line should suppress the inner angle variation, while the fourth line is a punishment term for constellations, where S/C 3 enters the SEZ. We note that the figure of merit can be written as a function of the target points (waypoints) $\vec{T} = (\vec{T}_{0,0},\ \vec{T}_{0,1},\ \vec{T}_{0,2},\ \vec{T}_{1,0},\ \vec{T}_{1,1},\ \vec{T}_{1,2},...,\ \vec{T}_{N-1,0},\ \vec{T}_{N-1,1},\ \vec{T}_{N-1,2})^\mathsf{T}$ and arrival times $\vec{t} = (t_{0,0},\ t_{0,1},\ t_{0,2},\ t_{1,0},\ t_{1,1},\ t_{1,2},...,\ t_{N-1,0},\ t_{N-1,1},\ t_{N-1,2})^\mathsf{T}$

$$F = F(\vec{T},\vec{t}), \tag{2.148}$$

since the trajectory (with minimal ΔV) through the target points and the evaluation data can be computed from the target points. A smaller value of F denotes a more rigid constellation and therefore a better applicability for a space base GW detector mission.

2.6.2 Gradient Descent

For the initial configuration (e.g. HHL120) the target points $\vec{T}_{j,i}^{(\mathrm{IC})}$ are on the natural orbits and one obtains a particular value for F. A straight forward method to decrease the figure of merit F is to use the gradient descent. Iteratively, the target points are changed according to

$$\vec{T}^{(s)} = \vec{T}^{(s-1)} - \gamma^{(s-1)} \cdot \vec{\nabla}_{\vec{T}} F(\vec{T}^{(s-1)}, \vec{t}), \qquad \vec{T}^{(0)} := \vec{T}^{(IC)} \tag{2.149}$$

where $\gamma^{(s-1)}$ is the step size of the gradient step and $\vec{\nabla}_{\vec{T}} F$ are the numerically computed partial derivatives of F w.r.t. the d components of $\vec{T}$ (eq. 2.138). It is well known that the gradient descent converges to a local minimum of the function F. However, the convergence might be very slow and can be improved by adjusting the step size $\gamma^{(s-1)}$ [Lau *et al.* , 2008, p.785], but this adaptive step size was not implemented here for the sake of simplicity. The computation of the derivatives is computational expensive, since for $N = 40$ target points (per S/C) the vector $\vec{T}$ has $d = 360$ components. Because a symmetric numerical differentiation scheme of the form

$$f'(x) \approx \frac{f(x+\epsilon) - f(x-\epsilon)}{2\epsilon}, \tag{2.150}$$

is used, one needs to evaluate $2 \cdot d = 720$ times the function f $(= F)$. This requires 720 orbit integrations. Here we reduce the computational effort by integrating not the trajectory for the whole mission duration, but only for the changed segments.
In fig. 2.23 an exemplary gradient descent of the HHL120 constellation for a three year period with $N = 40$ is shown. Every 28 days a ΔV thrust is applied and the figure of merit is decreased. The inner constellation angle variation was reduced from 17.6° to approximately 10°.
The final trajectory after 8 iteration steps is depicted in fig. 2.24. When the results are compared to the initial configuration (fig. 2.20), one can see that the trajectories moved only slightly. However, the SEZ angle as well as the inner constellation angle variation improved. The ΔV steps are visible as discontinuities in the Doppler rate (fig. 2.24, bottom plot). The total amount of ΔV is illustrated in the fig. 2.23 (top). Finally, approximately 700 m/s per S/C for three years are required. The value will increase further, if a constellation with lower figure of merit is desired.
With the gradient descent the target points are moved in the direction of steepest decrease of the figure of merit, without considering that other directions might decrease the figure of merit as well, but with less costs in terms of ΔV. Therefore, the gradient descent was introduced only for demonstration and validation purpose. In the next section we introduce a method to decrease the figure of merit in a less expensive with in terms of total ΔV.

2.6.3 Constrained Descent

The basic principle of the method called *constrained descent* within this thesis is based on a combination of

- the vector $\vec{\nabla}_{\vec{T}} F$, which describes how the figure of merit F changes upon a variation $\delta\vec{T}$ in the target points $\vec{T}$,
- the matrix $\widehat{Q}$, which is computed from the linearized flow in sec. 2.4.3 and describes how the $\Delta\vec{V}$ changes upon a variation $\delta\vec{T}$ in the target points $\vec{T}$,

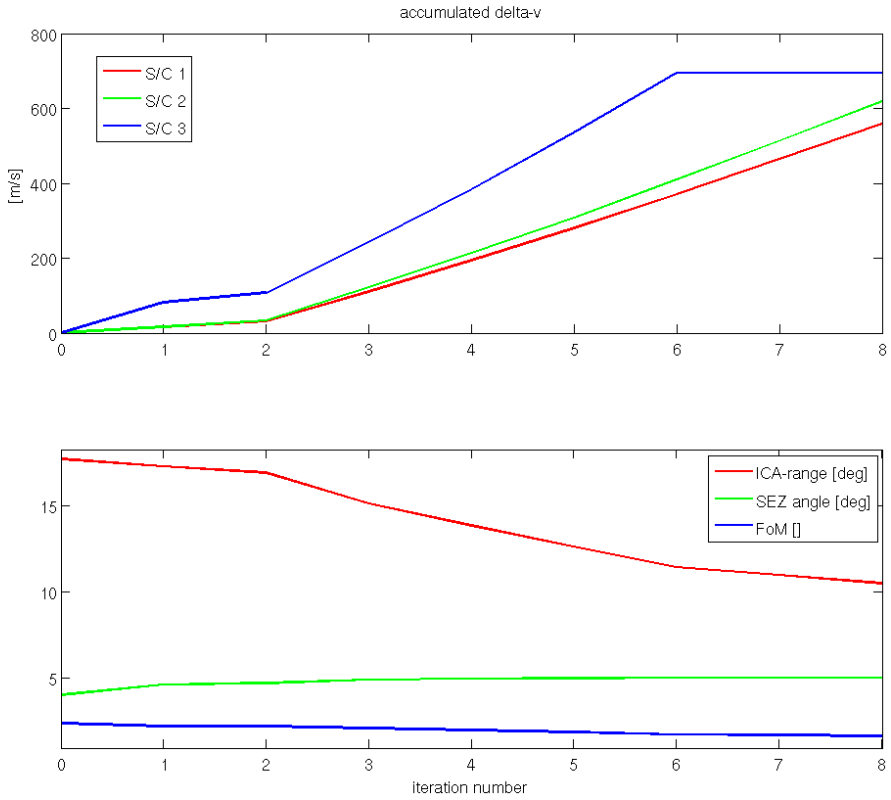

Figure 2.23: Top: The evolution of total ΔV for each S/C during a gradient descent. In the last two iteration steps only the target points of S/C 1 and 2 were varied, therefore the ΔV of S/C 3 stayed constant. For the first two iteration steps a smaller step size was used than for the other steps. **Bottom:** The peak-peak inner constellation angle variation (ICA-range), SEZ angle and figure of merit (FoM) during a gradient descent.

and on a solution for the constrained linear least-squares problem

$$\min_{\delta\vec{x}} ||\widehat{C}\cdot\delta\vec{x}-\vec{d_c}||^2 \quad \text{such that} \quad \begin{cases} \widehat{A}\cdot\delta\vec{x} \leqslant \vec{b} \\ \widehat{A}_e\cdot\delta\vec{x} = \vec{b}_e \\ \vec{l} \leqslant \delta\vec{x} \leqslant \vec{u} \end{cases}, \tag{2.151}$$

where $\delta\vec{x}$ is a variation in the target point positions and arrival (=thrust) times for all S/C, $\min ||\widehat{C}\cdot\delta\vec{x}-\vec{d_c}||^2$ minimizes the total ΔV, $\widehat{A}\cdot\delta\vec{x} \leqslant \vec{b}$ ensures a minimization of the figure of merit, $\widehat{A}_e\cdot\delta\vec{x} = \vec{b}_e$ constrains the instant of time for the thrusts to be equal on all S/C and $\vec{l} \leqslant \delta\vec{x} \leqslant \vec{u}$ guarantees that the variation $\delta\vec{x}$ is small enough to lie within the linearization regime.
The vector $\vec{x}$ consists of appended target points and arrival times for the three S/C:

$$\begin{aligned}\vec{x}^{(s)} = (&\vec{T}^{(s)}_{0,0}, t^{(s)}_{0,0}, \vec{T}^{(s)}_{1,0}, t^{(s)}_{1,0}, ..., \vec{T}^{(s)}_{N-1,0}, t^{(s)}_{N-1,0} \\ &\vec{T}^{(s)}_{0,1}, t^{(s)}_{0,1}, \vec{T}^{(s)}_{1,1}, t^{(s)}_{1,1}, ..., \vec{T}^{(s)}_{N-1,1}, t^{(s)}_{N-1,1} \\ &\vec{T}^{(s)}_{0,2}, t^{(s)}_{0,2}, \vec{T}^{(s)}_{1,2}, t^{(s)}_{1,2}, ..., \vec{T}^{(s)}_{N-1,2}, t^{(s)}_{N-1,2})^{\mathsf{T}},\end{aligned} \tag{2.152}$$

where we recall that the first index j in $\vec{T}_{j,i}$ and $t_{j,i}$ is the target point number, the index i is the S/C number and the superscript s is an iteration number.
In each iteration step eq. (2.151) is used to derive a variation in $\vec{x}$ and therefore a variation in the target point positions and arrival times. The state is updated

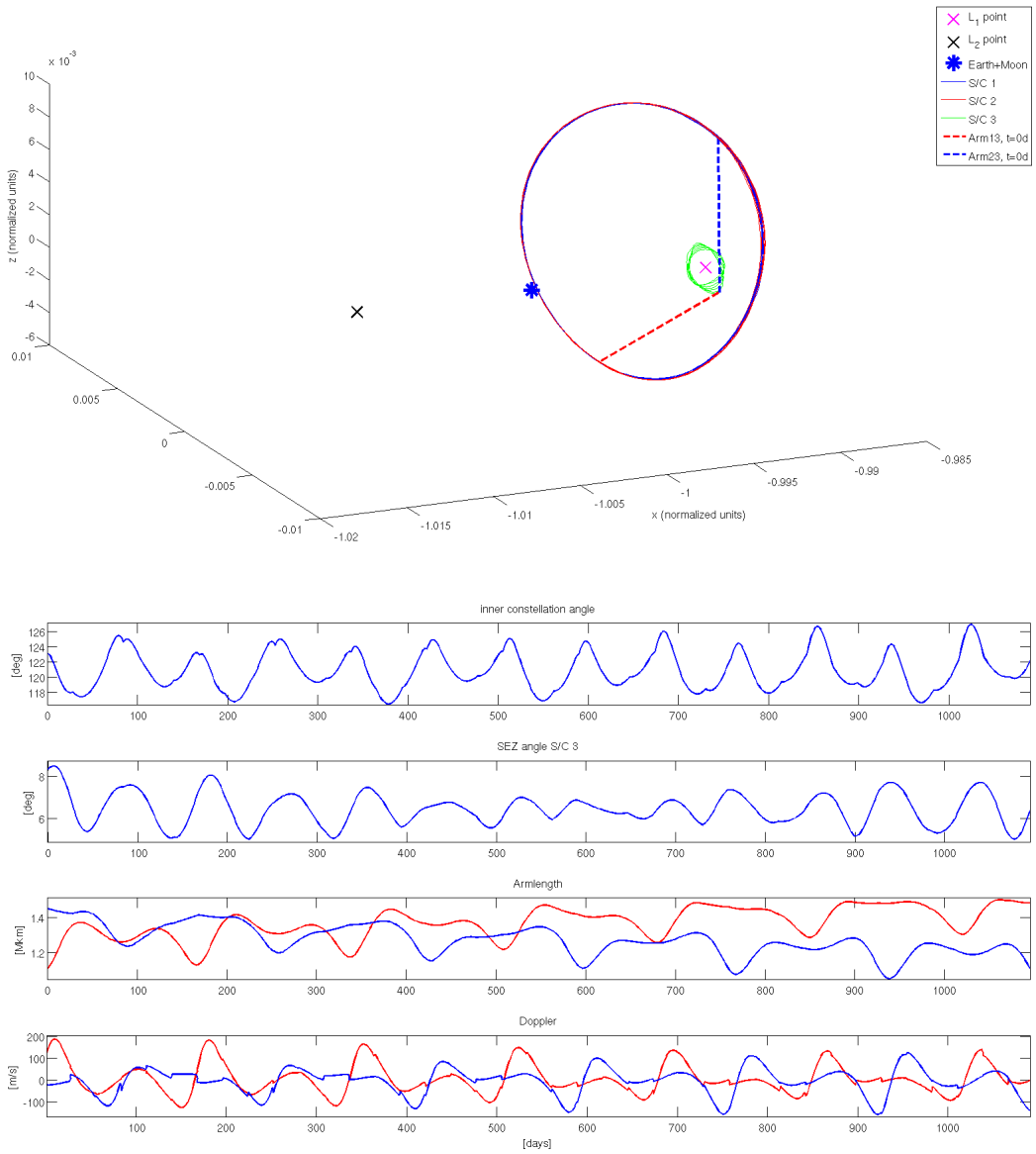

Figure 2.24: Satellite trajectories and constellation parameters of constellation HHL120 after a gradient descent with 8 iterations.

according to

$$\vec{x}^{(s+1)} = \vec{x}^{(s)} + \delta\vec{x}^{(s)}. \tag{2.153}$$

To derive the matrix $\widehat{A}$, the figure of merit F is expanded into a Taylor series of first order

$$F(\vec{T}, \vec{t_0}) \approx F(\vec{T_0}, \vec{t_0}) + \vec{\nabla}_{\vec{T}} F \cdot \delta\vec{T}. \tag{2.154}$$

From this the matrix $\widehat{A}$ is deduced, which can be written as vector:

$$\begin{aligned}\widehat{A} = (\vec{A})^{\mathsf{T}} = ((\vec{\nabla}_{\vec{T}}F)_{0,0}, 0, (\vec{\nabla}_{\vec{T}}F)_{1,0}, 0, ..., (\vec{\nabla}_{\vec{T}}F)_{N-1,0}, 0,\\ (\vec{\nabla}_{\vec{T}}F)_{0,1}, 0, (\vec{\nabla}_{\vec{T}}F)_{1,1}, 0, ..., (\vec{\nabla}_{\vec{T}}F)_{N-1,1}, 0,\\ (\vec{\nabla}_{\vec{T}}F)_{0,2}, 0, (\vec{\nabla}_{\vec{T}}F)_{1,2}, 0, ..., (\vec{\nabla}_{\vec{T}}F)_{N-1,2}, 0).\end{aligned} \tag{2.155}$$

It consists of the spatial partial derivatives of the figure of merit F

$$(\vec{\nabla}_{\vec{T}}F)_{j,i} := \left(\frac{\partial F}{\partial(\vec{T}_{j,i})_x}, \frac{\partial F}{\partial(\vec{T}_{j,i})_y}, \frac{\partial F}{\partial(\vec{T}_{j,i})_z}\right), \tag{2.156}$$

where j is again the target point number, i is the spacecraft number and the superscript s was neglected for simplicity. Thus, we can write eq. (2.154) as

$$F(\vec{T},\vec{t}_0) \approx F(\vec{T}_0,\vec{t}_0) + \vec{\nabla}_{\vec{T}} F \cdot \delta\vec{T} = F(\vec{T}_0,\vec{t}_0) + \widehat{A}\cdot\delta\vec{x} \tag{2.157}$$

and the condition $\widehat{A}\cdot\delta\vec{x} \leqslant \vec{b}$ in eq. (2.151) with $\vec{b} = b \leqslant 0$ yields a variation $\delta\vec{x}$, which decreases the figure of merit F.
The equality constraint in eq. (2.151) for the $\Delta\vec{V}$ thrust times can be stated as

$$\widehat{A}_e^{(s)}\cdot\delta\vec{x}^{(s)} = \vec{b}_e = \vec{0} \quad\Leftrightarrow\quad t_{j,0}^{(s)} = t_{j,1}^{(s)} \;\wedge\; t_{j,0}^{(s)} = t_{j,2}^{(s)} \quad \forall j, \tag{2.158}$$

and can be formulated by a sparse matrix $\widehat{A}_e^{(s)}$ with $2\cdot N$ rows and only two ones per row.
The minimization of the total ΔV thrust with $\min ||\widehat{C}\cdot\delta\vec{x} - \vec{d}_c||^2$ can be written as

$$\min \left\| \begin{pmatrix} \widehat{Q}_0 & 0 & 0 \\ 0 & \widehat{Q}_1 & 0 \\ 0 & 0 & \widehat{Q}_2 \end{pmatrix} \cdot \delta\vec{x} - \begin{pmatrix} \Delta\vec{V}_0 \\ \Delta\vec{V}_1 \\ \Delta\vec{V}_2 \end{pmatrix} \right\|^2, \tag{2.159}$$

with $\widehat{Q}_i$ being the correction matrix for S/C i (cf. eq. (2.119)) and $\Delta\vec{V}_i$ is a large vector consisting of N appended single thrust vectors for S/C i required to fly the current trajectory. This is basically an extension of the method described in sec. 2.4.3 for the minimization of the ΔV of one S/C to a minimization of the ΔV of three S/C at once. One should note that this method minimizes the accumulated ΔV of all S/C and not the ΔV of the individual S/C. However, the amount of thrust stayed balanced between the S/C as the final results will show.
Finally, the box-boundaries $\vec{l} \leqslant \delta\vec{x} \leqslant \vec{u}$ are simply given by

$$\vec{l} := \begin{pmatrix} -\alpha \\ -\alpha \\ \dots \\ -\alpha \end{pmatrix}, \quad \vec{u} := \begin{pmatrix} +\alpha \\ +\alpha \\ \dots \\ +\alpha \end{pmatrix}, \tag{2.160}$$

where $\alpha \approx 3\cdot 10^{-5}$ corresponds (in non-normalized units) to a spatial constraint of approx. $\pm 4500\,\mathrm{km}$ for a variation in the target point position and to a temporal constraint of $\pm 2.5\,\mathrm{min}$ for a variation in the thrust time in each iteration step.
A solution to eq. (2.151) can be obtained with the function `lsqlin`, which is implemented in `matlab` and based on Coleman & Li [1996] and Gill *et al.* [1981]. It is an iterative method and required in our case an initial estimate for $\delta\vec{x}_0$ to yield reasonable results. We use the gradient step (eq. 2.155) rescaled to fit into the box-boundaries as the initial estimate:

$$\delta\vec{x}_0 := \frac{\vec{A}}{\max\{\max\vec{A}, |\min\vec{A}|\}}\alpha, \tag{2.161}$$

where the denominator is the maximum absolute vector component in $\vec{A}$.

The *constrained descent* method minimizes the objective function F under the constrained of minimal ΔV in a local region. The locality is caused by the fact, that the minimization as well as the constraint are based on linearizations. It is therefore very likely, that the solution will converge to a local minimum instead of to a global minimum of the function F. Although in each iteration step the direction with the smallest possible ΔV increment is chosen, it does not guarantee a final constellation with minimal ΔV. Other effects may arise due to non-linearities, which are present if the step size is not infinitesimal small.
Therefore, it should be clear that the method presented here is not optimal and only an attempt under investigation. It was chosen because of it's relative simplicity and applicability for problems with high dimension number.

2.7 Constrained Descent Results

In this section the results for the optimization attempt with the *constrained descent* method are summarized. For the simulations we varied mainly the orbit correction frequency, the box-boundary size α (eq. (2.160)) and therefore the initial guess (eq. 2.161). The parameter $b = \vec{b}$ (eq. 2.151) was used to influences the rate of descent. Usually a smaller b value leads to a higher descent rate and a smaller figure of merit, however, to the detriment of a high ΔV consumption.

2.7.1 Constellation: HHL120

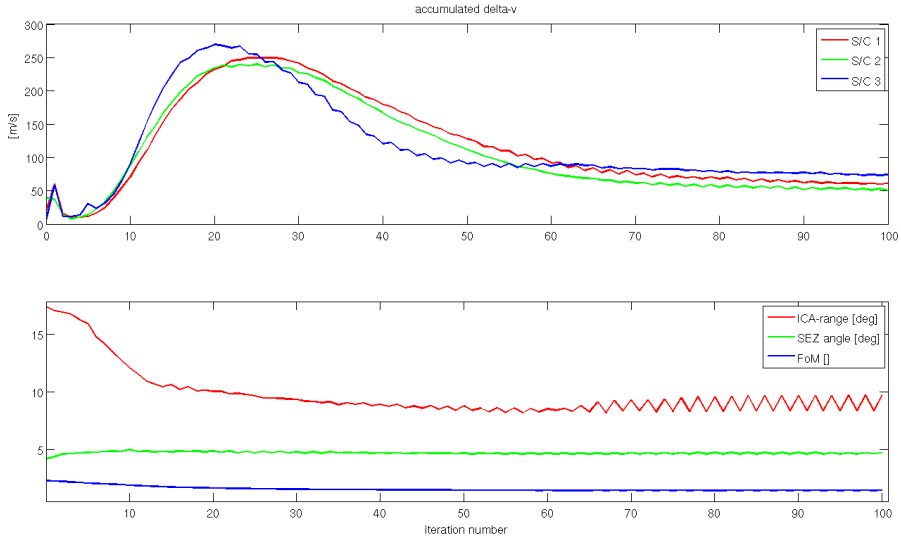

Figure 2.25: Evolution of the ΔV per S/C and constellation parameters during the optimization of constellation HHL120.

This constellation was simulated with a mission period of $T_m = 3$ years. Every 28 days a ΔV thrust was introduced, which corresponds to $N = 40$ target points. The evolution of the optimization for 100 iteration steps is shown in fig. 2.25. The amount of thrust increased initially, but decreased to 60 m/s, 52 m/s and 72 m/s for the three S/C for the three year period. Some objectives of the optimization are shown at the bottom plot of fig. 2.25. The inner-constellation angle variation (peak-peak) decreased from approx. 18° to 8.3° (ICA-range) and the figure of merit from 2.31 to 1.47. Also the third S/C avoids the SEZ, since the green trace is above 4.5°. One can see a *zick-zacking* of the objective parameters, especially in the last 30 iterations. This is a well known feature of gradient descent like methods.
The final trajectory is depicted in fig. 2.26 (top). In comparison to the initial trajectory (fig. 2.20) one notices a significant change in the orbit of S/C 3, which became more elliptical or Halo-like[10]. The bottom plot of fig. 2.26 confirms that the center S/C stays out of the SEZ. A secular trend is apparent in the armlengths due to the fact that the center S/C has a longer orbital period than the S/C on the large Halo.
The optimization was repeated with $N = 45$ target points, which corresponds to a $\Delta\vec{V}$ thrust every 24.9 days. The results are quite similar, although more iteration steps are required to decrease the total ΔV after an initial peak. A noteworthy improvement in the figure of merit (and inner-constellation angle variation) was not observed. Also for $N = 35$ target points no significant change was observed, neither

[10] Halo orbits with small amplitude, which are close to the Lagrangian points L_1 or L_2, are very elliptical.

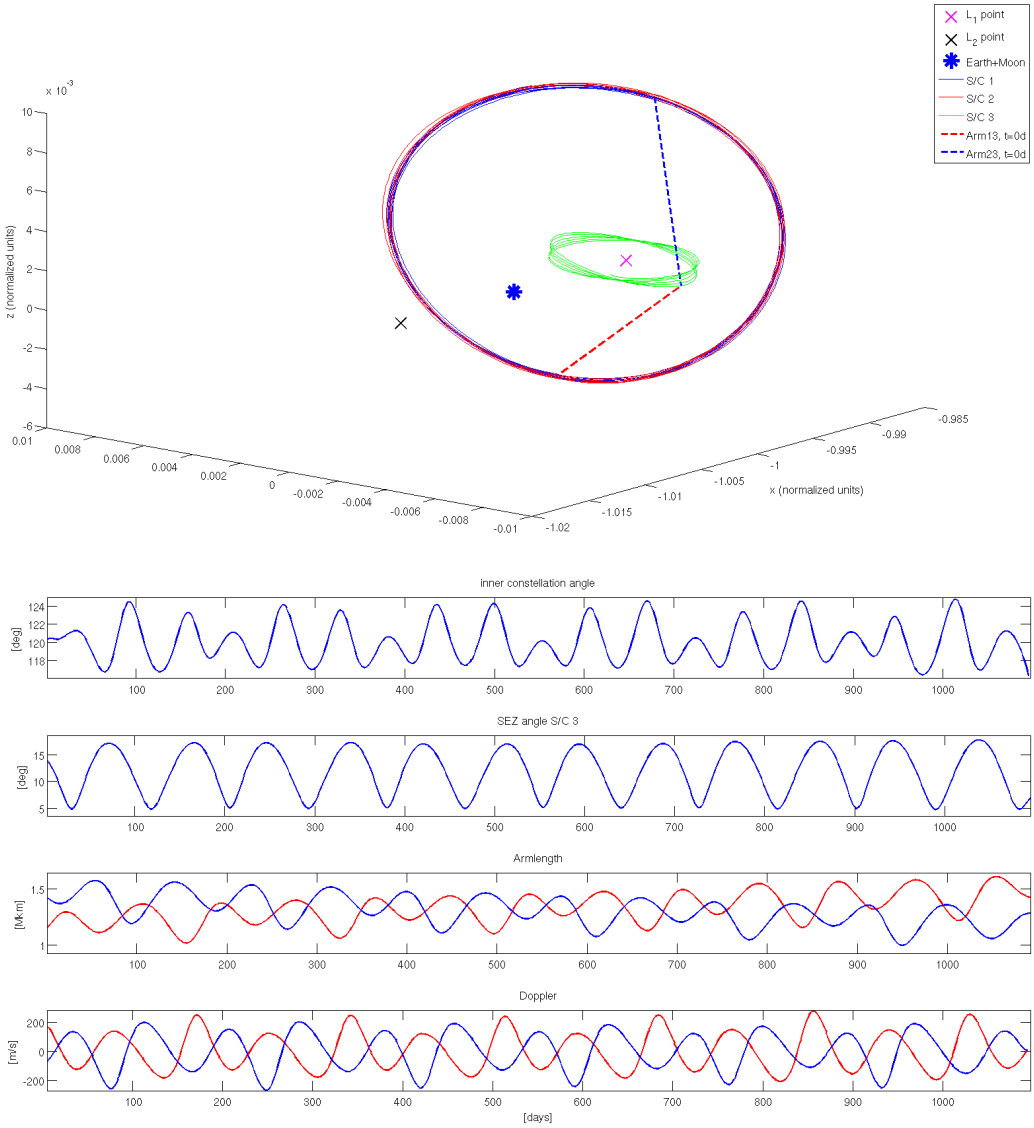

Figure 2.26: The constellation HHL120 in a 3-d plot (top) and constellation parameters (bottom) after the optimization.

in the figure of merit nor in the total ΔV. This indicates that even less frequent orbit corrections are sufficient to achieve this constellation.

2.7.2 Constellation: HHL90

The two arm configuration with 90° angle between the arms was optimized using changing parameters during the optimization (see fig. 2.27). For the first 10 iteration steps a steep descent of the figure of merit F was used (large $|b|$ value), which at the same time increased strongly the ΔV value. Then a less steep descent was set, which allowed a relaxation of the fuel consumption. At the end, during iteration 103 to 123, again a steep descent was forced. This should illustrate how the optimization parameters can be used to control the ΔV consumption and the figure of merit.
In this scenario a mission duration of 2 years was used and a $\Delta\vec{V}$ thrust was applied approximately every 18.7 days ($N = 40$). The trajectory at iteration step 102 is shown in fig. 2.28. Again, the small Lissajous orbit was optimized to an elliptical (Halo-like) orbit. The large Halos of S/C 1 and 2 moved away from the nominal trajectories, while in the HHL120 constellation the trajectories stayed close to the nominal path (cf. fig. 2.26). The inner angle variation (peak-peak) was reduced from

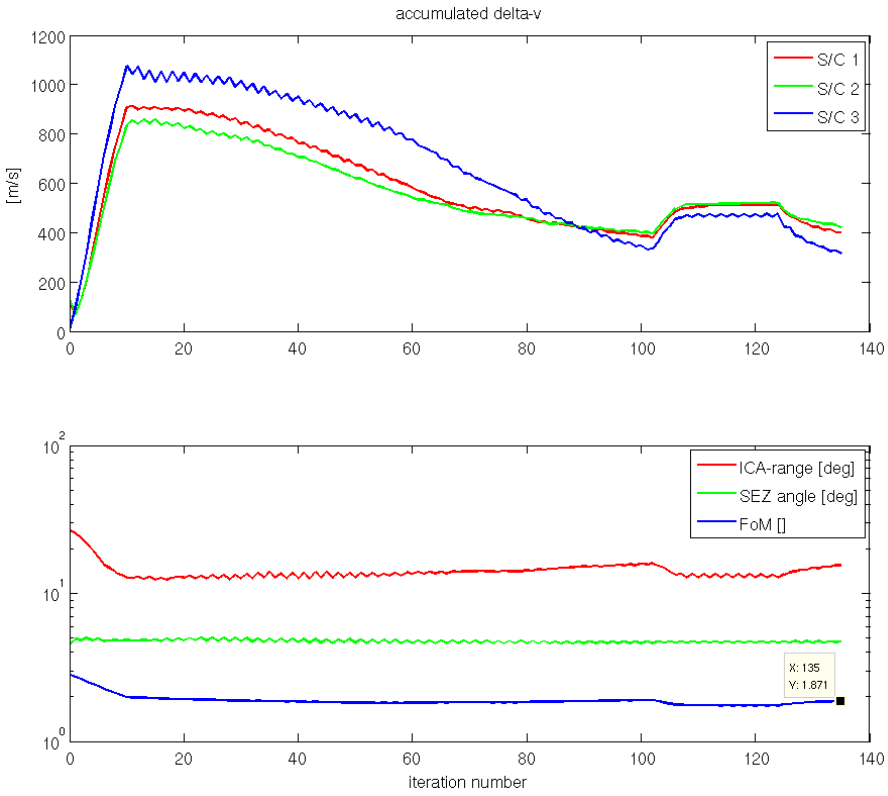

Figure 2.27: Evolution of the ΔV per S/C and constellation parameters during the optimization of the constellation HHL90.

26.8° to 16.0° due to the optimization. The actual thrust required at each target point for each S/C is shown in fig. 2.29. The maximum value is below 25 m/s.

2.7.3 Constellation: HHH60

The constellation HHH60 is an attempt for a LISA-like constellation with three arms in an equilateral triangle formation. The optimization evolution is shown in fig. 2.30, where a mission period of 3 years and $\Delta\vec{V}$ thrusts every 28 days ($N = 40$ target points) are used. As for the constellation HHH120 an initial peak in the accumulated ΔV is present, but the fuel consumption decreases during the optimization. A good compromise between low figure of merit and low ΔV seems to be at the iteration number 58. The trajectories of this iteration step are depicted in fig. 2.31 and require approximately 200 m/s per S/C per year.
The trajectories seem to run away at the start and ending points. This is a known feature of numerical optimization methods [11] and is usually suppressed by choosing s slightly larger simulation period than required. Another possibility to suppress the effect is by imposing some boundary conditions for the start and end points. However, in the inner time period the inner-angle variation (peak-peak) was reduced from approximately 24° to 13° by the optimization.
During the optimization the constellation armlength decreased from initially 2.0 Mkm to approximately 1.3 Mkm and the Doppler rate was reduced from approximately ±200 m/s to below ±100 m/s (fig. 2.31, third plot at the bottom). The distribution of the ΔV of 200 m/s per S/C per year over the simulated mission period is shown in fig. 2.32. The maximum required thrust at a target point is below 20 m/s.

[11] In the orbit simulations of the LISA mission the constellation breaks also quickly apart at the end of the optimization period.

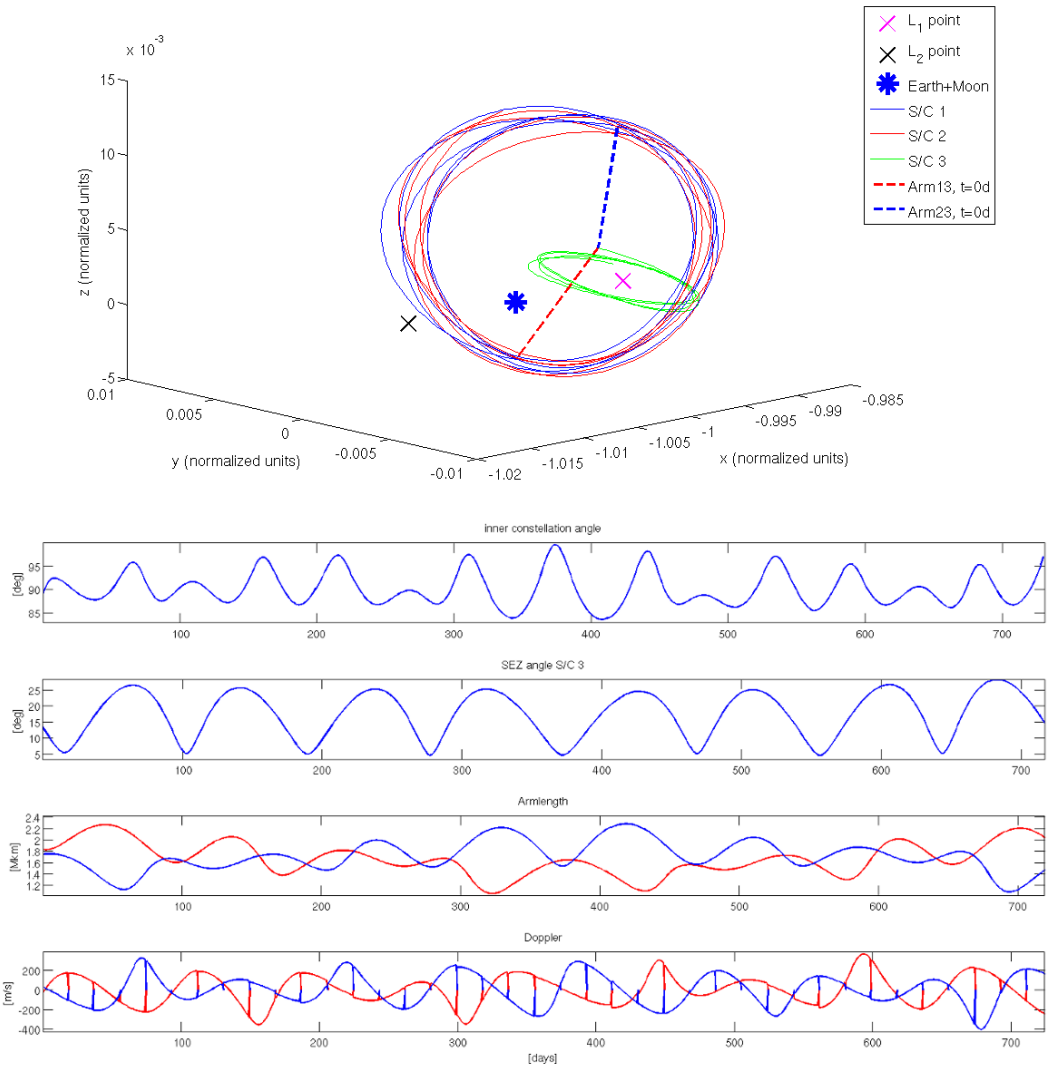

Figure 2.28: The constellation HHL90 in a 3-d plot (top) and constellation parameters (bottom) after the optimization. The glitches in the Doppler rate are spurious numerical artifacts and denote the ΔV thrusts.

2.8 Alternative Approach with Constellation HHh115

An alternative approach is introduced here, which was tried out in an early stage of the research presented in this thesis.
At first a constellation is defined using the analytical expressions in the CR3BP. We use a large Halo orbit to host two daughter S/C and a center S/C is on a small Halo orbit, which avoids the SEZ. The formed detector has an average angle of 115° between the two arms and an armlength of approximately 1.4 Mkm (see fig. 2.33). The initial parameters of the constellation (position and velocity) are transformed into a solar system barycentric frame. Then the orbits are integrated in a dynamical model considering the full solar system (JPL DE405 ephemeris). Every 80 days ΔV thrusts are introduced to keep the constellation stable, close to the nominal Halo orbits, and to reduce constellation distortions. The optimization is performed using a nonlinear multidimensional minimizer (combination of Nelder-Mead simplex and modified Levenberg-Marquardt [Heinzel, 2012]).
The obtained optimized trajectories are shown in fig. 2.34. They are close to the nominal Halo orbits, since the figure of merit contained a punishment term for trajectories getting away too far. This was required to keep the orbits in the vicinity

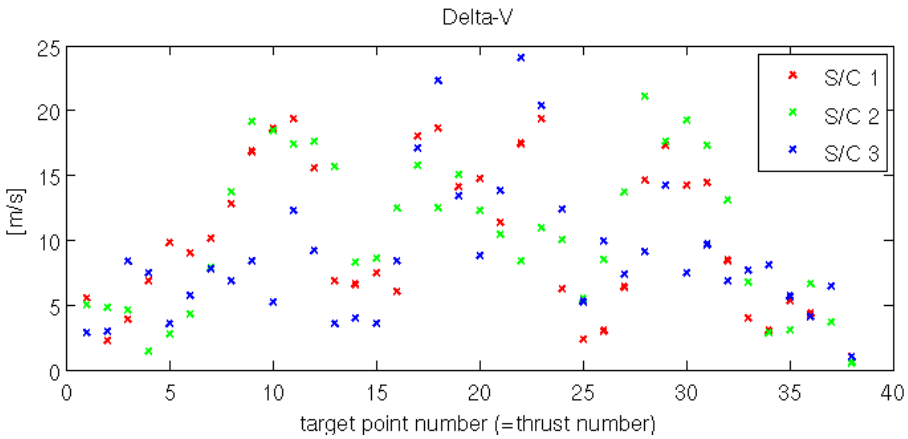

Figure 2.29: The magnitude of $\Delta\vec{V}$ thrusts at each target point for the optimized constellation HHL90.

of the Lagrangian point and the constellation stable. Therefore, the distortions of the constellation (e.g. inner angle variations) were suppressed only weakly. However, the proximity of analytical and optimized orbits indicates that the perturbations due to Earth's Moon, other planets or the eccentricity of Earth's orbit do not change the shape or position of the orbits significantly.
Another difficulty of the method arises due to the fact that a weighting is required between the minimal ΔV criterion and the constellation stability, since the numerical minimizer requires a single figure of merit function.
The constellation parameters after the optimization in the full ephemeris system are shown in fig. 2.35. The peak-peak variation in the inner constellation angle is approximately 14° and a secular drift in the armlengths is clearly apparent due to the different orbit periods of large and small Halo orbit. The ΔV consumption is below 50 m/s for each S/C for the two year period (see fig. 2.36). However, as already mentioned, this attempt did not suppress the constellation deformations well, since it was developed in an early stage of the research.

2.9 Summary, Conclusion and Outlook

The aim of this thesis chapter was the study of possible satellite constellations and orbits in the vicinity of the Sun-(Earth+Moon) Lagrangian points in particular for applications in space-based gravitational wave detectors.
In the beginning the orbits of the LISA mission and other LISA-like mission proposals were briefly introduced. Then the fundamental dynamics in the proximity of the Lagrangian points were studied in the simplified *circular restricted three body* dynamical model. The analytical expressions for Halo and Lissajous orbits were derived. Also numerical approaches for the determination of trajectories in the CR3BP were presented, which require only minimal orbit correction maneuvers.
Using these natural orbits three exemplary constellations (HHL120, HHL90, HHH60) were selected for further studies. These constellations are by far not as stable as the LISA constellation in terms of constellation deformations. The cartwheel formation of LISA, which can produced by three elliptical orbits, allows naturally a very rigid constellation. Whereas the trajectories in the vicinity of the Lagrangian points are more complex. For constellations with baseline armlengths of > 1 km, the inner constellation angle varies by a few tenth degree and the Doppler rates are in the order of ± 200 m/s.
One should also note that the LISA formation does not require any orbit corrections

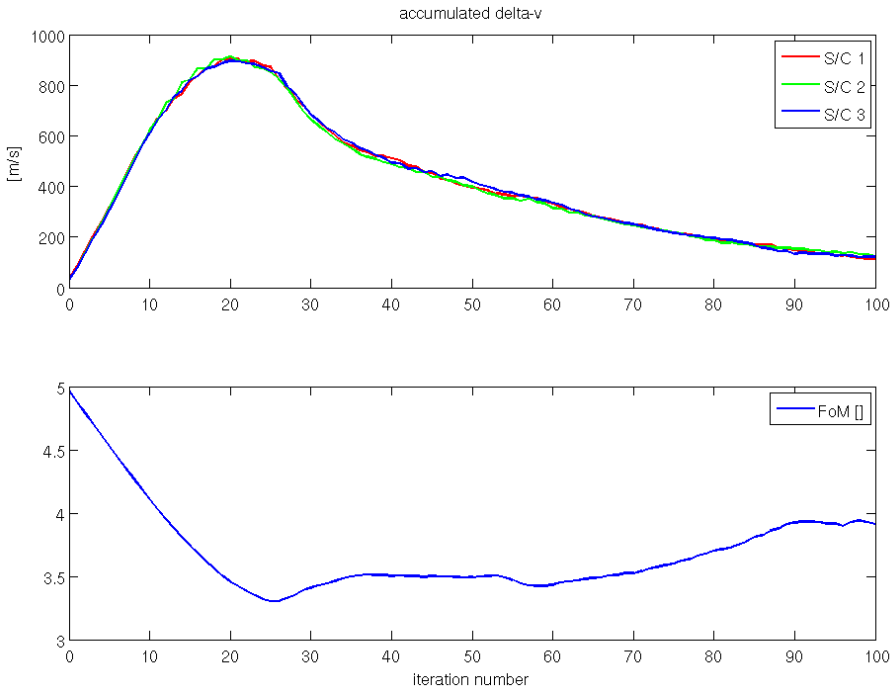

Figure 2.30: Evolution of the ΔV per S/C and constellation parameters during the optimization of the constellation HHH60.

for the mission duration of a few years, while trajectories at the Lagrangian points are in general intrinsically unstable. However, it is very likely that a space-based gravitational wave detector is also feasible with orbit corrections as long as they are rare, since the measurements need to be interrupted during the thrusts, where the testmasses do not follow geodesics. Therefore, it was also analyzed if the three constellations can be improved by introducing instantaneous ΔV thrusts. It was required that the orbit corrections are executed at the same time at all S/C to minimize the measurement gaps.
For the computation of thrust magnitude and direction (and partly of the instant of time) an optimization method based on linearizations was established. The driving factors were the improvement of the constellation goodness and simultaneous minimization of total amount of required thrust. The constellation goodness considered various aspects like detector armlength mismatch or avoidance of the solar exclusion zone, but the main focus was on the stabilization of the inner-constellation angle.
The results of the optimization revealed that the inner-constellation angle variation (peak-peak) could be reduced to below $\pm 4.5°$, $\pm 7.0°$ and $\pm 6.5°$ for the constellation HHL120, HHL90 and HHH60, respectively. The fuel consumption in terms of ΔV could be kept below 200 m/s per S/C per year.

It is very likely that these results can be improved further, although reaching the LISA stability with Doppler rates below 20 m/s and angle variations below $\pm 2°$ seems very challenging. There are several parameters in the optimization chain, which were not adjusted in this thesis and could yield better results. On the other hand the definition of the figure of merit does not account for the (peak-peak) variation and tuning of some constants may also allow improvements. Also the optimal thrust frequency was not determined, as well as the thrust times were allowed only to change a within small boundaries. Hence, the here presented method should be considered as immature.
In the future one could try to use small Halo orbits instead of Lissajous orbits as starting point for the constellations HHL120 and HHL60, since the optimization

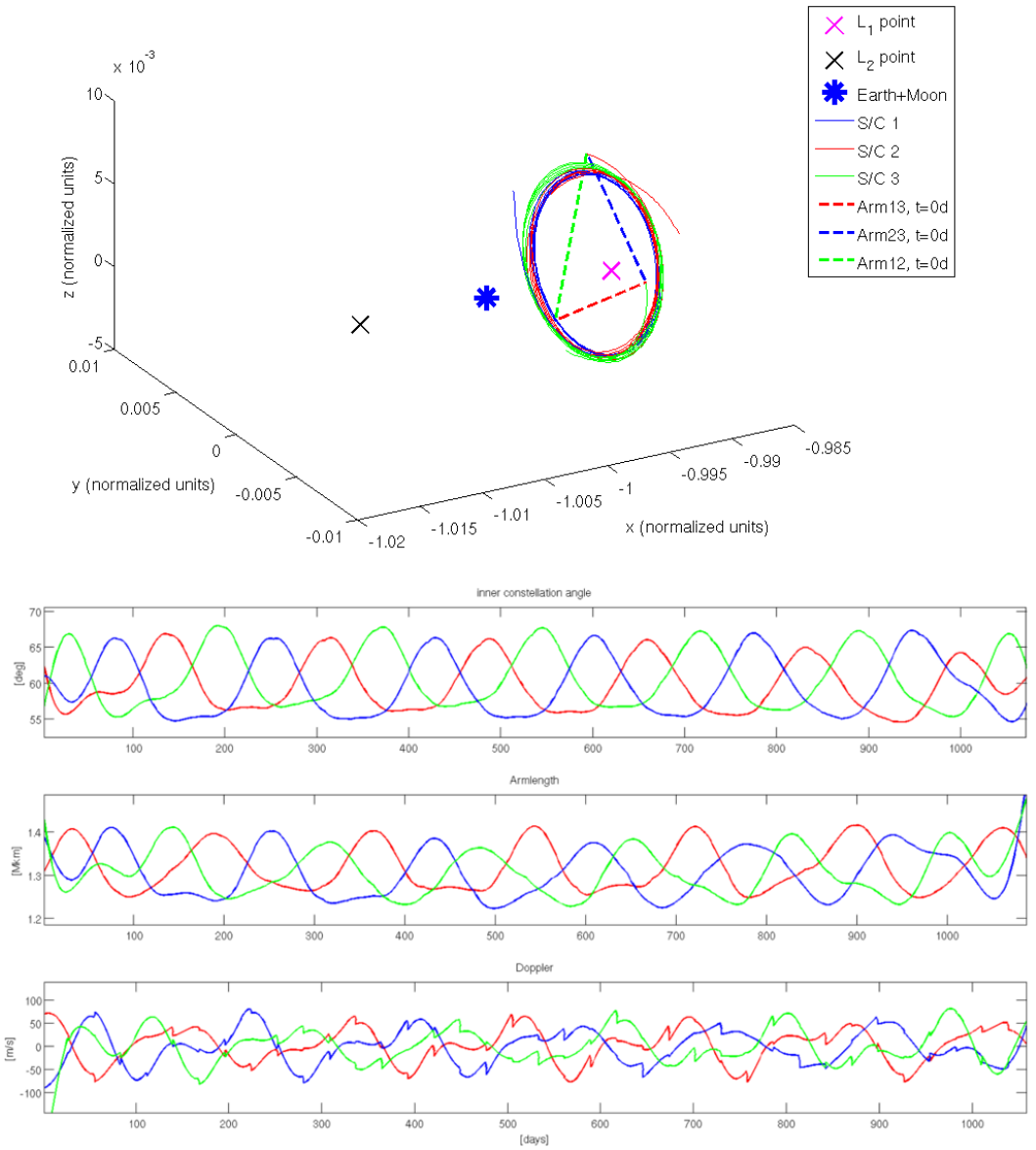

Figure 2.31: The constellation HHH60 in a 3-d plot (top) and constellation parameters (bottom) after the optimization. The glitches in the Doppler rate are due to the ΔV thrusts.

converges to small Halo-like orbits. One should also recall that the main simulations were performed within the idealized CR3BP and not in a full ephemeris system. Since all algorithms and methods presented here can be transitioned to a full ephemeris model, an optimization in the more realistic full ephemeris model should be performed to confirm the applicability *in the real world*. However, as the brief simulation on the constellation HHh115 showed, the deviations between CR3BP and full ephemeris model are assumed to be small.

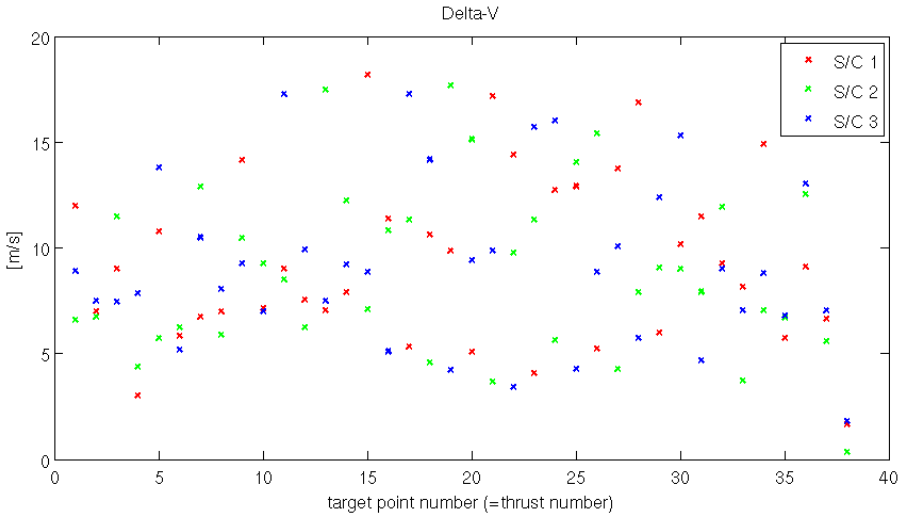

Figure 2.32: The magnitude of $\Delta\vec{V}$ thrusts at each target point for the optimized constellation HHH60.

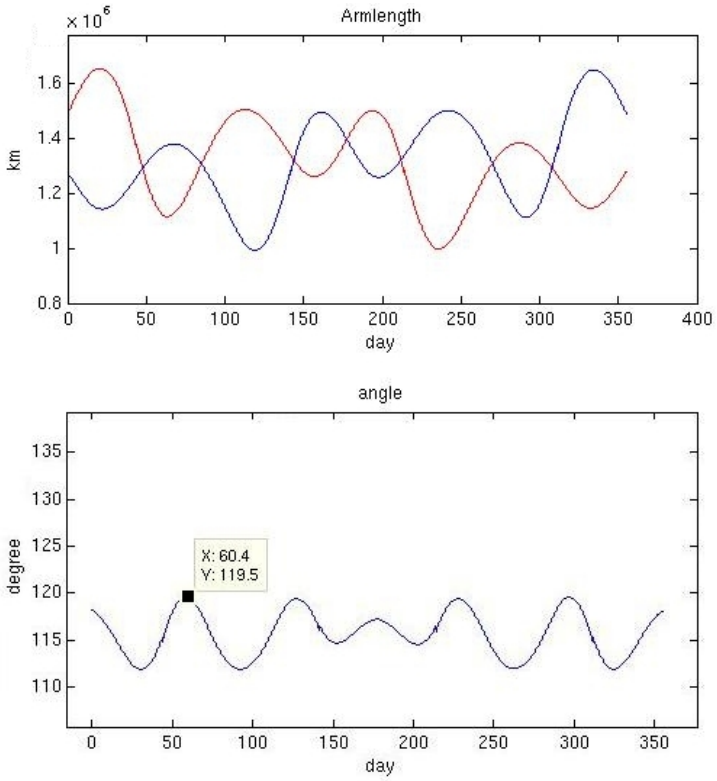

Figure 2.33: Armlength (top) and inner constellation angle (bottom) of the analytical (CR3BP) constellation HHh115 for a one year period.

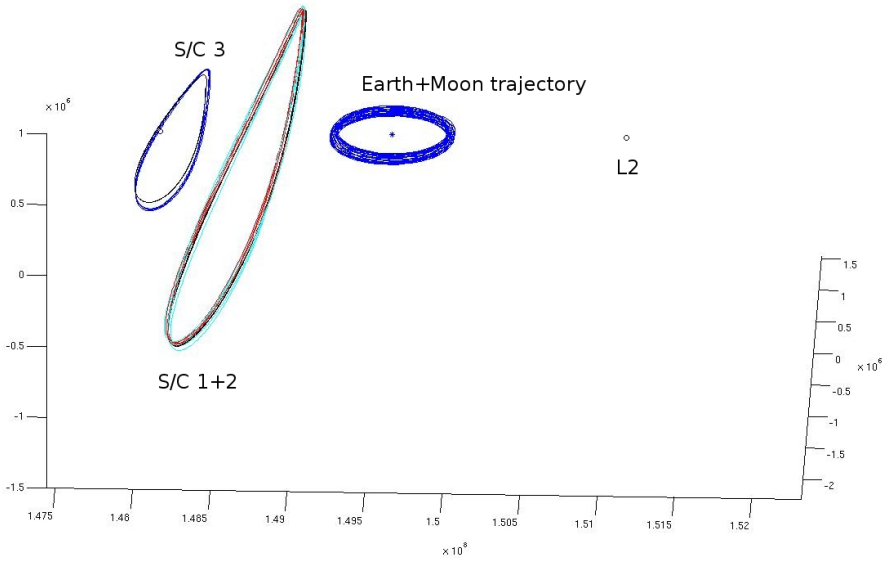

Figure 2.34: 3-d plot of the optimized constellation HHh115. The black traces (visible at S/C 3) are the nominal Halo orbits. The units of the axes are kilometer.

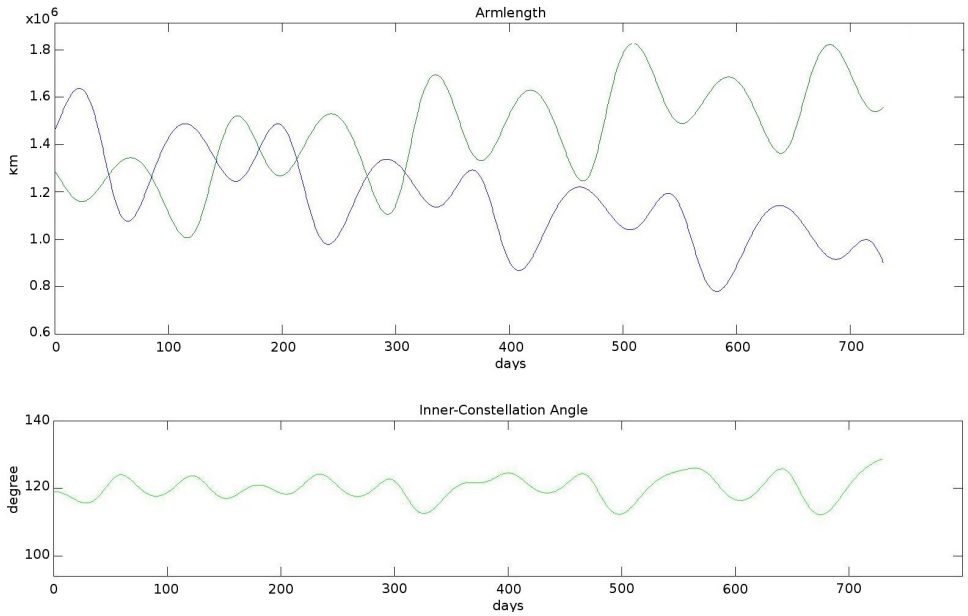

Figure 2.35: Armlength (top) and inner constellation angle (bottom) of the optimized constellation HHh115 for a two year period in a full ephemeris model. The constellation angle varies between 112° and 126°.

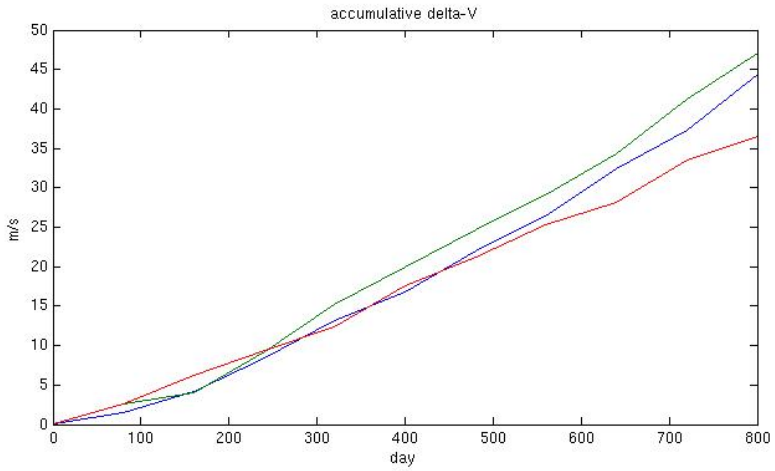

Figure 2.36: The ΔV consumption for each S/C of the optimized constellation HHh115 in a full ephemeris model.

Chapter 3

GRACE Follow-On LRI Simulations

The satellite pair GRACE (Gravity Recovery and Climate Experiment) was launched in 2002 to measure Earth's gravity field. The main scientific device is a microwave ranging instrument providing variations of the inter-satellite distance (low-low satellite tracking) down to the micrometer level. The signature of Earth's gravity field can be extracted in post-processing when ranging information is combined with other on-board instruments like GPS (high-low tracking) and accelerometer data.
The mission was designed for a nominal lifetime of 5 years, but was extended multiple times until now (2012) due to its great scientific impact. The monthly gravity field maps allow, for example, tracking of the hydrologic balance in Africa [Boy *et al.* , 2012] or inference on glacier ice melting over Greenland and Antarctic [Velicogna, 2009]. Figure 3.1 shows the major contributions to Earth's mass flux in spatial and temporal extent. Various disciplines in geoscience benefit from these data.
GRACE provides Earth gravity field maps with typical monthly temporal resolution, mainly due to the fact that enough data with global coverage has to be collected. The spatial resolution extents down to about 250 km. As these signals are observed with satellites flying with an orbital velocity of about 7.7 km/sec, the signal with 250 km spatial resolution corresponds to a frequency of approximately 31 mHz in the measured data.
In 2012 the battery capacity of GRACE was already critically low, leading to shutdown periods of some components and to gaps in the scientific data[1]. To keep the gap after the end of the GRACE mission as short as possible and ensure continuity of the recorded 10 year long-term data, a fast GRACE Follow-On (GFO) mission is planned by NASA/GFZ. The current mission design foresees a launch in 2017 into a circular polar orbit with 450 km height and with about 200 km spacecraft (S/C) separation. To accomplish the tight time schedule, the satellites for GFO should be basically a copy of the GRACE satellites. The main instruments and components for GFO will be taken over from GRACE and will be

- **K/Ka band ranging (KBR) ranging system**: positioned on-axis and measuring inter-satellite distance variations.
- **Accelerometer**: needs to be positioned at S/C center of mass (CoM) in order to measure non-gravitational forces like drag and solar-radiation pressure; data is used to correct ranging information for non-gravitational contributions in gravity field computation.
- **GPS receiver**: providing location of satellites down to cm level.

[1] see http://podaac.jpl.nasa.gov/grace/

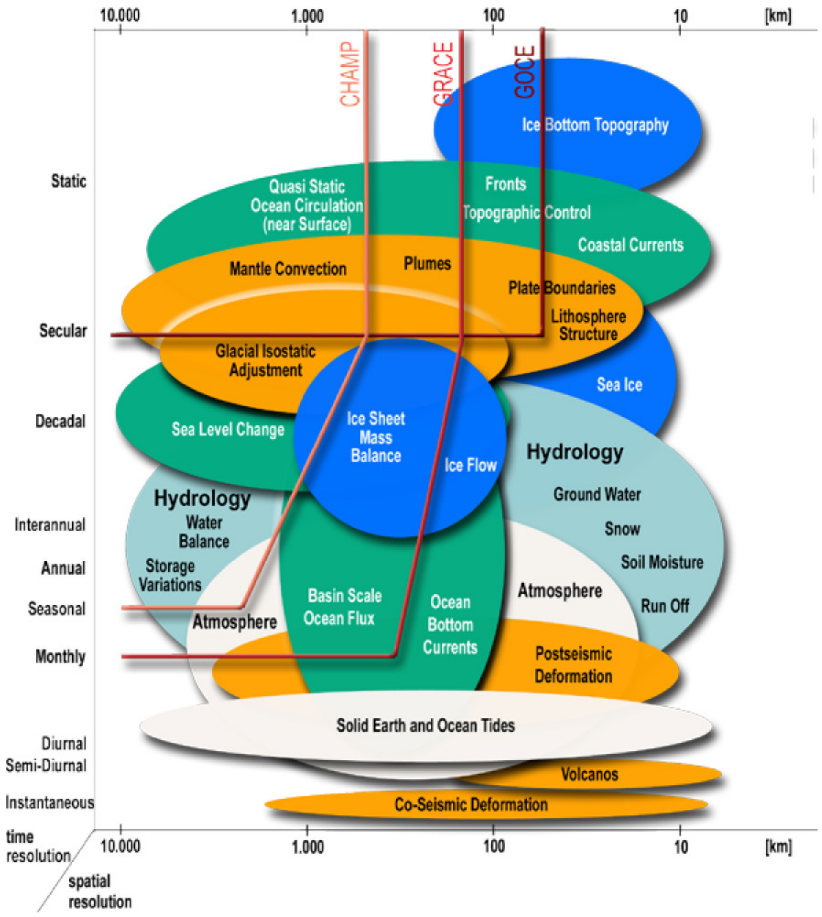

Figure 3.1: Spatial and temporal scales of geoid signals associated to solid Earth (orange), ocean (green), ice (dark blue) and continental hydrology (light blue) processes. The red lines show the spatial and temporal resolution limits of the CHAMP, GRACE and GOCE missions; from [Ilk *et al.* , 2005]

- **Star cameras**: attitude information of the S/C.
- **Magneto-torquers**: used for attitude control of S/C.
- **Cold-gas thruster**: for adjustment of orbits and attitude of S/C.

In contrast to GRACE, GFO will also include a laser ranging interferometer (LRI), which will fly as a technical demonstrator and will provide a second independent ranging measurement as well as pointing information [Sheard *et al.* , 2012]. The principle of measuring satellite distances with laser interferometers has been evolving for more than three decades in the context of space-based gravitational wave detectors (NGO-Yellowbook [2011], Faller *et al.* [1985]). Testing the first inter-satellite laser interferometer in space in the GFO mission provides the opportunity to compare the results to another ranging measurement and to validate the readiness of this technology for further space-based applications, in addition to producing better ranging measurements for GFO itself.

This chapter is structured as follows: In section 3.1, an overview of the LRI is given and the measured signal is derived from Doppler shifts. In section 3.2, a derivation of the measured phase is given, taking into account the different pathlengths on the optical bench. Furthermore, contributions of the laser phase or frequency noise as well as *off-racetrack* pathlength fluctuations are discussed. Corner-cubes

and in particular the Triple Mirror Assembly, which is a key component of the LRI concept, is treated are section 3.3. The optical bench and its subunits are described in section 3.4. Also second order effects like astigmatism are discussed there. The simulation of the LRI is divided into a model for the inter-satellite propagation and into a model of the LRI on one spacecraft. Details on the modeling can be found in section 3.5. The second last section contains various tables and simulation results for a particular optical bench setup, where the previously derived equations and models are applied. On the one hand the simulation section should verify the previously derived equation, for example for the desired position of the steering mirror. On the other hand a particular optical bench setup is analyzed in detail by computing various coupling factors and investigating their origin. This provides a better understanding of the optical system. The summary and some conclusive statements in the very end conclude this chapter.

3.1 Laser Ranging Interferometer Overview

The main scientific measurement in GRACE as well as in GFO is the inter-satellite distance, more precisely the distance variations measured between the CoM of one spacecraft to the CoM of the other spacecraft. In order to sense only non-gravitational forces, the accelerometer needs to be located at the CoM of the spacecraft, otherwise gravitational torque and corresponding attitude jitter disturbs the measurements[2]. This fact and the location of the KBR at the rear center on the leading spacecraft and at front center of the trailing spacecraft excludes an on-axis interferometer concept, where two mirrors (or test masses) are co-located with each CoM and laser beams measure along the CoM connection line (called Line Of Sight, LOS). Measuring not directly from CoM to CoM requires in the case of the KBR corrections, if one antenna phase center is not on the LOS. Then attitude information, e.g. from star cameras, has to be used to derive the equivalent LOS length changes (so called 'geometric correction', Horwath *et al.* [2011]).
Because the CoM is occupied by the accelerometer and the direct LOS by the microwave ranging system and cold-gas fuel tanks, an off-axis interferometer in a 'racetrack' configuration has been proposed for GFO[3]. In fig. 3.2 the optical setup is depicted. The Triple Mirror Assemblies (TMA) on each spacecraft act as retro-reflectors and form the 'racetrack', which is divided into symmetric halves by the red and blue beams. The total pathlength of the round track is twice the distance between both accelerometers or CoM of each S/C due to the special properties of the TMA (cf. section 3.3).
The current performance requirement is visualized in fig. 3.3. The measurement band is from 2 mHz up to 100 mHz, while lower frequencies are seen as goal (dashed lines). The upper frequency limit is due to the sampling rate of the data. It is assumed that the accelerometer noise[4] will limit the overall performance at low frequencies, because the correction for non-gravitational forces would have a higher noise than the ranging measurement. At high frequencies the laser frequency noise and spacecraft attitude jitter limit the LRI performance, but here the accuracy of the final gravity field is anyway limited by aliasing and not by the ranging performance.

[2] a detailed analysis can be found in [Wang, 2000]

[3] to my knowledge first by Dr. William (Bill) Folkner (Jet Propulsion Laboratory - NASA)

[4] assumed is the differential accelerometer noise of two uncorrelated accelerometer with a sensitivity of $10^{-10}\,\mathrm{m/s^2}$ for each, which are integrated in frequency domain to obtain a displacement noise

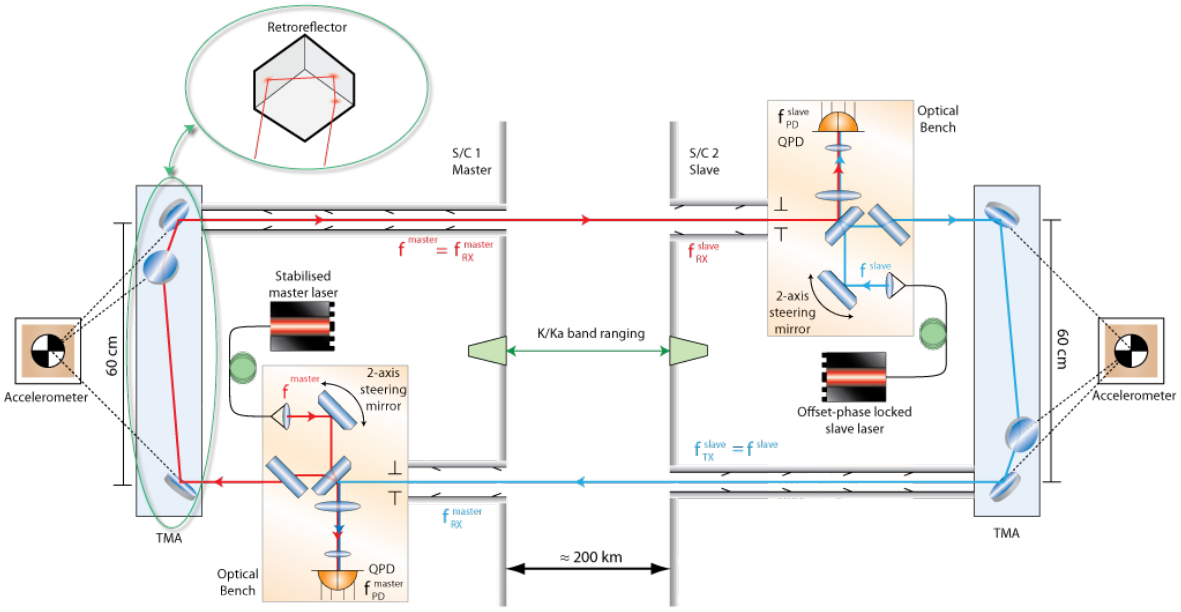

Figure 3.2: Optical LRI setup depicted without laser frequency stabilization unit; the spacecraft separation is approximately 200 km; from [Sheard *et al.* , 2012]; © Springer

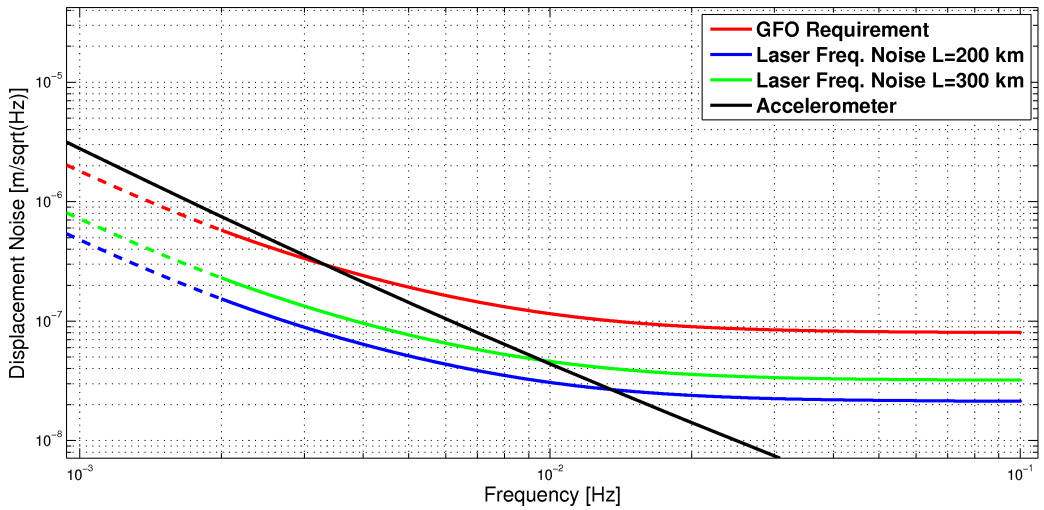

Figure 3.3: GFO LRI requirement (red), estimated accelerometer noise (black), and contribution due to laser frequency noise with $30\,\mathrm{Hz}/\sqrt{\mathrm{Hz}}$ for two different spacecraft separations.

3.1.1 LRI Basic Principle

The inter-satellite distance variations are measured by a round-trip measurement. Each spacecraft has a laser, whereby one S/C is designated as a master (fig. 3.2: S/C 1 on the left). The master laser light is guided over a steering mirror and two beam-splitter to the TMA, where it is retro-reflected towards the slave spacecraft. The slave spacecraft receives frequency shifted light from the master due to the Doppler effect, which is caused by the relative motion of the spacecrafts. The received light is interfered with the local light of the slave spacecraft (fig. 3.2: blue light), whereas most of the local light is sent back over the TMA to the master spacecraft. The interference is measured with a photodiode on the slave S/C (fig. 3.2: $\mathrm{f}_{\mathrm{PD}}^{\mathrm{slave}}$). This information is used to operate the slave S/C laser in a transponder mode, where the slave laser produces basically a phase-copy of the received light from the master.
On the way back to the master S/C, the light gains again a Doppler shift. On the master S/C the received light is also interfered with the local light, which was initially sent out. With a photodiode the frequency difference between the light, initially sent out, and the light, which was in total Doppler shifted twice, is measured (fig. 3.2: $\mathrm{f}_{\mathrm{PD}}^{\mathrm{master}}$). This yields the relative velocity and therefore the distance variations between both S/C.
The master and slave S/C will use a technique called *Differential Wavefront Sensing* to achieve an accurate pointing of the laser beams towards the distant spacecraft. Therefore the overlap of the received light with the local light is also measured with the photodiodes on each S/C. A control loop actuates the steering mirror such that both beams have perfect angular overlap. Then the outgoing light is parallel to the incoming due to the properties of the TMA and hence ensures pointing towards the distant spacecraft.

3.1.2 Principle of Active Transponder

The LRI is based on an active transponder system using an offset phase locked loop (PLL) [Sheard *et al.* , 2012]. One spacecraft is chosen to be the master spacecraft (fig. 3.2: S/C 1 on the left), but the S/C are designed to be interchangeable. The master emits frequency stabilized laser light with $\lambda = 1064\,\mathrm{nm}$ wavelength towards the other spacecraft in 200 km distance. The laser beam will diverge to a size of about 30 m radius at the distant (slave) spacecraft and is shifted in frequency by the Doppler shift [Halliday *et al.* , 2010, p.1040],

$$f_{\mathrm{RX}}^{\mathrm{slave}} = f^{\mathrm{master}} \sqrt{\frac{1 - \frac{v_r}{c}}{1 + \frac{v_r}{c}}}, \tag{3.1}$$

due to the relative LOS velocity v_r of the spacecraft. A fraction of the beam will be cut out by an 8 mm diameter aperture [Sheard *et al.* , 2012, tab. 1] on the optical bench. The received beam, in the best case a few hundred picowatt in optical power [Sheard *et al.* , 2012, fig. 8], is interfered with the local laser beam on the slave spacecraft. Because the slave laser is arranged to have a frequency offset f_{off} of a few MHz w.r.t. to the received light, a beatnote is produced on the photodiode of the slave spacecraft at f_{off},

$$f_{\mathrm{PD}}^{\mathrm{slave}} = f^{\mathrm{slave}} - f_{\mathrm{RX}}^{\mathrm{slave}} = f_{\mathrm{off}}. \tag{3.2}$$

This sinusoidal signal is kept at constant frequency and phase by adjusting the local laser frequency and phase via the PLL feedback control loop[5].

[5] this may sound contradictory, because the phase is the time integral of frequency. In the context of PLLs the phase is understood as the integrated frequency without the frequency offset, which is introduced in a mixer and desired from the spacecraft master oscillator.

Most of the light of the laser aboard the slave spacecraft is sent back to the master spacecraft, meaning that the slave spacecraft emits light with same phase as it has received, but shifted in frequency by an offset

$$f_{\mathrm{TX}}^{\mathrm{slave}} = f^{\mathrm{slave}} = f_{\mathrm{RX}}^{\mathrm{slave}} + f_{\mathrm{off}}. \tag{3.3}$$

Thus the slave spacecraft acts as an active retro-reflector (transponder), enhancing the laser power and shifting the frequency, but maintaining the phase. [6]
The master spacecraft receives light, which is Doppler shifted a second time:

$$f_{\mathrm{RX}}^{\mathrm{master}} = f_{\mathrm{TX}}^{\mathrm{slave}} \sqrt{\frac{1-\frac{v_r}{c}}{1+\frac{v_r}{c}}} = (f_{\mathrm{RX}}^{\mathrm{slave}} + f_{\mathrm{off}}) \sqrt{\frac{1-\frac{v_r}{c}}{1+\frac{v_r}{c}}} \tag{3.4}$$

$$= f^{\mathrm{master}} \left| \frac{1-\frac{v_r}{c}}{1+\frac{v_r}{c}} \right| + f_{\mathrm{off}} \sqrt{\frac{1-\frac{v_r}{c}}{1+\frac{v_r}{c}}}. \tag{3.5}$$

Again, only a few hundred picowatt of light power arrive at the optical bench, where the received light is interfered with the local laser light, which results in a beatnote on the photodiode with frequency

$$f_{\mathrm{PD}}^{\mathrm{master}} = f^{\mathrm{master}} - f_{\mathrm{RX}}^{\mathrm{master}}. \tag{3.6}$$

The LOS velocity v_r is time-dependent with assumed magnitude of a few m/s. Thus we can write the frequency of the beatnote on the photodiode of the master S/C in the 1st order series expansion as

$$f_{\mathrm{PD}}^{\mathrm{master}}(t) = f_{\mathrm{off}} - 2\frac{v_r(t)}{c}(f^{\mathrm{master}} + \frac{f_{\mathrm{off}}}{2}) + \mathcal{O}\left(\frac{v_r^2}{c^2}\right) \tag{3.7}$$

$$\approx f_{\mathrm{off}} - 2v_r(t)\left(\frac{1}{\lambda} + \frac{f_{\mathrm{off}}}{2c}\right). \tag{3.8}$$

This beatnote frequency contains the ranging information. A phasemeter will track this signal and provides a phase measurement

$$\Psi(t) = 2\pi \int_{t_0}^{t} f_{\mathrm{PD}}^{\mathrm{master}}(t') - f'_{\mathrm{off}}\, dt', \tag{3.9}$$

where a frequency offset f'_{off} has been subtracted. In the optimal case both offset frequencies are equal ($f'_{\mathrm{off}} = f_{\mathrm{off}}$), requiring that both S/C clocks can produce the same absolute frequency or the frequency difference is known. Then the following equations for the inter-satellite distance variations ρ are valid

$$\Psi(t) = -4\pi\left(\frac{1}{\lambda} + \frac{f_{\mathrm{off}}}{2c}\right)\int_{t_0}^{t} v_r(t')dt' = -4\pi\left(\frac{1}{\lambda} + \frac{f_{\mathrm{off}}}{2c}\right)(\rho(t) - \rho(t_0)) \tag{3.10}$$

$$\Leftrightarrow \rho(t) = -\frac{1}{2}\underbrace{\frac{2\lambda c}{2\pi(2c+\lambda f_{\mathrm{off}})}}_{=:1/k}\Psi(t) + \rho(t_0) = -\frac{1}{2\cdot k}\Psi(t) + \rho(t_0). \tag{3.11}$$

Eq. (3.11) differs from [Sheard *et al.* , 2012, eq. 12] by the initial bias $\rho(t_0)$ and the f_{off} term. The latter one causes for an offset frequency $f_{\mathrm{off}} = 10\,\mathrm{MHz}$ a relative

[6] this approximation holds for a perfect phase-lock on the transponder. In reality small phase deviations will remain due to the finite loop gain, but these will be recorded by the phasemeter of the slave S/C and will be used in the processing. In fact this system would also work with only a loose lock that just maintains the beatnote frequency in the operating range of the photodiodes and phasemeter.

deviation of $\approx 10^{-8}$ in the range computation. The wavelength λ and therefore the wavenumber k are assumed to be known well, however, they might be also estimated together with the initial bias $\rho(t_0)$ in post-processing (see also [Sheard *et al.* , 2012, sec. 12]). In case of a time-dependent offset frequency, the computation is more complicated, because the offset frequency needs to be integrated in eq. (3.10). This scenario is evaluated in appendix E, but current planning foresees a constant offset frequency.
The treatment presented herein does not consider phase fluctuations along the optical path, especially on the satellites. These contributions are treated in the next section.

3.2 Phase Propagation

A model of the measurement accounting for the light paths can be obtained by observing the phase evolution of the light. Recall that distances ρ are measured via the travel time τ of light. In a medium with refractive index n

$$\rho = \frac{v_{\text{medium}}}{\tau} = n\frac{c}{\tau} \tag{3.12}$$

provides the relation between both quantities. We define an operator $\tau[...]$, which returns the travel time of a distance, e.g. a_1, depicted in fig. 3.4. The optical pathlength of the distance is denoted by P,

$$P_{a_1} = c \cdot \tau[a_1].$$

The refractive index n at an orbit altitude of 400 km is assumed to be very close to 1 and index fluctuations are assumed to be negligible at the desired wavelength. However, we tried to account for these effects by distinguishing between optical pathlengths or travel times and (ordinary) geometrical pathlengths in this section. The aim of the derivation here is to obtain a very general formula for the measured longitudinal signal on the photodiode of the master spacecraft.
First we assume a static configuration with resting spacecraft. In this case, the round-trip is twice the separation of the spacecraft,

$$x_1 + L_{12} + y_2 + x_2 + L_{21} + y_1 = 2 \cdot \rho, \tag{3.13}$$

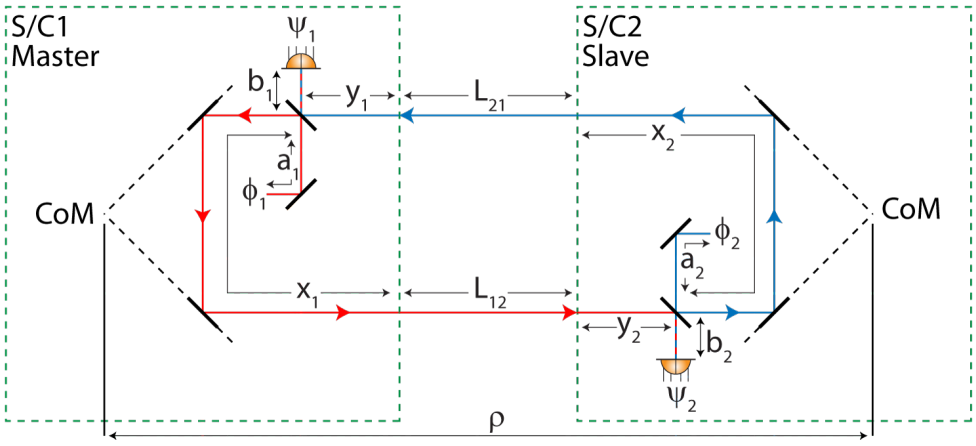

Figure 3.4: Light path separated into different segments, from [Sheard *et al.* , 2012], © Springer

which is due to the property of the TMAs (see section 3.3). The round-trip photon travel time is in the order of

$$\tau_{\mathrm{RT}} = \tau[2 \cdot \rho] \approx n \frac{2 \cdot 200\,\mathrm{km}}{c} \approx 1.3\,\mathrm{ms}. \tag{3.14}$$

It will be convenient to use a recursively defined time-delay operator $\mathbb{D}_{...}\Phi$, which delays $\Phi(t)$ by the photon travel time over distances (e.g. a_1, x_1, L_{12}) or introduces a delay by another time (e.g. $t_2(t)$):

$$\mathbb{D}_{a_1}\Phi = \Phi\left(t - \tau[a_1(t)]\right) \tag{3.15}$$

$$\mathbb{D}_{t_2}\mathbb{D}_{a_1}\Phi = \mathbb{D}_{a_1,t_2}\Phi = \Phi\left(t - \tau[a_1(t)] - t_2(t - \tau[a_1(t)])\right) \tag{3.16}$$

$$\mathbb{D}_{L_{12}}\mathbb{D}_{x_1}\mathbb{D}_{a_1}\Phi = \mathbb{D}_{a_1,x_1,L_{12}}\Phi \tag{3.17}$$

$$= \Phi\left(t - \tau[a_1(t)] - \tau[x_1(t - \tau[a_1(t)])] - \tau[L_{12}(t - \tau[x_1(t - \tau[a_1(t)])])]\right) \tag{3.18}$$

$$= \Phi\left(t - \tau[a_1(t)] - \tau[\mathbb{D}_{a_1}x_1] - \tau[\mathbb{D}_{x_1,a_1}L_{12}]\right) \tag{3.19}$$

As stated in [Tinto & Dhurandhar, 2005, p. 24] the inverse of a time delay operator can be obtained by requiring

$$\mathbb{D}_{a_1}^{-1}\mathbb{D}_{a_1}\Phi = \Phi = \mathbb{D}_{a_1,a_1^{-1}}\Phi, \tag{3.20}$$

which is not the same as a time advance,

$$\mathbb{D}_{a_1}^{-1}\mathbb{D}_{a_1}\Phi \neq \mathbb{D}_{-a_1}\mathbb{D}_{a_1}\Phi. \tag{3.21}$$

This operator is widely used in time-delay interferometry technique developed for LISA/NGO. Further information can be found in [Tinto & Dhurandhar, 2005].
We assume planar monochromatic electromagnetic waves being emitted by the lasers on each spacecraft with amplitude

$$E^{\mathrm{master}}(t) = A_0 \cdot \exp\left[i(\omega_{\mathrm{m}}t + \phi_1(t))\right] \tag{3.22}$$

$$E^{\mathrm{slave}}(t) = A_1 \cdot \exp\left[i(\omega_{\mathrm{s}}t + \phi_2(t))\right], \tag{3.23}$$

where each laser has a phase fluctuation ϕ on top of its nominal frequency ω. The local beam of the master spacecraft leaves the optical bench of the master spacecraft in the direction to the slave satellite. The electric fields at the photodiode of the slave spacecraft are

$$E_1^{\mathrm{PD,\ slave}}(t) = A_2 \cdot \exp\left[i(\omega_{\mathrm{m}} \cdot (t - t_1(t)) + \phi_1(t - t_1(t))\ )\right] \tag{3.24}$$

$$E_2^{\mathrm{PD,\ slave}}(t) = A_1 \cdot \exp\left[i(\omega_{\mathrm{s}} \cdot (t - t_2(t)) + \phi_2(t - t_2(t)))\right], \tag{3.25}$$

with accumulated travel time between the master and slave spacecraft (see fig. 3.4)

$$\begin{aligned} t_1(t) := \ & \tau[\mathbb{D}_{b_2,y_2,L_{12},x_1}a_1] + \tau[\mathbb{D}_{b_2,y_2,L_{12}}x_1] + \tau[\mathbb{D}_{b_2,y_2}L_{12}] \\ & + \tau[\mathbb{D}_{b_2}y_2] + \tau[b_2(t)] \end{aligned} \tag{3.26}$$

and for the short distance on the slave spacecraft

$$t_2(t) := \ \tau[\mathbb{D}_{b_2}a_2] + \tau[b_2(t)]. \tag{3.27}$$

The relation to the time-delay operator is

$$\phi_1(t - t_1(t)) = \mathbb{D}_{b_2,y_2,L_{12},x_1,a_1}\phi_1, \tag{3.28}$$

$$\phi_2(t - t_2(t)) = \mathbb{D}_{b_2,a_2}\phi_2. \tag{3.29}$$

The photodiode measures the intensity of the interfered beams, see for example [Saleh & Teich, 1991],

$$\left|E_1^{\text{PD, slave}}(t) + E_2^{\text{PD, slave}}(t)\right|^2 = \left||E_1(t)| \cdot e^{i\arg(E_1(t))} + |E_2(t)| \cdot e^{i\arg(E_2(t))}\right|^2 \tag{3.30}$$

$$= |E_1(t)|^2 + |E_2(t)|^2 + 2 \cdot \Re(E_1^*(t) \cdot E_2(t)) \tag{3.31}$$

$$= |E_1(t)|^2 + |E_2(t)|^2 + 2 \cdot |E_1(t)| \cdot |E_2(t)| \cdot \cos\left(\ \arg\left(E_1^*(t) \cdot E_2(t)\right)\ \right), \tag{3.32}$$

where "arg" is the phase argument of a complex number. The oscillations at optical frequencies cannot be resolved by the photodiode, therefore the first two terms are time-averaged and equal to the DC power of the light fields. The previous equation can be proved easily by showing that

$$|A_1 \cdot e^{i\cdot\alpha} + A_2 \cdot e^{i\cdot\beta}|^2 = (A_1 \cdot e^{i\cdot\alpha} + A_2 \cdot e^{i\cdot\beta}) \cdot (A_1^* \cdot e^{-i\cdot\alpha} + A_2^* \cdot e^{-i\cdot\beta}) \tag{3.33}$$

$$= |A_1|^2 + |A_2|^2 + 2 \cdot |A_1| \cdot |A_2| \cdot \cos(\alpha - \beta), \tag{3.34}$$

using Euler's relation for complex numbers and trigonometric identities. This complex notation with the exponential function for the electric field does not require time-averaging in contrast to pure trigonometric functions.
The phase of the measured beatnote is then

$$\begin{aligned}\Psi_2(t) &= \arg\left(E_1^{*\text{PD, slave}}(t) \cdot E_2^{\text{PD, slave}}(t)\right) \\ &= -\omega_\text{m} \cdot (t - t_1(t)) - \phi_1(t - t_1(t)) + \omega_\text{s} \cdot (t - t_2(t)) + \phi_2(t - t_2(t)) \\ &= (\omega_\text{s} - \omega_\text{m}) \cdot t + \omega_\text{m} t_1(t) - \omega_\text{s} t_2(t) - \phi_1(t - t_1(t)) + \phi_2(t - t_2(t)),\end{aligned} \tag{3.35}$$

where E_1 and therefore ω_m is assumed to have a lower optical frequency than E_2 or ω_s. This defines the sign convention for phases in this derivation.
In the optimal case, the PLL will drive the signal (eq. (3.35)) to a desired value [Sheard *et al.* , 2012, sec. 4],

$$\Psi_2(t) = \omega_\text{off} t,$$

by changing ω_s and ϕ_2 to these values[7]:

$$\omega_\text{s} = \omega_\text{m} + \omega_\text{off}, \tag{3.36}$$

$$\phi_2(t - t_2) = \mathbb{D}_{t_2}\phi_2 = \omega_\text{s} t_2(t) - \omega_\text{m} \cdot t_1(t) + \mathbb{D}_{t_1}\phi_1. \tag{3.37}$$

The inverse of the time-delay operator leads to the function

$$\phi_2(t) = \omega_\text{s}\mathbb{D}_{t_2^{-1}} t_2 - \omega_\text{m} \cdot \mathbb{D}_{t_2^{-1}} t_1 + \mathbb{D}_{t_2^{-1}, t_1}\phi_1. \tag{3.38}$$

The slave spacecraft sends the light back to the master spacecraft, where it interferes with the local beam of the master S/C leading to the field amplitudes on the photodiode

$$E_1^{\text{PD, master}}(t) = A_3 \cdot \exp\left[i(\omega_\text{s} \cdot (t - t_3(t)) + \phi_2(t - t_3(t)))\right], \tag{3.39}$$

$$E_2^{\text{PD, master}}(t) = A_0 \cdot \exp\left[i(\omega_\text{m} \cdot (t - t_4(t)) + \phi_1(t - t_4(t)))\right], \tag{3.40}$$

with the accumulated delays

$$\begin{aligned}t_3(t) := \ & \tau[\mathbb{D}_{b_1, y_1, L_{21}, x_2} a_2] + \tau[\mathbb{D}_{b_1, y_1, L_{21}} x_2] + \tau[\mathbb{D}_{b_1, y_1} L_{21}] \\ & + \tau[\mathbb{D}_{b_1} y_1] + \tau[b_1(t)]\end{aligned} \tag{3.41}$$

$$t_4(t) := \tau[\mathbb{D}_{b_1} a_1] + \tau[b_1(t)]. \tag{3.42}$$

[7] it has been assumed that the frequencies ω are constant in this derivation

Evaluation of the ϕ_2 term using eq. (3.38) provides

$$\begin{aligned}\phi_2(t-t_3(t)) &= \omega_\mathrm{s}\cdot\mathbb{D}_{t_3,t_2^{-1}}t_2 - \omega_\mathrm{m}\cdot\mathbb{D}_{t_3,t_2^{-1}}t_1 + \mathbb{D}_{t_3,t_2^{-1},t_1}\phi_1\\ &= (\omega_\mathrm{m}+\omega_\mathrm{off})\cdot\mathbb{D}_{t_3,t_2^{-1}}t_2 - \omega_\mathrm{m}\cdot\mathbb{D}_{t_3,t_2^{-1}}t_1 + \mathbb{D}_{t_3,t_2^{-1},t_1}\phi_1\\ &= \omega_\mathrm{m}\cdot(\mathbb{D}_{t_3,t_2^{-1}}t_2 - \mathbb{D}_{t_3,t_2^{-1}}t_1) + \omega_\mathrm{off}\mathbb{D}_{t_3,t_2^{-1}}t_2 + \mathbb{D}_{t_3,t_2^{-1},t_1}\phi_1. \end{aligned} \tag{3.43}$$

This result can be used to compute the phase signal at the photodiode of the master spacecraft

$$\begin{aligned}\Psi_1(t) =& \arg\left(E_2^{*\mathrm{PD,\ master}}E_1^{\mathrm{PD,\ master}}\right) \\ =&\omega_\mathrm{s}\cdot(t-t_3(t)) + \phi_2(t-t_3(t)) - \omega_\mathrm{m}\cdot(t-t_4(t)) - \phi_1(t-t_4(t))\\ =&\omega_\mathrm{off}\cdot t + \omega_\mathrm{m}\cdot\underbrace{(-t_3(t)+t_4(t)+\mathbb{D}_{t_3,t_2^{-1}}t_2 - \mathbb{D}_{t_3,t_2^{-1}}t_1)}_{=:\alpha(t)}\\ &+\omega_\mathrm{off}\cdot(\mathbb{D}_{t_3,t_2^{-1}}t_2 - t_3(t)) \quad + \mathbb{D}_{t_3,t_2^{-1},t_1}\phi_1 - \mathbb{D}_{t_4}\phi_1.\end{aligned} \tag{3.44}$$

A further evaluation of $\alpha(t)$ is necessary to simplify the result:

$$\mathbb{D}_{t_3,t_2^{-1}} = \mathbb{D}_{b_1,y_1,L_{21},x_2,a_2,a_2^{-1},b_2^{-1}} = \mathbb{D}_{b_1,y_1,L_{21},x_2,b_2^{-1}} \tag{3.45}$$

$$\begin{aligned}\mathbb{D}_{t_3,t_2^{-1}}t_1 =&\tau[\mathbb{D}_{b_1,y_1,L_{21},x_2,y_2,L_{12},x_1}a_1] + \tau[\mathbb{D}_{b_1,y_1,L_{21},x_2,y_2,L_{12}}x_1] +\\ &\tau[\mathbb{D}_{b_1,y_1,L_{21},x_2,y_2}L_{12}] + \tau[\mathbb{D}_{b_1,y_1,L_{21},x_2}y_2]\\ &+\tau[\mathbb{D}_{b_1,y_1,L_{21},x_2,b_2^{-1}}b_2]\end{aligned} \tag{3.46}$$

$$\mathbb{D}_{t_3,t_2^{-1}}t_2 = \tau[\mathbb{D}_{b_1,y_1,L_{21},x_2}a_2] + \tau[\mathbb{D}_{b_1,y_1,L_{21},x_2,b_2^{-1}}b_2] \tag{3.47}$$

$$\begin{aligned}\alpha(t) =& -\tau[\mathbb{D}_{b_1,y_1,L_{21},x_2}a_2] - \tau[\mathbb{D}_{b_1,y_1,L_{21}}x_2] - \tau[\mathbb{D}_{b_1,y_1}L_{21}]\\ &-\tau[\mathbb{D}_{b_1}y_1] - \tau[b_1(t)] + \tau[\mathbb{D}_{b_1}a_1] + \tau[b_1(t)]\\ &+\tau[\mathbb{D}_{b_1,y_1,L_{21},x_2}a_2] + \tau[\mathbb{D}_{b_1,y_1,L_{21},x_2,b_2^{-1}}b_2]\\ &-\tau[\mathbb{D}_{b_1,y_1,L_{21},x_2,y_2,L_{12},x_1}a_1] - \tau[\mathbb{D}_{b_1,y_1,L_{21},x_2,y_2,L_{12}}x_1]\\ &-\tau[\mathbb{D}_{b_1,y_1,L_{21},x_2,y_2}L_{12}] - \tau[\mathbb{D}_{b_1,y_1,L_{21},x_2}y_2]\\ &-\tau[\mathbb{D}_{b_1,y_1,L_{21},x_2,b_2^{-1}}b_2]\\ =& -\mathbb{D}_{b_1}\tau_\mathrm{RT} + \tau[\mathbb{D}_{b_1}a_1] - \tau[\mathbb{D}_{b_1,\mathrm{RT}}a_1].\end{aligned} \tag{3.48}$$

Six of the 14 terms cancel in $\alpha(t)$, while other six of the 14 terms provide the round-trip time τ_RT. All three remaining terms have a common delay $\mathbb{D}_{b_1}$, which is due to the common path between beamsplitter and photodiode on the master spacecraft. The equation

$$\begin{aligned}\Psi_1(t) =& \ \omega_\mathrm{off}\cdot t + \omega_\mathrm{m}\cdot(-\mathbb{D}_{b_1}\tau_\mathrm{RT}(t) + \tau[\mathbb{D}_{b_1}a_1] - \tau[\mathbb{D}_{b_1,\mathrm{RT}}a_1])\\ &+\omega_\mathrm{off}\cdot(\mathbb{D}_{t_3,t_2^{-1}}t_2 - t_3(t)) \quad + \mathbb{D}_{t_3,t_2^{-1},t_1}\phi_1 - \mathbb{D}_{t_4}\phi_1 + \Psi_\mathrm{bias}\end{aligned} \tag{3.49}$$

provides the most general description of the measured phase in this derivation. The term Ψ_bias accounts for the fact that the absolute phase is not measurable. It is also worthy to notice that an ideal PLL has been considered without introducing any delays or residual phase offsets. The delays due to b_1, t_2 and t_4 are in the order of nanoseconds and can be neglected in the time arguments, because distances on the spacecraft are assumed not to change within such timescales. It is convenient to use flight-times, because this incorporates the effect of fluctuations of the refractive

index in the measurement. The use of optical pathlenghts $P(t)$ instead of flight-times would be equivalently

$$\begin{aligned}\Psi_1(t) \approx\ & \omega_{\text{off}} \cdot t + \frac{\omega_{\text{m}}}{c} \cdot (-P_{\text{RT}}(t) + P_{a_1}(t) - P_{a_1}(t - \tau_{\text{RT}})) \qquad (3.50)\\ & - \frac{\omega_{\text{off}}}{c} \cdot P_{b_1,y_1,L_{21},x_2}(t) \quad + \phi_1(t - \tau_{\text{RT}}) - \phi_1(t) + \Psi_{\text{bias}}\\ \approx\ & \omega_{\text{off}} \cdot t + \frac{2\pi}{\lambda} \cdot (-2\rho_{\text{meas}}(t) + P_{a_1}(t) - P_{a_1}(t - \tau_{\text{RT}})) \qquad (3.51)\\ & - \frac{\omega_{\text{off}}}{c} \cdot \rho_{\text{meas}}(t) \quad + \phi_1(t - \tau_{\text{RT}}) - \phi_1(t) + \Psi_{\text{bias}}.\end{aligned}$$

However, as stated in the beginning of this subsection, the deviation of the refractive index from 1 is considered to be negligible. The use of the quantity

$$\rho_{\text{meas}}(t) = \frac{1}{2} P_{\text{RT}}(t) = P_{b_1,y_1,L_{21},x_2}(t) \qquad (3.52)$$

is justified in the subsequent section. P_{b_1,y_1,L_{21},x_2} is the optical pathlength from the beamsplitter at the slave spacecraft to the photodiode of the master spacecraft. The term $\phi_1(t - \tau_{\text{RT}}) - \phi_1(t)$ in eq. (3.51) accounts for the laser frequency noise and is treated in section 3.2.2. The term $P_{a_1}(t) - P_{a_1}(t - \tau_{\text{RT}})$ is analyzed in section 3.2.3. The ratio $\omega_{\text{off}}/\omega_{\text{m}} \approx 10^{-7}$ indicates that the 3rd term might be neglected in eq. (3.51) as it was done in [Sheard *et al.* , 2012, eq. 2]. Assuming a particular form with constant velocity v_r for $\rho_{\text{meas}}(t)$,

$$\rho_{\text{meas}}(t) = v_r \cdot t, \qquad (3.53)$$

yields the same expression for the beatnote frequency in the phase measurement as derived in the previous section (eq. (3.7))

$$\begin{aligned}\Psi_1(t) \approx & \left(\omega_{\text{off}} - 2v_r \frac{\omega_{\text{m}}}{c} - v_r \frac{\omega_{\text{off}}}{c}\right) \cdot t \qquad (3.54)\\ & + \frac{\omega_{\text{m}}}{c} \cdot (P_{a_1}(t) - P_{a_1}(t - \tau_{\text{RT}}))\\ & + \phi_1(t - \tau_{\text{RT}}) - \phi_1(t) + \Psi_{\text{bias}}.\end{aligned}$$

3.2.1 Instantaneous Range and Special Relativity

In eq. (3.51) a phase-derived range ρ_{meas} was introduced. This quantity is one-half of a round-trip length measurement performed at the master spacecraft with the on-board clock and it is subject to time-delays due to the finite speed of light. For simplicity we assume that both spacecraft move along the LOS. In fig. 3.5 the world line of the slave spacecraft is depicted. The instantaneous spacecraft separation is given by $\rho_{\text{inst}}(t)$, whereas the time-derivate of ρ_{inst} is assumed to be constant over the travel time of light. The relation of flight times to the phase-derived range is

$$2 \cdot \rho_{\text{meas}}(t) + \rho_{\text{bias}} = c\tau_{12}(t) + c\tau_{21}(t) = 2 \cdot c\tau_{21}(t) =: c\tau_{\text{RT}}(t). \qquad (3.55)$$

The unknown initial offset is denoted as ρ_{bias}. Simple geometric derivation using line intersections leads to

$$\tau_{21}(t) = \frac{\rho_{\text{inst}}(t)}{c + \dot{\rho}_{\text{inst}}} = \tau_{12}(t) \qquad (3.56)$$

and finally to a relation between the instantaneous and measured range:

$$\rho_{\text{inst}}(t) = \frac{c + \dot{\rho}_{\text{inst}}}{2c} \cdot 2c\tau_{21}(t) = \frac{1}{2} \cdot c\tau_{\text{RT}}(t) + \frac{1}{2}\tau_{\text{RT}}(t)\dot{\rho}_{\text{inst}} \qquad (3.57)$$

$$= \rho_{\text{meas}}(t) + \frac{1}{2}\rho_{\text{bias}} \underbrace{+\frac{1}{2}\tau_{\text{RT}}(t)\dot{\rho}_{\text{inst}}}_{\text{light time correction}} . \qquad (3.58)$$

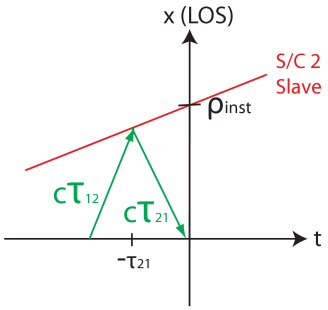

Figure 3.5: Measurement as seen from master spacecraft.

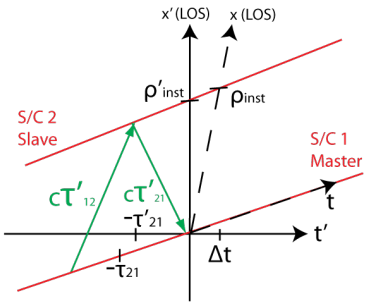

Figure 3.6: Measurement in an inertial frame.

With $\dot{\rho}_{\text{inst}} \approx \dot{\rho}_{\text{meas}}$ the second term is called light-time correction for a round-trip measurement [Montenbruck & Gill, 2000, p.213]. Because the distances $c\tau_{21}$ and $c\tau_{12}$ in fig. 3.5 are equal, the measured inter-satellite distance ρ_{meas} can be defined through the one-way pathlength or through one half of the round-trip measurement, as done in eq. (3.52).
With given S/C positions $\vec{S}_1(t) = (0,0,0)^\mathsf{T}$ and $\vec{S}_2(t)$, the following relations are valid

$$2 \cdot \rho_{\text{meas}}(t) + \rho_{\text{bias}} = P_{\text{RT}}(t) = \left|\vec{S}_1(t) - \mathbb{D}_{\tau_{21}}\vec{S}_2\right| + \left|\mathbb{D}_{\tau_{21}}\vec{S}_2 - \mathbb{D}_{\tau_{21},\tau_{12}}\vec{S}_1\right|, \tag{3.59}$$

$$\rho_{\text{inst}}(t) = \left|\vec{S}_1(t) - \vec{S}_2(t)\right|, \tag{3.60}$$

where a refractive index of $n = 1$ was assumed.
For the GRACE data analysis an instantaneous range is used, which is referred to an inertial frame with global time t provided, for example, by GPS [Case *et al.* , 2010, Light time correction].
As stated by Special Relativity, the simultaneous or instantaneous measurement is in general not instantaneous in the non-moving frame. The Minkowski-like diagramm in fig. 3.6 illustrates a measurement in the non moving frame. The time deviation Δt from an instantaneous measurement can be computed by the Lorentz transformation [Bowler, 1976, eq. 1.1.11],

$$\gamma = \frac{1}{\sqrt{1 - \left(\frac{v}{c}\right)^2}} \approx 1 + 3 \cdot 10^{-10}, \tag{3.61}$$

$$\Delta t' = \gamma \frac{vx}{c^2} \approx 1.7 \cdot 10^{-8}\,\text{s}, \tag{3.62}$$

for an orbital velocity of 7700 m/s and a measured length of $x \approx 200$ km. In GRACE and GFO the LOS and orbital velocity vector are almost parallel, otherwise the absolute velocity along the LOS would have to be used. The result indicates that the

measurement in the non-co-moving frame is separated by negligible 17 nanoseconds. The effect of length contraction is also sufficiently small, especially considering that the LRI is not able to measure absolute distances,

$$\rho'_{\text{inst}} = \frac{1}{\gamma}\rho_{\text{inst}} \approx \rho_{\text{inst}}. \tag{3.63}$$

The fact that KBR phase measurements are taken on both GRACE satellites and need to be combined without time-shifts complicates the flight time correction for the KBR [Kim, 2000, p. 117]. In case of the GFO LRI, a combination of measurements from both spacecraft will be required, if the PLL does not drive the phase at the photodiode of the slave spacecraft to zero.
It is also noteworthy that the distances $c\tau'_{21}$ and $c\tau'_{12}$ in fig. 3.6 measured in the non-co-moving frame differ by several meters, which is due to the 17 nanoseconds time difference.

3.2.2 Laser Frequency Noise

The frequency and phase fluctuations of the master laser couple via the term

$$\phi_1(t - \tau_{\text{RT}}) - \phi_1(t) \tag{3.64}$$

in eq. (3.50) into the phase and hence length measurement. The equivalent single-way pathlength contribution due the laser noise ρ_{LN} can be written as

$$\frac{2\pi}{\lambda} \cdot 2 \cdot \rho_{\text{LN}}(t) = \phi_1(t - \tau_{\text{RT}}) - \phi_1(t) \tag{3.65}$$

Transforming this equation to the frequency domain by a Fourier transform and utilizing the rule for time-shifts in the frequency domain results in

$$\begin{aligned}&\frac{2\pi}{\lambda} \cdot 2 \cdot \widetilde{\rho_{\text{LN}}}(f) = \\ &\tilde{\phi}_1(f) \cdot (1 - \exp[-i \cdot 2\pi f \cdot \tau_{\text{RT}}]) \approx \tilde{\phi}_1(f) \cdot i \cdot 2\pi f \cdot \tau_{\text{RT}} = \tilde{\phi}_1(f) \cdot i \cdot \frac{2\pi f}{c} \cdot c\tau_{\text{RT}}\end{aligned} \tag{3.66}$$

$$\Leftrightarrow 2 \cdot \widetilde{\rho_{\text{LN}}}(f) \approx \tilde{\phi}_1(f) \cdot i \cdot f \cdot \frac{c\tau_{\text{RT}} \cdot \lambda}{c}, \tag{3.67}$$

where the approximation holds only for $|2\pi f \cdot \tau_{\text{RT}}| \ll 1$. This is justified, because the round-trip time is $\tau_{\text{RT}} \approx 1.3\,\text{ms}$ and the interesting frequency band is below 1 Hz. The term $c\tau_{\text{RT}}$ can be denoted as arm mismatch ΔL in the interferometer, which is the round-trip length in the case of the LRI. ϕ_1 is a phase and has units of radian. The connection to the optical frequency ν is given by

$$\dot{\phi}_1(t) = \omega(t) = 2\pi\nu(t), \tag{3.68}$$

which is in frequency domain with Fourier frequency f given by

$$2\pi f i\tilde{\phi}_1(f) = 2\pi\tilde{\nu}(f). \tag{3.69}$$

Combining eq. (3.67) and eq. (3.69) and switching to linear spectral densities[8], which are denoted with a δ, yields

$$2 \cdot \widetilde{\delta\rho_{\text{LN}}}(f) = if\widetilde{\delta\phi}_1(f) \cdot \frac{\Delta L \cdot \lambda}{c} = \widetilde{\delta\nu(f)} \cdot \frac{\Delta L}{\nu} \tag{3.70}$$

[8] replacing the Fourier transforms by the corresponding linear spectral densities (LSD). Signs and imaginary units are omitted, because a LSD is the square root of a power spectral density, which is real and positive. For information on spectral density estimation refer to [Heinzel *et al.* , 2002]

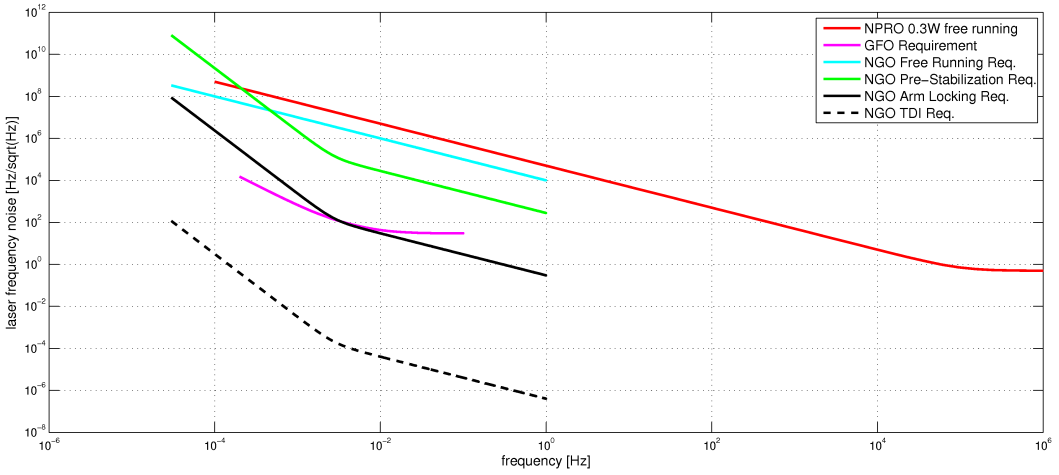

Figure 3.7: Requirements for laser frequency noise for GFO-LRI, for NGO from [NGO-Yellowbook, 2011] and a model for a free running NPRO based on data from [Troebs *et al.* , 2009]

$$\text{with} \quad [\widetilde{\delta\nu}(f)] = \text{Hz}/\sqrt{\text{Hz}}, \quad [\widetilde{\delta\rho_{\text{LN}}}(f)] = \text{m}/\sqrt{\text{Hz}} \tag{3.71}$$

and with $\widetilde{\delta\rho_{\text{LN}}}$ being the single-way pathlength fluctuations due to laser noise, ν the optical laser frequency and $\widetilde{\delta\nu}(f)$ the laser frequency noise. For the LRI a laser frequency noise of $30\,\text{Hz}/\sqrt{\text{Hz}}$ causes a single-way pathlength noise of about $25\,\text{nm}/\sqrt{\text{Hz}}$. The requirement on laser frequency noise is shown in fig. 3.7, whereas the equivalent displacement noise was plotted in fig. 3.3.
As depicted, the laser frequency noise of a free-running laser is several orders of magnitude higher than $30\,\text{Hz}/\sqrt{\text{Hz}}$ and causes the necessity for a laser frequency stabilization. Various techniques are currently under investigation for the GFO laser frequency stabilization. Using conventional locking of the laser frequency to the resonance frequency of a cavity via the Pound-Drever-Hall technique has almost shown the required performance (see Folkner *et al.* [2011] and Thompson *et al.* [2011]). Other approaches under investigation are tilt-locking or a fibre-resonator scheme [ANU, 2012, ANU-website].
The frequency stabilization is only necessary for the master spacecraft. However, to allow switching of the master/slave role and for the associated redundancy, it will be present on both satellites.

3.2.3 Off-Racetrack Pathlength Noise

The term "off-racetrack" pathlength within this thesis is used for distances a_1, a_2, b_1, b_2 in fig. 3.4.
In the final measurement equation (3.50) the optical pathlength from the fiber coupler via the steering mirror to the beamsplitter is present (cf. figure 3.4)

$$P_{a_1}(t) - P_{a_1}(t - \tau_{\text{RT}}) =: 2 \cdot \rho_{a_1}(t), \tag{3.72}$$

which can be seen as a single-way pathlength contribution $\rho_{a_1}(t)$ on the ray path a_1 in the final range measurement ρ[9]. According to eq. (3.67) the formula can be rewritten in the frequency domain to

$$\widetilde{P_{a_1}}(f) \cdot (1 - \exp[-i \cdot 2\pi f \cdot \tau_{\text{RT}}]) \approx \widetilde{P_{a_1}}(f) \cdot i \cdot 2\pi f \cdot \tau_{\text{RT}}. \tag{3.73}$$

[9] another way of looking at fluctuations of a_1 is to consider the laser noise Φ_1 only at the point when it first becomes measurable by interference, i.e. at the beamsplitter, and to include any fluctuation of a_1 or the steering mirror into Φ_1.

This equation can be transformed directly to spectral densities. Assuming a round-trip time $\tau_{\mathrm{RT}} \approx 1.3\,\mathrm{ms}$ and the interesting frequency band limit at $f \approx 0.1\,\mathrm{Hz}$ results in a suppression factor of approximately 1000. Effects due to thermal expansion, which are assumed to be below $1\,\mu\mathrm{m}/\sqrt{\mathrm{Hz}}$, will have a level below $1\,\mathrm{nm}/\sqrt{\mathrm{Hz}}$ in the round-trip measurement. For lower frequencies the suppression is even higher.
Another contribution causing off-racetrack pathlength changes is the steering mirror motion. The steering mirror will move to compensate spacecraft attitude jitter (also called receiver tip/tilt within this thesis). In section 3.6.9 the coupling factors of spacecraft rotations into optical pathlength P_{a_1} change are determined to be

$$\begin{aligned} \frac{\partial^2 P_{a_1}}{\partial v^2} &= 28\,\mathrm{nm/mrad^2}, \\ \frac{\partial P_{a_1}}{\partial h} &= 70\,\mu\mathrm{m/mrad}, \end{aligned} \tag{3.74}$$

which are valid for a particular optical bench setup. We linearize the quadratic coupling at a working point of 0.5 mrad, because non-linear coupling effects cannot be treated with transfer functions. The linearization results in a coupling of

$$\frac{\partial P_{a_1}}{\partial v} = 28\,\mathrm{nm/mrad}. \tag{3.75}$$

The vertical v rotation corresponds to spacecraft pitch, while the horizontal h is for the yaw direction. If the S/C jitter spectral density $\widetilde{\delta j}(f)$ for yaw and pitch is known, the following equations provide the connection to the noise in the length measurement

$$\begin{aligned} 2\widetilde{\delta\rho_{a_1}}(f) &\approx 2\pi \cdot f \cdot \tau_{\mathrm{RT}} \cdot \frac{\partial P_{a_1}}{\partial v} \cdot \widetilde{\delta j_{\mathrm{pitch}}}(f), \\ 2\widetilde{\delta\rho_{a_1}}(f) &\approx 2\pi \cdot f \cdot \tau_{\mathrm{RT}} \cdot \frac{\partial P_{a_1}}{\partial h} \cdot \widetilde{\delta j_{\mathrm{yaw}}}(f). \end{aligned} \tag{3.76}$$

From these equations one can derive the jitter noise causing a round-trip pathlength noise with $1\,\mathrm{nm}/\sqrt{\mathrm{Hz}}$ at 0.1 Hz and with the characteristic noise-shape function given in fig. 3.3.

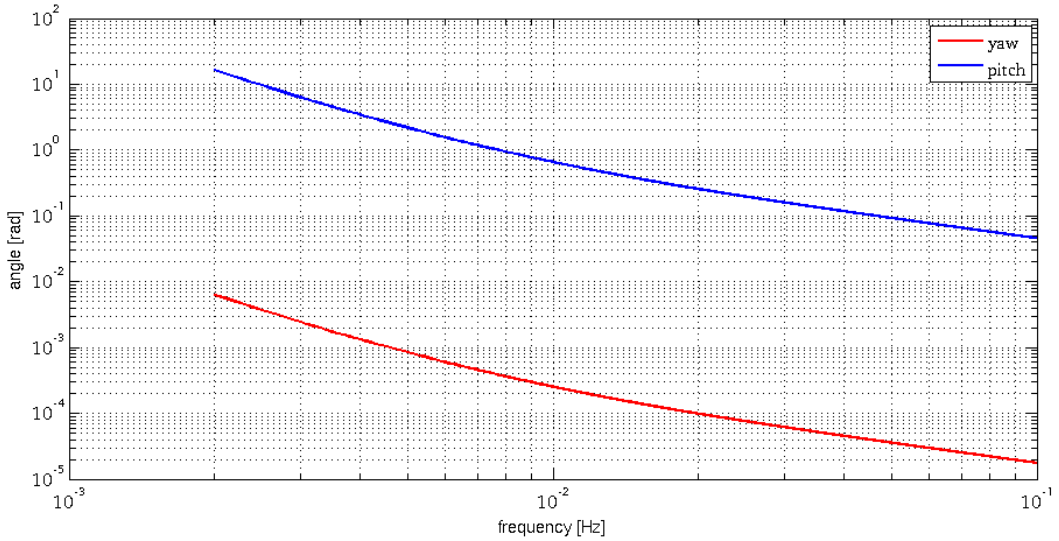

Figure 3.8: Spacecraft attitude jitter noise causing $1\,\mathrm{nm}/\sqrt{\mathrm{Hz}}$ length noise for a particular optical bench setup.

Current simulations of the spacecraft attitude control system perform with an approximately three orders of magnitude lower residual noise than depicted in fig. 3.8.

One should keep here in mind that power spectral densities are not suited to describe sinusoidal deterministic signals (tones), which need to be addressed separately.
Another off-racetrack noise contribution might come from the path b_1 going from the beamsplitter through the lenses to the photodiode. This path is common to both beams, but due to the different amplitude and phase shape of the beams, fluctuations in the lens or photodiode position can cause a phase change on the photodiode. This effect has been observed in simulations in section 3.6.8. It might add up in the final measurement for the slave and master spacecraft, but the magnitude of this effect was uncritical in the simulations.

3.3 Triple Mirror Assembly

In the previous section the general working principle of the LRI was presented, as well as a connection between inter-satellite range, instantaneous range and measured phase established. Furthermore, the contributions of laser frequency noise and off-racetrack noise were estimated.
In this section the Triple Mirror Assembly (TMA) is treated, which is together with the Optical Bench (see next section 3.4), a subunit of the LRI and a centerpiece of the optical setup.
The TMA consists of three mutual perpendicular mirrors, which are rigidly mounted to a tube-like housing with a few centimeter diameter and about 60 cm length (see fig. 3.9). The task of the TMA on each spacecraft is to retro-reflect an incoming beam anti-parallelly, but with sufficiently large lateral displacement, such that the racetrack is not blocked by the gas tank or KBR instrument (see fig. 3.2). The three mirror planes of the TMA intersect in one point called vertex and form a so-called corner-cube.

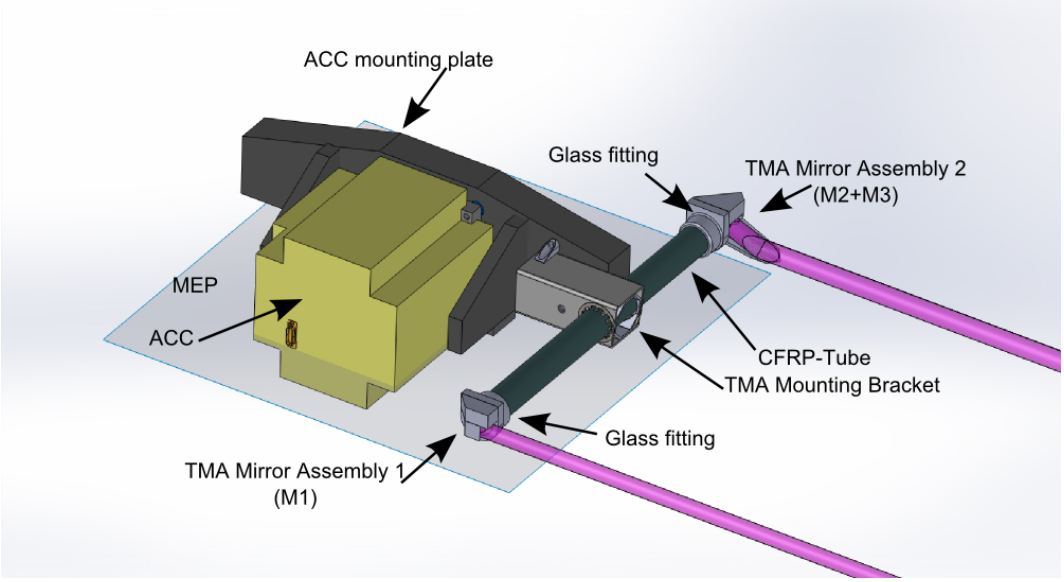

Figure 3.9: Model of the GRACE Follow-On Triple Mirror Assembly (on the right side) and holding structure; Acc: Accelerometer, MEP: Main Equipment Platform (source: SpaceTech GmbH Immenstaad).

In the following subsection general information and properties of corner-cubes are summarized.

3.3.1 Corner-Cubes

A corner-cube is like a Cat's-Eye a retro-reflector. One distinguishes between solid and hollow corner-cubes. A solid (also called prismatic) corner-cube is a tetrahedron, consisting of a transparent material, a base surface and three mutually perpendicular surfaces at the back. It can be produced by diagonally cutting a solid glass cube. Light entering at the base is refracted towards the diagonal line of the former cube and is being deflected three times due to total internal reflection, before leaving through the base anti-parallelly to the incident light (Scholl [1995], Liu & Azzam [1997]).
A hollow corner-cube consists of only three mutually orthogonal mirrors and has no solid interior. As for the solid corner-cube the incident light ray is reflected at each surface and exits the corner-cube anti-parallel to the incoming beam (see fig. 3.10). The acceptance angle for a solid corner-cube is usually higher, due to the refraction at the base surface, in comparison to a hollow corner-cube with same geometry. Corner-cube retro-reflectors are widely used in laser tracking systems and in traffic signs [Kim & Lee, 2007].

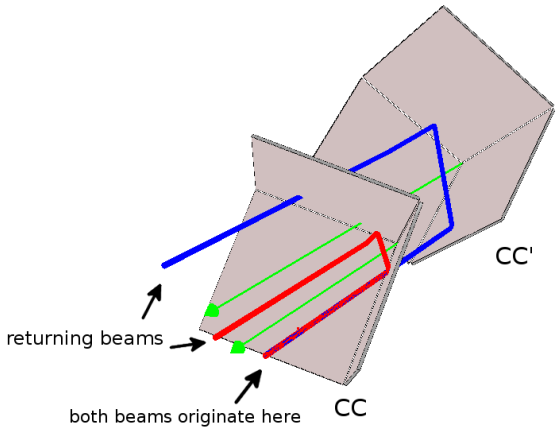

Figure 3.10: Two corner-cubes (in 3-d): The red beam is reflected at the first corner-cube (CC) while the blue beam is transmitted and reflected at the second corner-cube (CC'), which is shifted and rotated. The green vectors are parallel to the initial and returning beams and originate at the vertex. The lateral displacement is divided into equal halves by the green vectors.

In the following the word *corner-cube* always stands for for *hollow corner-cubes* and it is always assumed that light is being reflected at all three mirror surfaces before leaving the corner-cube.

3.3.2 Ray properties

In this section a summary of the ray properties of corner-cubes valid in 2-d and 3-d is given. The concept of a corner-cube can be simplified to two dimensions by using just two perpendicular mirror surfaces. In fig. 3.11 the ray path through two corner-cubes in 2-d is shown. The solid red vectors $(\vec{1}, \vec{2}, \vec{3})$ indicate the path through a corner-cube CC, while the dashed blue vectors $(\vec{1}', \vec{2}', \vec{3}')$ show the path through a shifted and rotated corner-cube CC'. A virtual plane (VP), perpendicular to the initial rays ($\vec{1}$ and $\vec{1}'$), serves as boundary for returning beams. The vertex of a corner-cube is the intersection point of all mirror planes[10]. If a corner-cube is

[10]The intersection of two (non-parallel) planes forms a line, which is intersected with the third plane yielding the vertex point.

subject to motion, the vertex displacement vector (purple vector $\vec{d}$ in fig. 3.11) turns out to be a helpful quantity.

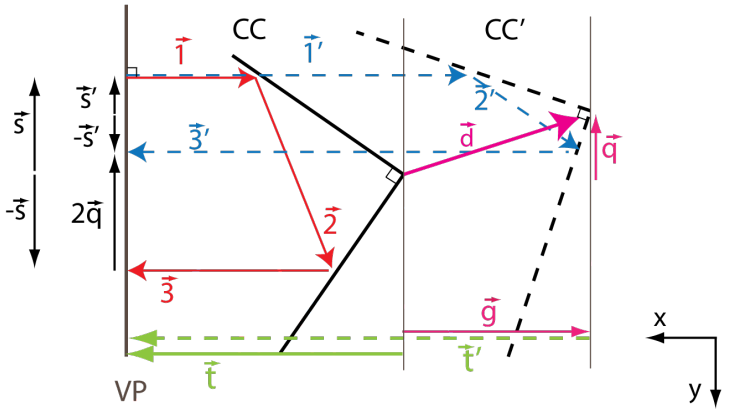

Figure 3.11: Two corner-cubes in 2-d (perpendicular mirrors) with ray paths and additional parameters (see text for description).

Ray Properties:

1. The returning beam ($\vec{3}$ and $\vec{3}'$) is always anti-parallel to the initial beam ($\vec{1}$ and $\vec{1}'$), thus independent of the orientation of the corner-cube

2. A transverse vector between vertex and initial beam ($\vec{s}$ and $\vec{s}\,'$) is equal to the negative transverse vector connecting vertex and returning beam ($-\vec{s}$ and $-\vec{s}\,'$).
   In other words: a vector between initial and returning beam is divided into equal halves by the vertex.

3. The accumulated pathlength ($|\vec{1}| + |\vec{2}| + |\vec{3}|$ and $|\vec{1}'| + |\vec{2}'| + |\vec{3}'|$) through a corner-cube is twice the distance from the virtual plane to the vertex ($2 \cdot |\vec{t}|$ and $2 \cdot |\vec{t}\,'|$).

4. If a corner-cube is subject to motion along the beam direction, the accumulated pathlength change is twice the projection of the displacement vector on the beam direction

$$(|\vec{1}'| + |\vec{2}'| + |\vec{3}'|) - (|\vec{1}| + |\vec{2}| + |\vec{3}|) = 2 \cdot |\vec{g}| = 2 \cdot \frac{\vec{d} \cdot \vec{1}}{|\vec{1}|}. \tag{3.77}$$

5. If a corner-cube is subject to motion transverse to the beam direction, the transverse displacement of the returning beam is twice the transverse displacement vector ($2 \cdot \vec{q}$). The accumuluated optical pathlength does not change.

6. Rotations of a corner-cube around the vertex do not change the accumulated pathlength or the returning beam direction.

7. Rotations of a corner-cube around other points than the vertex can be decomposed into rotations around the vertex and a translation, which is a general property of *proper rigid transformations* in the Euclidean space.

For 3-d corner-cubes four rays have to be used, because reflections occur at three mirror surfaces. However, the property statements 1-7 remain valid. Proving the properties in 2-d is easily done by trigonometry. For 3-d corner-cubes the properties have been verified by ray-tracing simulations. A proof of some properties in three

dimensions for a solid corner-cube can be found in [Peck, 1948]. The results for the optical pathlength in that paper can be related to hollow corner-cubes by setting the refractive index μ of the glass to 1 (vacuum).

3.3.3 TMA Working Principle

As already mentioned, the TMA mirrors form a hollow corner-cube retro-reflector. Stede [2011] uses the term *virtual* corner-cube for such a mirror configuration, where not the full faces of the cube, but only small segments around the actual reflection points are present.
The basic property of a retro-reflector is that the direction of the reflected beam is fixed in inertial space, especially invariant under rotations of the retro-reflector, if the incoming beam stays fixed in inertial space. Furthermore, the incoming and outgoing beams are always anti-parallel. In case of the LRI this guarantees a correct pointing of the outgoing beam towards the distant spacecraft, if the incident beam is coming from the distant spacecraft.
From property 3 above it follows, that the accumulated optical pathlength of the racetrack, depicted in figure 3.2, is twice the distance between both TMA vertices. If the TMA vertices are co-located with the CoM of the spacecraft, the racetrack pathlength is twice the inter-satellite distance and spacecraft rotations around the CoM will not change the distance measurement.
The anti-parallelism and the immunity of the optical pathlength to spacecraft rotations are the key-properties of the TMA.
Latter one holds only, if the TMA vertex and the CoM (or center of rotation) coincides. The effect of TMA vertex misplacements is treated in the next subsection.

3.3.4 Linearized Coupling of Rotations

The property 7 in section 3.3.2 can be used to derive simple equations for measured pathlength changes upon rotations by angles u, v, w around a pivot point $\vec{P}$, which does not coincide with the vertex $\vec{V}$ of the corner-cube. Therefore, we define a rotation matrix $\hat{R}$ by

$$\hat{R}(u,v,w) = \hat{R}(\vec{e}_z, w) \cdot \hat{R}(\vec{e}_y, v) \cdot \hat{R}(\vec{e}_x, u), \tag{3.78}$$

where u, v, w, are the angles for rotations around $\vec{e}_x, \vec{e}_y, \vec{e}_z$, respectively. The vertex displacement vector due to a rotation is then

$$\vec{d} = \hat{R}(u,v,w) \cdot (\vec{V} - \vec{P}) - (\vec{V} - \vec{P}). \tag{3.79}$$

The measured change in the optical pathlength is (property 4, eq. (3.77))

$$\delta\rho = -2 \cdot \vec{d} \cdot \vec{e}_x, \tag{3.80}$$

where the initial (sensing) beam direction is defined along $-\vec{e}_x$ (see fig. 3.11). Using a small angle approximation and $(\vec{V} - \vec{P}) = (\delta x, \delta y, \delta z)$, the following relationship can be obtained:

$$\begin{aligned} \delta\rho \approx & -2 \cdot \delta z \cdot v + 2 \cdot \delta y \cdot w - 2 \cdot \delta y \cdot u \cdot v - 2 \cdot \delta z \cdot u \cdot w \\ = & (\delta x, \delta y, \delta z) \cdot \begin{pmatrix} 0 & 0 & 0 \\ 0 & -2u & +2 \\ 0 & -2 & -2u \end{pmatrix} \cdot \begin{pmatrix} u \\ v \\ w \end{pmatrix}. \end{aligned} \tag{3.81}$$

If the corner-cube vertex and the center of rotation are misplaced by $\delta y = 1\,\mathrm{mm}$, the coupling factor for a rotation w into a round-trip pathlength is

$$\frac{\partial \delta\rho}{\partial w} = 2\,\mathrm{mm/rad} = 2\,\mu\mathrm{m/mrad} = 2000\,\mathrm{nm/mrad}. \tag{3.82}$$

This coupling factor can be multiplied with a satellite attitude jitter spectrum to calculate the contribution of pointing jitter noise in the length measurement. The pointing jitter and the laser frequency noise are assumed to have the highest noise contributions in the LRI [Sheard *et al.* , 2012].
Based on actual simulations of the attitude control system and an allocation of $20\,\mathrm{nm}/\sqrt{\mathrm{Hz}}$ for the pointing jitter noise, the position of the TMA vertex needs be co-located with the CoM within $100 - 200\,\mu\mathrm{m}$ in the sensitive y and z directions.
It is noteworthy that in case of misaligned TMA mirror planes rotations around the TMA vertex will produce in general a change in the optical pathlength. For the LRI the point of minimal coupling (POMC) is of interest, where the pathlength changes are minimal. In other words: if the mirror planes are not mutually orthogonal, the TMA vertex and the POMC do not coincide in general. Therefore the POMC and not the TMA vertex should be co-located with the CoM, although the separation between POMC and vertex is small.
In Appendix F the theoretical effect of TMA mirror misalignments is analyzed, while in [Schütze *et al.* , 2013] a method for the determination of the POMC for the GFO LRI breadboard setup is discussed.
Additional pathlength errors, and hence distance measurement errors, might be caused by the TMA polarization. This effect is discussed in the following subsection.

3.3.5 TMA Polarization

A corner-cube with perfectly aligned mirrors conjugates the phase of a beam with plane wavefront and with uniform amplitude [Scholl, 1995] and [Chipman *et al.* , 1988], which means the polarization vector is rotated by 180°. In various other papers (Liu & Azzam [1997], Segre & Zanza [2003], Peck [1962]) polarization properties of solid corner-cubes are analyzed. In Mayer [1993] the depolarization effects of a hollow corner-cube in the context of laser-trackers is treated. According to this work, a ray can propagate on six different paths through a corner-cube depending on the incidence position. If a large Gaussian laser beam is used, different portions of the beam propagate along different paths through the corner-cube and result in a degradation of laser-tracking precision, because each path has different polarization properties. These results are not directly applicable to the LRI TMA, because in case of the LRI the ray path is always the same and the incidence angle on each mirror changes only slightly. An analysis of the TMA polarization can be found in appendix D. The simulated scenarios considering simple Fresnel reflection showed only very small phase variations, induced by attitude dependent polarization changes. Also the linear polarization of the light was mainly retained, which is important for the contrast of the interferometric measurement.

3.4 Optical Bench

In the nominal case each satellite receives a Gaussian beam with a spot size radius of 27 m, from which a fraction will be cut out by an aperture at the front or rear of the spacecraft, respectively. The received light from the distant spacecraft with a phase front radius of curvature of 200 km, i.e. nearly a plane wave, propagates through a baffle to the entrance aperture at the optical bench with 4 mm radius (fig. 3.12).
The large radius of curvature leads to a flat top profile in phase with less than 60 μrad phase deviation on the aperture, while the large original spot size guarantees a flat intensity profile with a few hundred picowatt power (in the best case). The flat top beam (also called 'top hat beam', shown in red in fig. 3.12 on the OB) is interfered with the local Gaussian beam (green in fig. 3.12) at a beamsplitter (BS) with 95% reflectivity, such that most of the power of the flat top beam is reflected towards a

quadrant photodiode (QPD). The interference of local and remote beam causes a beatnote on the QPD.
The local beam has initially about 15 mW of optical power and a waist radius of 2.5 mm, which is located at the steering mirror front surface. These parameters are compromises and derived in [Sheard & Heinzel, 2011]. Most of the local beam power is reflected towards compensation beamsplitter (CBS) and the TMA. Thus, the optical bench effectively replaces the weak received beam by a fresh beam.
On the one hand the OB needs to ensure parallelism between outgoing and received beam, on the other hand it shall measure the relative phase between the received light and local oscillator beam. To achieve the parallelism, the relative tilt angle between the local beam and received light can be controlled by a steering mirror (see subsequent section 3.4.5), while a technique called *Differential Wavefront Sensing* (see section 3.4.4 and 3.4.6) provides a measurement of the relative tip and tilt angle. For the latter one it is beneficial to have fixed beam positions at the QPD of the local and received beam, regardless the beam tip and tilt angles [Morrison *et al.* , 1994]. Therefore a beam compressor is placed in front of the QPD, which is discussed in detail in the next subsection.

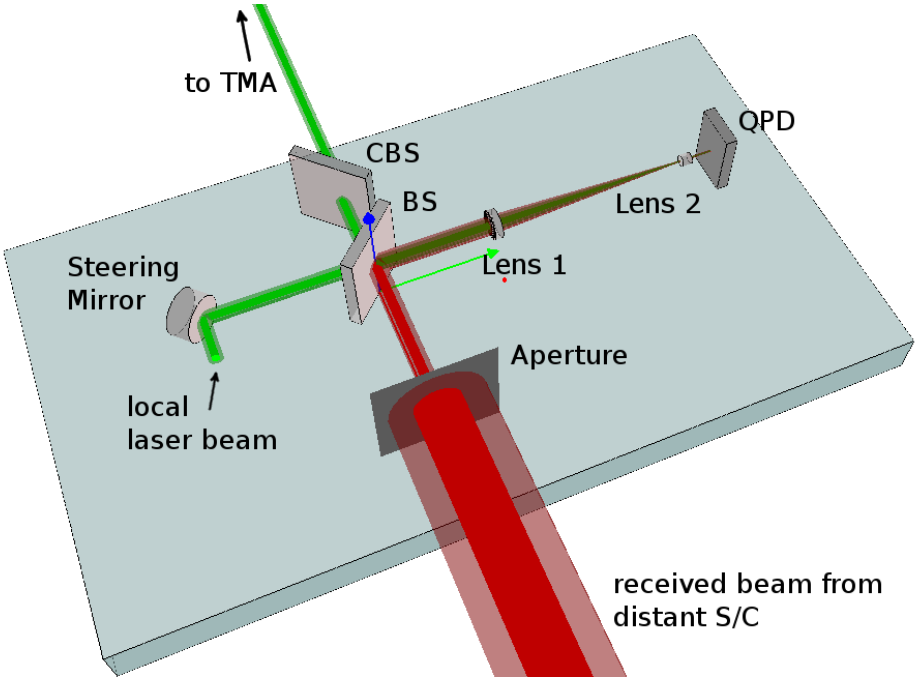

Figure 3.12: Model of the LRI Optical Bench.

3.4.1 Beam Compressor

In front of the quadrant photodiode a beam compressor is placed, which decreases the beam sizes of local and received beam by a factor of 8, so they fit onto a 1 mm diameter quadrant photodiode. The relation between active area size, capacitance and bandwidth requires a small photodiode with low capacitance to achieve a bandwidth of about 2-20 MHz for the QPD.

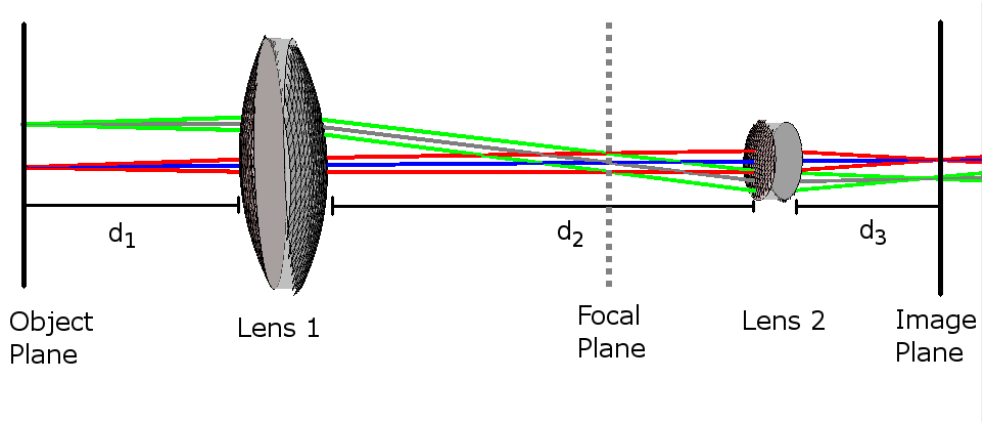

Figure 3.13: Two lenses beam compressor.

Furthermore, it keeps the beams at a fixed position on the QPD, independent of the steering mirror state or the incidence angle at the receive aperture.
A scheme of a two lens beam compressor is depicted in fig. 3.13. The properties of such an optical system can be computed with a ray transfer formalism using ABCD matrices [Saleh & Teich, 1991, p.28]. Let $\hat{T}(d)$ be the transfer matrix for a propagation by a distance d, $\hat{L}(f)$ for a thin lens with focal length f, $\hat{R}(r, n_1, n_2,)$ the refraction at a curved surface with radius of curvature r and a refractive index change from n_1 to n_2, while $\hat{B}(n_1, n_2)$ is used for a refraction at a flat surface, where the refractive index changes from n_1 to n_2. In the ABCD formalism a ray is characterized by a vector $(y, \theta)^\mathsf{T}$, where y is the distance of the ray from the optical axis and θ the angle between ray and optical axis.
Assuming thin lenses for the beam compressor, the transfer matrix of the optical system can be derived as [Sheard & Heinzel, 2011]

$$\hat{M}_1 = \hat{T}(d_3) \cdot \hat{L}(f_2) \cdot \hat{T}(d_2) \cdot \hat{L}(f_1) \cdot \hat{T}(d_1) = \begin{pmatrix} m & 0 \\ 0 & m^{-1} \end{pmatrix}, \tag{3.83}$$

with magnification

$$m = -f_2/f_1, \tag{3.84}$$

and the following values for d_2 and d_3:

$$\begin{aligned} d_2 &= f_1 + f_2, \\ d_3 &= -m^2 d_1 - m(1-m) f_1, \end{aligned} \tag{3.85}$$

where f_1 and f_2 are the focal lengths of lens 1 and lens 2. Two collimated rays $(0, 0)^\mathsf{T}$ and $(y, 0)^\mathsf{T}$, which are parallel to the optical axis and separated by y at the object plane, will be still collimated and parallel to the optical axis at the image plane. However, the separation of the rays changes to $m \cdot y$, meaning that the size of a collimated beam w changes to $m \cdot w$. The transfer matrix reveals that ray offsets are decreased by m ($|m|$ is smaller than 1), while tilts are magnified by $1/m$ [Sheard & Heinzel, 2011]. In addition, due to B element of the transfer matrix being zero, ray tilts at the object plane do not result in a change of the ray position at the image plane. Thus, placing the steering mirror and receive aperture at the object plane, provides a fixed beam position at a QPD in the image plane, as recommended for *Differential Wavefront Sensing*.
The values derived for d_1, d_2, d_3 in [Sheard & Heinzel, 2011] are all with respect to principal points of the lenses, while the distances shown in fig. 3.13 are measured between the vertex points of the surfaces. For some applications like IfoCad

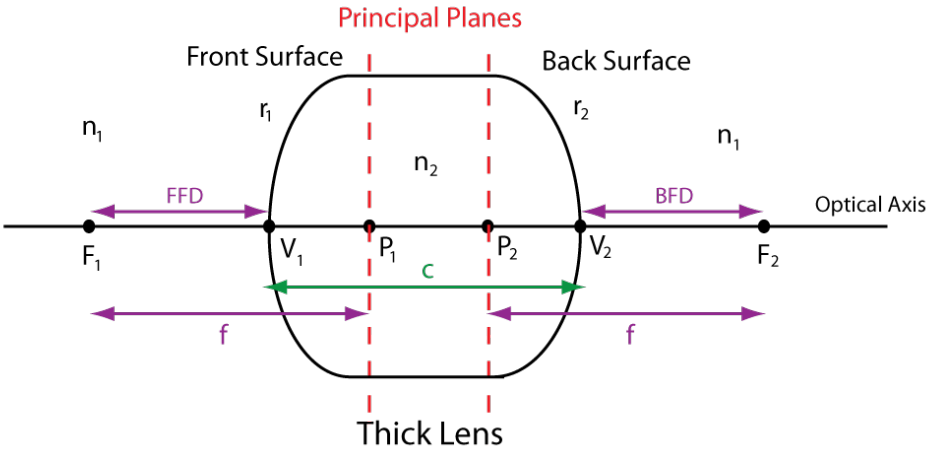

Figure 3.14: Lens with center thickness c, surface curvature radii of r_1 and r_2, and substrate with refractive index n_2. The surface vertex points are denoted with V_1 and V_2, while the principal points are P_1 and P_2. The focal length f is equal on both sides, while the front focal distance (FFD) and back focal distance (BFD) are in general unequal. The sign convention used in this thesis assumes $r_2 < 0$ for a biconvex lens.

simulations or component placement it is useful to have the distances w.r.t. the surface vertices, because these are physically accessible. Therefore, we compute the separation of the lenses without the thin lens approximation.
Characteristic points and distances of thick lenses are depicted in fig. 3.14 and equations for the focal length and focal distances of a thick lens with substrate refractive index n and center thickness c are given in [Hobbs, 2011, eq. 4.15f]:

$$\begin{aligned}
\frac{1}{f(r_1, r_2, n, c)} &= (n-1)\left(\frac{1}{r_1} - \frac{1}{r_2} + \frac{(n-1)c}{n \cdot r_1 \cdot r_2}\right), \\
\mathrm{FFD}(r_1, r_2, n, c) &= f(r_1, r_2, n, c)\left(1 + \frac{(n-1)c}{n \cdot r_1}\right), \\
\mathrm{BFD}(r_1, r_2, n, c) &= f(r_1, r_2, n, c)\left(1 - \frac{(n-1)c}{n \cdot r_2}\right).
\end{aligned} \tag{3.86}$$

In the very general case a thick lens can have different radii of curvature for the front and back surface. However, as shown in [Jha, 2009, p.181] plano-convex lenses minimize spherical aberration, if the convex side is pointing towards a collimated beam. The ABCD formalism is not suited to model spherical aberration, because the formalism is based on a paraxial approximation.
The previous equations can be referred to as the plano-convex case by taking the limit for r_1 or r_2 to infinity. Assuming a beam compressor with plano-convex lenses with lens center thickness c_1 and c_2 yields the following transfer matrix:

$$\begin{aligned}
\hat{M}_2 &= \hat{T}(d_3) \cdot \hat{R}(r_2, n_2, n_1) \cdot \hat{T}(c_2) \cdot \hat{B}(n_1, n_2) \cdot \hat{T}(d_2) \cdot \hat{B}(n_2, n_1) \cdot \hat{T}(c_1) \\
&\quad \cdot \hat{R}(r_1, n_1, n_2) \cdot \hat{T}(d_1) \\
&= \begin{pmatrix} \frac{r_2}{r_1} & 0 \\ 0 & \frac{r_1}{r_2} \end{pmatrix} = \begin{pmatrix} m & 0 \\ 0 & m^{-1} \end{pmatrix}.
\end{aligned} \tag{3.87}$$

Here, $m = f_2/f_1 = f(r = +\infty, r_2, n_2, c_2)/f(r_1, r = -\infty, n_2, c_1) = r_2/r_1$ was used. The negative sign is missing in comparison to eq. (3.84) due to the fact that r_2

and hence f_2 are negative, while r_1 and f_1 are positive in this derivation. The magnification factor is still negative.
The following assumptions need to be made to obtain the result (3.87):

$$\begin{aligned} n_1 &= 1, \\ d_2 &= \frac{c_1 + c_2 + n_2(-c_1 - c_2 + r_1 - r_2)}{(n_2 - 1)n_2} \\ &= \mathrm{BFD}(r_1, r = -\infty, n_2, c_1) + \mathrm{FFD}(r = +\infty, r_2, n_2, c_2), \qquad (3.88) \\ d_3(d_1) &= \frac{r_2(-r_1^2 + d_1 r_1(1 - n_2) + r_1 r_2)}{(n_2 - 1)r_1^2} \\ &= -d_1 m^2 - (1 - m) \cdot m \cdot \mathrm{FFD}(r_1, r = -\infty, n_2, c_1). \qquad (3.89) \end{aligned}$$

As expected, the result is very similar to eq. (3.85), where the focal lengths have been exchanged by focal distances.
The purpose of the beam compressor is not only to downsize the diameter of the laser beams and to keep the beams fixed at the QPD. In addition both the entrance aperture and the waist of the local beam should be imaged onto the photodiode. Imaging the aperture is necessary, because light that propagated through a small aperture stop shows in general diffraction patterns [Baune, 2009, p. 11 and App. C]. Imaging the aperture plane cancels the diffraction rings at the image plane and yields an almost flat phase front of the received beam at the QPD. Imaging the local Gaussian beam waist provides also a flat phase front of the local beam at the photodetector. Thus, the local Gaussian beam waist, the steering mirror front surface[11] and the receive aperture should all be located at the object plane.
The geometrical distance between object plane and image plane, d_{OI}, is given by

$$d_{\mathrm{OI}} := d_1 + d_2 + d_3(d_1) + c_1 + c_2. \qquad (3.90)$$

Hence, the position of the photodiode and aperture is determined by the positions and by the parameters of the lens system. As one can see in fig. 3.12, the light from the steering mirror is transmitted through the beamsplitter. For the local beam with its waist location at the steering mirror surface, the distance d_1 in eq. (3.90) has to be corrected for the effects due to the beamsplitter. This correction is discussed in the subsequent section 3.4.2 about astigmatism.

The design and working principle can be summarized as follows: The aperture is located at the object plane of the beam compressor and centered with the optical axis of the lens system. The propagation direction of light passing through the aperture changes upon rotation of the spacecraft. In the optimal case no beamwalk will occur on the photodiode, because the B element in the ABCD-transfer matrix is zero. If the light at the aperture is tilted by an angle α w.r.t. the optical axis, the tilt at the image plane (photodetector) is $\alpha/m > \alpha$. Furthermore, the almost flat phase front at the receive aperture is imaged onto the photodiode.
The steering mirror is also located in the object plane of the beam compressor, although a correction due to the beamsplitter needs to be applied. Rotations of the steering mirror leading to an angle α of the local beam w.r.t. the optical axis are transformed to a tilt of α/m at the photodetector. Because the pivot point of the steering mirror is not directly at the front surface of the mirror, rotations cause a small lateral offset[12] at the object plane. This beamwalk is suppressed by the factor m at the photodiode. A flat phase front of the local beam at the QPD is obtained

[11] more precisely: an effective pivot plane of the steering mirror
[12] at nanometer level, because the offset of a few millimeter is multiplied with the square of the rotation angle

by placing the waist of the local Gaussian beam close to the steering mirror front surface (object plane).

3.4.2 Astigmatism

Unfortunately, a flat plate like a beamsplitter introduces astigmatism, as mentioned in [Meschede, 2008, p.171] and [Steel, 1983, p.128]. The beamsplitter breaks the rotational symmetry around the optical axis of the optical system. An example setup with a beam compressor with plano-convex lenses and a beamsplitter is shown in fig. 3.15.

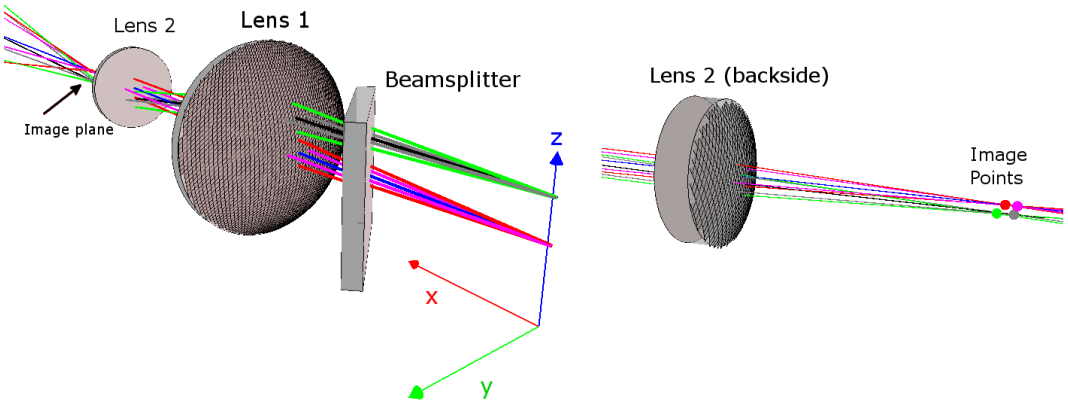

Figure 3.15: Ray tracing simulation for a beam compressor shows astigmatism due to the beamsplitter.

The blue light ray marks the optical axis of the two lenses, while the black ray is an off-axis beam, which is parallel to the optical axis (x-direction). We define the s-direction along the z-axis, while the p-direction is in the incidence plane (xy-plane), as one might be used to from polarization analysis of a beamsplitter. The two red and green rays are deflected along the s-direction, whereas the gray and purple rays initially diverge along the p-direction. At the backside of the second lens the rays converge and form the image plane. However due to the beamsplitter the red and green image points (s-direction) are closer to the lens than the other two (p-direction). Such optical systems having two different focal lengths are called *astigmatic*. In addition to the astigmatism, the beamsplitter introduces a transverse offset (here in $-y$ direction), such that the blue ray does not enter the lens centrally along the optical axis any more. This effect is canceled by shifting the initial blue beam, such that the lens is entered centrally (on-axis).
We now compute the shift of the image points due to the beamsplitter. We therefore use the ABCD formalism independently for the s- and for the p-direction. The components of a ray vector characterize the offset and deflection angle along the s- or p-direction.

Image Points: s-case

Along the s-direction the beamsplitter looks like a non-tilted flat plate. We assume a beamsplitter with thickness c_{BS} and refractive index n_{BS}, which is placed d_{BS} before the first lens. The transfer matrix of the optical system is then given by

$$\begin{aligned}\hat{M}_3^s =&\hat{T}(d_3^s)\cdot\hat{R}(r_2,n_2,n_1)\cdot\hat{T}(c_2)\cdot\hat{B}(n_1,n_2)\cdot\hat{T}(d_2^s)\cdot\hat{B}(n_2,n_1)\cdot\hat{T}(c_1)\cdot\hat{R}(r_1,n_1,n_2)\\ &\cdot\hat{T}(d_{\mathrm{BS}})\cdot\hat{B}(n_{\mathrm{BS}},n_1)\cdot\hat{T}(\mathrm{GPL})\cdot\hat{B}(n_1,n_{\mathrm{BS}})\cdot\hat{T}(d_1^s-c_{\mathrm{BS}}^{\mathrm{oa}}-d_{\mathrm{BS}}),\end{aligned}\tag{3.91}$$

where GPL is the geometrical pathlength inside a beamsplitter (see fig. 3.16). It can be derived easily from trigonometry that

$$\mathrm{GPL}(\alpha_0) = \frac{c_{\mathrm{BS}}}{\cos(\delta)} = \frac{c_{\mathrm{BS}}}{\sqrt{1 - \sin(\alpha_0)^2/n_{\mathrm{BS}}^2}}. \tag{3.92}$$

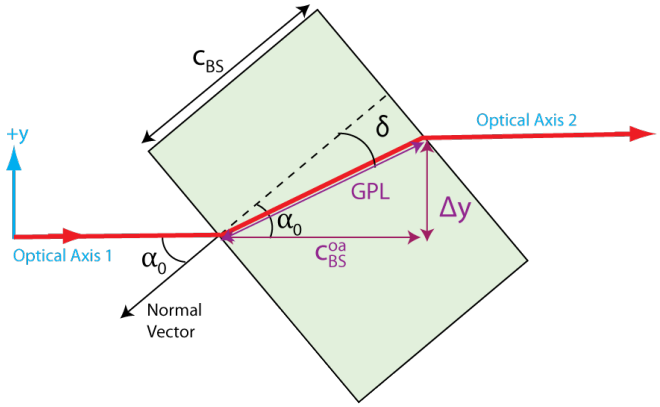

Figure 3.16: Ray path (red) through a tilted beamsplitter in the p-plane.

The matrix $\hat{B}(n_{\mathrm{BS}}, n_1) \cdot \hat{T}(\mathrm{GPL}) \cdot \hat{B}(n_1, n_{\mathrm{BS}})$ is called the sagittal[13] transfer matrix for a tilted slab in [Hodgson & Weber, 1997, eq. 1.83], although it is not specified there which length has to be used. The parameter $c_{\mathrm{BS}}^{\mathrm{oa}}$ is the GPL projected onto the optical axis and can be computed as

$$c_{\mathrm{BS}}^{\mathrm{oa}} = \mathrm{GPL}(\alpha_0) \cdot \cos(\alpha_0 - \delta) = \mathrm{GPL}(\alpha_0) \cdot \cos(\alpha_0 - \arcsin(\sin(\alpha_0)/n_{\mathrm{BS}})). \tag{3.93}$$

Choosing appropriate values for d_2^s and d_3^s as in the previous section leads again to a diagonal form of the transfer matrix $\hat{M}_3^s$. The value of d_2^s is equal to the sum of both focal distances as in eq. (3.88),

$$d_2^s = d_2, \tag{3.94}$$

whereas

$$d_3^s(d_1) = d_3(d_1) + m^2 \cdot \underbrace{\mathrm{GPL}(\alpha_0) \cdot \left(\cos(\alpha_0 - \arcsin(\sin(\alpha_0)/n_{\mathrm{BS}})) - \frac{1}{n_{\mathrm{BS}}}\right)}_{=:\Delta d^s}. \tag{3.95}$$

The first term $d_3(d_1)$ is the distance without the beamsplitter, which is given in eq. (3.89). For the optical bench the aperture and the steering mirror are imaged at the same time. The value for d_3 might be fixed by the distance d_1 (aperture → first lens). Therefore, one can express the effect of the beamsplitter also with a shift of the object plane distance (d_1, steering mirror - first lens) using eq. (3.95) and (3.89):

$$d_1^s = d_1(d_3) + \Delta d^s = d_1(d_3) + \mathrm{GPL}(\alpha_0) \cdot \left(\cos(\alpha_0 - \arcsin(\sin(\alpha_0)/n_{\mathrm{BS}})) - \frac{1}{n_{\mathrm{BS}}}\right). \tag{3.96}$$

The second term is positive so that the steering mirror and the waist position of the local beam needs to be shifted away from the lenses, if the image of the steering mirror front surface is to be co-located with the image of the aperture.

[13] here: s-direction

Image Points: p-case

The effect of the beamsplitter in p-direction is a transverse shift Δy (see fig. 3.16 and fig. 3.17). The direction of the beam stays unchanged, as long as the beamsplitter has zero wedge angle. The transverse shift can be computed as $c_{\mathrm{BS}}^{\mathrm{oa}}$:

$$\begin{aligned}\Delta y(\alpha_0, \alpha) &:= \sin(\alpha_0 - \delta) \cdot \mathrm{GPL}(\alpha_0 - \alpha) \\ &= c_{\mathrm{BS}} \frac{\sin(\alpha_0 - \arcsin(\sin(\alpha_0 - \alpha)/n_{\mathrm{BS}}))}{\sqrt{1 - \sin(\alpha_0 - \alpha)^2/n_{\mathrm{BS}}^2}},\end{aligned} \tag{3.97}$$

where an initial ray misalignment of $-\alpha$ was incorporated. The offset Δy should be given w.r.t. the optical axis, therefore $\sin(\alpha_0 - \delta)$ is used instead of $\sin(\alpha_0 - \alpha - \delta)$. The offset can be expanded in a series for small ray angles α,

$$\Delta y(\alpha_0, \alpha) \approx \Delta y(\alpha_0, 0) + \alpha \cdot \Delta y'(\alpha_0, 0), \tag{3.98}$$

where the prime ($'$) denotes a derivative w.r.t. α.
The only difference in the transmitted ray of a tilted and a non-tilted beamsplitter is the offset. The transformation of a ray $(y, \alpha)^{\mathsf{T}}$ from the ray transfer matrix formalism can be written as

$$\begin{pmatrix} y_{\mathrm{new}} \\ \alpha_{\mathrm{new}} \end{pmatrix} := \begin{pmatrix} \Delta y(\alpha_0, 0) \\ 0 \end{pmatrix} + \underbrace{\begin{pmatrix} 1 & \Delta y'(\alpha_0, 0) \\ 0 & 1 \end{pmatrix}}_{=:\hat{Q}} \begin{pmatrix} y \\ \alpha \end{pmatrix}. \tag{3.99}$$

The constant first term indicates that even an on-axis ray $(0, 0)^{\mathsf{T}}$ will gain some offset, if it passes through the beamsplitter. α_0 is still the tilt angle of the beamsplitter. We neglect the constant first term, because initial rays can simply be shifted by $-\Delta y(\alpha_0, 0)$. Under this condition a ray $(0, 0)^{\mathsf{T}}$ passes the lenses centrally on the optical axis. Neglecting the term corresponds to a shift of the coordinate system from optical axis 1 to optical axis 2 in fig. 3.17. This derivation for $\hat{Q}$ is basically the explanation for the tangential transfer matrix for a tilted slab given in [Hodgson & Weber, 1997, eq. 1.82].

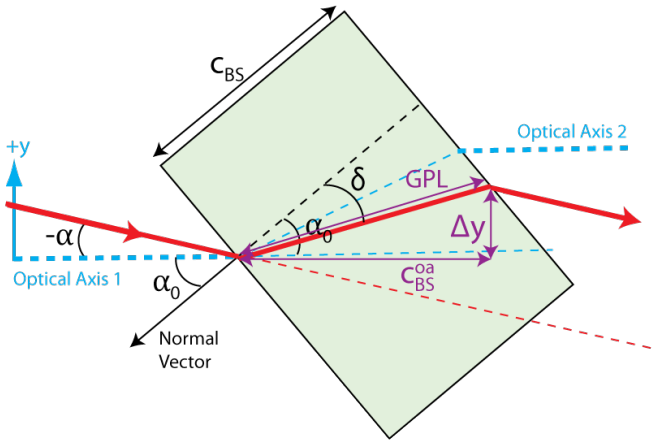

Figure 3.17: Ray path (red) through a tilted beamsplitter with initial ray misalignment.

With the knowledge of $\hat{Q}$, the beam compressor p-transfer matrix including the beamsplitter is

$$\begin{aligned}\hat{M}_3^p :=& \hat{T}(d_3^p) \cdot \hat{R}(r_2, n_2, n_1) \cdot \hat{T}(c_2) \cdot \hat{B}(n_1, n_2) \cdot \hat{T}(d_2^p) \cdot \hat{B}(n_2, n_1) \cdot \hat{T}(c_1) \cdot \hat{R}(r_1, n_1, n_2) \\ &\cdot \hat{T}(d_{\mathrm{BS}}) \cdot \hat{Q} \cdot \hat{T}(d_1^p - c_{\mathrm{BS}}^{\mathrm{oa}} - d_{\mathrm{BS}}).\end{aligned} \tag{3.100}$$

Again, this matrix can be simplified to a diagonal form, if

$$d_2^p = d_2, \tag{3.101}$$

$$\text{or} \quad \begin{aligned} d_3^p(d_1) &= d_3(d_1) + m^2 \cdot \Delta d^p = d_1(d_3) + m^2 \cdot \left(c_{\mathrm{BS}}^{\mathrm{oa}} - \Delta y'(\alpha_0, 0)\right) \\ d_1^p(d_3) &= d_1(d_3) + \Delta d^p, \end{aligned} \tag{3.102}$$

with

$$\begin{aligned} \Delta d^p &= + c_{\mathrm{BS}}^{\mathrm{oa}} - \Delta y'(\alpha_0, 0), \\ &= c_{\mathrm{BS}}^{\mathrm{oa}} - \frac{c_{\mathrm{BS}} \cdot n_{\mathrm{BS}} \cdot \cos(\alpha_0)^2}{(n_{\mathrm{BS}}^2 - \sin(\alpha_0)^2) \cdot \sqrt{1 - \sin(\alpha_0)^2 / n_{\mathrm{BS}}^2}} \\ &= \mathrm{GPL}(\alpha_0) \cdot \left(\cos(\alpha_0 - \arcsin(\sin(\alpha_0)/n_{\mathrm{BS}})) - \frac{\cos(\alpha_0)^2}{n_{\mathrm{BS}} \cdot (1 - \sin(\alpha_0)^2 / n_{\mathrm{BS}}^2)} \right). \end{aligned} \tag{3.103}$$

Here the shift Δd^p is positive as well, making it necessary to shift the steering mirror and the local beam waist away from the lenses, such that the image of steering mirror front surface and aperture are co-located.
The resulting shifts Δd in s- and p-case simplify for a non-tilted beamsplitter $\alpha_0 = 0$ to the same equation and for $n_{\mathrm{BS}} = 1.0$ to $\Delta d^p = \Delta d^s = 0$, as one would expect. It is important to notice, that the shifts Δd^s and Δd^p are in general unequal. This means the object planes for the s- and p-direction are not at the same distance from the lens (or beamsplitter). The position of the steering mirror can be defined, for example, by the mean of the shifts in each direction. Nevertheless, rotations of the steering mirror lead to a beamwalk on the photodiode.
The application and verification of these equations in sec. 3.6.1 yields the following values for a typical setup:

$$\Delta d^s = 1.6\,\mathrm{mm}, \qquad \Delta d^p = 3.0\,\mathrm{mm}. \tag{3.104}$$

As we will see later in sec. 3.6.3, a misplacement of the object plane of 1 mm results only in a very small beamwalk of 0.1 μm at the photodiode, when the beam deflection by the steering mirror is 1 mrad. In addition to the beamwalk due to astigmatism of the beamsplitter, an almost negligible beamwalk is also caused by the offset in the center of rotation of the steering mirror (see end of sec. 3.4.1).
The results for the astigmatism and the ABCD matrices can be directly applied to Gaussian beams. So far the derivation used geometrical optics. However, the local laser beam is supposed to be a Gaussian beam in the fundamental TEM_{00} mode with a waist radius of 2.5 mm. The phase and the intensity of the light is of importance for interferometric measurements and is also subject to changes due to astigmatism, as we will see subsequently.

Astigmatic Gaussian Beams

Recall that a Gaussian beam can be described with the complex beam parameter [Saleh & Teich, 1991, eq. 3.1-5]

$$q(z) = z + i \cdot z_r, \tag{3.105}$$

where z is the coordinate of the evaluation point measured from the waist along the beam propagation direction and z_r is the Rayleigh range. The expression [Saleh & Teich, 1991, eq. 3.1-6]

$$\frac{1}{q(z)} = \frac{1}{z + i \cdot z_r} = \frac{z^2}{z^2 + z_r^2} - i \frac{z_r^2}{z^2 + z_r^2} = \frac{1}{R(z)} - i \frac{\lambda}{\pi \omega(z)^2} \tag{3.106}$$

relates the beam parameter q to accessible physical quantities like the radius of curvature of the phase front $R(z)$, the wavelength λ and the waist size $\omega(z)$.
The effect of an optical system on the q-parameter can be described with the corresponding ABCD matrix [Saleh & Teich, 1991, eq. 3.2-21]

$$q_{\text{new}} = \frac{Aq_{\text{old}} + B}{Cq_{\text{old}} + D}. \tag{3.107}$$

Assuming an initial Gaussian beam with a waist located at the object plane of the beam compressor with magnification m, e.g. $m = 1/8$, the q-parameter is purely imaginary $q = q_{\text{initial}} = im^2 \cdot z_{r,\text{initial}}$. The ABCD matrix of the beam compressor has only diagonal entries m and $1/m$. The beam parameter after transformation is therefore

$$q = m^2 q_{\text{initial}} = im^2 \cdot z_{r,\text{initial}} \tag{3.108}$$

and is also purely imaginary. This indicates that the waist and hence flat phase front of the final beam is at the image plane and the beam radius has been reduced by $1/m$ according to 3.106. Also the Rayleigh range and hence divergence of the beam changes due to the beam compressor.
In the more general case considering an initial waist position $z_{0,\text{initial}}$, the result is very similar:

$$q = m^2 q_{\text{initial}} = m^2 \cdot z_{0,\text{initial}} + im^2 \cdot z_{r,\text{initial}}. \tag{3.109}$$

A Gaussian beam, which has propagated 200 km and has therefore roughly a phase front radius of curvature $R \approx 200\,\text{km}$ at the object plane, is transformed to a beam with

$$R \approx m^2 \cdot 200\,\text{km} \approx 3.1\,\text{km} \tag{3.110}$$

at the image plane, where $m^2 \approx 1/64$ was used.
If a beamsplitter is placed in front of the first lens, the ABCD matrices for the s- and p-direction are different. The propagation of a Gaussian beam through such a system can be described by simple astigmatic Gaussian beams, sometimes also called 'orthogonal astigmatic Gaussian beams'. These beams have two complex parameters, which are in IfoCad denoted to be along sagittal and tangential direction[14]. Here the notation q_s and q_p is used for consistency. The ABCD matrices for p- and s-direction of the beam compressor with beamsplitter cannot be diagonalized at the same time. Assuming that d_3 is chosen such that $\hat{M}_3^p$ is diagonal, the following complex beam parameters can be obtained

$$q_p = m^2 q_{\text{initial}} = im^2 \cdot z_{r,\text{initial}} \quad , \quad \hat{M}_3^s = \begin{pmatrix} m & m \cdot (\Delta d^s - \Delta d^p) \\ 0 & 1/m \end{pmatrix}, \tag{3.111}$$

$$q_s = m^2 q_{\text{initial}} + m^2(\Delta d^s - \Delta d^p) = m^2(\Delta d^s - \Delta d^p) + im^2 \cdot z_{r,\text{initial}}, \tag{3.112}$$

and the phase front radii of curvature are

$$\begin{aligned} R_p(z) &= \infty, \\ R_s(z) &= z\left(1 + \frac{z_r^2}{z^2}\right) = m^2(\Delta d^s - \Delta d^p)\left(1 + \frac{m^4 \cdot z_{r,\text{initial}}^2}{m^4(\Delta d^s - \Delta d^p)^2}\right). \end{aligned} \tag{3.113}$$

[14] originally 'sagittal'/'transverse' and 'meridional'/'tangential' rays are defined w.r.t. an optical axis of an optical system [Benenson *et al.* , 2002, p.359]. In [Freise & Strain, 2010, p.57] 'sagittal' and 'tangential' are used for the in-plane and out-of-plane direction of an interferometer, which is confined in one plane. In the context of the beam compressor with beamsplitter (or the whole LRI), sagittal would be the p-direction.

The amplitude and intensity of the beam have an elliptical shape in transverse direction, because the spot size w is unequal in both directions. At the waist in p-direction, the spot sizes are given by the Rayleigh range [Saleh & Teich, 1991, eq.3.1-8f] and the offsets Δd^s, Δd^p:

$$\omega_p(z) = \sqrt{\frac{\lambda z_r}{\pi}\left(1+\frac{z^2}{z_r^2}\right)} = \sqrt{\frac{\lambda m^2 z_{r,\text{initial}}}{\pi}} = m\cdot\omega_0, \tag{3.114}$$

$$\begin{aligned}\omega_s(z) =& \sqrt{\frac{\lambda z_r}{\pi}\left(1+\frac{z^2}{z_r^2}\right)} = \sqrt{\frac{\lambda m^2 z_{r,\text{initial}}}{\pi}\left(1+\frac{m^4(\Delta d^s-\Delta d^p)^2}{m^4 z_{r,\text{initial}}^2}\right)}\\ =& m\cdot\omega_0\cdot\sqrt{1+\frac{(\Delta d^s-\Delta d^p)^2}{z_{r,\text{initial}}^2}},\end{aligned} \tag{3.115}$$

whereas $\omega_0 = 2.5\,\text{mm}$ is the initial waist size of the local Gaussian beam.
Applications and evaluation of these equations can be found in section 3.6.1 about simulation results. The resulting phase front distortion and intensity ellipticity are very small in comparison to effects due to misplacement and misalignment of components, which are described in the subsequent section and evaluated in section 3.6.3. Thus, the here presented analysis using simple astigmatic Gaussian beams confirms that these effects are not important practically.
In addition, the later simulations of the optical bench are performed using *general astigmatic Gaussian beams*. These beams can be described with two q-parameters and a complex angle θ. General astigmatic Gaussian beams can also handle non-orthogonal astigmatism. Corresponding functions are implemented in the IfoCad software [Kochkina *et al.* , 2013]. For an overview of general astigmatic beam propagation see for example [Alda, 2003] or [Arnaud & Kogelnik, 1969].

Sensitivity on Misalignment and Misplacement

The beam compressor can only be built with a limited precision. The effect of small variations in the parameters on the ABCD matrix and hence on the output q-beam parameter or ray offset and direction needs to be investigated. To simplify the equations, the thin lens equations (eq. (3.84f.)) are used such that d_1, d_2, d_3 are referred to the principal points of the lenses and not to the vertices. The effect of the beamsplitter is also omitted here.
If a nominal ABCD matrix $\hat{M}_{1,\text{nom}}$ corresponds to a parameter set $p_i = (d_1, d_2, d_3, f_1, f_2)$, small variations will result in the following ABCD matrix:

$$\hat{M}_1^m \approx \hat{M}_{1,\text{nom}} + \sum_i \delta p_i \cdot \frac{\partial M_1}{\partial p_i}_{|\text{nom}}. \tag{3.116}$$

For an initial ray $\vec{r}_{\text{initial}} = (y_{\text{initial}}, \theta_{\text{initial}})^\mathsf{T}$ or Gassian beam $q_{\text{initial}} = z_{r,\text{initial}} + i\cdot z_{r,\text{initial}}$ the final state

$$\vec{r}_{\text{final}} = \hat{M}_1^m \cdot \vec{r}_{\text{initial}} \qquad q_{\text{final}} = \frac{A q_{\text{initial}} + B}{C q_{\text{initial}} + D} \tag{3.117}$$

reveals much insight when it is evaluated numerically (see sec. 3.6.3 with simulation results). In the general case the analytical expressions are, however, quite long and are not given here.

3.4.3 Beamsplitter Intersection and Lateral Shifts

Another effect caused by the beamsplitter and the corresponding astigmatism is that a light ray coming from the aperture will intersect with the beamsplitter front

surface at another position than a light ray from the steering mirror, if the steering mirror position has not been corrected (see fig. 3.18). The correction terms are the same as for the astigmatism (eq. (3.95), (3.97), (3.103)), because the ABCD formalism is actually describing ray deflections:

$$\Delta y = \Delta y(\alpha_0, 0) = c_{\mathrm{BS}} \frac{\sin\left(\alpha_0 - \arcsin(\sin(\alpha_0)/n_{\mathrm{BS}})\right)}{\sqrt{1 - \sin(\alpha_0)^2/n_{\mathrm{BS}}^2}}, \tag{3.118}$$

$$\Delta d^s = \mathrm{GPL}(\alpha_0) \cdot \left(\cos(\alpha_0 - \arcsin(\sin(\alpha_0)/n_{\mathrm{BS}})) - \frac{1}{n_{\mathrm{BS}}}\right), \tag{3.119}$$

$$\Delta d^p = \mathrm{GPL}(\alpha_0) \cdot \left(\cos(\alpha_0 - \arcsin(\sin(\alpha_0)/n_{\mathrm{BS}})) - \frac{\cos(\alpha_0)^2}{n_{\mathrm{BS}} \cdot (1 - \sin(\alpha_0)^2/n_{\mathrm{BS}}^2)}\right), \tag{3.120}$$

with (eq. (3.92))

$$\mathrm{GPL}(\alpha_0) = \frac{c_{\mathrm{BS}}}{\sqrt{1 - \sin(\alpha_0)^2/n_{\mathrm{BS}}^2}}, \tag{3.121}$$

where α_0 is the beamsplitter tilt angle, c_{BS} and n_{BS} the beamsplitter thickness and refractive index, respectively. It is noteworthy that the offsets do not depend on the beamsplitter position.
The correction terms for the s- and p-directions are in general unequal. This means the intersection points of both beams with the beamsplitter front surface cannot coincide for arbitrary deflections. The separation between the intersection points can have a magnitude of a few μm, depending on the beamsplitter and deflection angle. This leads also to a lateral separation of the beams propagating towards the beam compressor. However, it turns out that this discontinuity in the racetrack has no influence on the length measurement in case of plane waves, as discussed later in section 3.5.2.

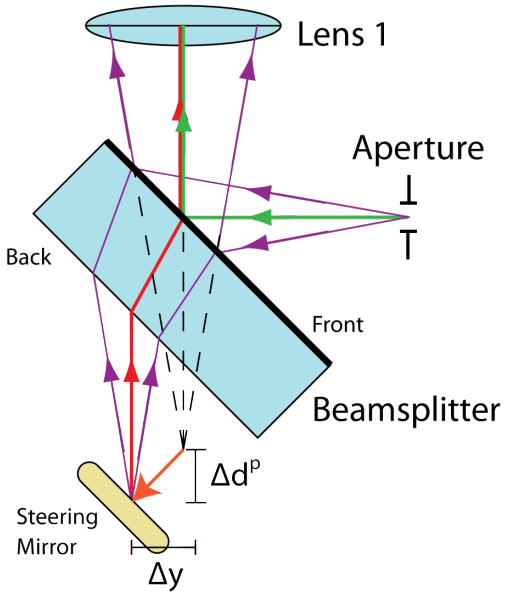

Figure 3.18: Correction of the steering mirror position in the p-plane.

3.4.4 Photodiode and Phasemeter Signals

A photodiode exploits the photoelectric effect and provides an electric current I_C, which is proportional to the intensity of the total impinging light field. Considering

two light beams, the electric current can be derived using complex electric fields with amplitude $A_1,\ A_2$, angular frequency $\omega_1,\ \omega_2$ and phase $\varphi_1,\ \varphi_2$:

$$\begin{aligned} I_C(t) =& k \int_{\mathrm{PD}} |A_1 \cdot \exp(i\omega_1 t + i\varphi_1) + A_2 \cdot \exp(i\omega_2 t + i\varphi_2)|^2 \ \mathrm{dx\ dy} \\ =& \ k \int_{\mathrm{PD}} |A_1|^2 + |A_2|^2 + 2 \cdot A_1 \cdot A_2 \cdot \cos((w_1 - w_2)t + \varphi_1 - \varphi_2) \ \mathrm{dx\ dy} \\ =& \ k \left(\underbrace{P_1 + P_2}_{=:P_{\mathrm{DC}}} + \underbrace{2\sqrt{\eta P_1 P_2}}_{=:A_{\mathrm{AC}}} \cdot \cos((w_1 - w_2)t + \Phi) \right). \end{aligned} \tag{3.122}$$

P_1 and P_2 denote here the power of each beam detected by the photodiode. The sum of them is the average power P_{DC} on the photodiode, while A_{AC} is called the heterodyne amplitude (although it has units of power). $A_1, A_2, \varphi_1, \varphi_2$ are in general spatial dependent functions. η is called the heterodyne efficiency and k is the photodiode responsivity. The electric current oscillates with the beatnote frequency $w_1 - w_2$. The heterodyne efficiency is connected to the contrast c of a photodiode signal by the expression

$$c = \frac{I_{\max} - I_{\min}}{I_{\max} + I_{\min}} = \frac{\sqrt{\eta P_1 P_2}}{P_1 + P_2}, \tag{3.123}$$

where $I_{\max}$ and $I_{\min}$ are the maximal and minimal electric current values, respectively. For the LRI a quadrant photodiode is foreseen, where the circular active area is divided into four quadrants (see fig. 3.19). As depicted, a small gap with width d_g separates the quadrants. The gap is a dead space and has no photoelectric effect, therefore the received light power decreases due to the gaps in comparison to a single element diode. The direction of the gaps is used to define a photodiode coordinate frame. The vertical gap (normal to the bench) defines $\vec{e}_v$, while the horizontal gap is parallel to $\vec{e}_h$.

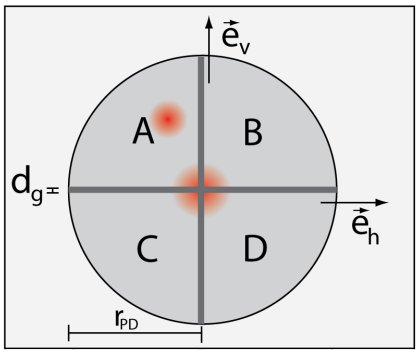

Figure 3.19: Quadrant photodiode with slit width d_g

The phase Φ, heterodyne amplitude A_{AC} and DC power P_{DC} of each quadrant can be tracked by a phasemeter, if the signal-to-noise ratio is high enough. The signal is proportional to the contrast c or $\sqrt{\eta}$ and therefore determined by the spatial wavefront overlap (integral in eq. (3.122)) of the two beams. The main noise sources are shot-noise and electronic-noise (see [Sheard *et al.* , 2012] and [Sheard & Heinzel, 2011]). The DC power P_{DC} can be obtained by averaging an integer multiple of beatnote oscillation cycles. The computation of these heterodyne signals for simulations is described in Wanner [2010] and Wanner *et al.* [2012].
The average phase of all segments provides the length measurement, also called longitudinal signal. One way of computing the phase using a complex notation is

given by

$$\phi = \arg\left(A^A_{\mathrm{AC}} \cdot e^{i\Phi^A} + A^B_{\mathrm{AC}} \cdot e^{i\Phi^B} + A^C_{\mathrm{AC}} \cdot e^{i\Phi^C} + A^D_{\mathrm{AC}} \cdot e^{i\Phi^D}\right), \tag{3.124}$$

where $\phi = \phi(t)$ is time-dependent. A change in the phase can be related to a change in the optical pathlength δz via

$$\delta\phi = \phi(t_{n+1}) - \phi(t_n) = \delta z \frac{2\pi}{\lambda}, \tag{3.125}$$

whereas one needs to keep in mind that ϕ is only defined on $0..2\pi$ (or equivalent $-\pi... + \pi$). By tracking the phase changes one can obtain length changes, but not an absolute distance measurement. Sudden phase changes larger than 2π are ambiguous (*phase wrapping*) and are not measured correctly, but slow changes over many periods ("fringes") can be tracked by a "phase-tracking" algorithm.
With a differential combination of the DC values one can compute the power centroid w.r.t. to the photodiode center [Wanner, 2010, eq. 2.44]:

$$\begin{aligned}
\mathrm{DPS}_h &= \frac{P_{\mathrm{left}} - P_{\mathrm{right}}}{P_{\mathrm{left}} + P_{\mathrm{right}}} = \frac{P^A_{\mathrm{DC}} + P^C_{\mathrm{DC}} - (P^B_{\mathrm{DC}} + P^D_{\mathrm{DC}})}{P^A_{\mathrm{DC}} + P^B_{\mathrm{DC}} + P^C_{\mathrm{DC}} + P^D_{\mathrm{DC}}}, \\
\mathrm{DPS}_v &= \frac{P_{\mathrm{top}} - P_{\mathrm{bottom}}}{P_{\mathrm{top}} + P_{\mathrm{bottom}}} = \frac{P^A_{\mathrm{DC}} + P^B_{\mathrm{DC}} - (P^C_{\mathrm{DC}} + P^D_{\mathrm{DC}})}{P^A_{\mathrm{DC}} + P^B_{\mathrm{DC}} + P^C_{\mathrm{DC}} + P^D_{\mathrm{DC}}}.
\end{aligned} \tag{3.126}$$

This *Differential Power Signal* (DPS) is unitless and can be used to detect beamwalk on the photodiode, though the power center is of course dependent on the position and power of both beams. For a single beam the DPS is linear for small displacements from center [Wanner, 2010, p. 46], but has also non-linear contributions and cross-talk between h and v direction for larger offsets. The power on the photodiode is additive, such that the equations can be applied for two beams, whereas the centroid is is an average scaled with the relative power of the beams. If the beam parameters are known or the QPD has been calibrated [Sommerfeld, 2010], the beamwalk on the photodiode can be measured and converted to a proper position (with units of meter).
In the LRI the beam power levels at the photodiodes are in the order of 1 mW for the local laser beam and 100 pW for the received beam. Hence, the DPS will be dominated by the local oscillator. Furthermore, the beam compressor suppresses the beamwalk on the photodiode, such that the DPS is close to zero.
Using the differential phase between the photodiode segments yields information on the relative wavefront angle between the beams at the photodiode. This technique is called *Differential Wavefront Sensing* (DWS) and is used for example in GEO600 [Grote *et al.* , 2002]. The signal is obtained by [Wanner, 2010, eq. 2.46]

$$\begin{aligned}
\mathrm{DWS}_h &= \frac{\Phi^A + \Phi^C}{2} - \frac{\Phi^B + \Phi^D}{2}, \\
\mathrm{DWS}_v &= \frac{\Phi^A + \Phi^B}{2} - \frac{\Phi^C + \Phi^D}{2}.
\end{aligned} \tag{3.127}$$

As it will turn out subsequently, the DWS signal is in first order proportional to the wavefront tilt with an amplification factor, which depends on the wavelength and on the integrated area on the photodiode. However, DWS is sensitive to beamwalk on the photodiode. Often common mode beamwalk of both beams is less critical than differential beamwalk, but in general the influence of beamwalk on DWS is dependent on the beam and photodiode parameters. Although DWS can also be used without optics that provide fixed beam positions ([Wanner, 2010, LISA Pathfinder OB], [Hechenblaikner, 2010]), the DWS signal can be maximized with a beam compressor,

which at the same time suppresses the beamwalk and magnifies the wavefront tilt. A beamwalk on the photodiode leads also to varying heterodyne amplitudes on the quadrants and in case of the small photodiode also to a drop in the SNR, if the beam moves off the QPD.
Assuming a flat phase front and a flat top amplitude with radius w_r[15] for both beams, the DWS signal for a photodiode without slits and active area radius larger than w_r is [Sheard & Heinzel, 2011]

$$\mathrm{DWS}_{h,v} = \alpha^{\mathrm{PD}}_{h,v} \cdot m_{\mathrm{DWS}} = \alpha^{\mathrm{PD}}_{h,v} \cdot \frac{16 \cdot w_r}{3\lambda}, \tag{3.128}$$

where α^{PD} is an infinitesimal small relative tilt (h) or tip (v) between the wavefronts in front of the photodiode (and not in front of the beam compressor). Since the beam sizes are reduced by $1/m = 8$ by the beam compressor, the flat top radius at the photodiode is approximately $w_r = 4.0/8\,\mathrm{mm} = 0.5\,\mathrm{mm}$. Then a wavelength of 1064 nm results in an amplification factor of $m_{\mathrm{DWS}} = 2506\,\mathrm{rad/rad}$. If the wavefront tilt before the beam compressor α^{BC} is used, the α^{PD} in eq. (3.128) needs no be replaced by α^{BC}/m, because the beam compressor magnifies the wavefront tilt. The amplification is then $m_{\mathrm{DWS}}/m = 20050\,\mathrm{rad/rad}$. It is noteworthy that the radian in the denominator describes a geometrical angle between wavefronts in front of the photodiode or beam compressor, while the radian in the numerator stands for the phase of an electric signal (generated by the photodiode). However, this derivation assumes two flat top beams. A more general analytical treatment of DWS can be found in [Hechenblaikner, 2010]. Another equation for two beams with Gaussian intensity shape and waist radii w_1 and w_2 and flat phase profile is derived in appendix C. The photodiode radius is denoted as r_{PD}, while Erf() is the error function:

$$\mathrm{DWS}_{h,v} = m_{\mathrm{DWS}} \cdot \alpha^{\mathrm{PD}}_{h,v} = \frac{4 \cdot \alpha^{\mathrm{PD}}_{h,v}}{\lambda} \cdot \frac{2 \cdot r_{\mathrm{PD}} \cdot z - \sqrt{\pi} \cdot e^{r^2_{\mathrm{PD}} \cdot z^2} \cdot \mathrm{Erf}(r_{\mathrm{PD}} \cdot z)}{(e^{r^2_{\mathrm{PD}} \cdot z^2} - 1) \cdot z}$$
$$\text{with} \quad z = \sqrt{1/w_1^2 + 1/w_2^2}. \tag{3.129}$$

In the case of flat intensity ($w_1 = w_2 \to \infty$) over the whole photodiode, the equation simplifies to

$$\mathrm{DWS}_{h,v} = \frac{16 \cdot \alpha^{\mathrm{PD}}_{h,v} \cdot r_{\mathrm{PD}}}{3\lambda}. \tag{3.130}$$

While the case of one flat intensity profile ($w_1 \to \infty$) over the whole photodiode and a Gaussian profile with $w_2 = 2.5/8\,\mathrm{mm}$ provides an amplification factor of

$$m_{\mathrm{DWS}} = 1888\,\mathrm{rad/rad} \tag{3.131}$$

for a photodiode radius of $r_{\mathrm{PD}} = 0.5\,\mathrm{mm}$. The corresponding IfoCad result for the same parameter is 1885 rad/rad. The photodiode slit was neglected in this derivation.
For the LRI the ratio of DWS signal and wavefront tilt before the beam compressor (and not before the photodiode) is of interest. Thus the effective DWS amplification factor is

$$\frac{m_{\mathrm{DWS}}}{m} \approx 1888\,\mathrm{rad/rad} \cdot 8 = 15104\,\mathrm{rad/rad}, \tag{3.132}$$

whereas this is the more important ratio of relative wavefront tilt before the beam compressor to phase angle of the electric signal. This effective factor (eq. 3.132) is independent of the beam compressor magnification m to first order, because the waist sizes and hence m_{DWS} is proportional to m and cancels with the denominator. This is obvious for the simplified formula for m_{DWS} (eq. (3.128)), whereas eq. (3.129) requires a first order expansion in $z \sim 1/m$.

[15] amplitude has a sharp drop to zero at w_r

3.4.5 Steering Mirror

The LRI requires a two axes (tip/tilt) steering mirror (SM) with a few milliradian range in tip and tilt to compensate the spacecraft attitude jitter and static misalignment between LRI and spacecraft, which might be caused by the spacecraft launch. It should allow a pointing of the outgoing beam towards the distant spacecraft with errors far below 100 μrad, as we will see later in section 3.5.1.
The actuator can be based for example on the piezo effect or voice-coils.
The local coordinate system of the steering mirror is shown in figure 3.20. A tilt is defined as a rotation around $\vec{e}_w$ by an angle h_{SM} (horizontal), while a tip is around $\vec{e}_v$ by an angle v_{SM} (vertical). The mirror normal vector $\vec{e}_u$ forms roughly a 45 degree angle with the x-axis, which is the optical axis. Furthermore, we consider small initial misalignments of the mirror, which are given as rotations by the angles u, v, w around the axes $\vec{e}_u, \vec{e}_v, \vec{e}_w$, respectively. A rotation matrix around a vector $\vec{a}$ with rotation angle α is denoted with $\hat{R}(\vec{a}, \alpha)$. With this notation, the mirror coordinate system can be derived as

$$\vec{e}_u = \hat{R}(\vec{e}_z, 45°) \cdot \hat{R}(\vec{e}_z, w) \cdot \hat{R}(\vec{e}_y, v) \cdot \hat{R}(\vec{e}_x, u) \cdot \vec{e}_x, \tag{3.133}$$

$$\vec{e}_v = \hat{R}(\vec{e}_z, 45°) \cdot \hat{R}(\vec{e}_z, w) \cdot \hat{R}(\vec{e}_y, v) \cdot \hat{R}(\vec{e}_x, u) \cdot \vec{e}_y, \tag{3.134}$$

$$\vec{e}_w = \hat{R}(\vec{e}_z, 45°) \cdot \hat{R}(\vec{e}_z, w) \cdot \hat{R}(\vec{e}_y, v) \cdot \hat{R}(\vec{e}_x, u) \cdot \vec{e}_z. \tag{3.135}$$

Because small angles u, v, w are assumed, the corresponding rotation matrices commute and the order of rotations does not matter. The angle w can be seen as additional offset to the 45°.

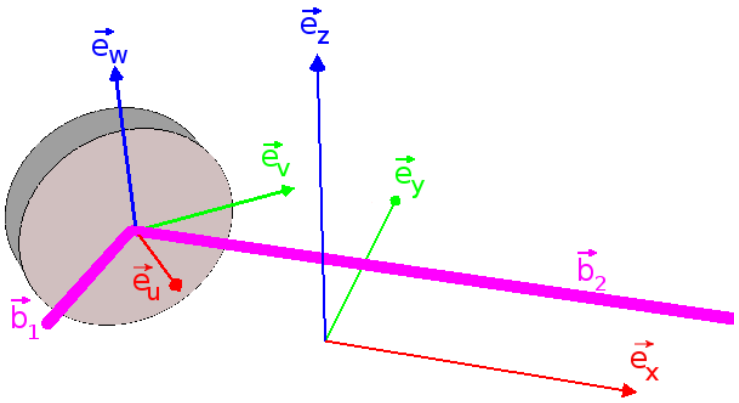

Figure 3.20: Coordinate system of the steering mirror. Beam b_1 is reflected at the mirror into b_2 and propagates parallel to the x-axis.

In the nominal state of the steering mirror, a beam $\vec{b}_1$ is reflected into beam $\vec{b}_{2,\mathrm{ini}}$, whereas $\vec{b}_{2,\mathrm{ini}}$ is parallel to the optical axis (x-direction). If the normal vector direction $\vec{e}_u$ is given, the direction of $\vec{b}_1$ is determined by

$$\vec{b}_1 := -\hat{R}(\vec{e}_u, 180°) \cdot \vec{b}_{2,\mathrm{ini}}. \tag{3.136}$$

It is useful to know how rotations by v_{SM} and h_{SM} around the steering mirror axes change the angle of the reflected beam b_2 w.r.t. the y- and z-direction, which are denoted by $h_{\mathrm{BC}}, v_{\mathrm{BC}}$. These are the angles of the local laser beam before the beam compressor relative to the optical axis. For small angles these expressions can be

derived:

$$\begin{aligned}
h_{\mathrm{BC},v} &\approx \vec{b}_2 \cdot \vec{e}_y = (-\hat{R}(\ \hat{R}(\vec{e}_v, v)\vec{e}_u, 180°) \cdot \vec{b}_1) \cdot \vec{e}_y, \\
h_{\mathrm{BC},h} &\approx \vec{b}_2 \cdot \vec{e}_y = (-\hat{R}(\ \hat{R}(\vec{e}_w, h)\vec{e}_u, 180°) \cdot \vec{b}_1) \cdot \vec{e}_y, \\
v_{\mathrm{BC},v} &\approx \vec{b}_2 \cdot \vec{e}_y = (-\hat{R}(\ \hat{R}(\vec{e}_v, v)\vec{e}_u, 180°) \cdot \vec{b}_1) \cdot \vec{e}_z, \\
v_{\mathrm{BC},h} &\approx \vec{b}_2 \cdot \vec{e}_y = (-\hat{R}(\ \hat{R}(\vec{e}_w, h)\vec{e}_u, 180°) \cdot \vec{b}_1) \cdot \vec{e}_z,
\end{aligned} \tag{3.137}$$

while a linearization provides

$$\begin{aligned}
h_{\mathrm{BC},v} &\approx 2 \cdot u \cdot v_{\mathrm{SM}} \\
h_{\mathrm{BC},h} &\approx 2 \cdot h_{\mathrm{SM}} \\
v_{\mathrm{BC},v} &\approx -\sqrt{2} \cdot v_{\mathrm{SM}} \cdot (1 + w) \\
v_{\mathrm{BC},h} &\approx -\sqrt{2} \cdot h_{\mathrm{SM}} \cdot (u + v).
\end{aligned} \tag{3.138}$$

This means, if there are no initial misalignments ($u = v = w = 0$) and the mirror reflects the initial beam b_1 by 90° into the optical axis, a tilt h_{SM} of the steering mirror causes a beam tilt (and in the plane wave approximation also a wavefront tilt) at the beam compressor by $2 \cdot h_{\mathrm{SM}}$, whereas a tip by v_{SM} produces a tip by $-\sqrt{2} \cdot v_{\mathrm{SM}}$ at the beam compressor. The sign convention for angles $h_{\mathrm{BC},v/h}, v_{\mathrm{BC},v/h}$ was chosen arbitrarily in this derivation.

3.4.6 DWS Control Loop

In the last two sections we introduced the signals measured by the photodiode on the optical bench and the steering mirror. In this section the combination of both in a DWS control loop is explained, which ensures the parallelism of incoming and outgoing beam on the OB.
The racetrack configuration only works if the incoming received and the outgoing local beam are sufficiently parallel. If the optical bench introduces a deflection of the beam in the racetrack, the light might miss the distant spacecraft after the the propagation of 200 km (see fig. 3.2 and subsequent sec. 3.5.1). Assuming a perfect TMA, the angle between the received beam and outgoing beam towards the distant spacecraft depends on the direction of the incoming beam w.r.t. the OB and the steering mirror state. On left side of figure 3.21, the incoming received beam and outgoing local beam on the optical bench are parallel. If the local spacecraft is tilted by β (fig. 3.21, middle), the wavefront of local and received beam will be tilted by β, assuming a plane wave approximation. The wavefront angle is magnified by $1/m$ due to the beam compressor and measured by the DWS at the photodiode. The tip angle is measured in the same way. This information is used in a feedback control loop to rotate the steering mirror, such that the DWS signal is kept close to zero in both axes. In this case the outgoing beam and the received beam will stay parallel (fig. 3.21, right).

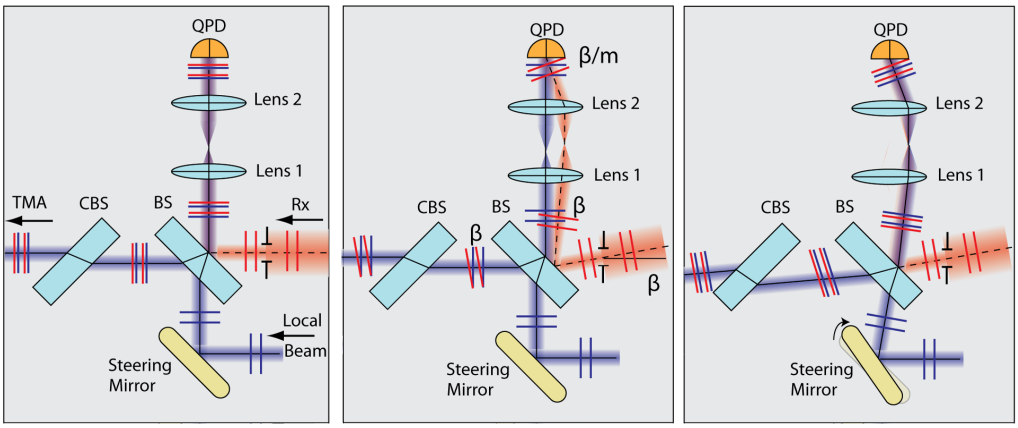

Figure 3.21: Left: Nominal configuration, where outgoing and incoming beam are parallel. **Middle**: Incoming beam is tilted by β, which results in a wavefront tilt by β/m at the QPD, beams are non-parallel. **Right**: Steering mirror rotates such that DWS is kept close to zero and outgoing and incoming beam are parallel.

It is noteworthy that the received light at the spacecraft is an almost spherical wave with 200 km phase front radius of curvature and a waist radius of about 27 m. Only a small fraction is cut out, therefore, the phase front is assumed to be almost flat and a plane wave approximation on the optical bench is justified. Due the fact that Gaussian beams are almost spherical in the far-field, the propagation direction of the light is to first order independent on transmitter rotations. Thus, transmitter rotations (rotations of the distant spacecraft) do not change the received wavefront direction in fig. 3.21. This topic is treated in detail in sec. 3.5.1.
When the control loop is closed, the attitude of the steering mirror necessary to obtain zero DWS signal gives precise information on the spacecraft attitude w.r.t. the LOS. These data will be collected as part of the science data and used in the on-ground processing.

3.4.7 Compensation Beamsplitter

A problem arises due to the fact that the optical pathlength through a beamsplitter is dependent on the incidence angle on the beamsplitter.
Placing a beamsplitter or just a glass plate with a tilt of α_0 in an optical path will in general result in a lateral shift of the transmitted beam as well as in a change of phase (or accumulated optical pathlength). The pathlength effect can be computed easily using figure 3.16. The geometrical pathlength $\mathrm{GPL}(\alpha_0)$ through a beamsplitter is given in equation (3.92). If this distance is projected onto the original ray direction, the equivalent pathlength without beamsplitter $c_{\mathrm{BS}}^{\mathrm{ao}}(\alpha_0)$ is obtained (eq. (3.93)). All other paths are common. If the ray is tilted by α w.r.t. the optical axis, the optical pathlength difference due to the beamsplitter is

$$\Delta p = n_{\mathrm{BS}} \cdot \mathrm{GPL}(\alpha_0 + \alpha) - n_{\mathrm{vac}} \cdot c_{\mathrm{BS}}^{\mathrm{ao}}(\alpha_0 + \alpha). \tag{3.139}$$

For the orthogonal s-direction, the beam may be deflected by an angle β. For the beamsplitter, the refraction angle $\arcsin(\sin(\beta)/n_{\mathrm{BS}})$ has to be used, while without beamsplitter, the angle is just β. The contribution is

$$\Delta s = n_{\mathrm{BS}} \cdot \frac{\mathrm{GPL}(\alpha_0)}{\cos(\arcsin(\sin(\beta)/n_{\mathrm{BS}}))} - n_{\mathrm{vac}} \cdot \frac{c_{\mathrm{BS}}^{\mathrm{ao}}(\alpha_0)}{\cos(\beta)}. \tag{3.140}$$

The lateral shift has no effect in the case of plane waves and a beamsplitter with zero wedge angle. Using a series expansion one can obtain a combined equation for

the optical pathlength change due to a beamsplitter:

$$\begin{aligned}\Delta\mathrm{OPL}(\alpha_0,\,\alpha) = \;& c_{\mathrm{BS}} \cdot \left(n_{\mathrm{BS}} \sqrt{1 - \sin(\alpha_0)^2 / n_{\mathrm{BS}}^2} - \cos(\alpha_0) \right) \\ & + \alpha \cdot c_{\mathrm{BS}} \cdot \frac{\sin\left(\alpha_0 - \arcsin(\sin(\alpha_0)/n_{\mathrm{BS}})\right)}{\sqrt{1 - \sin(\alpha_0)^2 / n_{\mathrm{BS}}^2}} \\ & + \frac{1}{2}\alpha^2 \cdot c_{\mathrm{BS}} \cdot \left(\cos(\alpha_0) - \frac{n_{\mathrm{BS}}^2 \cdot \cos(\alpha_0)^2}{\sqrt{n_{\mathrm{BS}}^2 - \sin(\alpha_0)^2}^3} + \frac{\sin(\alpha_0)^2}{\sqrt{n_{\mathrm{BS}}^2 - \sin(\alpha_0)^2}} \right) + O[\alpha^3] \\ & - \frac{1}{2}\beta^2 \cdot c_{\mathrm{BS}} \cdot \left(\cos(\alpha_0) + \frac{\sin(\alpha_0)^2 - 1}{n_{\mathrm{BS}} \sqrt{1 - \sin(\alpha_0)^2 / n_{\mathrm{BS}}^2}} \right) + O[\beta^4]. \end{aligned} \tag{3.141}$$

Evaluation of the formula for a 5 mm BK7 beamsplitter with $\pm 45°$ tilt angle provides

$$\begin{aligned}\Delta\mathrm{OPL} = \;& 3.116\,\mathrm{mm} \pm 1.65639\,\mu\mathrm{m/mrad} \cdot \alpha + 1.50\,\mathrm{nm/mrad}^2 \cdot \alpha + O[\alpha^3] \\ & - 0.83\,\mathrm{nm/mrad}^2 \cdot \beta^2 + O[\beta^4], \end{aligned} \tag{3.142}$$

which is compared to raytracing results in section 3.6.7. The constant offset is unimportant[16], because the LRI measures only length changes. For a beam tip the coupling into length change is sufficiently small. The angular dependency for beam tilts can be decreased by placing a second beamsplitter, which is rotated by 90°. In the sum of both contributions the linear term cancels, because the sign of the linear term is dependent on the beamsplitter orientation. However, the constant offsets and quadratic terms add up.

In figure 3.22 the different pathlengths for the LRI setup are depicted: on the left side for a non-tilted beam traveling along the optical axis, while on the right side a beam tilt of $-\alpha$ is used. The local beam is transmitted through the substrate and is interfering with the received light from the aperture at the interference point (IP in figure 3.22). In the nominal (and simplified) case, the phase difference of the local beam and received beam at this point is measured by the photodiode, because the remaining distance to the QPD is common to both beams. Most of the local beam light at the IP is reflected towards the TMA. The light passes a second time through the beamsplitter substrate and accumulates extra pathlength due to the distance s and some vacuum propagation over t. If the beam is initially tilted by $-\alpha$, the tilt at the compensation beamsplitter is $+\alpha$ yielding different angles in the beamsplitter and a distance s'. Afterwards, the beam travels towards the TMA. The second beamsplitter also compensates the lateral shift introduced by the first beamsplitter, which is actually not required.

[16] The term becomes interesting, if fluctuations of the beamsplitter thickness and refractive index due to temperature are analyzed.

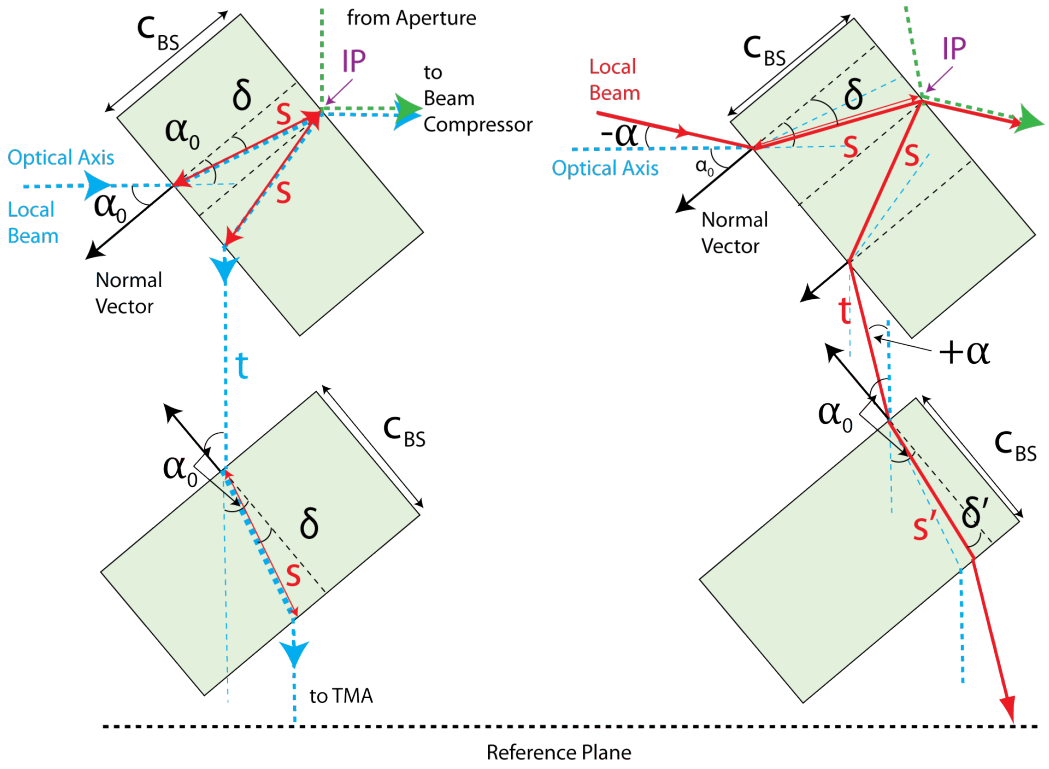

Figure 3.22: Working principle of the compensation plate. **Left**: Local beam has no tilt and travels along the optical axis. **Right**: Local beam has a tilt of $-\alpha$.

The interesting distance is the one between IP and the reference plane. One can simplify the drawing (figure 3.22) to the schematic shown in fig. 3.23. The path t is parallel to the initial ray and can be swapped with s'. The additional phase has to be gained on the distance

$$s + s' = \Delta\mathrm{OPL}(\alpha_0, -\alpha) + \mathrm{OPL}(\alpha_0, +\alpha), \tag{3.143}$$

which has no linear term. Furthermore, the distance between both beamsplitters is unimportant in case of zero-wedged components.

The backside of the recombination beamsplitter and both sides of the compensation plate should have an anti-reflective coating to minimize undesired reflections.

An alternative approach to decrease the influence of angle-dependent pathlength changes in the beamsplitter is to reduce the tilt α_0 of the beamsplitter.

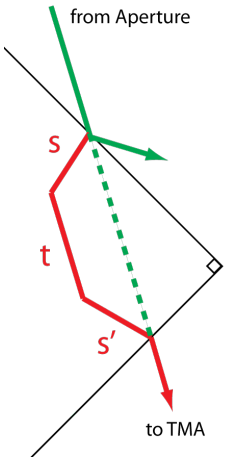

Figure 3.23: Detour through beamsplitter and compensation plate

The linear term magnitude is approximately proportional to α_0. Decreasing α_0 would also decrease the astigmatism, but the linear term might be still too large.

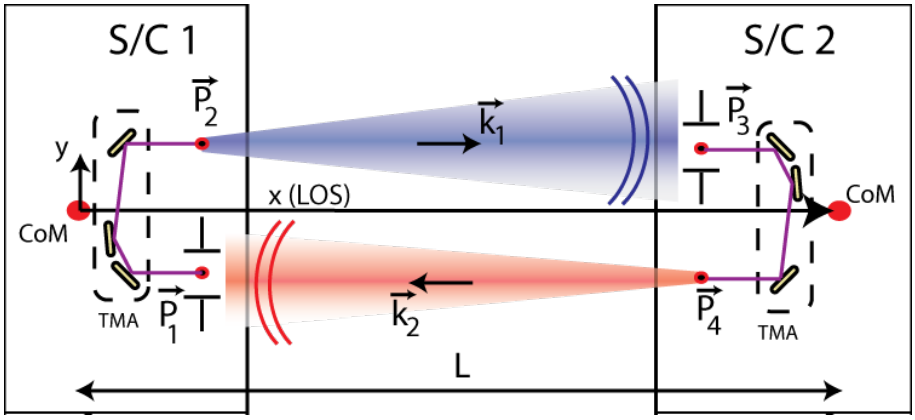

Figure 3.24: Simplified model of the two spacecrafts.

3.5 Simplified LRI Model

The LRI measures the distance between two spacecraft, which are separated by about 200...300 km. If each satellite is assumed to be a rigid body, each has physically six degrees of freedom. In addition, each of the steering mirrors provide two angles, which can be adjusted. Furthermore, the optical bench can introduce further errors in the optical pathlength or the beam direction.
It is advisable to separate this complex system into smaller subsets, which can be understood more easily.
In the first subsection, the far-field behavior of a Gaussian beam is analyzed. The power of the top hat beams on each spacecraft and the propagation direction of the beams are estimated. Also the phase error at a distant aperture is derived, for example if the steering mirror does not guide the outgoing beam perfectly to the distant spacecraft. Finally, a model for the measured phase in a racetrack configuration accounting for the S/C attitude and the steering mirror state is presented, whereas optical bench or TMA construction errors are neglected.
In the second subsection (3.5.2) a simplified model for round-trip measurements including the optical bench is presented. Based on this model, a particular optical bench setup is simulated in detail in section 3.6.

3.5.1 Inter-Satellite Propagation

Each satellite receives light at an aperture and sends out a Gaussian beam. We assume that each spacecraft has a receive aperture for the entering beam at center $\vec{P}_1$ and $\vec{P}_2$, as depicted in figure 3.24. $\vec{P}_2$ and $\vec{P}_4$ are virtual points which are placed on the transmitted beam. The position and purpose of these points will be explained later. If the DWS control loop and the optical bench is working on both spacecrafts without any disturbances, the propagation directions $\vec{k}_1$ and $\vec{k}_2$ are anti-parallel regardless of the attitude of both spacecrafts.
The coordinate system origin is co-located with the CoM of S/C 1 and aligned with the LOS. Thus, each satellite has 3 degrees of freedom (yaw, pitch and roll)[17]. In addition the inter-satellite distance L can change.

Top hat beam power

An interesting quantity for the interferometer is the power of the top hat beam on each spacecraft, because it influences the contrast of the interferometer and the

[17] roll: rotation around LOS; yaw: rotation around z-axis in fig. 3.24

signal level at the photodiode. The power of the top hat beams is equal to the power collected by apertures at $\vec{P}_1$ and $\vec{P}_3$. For the computation of the collected power, the intensity at the apertures is required. In case of the intensity at S/C 2 (S/C 2 is the receiver, RX) a misalignment of S/C 1 (transmitter, TX) results in a drop of intensity, as one can see in figure 3.25. A misalignment of the receiver has only a small influence.

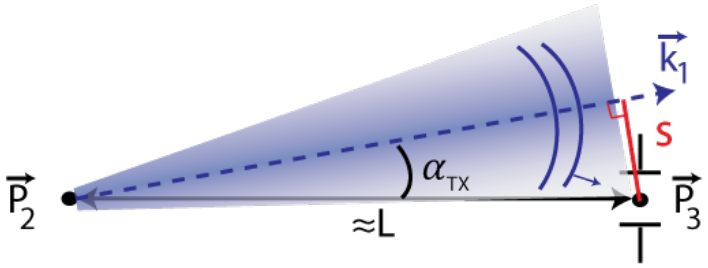

Figure 3.25: Tilted Gaussian beam in the far-field.

Recall that the electric field of a Gaussian beam with z-propagation direction can be written as [Saleh & Teich, 1991, eq.3.1-7]

$$E(x,y,z) = A_0 \frac{w_0}{w(z)} e^{-\frac{x^2+y^2}{w(z)^2}} e^{-i(k\cdot z + k\frac{x^2+y^2}{2R(z)} - \zeta(z)/k)}, \tag{3.144}$$

with Gouy phase

$$\zeta(z) = \arctan\left(\frac{z}{z_0}\right). \tag{3.145}$$

The intensity can be rewritten in normalized form as [Saleh & Teich, 1991, eq.3.1-15]

$$I(x,y,z) = |E(x,y,z)|^2 = P\frac{2}{\pi\omega(z)^2} e^{-2\left(\frac{x^2+y^2}{\omega(z)^2}\right)}. \tag{3.146}$$

The transverse distance

$$s \approx \sin(\alpha_{TX}) \cdot L \approx \alpha_{TX} \cdot L \tag{3.147}$$

to the evaluation point $\vec{P}_3$ in fig. 3.25 is equal to $x^2 + y^2$ in eq. (3.144). Thus, one can write the received intensity I_{RX} as

$$I_{\mathrm{RX}}(\alpha_{\mathrm{TX}}) \approx P_{\mathrm{TX}} \frac{2}{\pi\omega_{\mathrm{RX}}^2} e^{-2\left(\frac{\alpha_{\mathrm{TX}}\cdot L}{\omega_{\mathrm{RX}}}\right)^2}, \tag{3.148}$$

where ω_{RX} is the approximately 30 m spot size radius at the receiver spacecraft and L the satellite separation. The spot size ω_{RX} depends on the initial waist size w_0 and on the spacecraft separation. The transmitter power P_{TX} is assumed to be 15 mW and α_{TX} is the misalignment angle of the transmitter w.r.t. the LOS. Since Gaussian beams are circularly symmetric around their propagation axis, the pitch and yaw rotation of the spacecraft have the same effect, while roll has no influence in the far field in this derivation. The power collected by the aperture and hence the power of the flat top beam on the optical bench is then given approximately by the product of intensity and effective area of the aperture:

$$P_{\mathrm{RX}}(\alpha_{\mathrm{TX}}, \alpha_{\mathrm{RX}}) = \int_{\mathrm{Aperture}} I_{\mathrm{RX}}\, \mathrm{d}a \approx I_{\mathrm{RX}}(\alpha_{\mathrm{TX}}) \cdot \pi r_{\mathrm{AP}}^2 \cdot \cos(\alpha_{\mathrm{RX}}), \tag{3.149}$$

although an integration would be more precise, but disproportionately expensive in terms of computation time, considering that for the 200 km spacecraft separation the intensity is almost constant over the small receive aperture area.
The received beam power as a function of transmitter misalignment for different spacecraft separations is shown in fig. 3.26. The sharp drop starting at approximately 100 μrad underlines the necessity for a steering mirror to compensate for spacecraft attitude jitter, which is assumed to be larger than 100 μrad, and for static misalignments between the LRI and spacecraft, which might be caused by the vibration during the S/C launch.

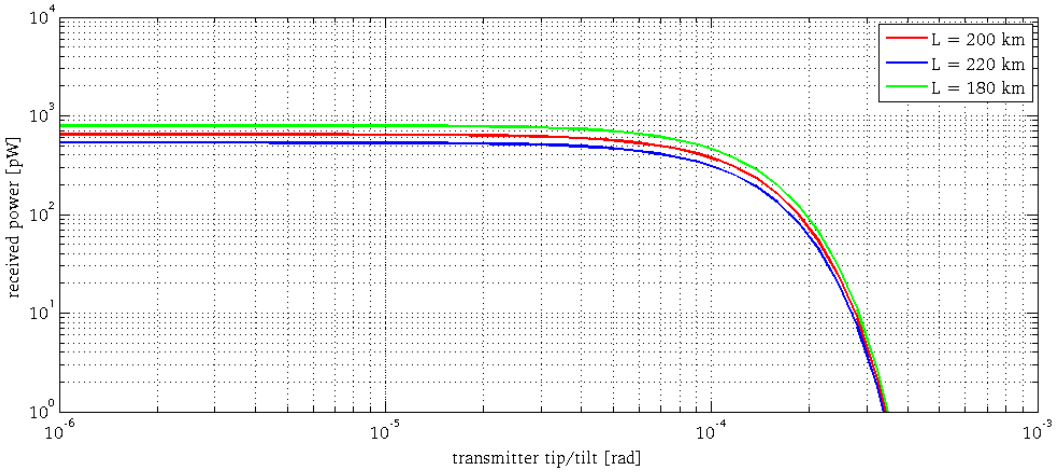

Figure 3.26: Light power received at an apperture with radius $r_{\mathrm{AP}} = 4\,\mathrm{mm}$, transmitted power of $P_{\mathrm{TX}} = 15\,\mathrm{mW}$ and waist size of $w_0 = 2.5\,\mathrm{mm}$ for three different spacecraft separations.

Top hat beam direction

The (local) propagation direction $\vec{k}_{\mathrm{loc}}$ of the light, e.g. at the receive apertures, is not parallel to the $\vec{k}_{1,2}$ vectors, because Gaussian beams have spherical wavefronts in the far field. This effect was indicated with the small blue vector in fig. 3.25. We assume the propagation direction to be normal to the wavefront of the light, which holds for isotropic loss-free media [Mayer, 1993, p. 33]. Under this assumption, the normalized (local) propagation direction at the aperture center can be computed by the normalized gradient of the phase:

$$\vec{k}_{\mathrm{loc,norm}}(x,y,z) = \frac{(\frac{\partial\varphi}{\partial x}, \frac{\partial\varphi}{\partial y}, \frac{\partial\varphi}{\partial z})^{\mathsf{T}}}{\left|(\frac{\partial\varphi}{\partial x}, \frac{\partial\varphi}{\partial y}, \frac{\partial\varphi}{\partial z})^{\mathsf{T}}\right|}, \tag{3.150}$$

where $\varphi = \varphi(x,y,z)$ is the phase of the Gaussian beam and the derivatives are evaluated at the aperture center.
Instead of the phase one can also use a phase-derived optical pathlength ρ, which is proportional to the phase:

$$\rho := \varphi\frac{\lambda}{2\pi}. \tag{3.151}$$

For a Gaussian beam with propagation direction along z and with an offset z_{off} in the waist position, eq. (3.144) yields

$$\rho(x,y,z) = z + \frac{x^2+y^2}{2\cdot R(z-z_{\mathrm{off}})} - \lambda\frac{\arctan((z-z_{\mathrm{off}})/z_r)}{2\pi}, \tag{3.152}$$

where a refractive index of 1.0 is assumed. According to fig. 3.24 and 3.25, an expression for an arbitrary beam direction $\vec{k}$ is preferred, where the beam originates at $\vec{o}$ and the evaluation point is $\vec{x}$. A straight forward derivation leads to

$$\rho(\vec{o},\vec{k},\vec{x},w_0,z_{\text{off}}) = (\vec{x}-\vec{o})\cdot\vec{k} + \frac{|\vec{x}-\vec{o}|^2 - |(\vec{x}-\vec{o})\cdot\vec{k}|^2}{2\cdot R((\vec{x}-\vec{o})\cdot\vec{k}-z_{\text{off}})} - \frac{\lambda}{2\pi}\arctan\left(\frac{(\vec{x}-\vec{o})\cdot\vec{k}-z_{\text{off}}}{z_r}\right), \tag{3.153}$$

where the phase front radius of curvature $R(z)$ and the Rayleigh range z_r depend on the waist size w_0. The equation

$$\vec{k}_{\text{loc}}(x,y,z) = \left(\frac{\partial\rho}{\partial x},\frac{\partial\rho}{\partial y},\frac{\partial\rho}{\partial z}\right)^{\mathsf{T}} \tag{3.154}$$

is the non-normalized version of eq. (3.150) and needs to be evaluated. Therefore we assume the configuration shown in fig. 3.25:

$$\vec{P}_2 = \begin{pmatrix}0\\0\\0\end{pmatrix}, \quad \vec{P}_3 = \begin{pmatrix}L\\0\\0\end{pmatrix}. \tag{3.155}$$

The inter-satellite separation is set to $L = 200\,\text{km}$ and a waist size of $w_0 = 2.5\,\text{mm}$ is used. The nominal beam direction $\vec{k}_1 = (1,0,0)^{\mathsf{T}}$ is rotated by an angle u around x (roll), y (pitch) and z (yaw), respectively, with center of rotation at $\vec{P}_2$. The resulting non-normalized local direction of the wavefront at the aperture $\vec{P}_3$ is then

$$\vec{k}_{\text{loc,yaw}} \approx \begin{pmatrix} 1.0 + \frac{4.26\cdot10^{-9}}{\text{rad}^2}u^2 \\ \frac{8.5\cdot10^{-9}}{\text{rad}}u - \frac{5\cdot10^{-6}}{\text{m}\cdot\text{rad}}u\cdot z_{\text{off}} \\ 0.0 \end{pmatrix}, \tag{3.156}$$

$$\vec{k}_{\text{loc,pitch}} \approx \begin{pmatrix} 1.0 + \frac{4.26\cdot10^{-9}}{\text{rad}^2}u^2 \\ 0.0 \\ -\frac{8.5\cdot10^{-9}}{\text{rad}}u + \frac{5\cdot10^{-6}}{\text{m}\cdot\text{rad}}u\cdot z_{\text{off}} \end{pmatrix}, \tag{3.157}$$

$$\vec{k}_{\text{loc,roll}} = \begin{pmatrix}1.0\\0.0\\0.0\end{pmatrix}, \tag{3.158}$$

where z_{off} is the waist distance from the origin given in meters, while u has units of radians. The results show that in the inertial frame the local wavefront direction on the optical bench is almost parallel to the LOS ($(1,0,0)^{\mathsf{T}}$) even for 1 mrad beam deflection. This means that the direction of the top hat beam is parallel to the LOS and independent of the transmitter and receiver misalignment[18], in contrast to the top hat beam power, which drops rapidly with transmitter misalignment.

Pointing induced phase changes

One should note that the phase and the radius of curvature of the phase fronts at the receive aperture are slightly different in the tilted transmitter compared to the non-tilted transmitter case, because the center of phase front curvature is not co-located with the center of rotation. This introduces a phase change on the receive aperture, if the transmitter steering mirror is rotated. This error shall be investigated.

[18] In a satellite fixed coordinate system the direction of the top hat beam and the LOS is apparently dependent on the satellite rotation.

As before we assume the beam origin at the center of the coordinate system and an aperture in $L = 200\,\mathrm{km}$ distance. The rotation of the beam is described with the rotation matrix $\hat{R}_u$. The phase-derived pathlength error is computed with

$$\delta\rho = \rho(\vec{P}_2, \hat{R}_u \cdot \vec{k}_1, \vec{P}_3, w_0, z_{\mathrm{off}}) - \rho(\vec{P}_2, \vec{k}_1, \vec{P}_3, w_0, z_{\mathrm{off}}). \tag{3.159}$$

For the different rotation axes one obtains

$$\delta\rho_{\mathrm{yaw}} = \delta\rho_{\mathrm{pitch}} \approx \frac{-8.5 \cdot 10^{-4}\mathrm{m}}{\mathrm{rad}^2} \cdot u^2 + \frac{0.5}{\mathrm{rad}^2} \cdot u^2 \cdot z_{\mathrm{off}}, \tag{3.160}$$

$$\delta\rho_{\mathrm{roll}} = 0. \tag{3.161}$$

Due to the circular symmetry of the Gaussian beam, the yaw and pitch direction have the same result, while the roll contribution is zero. In the far-field a Gaussian beam approximates (only) asymptotically a spherical phase front [Saleh & Teich, 1991, fig.3.1-6]. This means that the center of phase front curvature is not exactly at the waist position. Thus, a small phase change at the aperture is obtained, even if the Gaussian beam waist is co-located with the center of rotation ($z_{\mathrm{off}} = 0$). With a waist position $z_{\mathrm{off}} = -z_r^2/L \approx -14\,\mathrm{mm}$ the center of rotation and center of phase front curvature coincide and the coupling vanishes.
A waist distance $z_{\mathrm{off}} = 2\,\mathrm{m}$ from the center of rotation and a beam misalignment of $u = 50\,\mu\mathrm{rad}$ yields a phase-derived pathlength change of 2.5 nm. The u value corresponds to the residual error in the beam pointing, for example, if the DWS loop and steering mirror do not compensate the spacecraft attitude jitter completely or the TMA introduces a deflection. Because the coupling is quadratic, we assume a working point at $50\,\mu\mathrm{rad}$. This means that there is a constant misalignment between LOS and the beam direction by $50\,\mu\mathrm{rad}$. In this case, the coupling factor can be linearized around the working point to

$$\begin{aligned}\delta\rho_{\mathrm{yaw}} = \delta\rho_{\mathrm{pitch}} &\approx \frac{-8.5 \cdot 10^{-11}\mathrm{m}}{\mathrm{mrad}} \cdot u + \frac{0.5 \cdot 10^{-7}}{\mathrm{mrad}} \cdot u \cdot z_{\mathrm{off}} \\ &= -85\mathrm{nm} \cdot \frac{u}{1\,\mathrm{rad}} + 5 \cdot 10^{-5} \cdot z_{\mathrm{off}} \cdot \frac{u}{1\,\mathrm{rad}}.\end{aligned} \tag{3.162}$$

Finally, a jitter $\delta\tilde{u} = 10\,\mu\mathrm{rad}/\sqrt{\mathrm{Hz}}$ causes a phase error equivalent to $1\,\mathrm{nm}/\sqrt{\mathrm{Hz}}$, where $z_{\mathrm{off}} = 2\,\mathrm{m}$ was assumed again. This jitter might be introduced by steering mirror motion. Current stability measurements of the steering mirror (using DWS) in the laboratory experiment showed a residual noise below $10\,\mu\mathrm{rad}/\sqrt{\mathrm{Hz}}$ in the interesting frequency band.

Racetrack phase-derived pathlength

The phase variations at an aperture in the previous subsection were derived for an on-axis Gaussian beam with origin at the coordinate system center. In this section a model for the phase-derived racetrack pathlength ρ_{RT} is established, which can be computed by the sum of the pathlengths of each section (see fig. 3.24):

$$\begin{aligned}\rho_{\mathrm{RT}} =& \rho(\vec{P}_1, \vec{P}_2) + \rho(\vec{P}_2, \vec{k}_1, \vec{P}_3, w_0, z_{\mathrm{off}}) \\ &+ \rho(\vec{P}_3, \vec{P}_4) + \rho(\vec{P}_4, \vec{k}_2, \vec{P}_1, w_0, z_{\mathrm{off}}).\end{aligned} \tag{3.163}$$

If the waist offset z_{off} is zero, the waists of the emitted Gaussian beams are at the origin points $\vec{P}_2$ or $\vec{P}_4$, respectively.

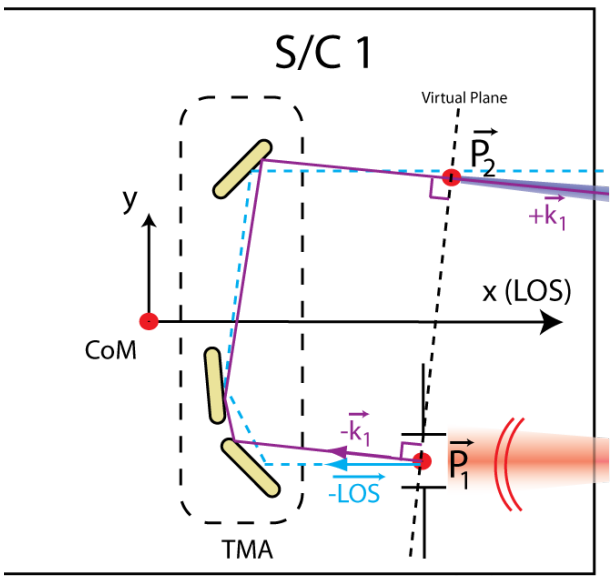

Figure 3.27: Ray propagation through S/C 1 in the case of a deflected beam at the aperture.

The points $\vec{P}_2$ and $\vec{P}_4$ have not been defined yet. To simplify the computation of the pathlength through the TMA, it is advisable to choose $\vec{P}_2$ (and $\vec{P}_4$) such that the points are located in the virtual plane on each S/C as depicted in fig. 3.27 for one S/C. The plane is normal to the ray $-\vec{k}_1$, which starts at the receive aperture and propagates through the TMA. The virtual plane has already been discussed in the section 3.3 about the TMA. It is assumed that the initial ray $-\vec{k}_1$ is not parallel to the LOS, which would be caused in a full scale model, considering the optical bench, by a rotation of the steering mirror. The TMA is assumed here to act as perfect retro-reflector, such that the emitted light from the S/C 1 has a direction $+\vec{k}_1$.
The deflection of the ray direction $-\vec{k}_1$ from the LOS is denoted with the angles h and v. Therefore, the ray direction is a function of these angles

$$\vec{k}_1 = \vec{k}_1(h,\ v) = \vec{k}_1^{h,v} = \hat{R}(h,v) \cdot \vec{k}_{LOS}, \tag{3.164}$$

where $\hat{R}$ is a rotation matrix. The deflection may incorporate undesired deflections due to TMA imperfections, the Optical Bench and the DWS control loop, The point $\vec{P}_2$ (and analogously $\vec{P}_4$) can be computed easily with

$$\vec{P}_2(\vec{k}_1^{h,v}, \vec{P}_1) = 2 \cdot (\vec{k}_1^{h,v} \cdot \vec{P}_1) \cdot \vec{k}_1^{h,v} - \vec{P}_1. \tag{3.165}$$

With this definition, the pathlength from $\vec{P}_1$ to $\vec{P}_2$ (and analogously from $\vec{P}_3$ to $\vec{P}_4$) can be obtained easily (see property list of corner-cubes, item 3, in sec. 3.3.2):

$$\rho(\vec{P}_1, \vec{P}_2) = 2 \cdot \vec{k}_1^{h,v} \cdot \vec{P}_1. \tag{3.166}$$

For simplicity we assume that only S/C 1 can rotate by angles α, β, γ, which correspond to roll, pitch and yaw, respectively. A rotation of the satellite changes the position of $\vec{P}_1$ according to

$$\vec{P}_1^{\alpha,\beta,\gamma} = \hat{R}(\alpha,\beta,\gamma) \cdot \vec{P}_1, \tag{3.167}$$

and the position of $\vec{P}_2$, because $\vec{P}_2$ depends on $\vec{P}_1$. $\hat{R}$ is a rotation matrix.
A problem arises due to the definition of the waist position of the emitted Gaussian beam. The waist position is measured from the beam origin $\vec{P}_2$, which is dependent

on the angles h and v. Thus, the waist position varies in LOS direction with angles h and v. We redefine the waist origin to be referred to the receive aperture by changing

$$z_{\text{off}} \rightarrow z_{\text{off}} - \rho(\vec{P}_1, \vec{P}_2). \tag{3.168}$$

This results in the following round-trip phase-derived pathlength:

$$\begin{aligned}\rho_{\text{RT}}(h, v, \alpha, \beta, \gamma) = \; & \rho(\vec{P}_1^{\,\alpha,\beta,\gamma}, \vec{P}_2(\vec{k}_1^{\,h,v}, \vec{P}_1^{\,\alpha,\beta,\gamma})) \\ & + \rho(\vec{P}_2(\vec{k}_1^{\,h,v}, \vec{P}_1^{\,\alpha,\beta,\gamma}), \vec{k}_1^{\,h,v}, \vec{P}_3, w_0, z_{\text{off}} - \rho(\vec{P}_1^{\,\alpha,\beta,\gamma}, \vec{P}_2(\vec{k}_1^{\,h,v}, \vec{P}_1^{\,\alpha,\beta,\gamma}))) \\ & + \rho(\vec{P}_3, \vec{P}_4) \\ & + \rho(\vec{P}_4, \vec{k}_2, \vec{P}_1^{\,\alpha,\beta,\gamma}, w_0, z_{\text{off}} - \rho(\vec{P}_3, \vec{P}_4)),\end{aligned} \tag{3.169}$$

accounting for spacecraft rotations (α, β, γ) and beam deflections (h, v) on S/C 1. In this derivation the phase at the receive apertures is assumed to be constant over the whole aperture area. Upon spacecraft rotation the aperture center will sweep over the phase front of the large Gaussian beam coming from S/C 2. While varying the beam deflection angles h and v results in a change of the phase and of the intensity at the receive aperture of the distant S/C 2.
The previous equation can be evaluated using an algebraic and symbolic math program (like `Mathematica`). Solving the equations completely numerically or using a raytacing approach potentially introduces numerical errors, because the magnitude of the phase-derived pathlength is in the order of 400 km, while nanometer changes shall be observered[19]. In the following, again a spacecraft separation of $L = 200\,\text{km}$ is assumed, while the receive apertures are placed at

$$\vec{P}_1 = \begin{pmatrix} 1\,\text{m} \\ -0.3\,\text{m} \\ 0 \end{pmatrix}, \quad \vec{P}_3 = \begin{pmatrix} L - 1\,\text{m} \\ +0.3\,\text{m} \\ 0 \end{pmatrix}. \tag{3.170}$$

The CoM and TMA vertex of S/C 1 is at the coordinate system origin. This results in a lateral distance between incoming and outgoing beam of 60 cm. The waist size is again $w_0 = 2.5\,\text{mm}$ and a wavelength of $\lambda = 1064\,\text{nm}$ is used.
For rotations α, β, γ (roll, pitch and yaw) of S/C 1 the following series expansion of the round-trip optical pathlength can be obtained:

$$\begin{aligned}\rho_{\text{RT}}(h = 0, v = 0, \alpha, \beta, \gamma) \approx \; & 400\,\text{km} - 532.0\,\text{nm} \\ & + 4.5 \cdot \frac{10^{-7}\,\text{m}}{\text{rad}^2}\alpha^2 + 5.0 \cdot \frac{10^{-6}\,\text{m}}{\text{rad}^2} \cdot \beta^2 + 5.0 \cdot \frac{10^{-6}\,\text{m}}{\text{rad}^2} \cdot \gamma^2 \\ & + 3.0 \cdot \frac{10^{-6}\,\text{m}}{\text{rad}^2} \cdot \alpha \cdot \beta \\ & + z_{\text{off}} \cdot (0.225\alpha^2 + 2.5\beta^2 + 2.5\gamma^2) \cdot \frac{10^{-11}}{\text{rad}^2}.\end{aligned} \tag{3.171}$$

The first line of eq. (3.171) has a constant term of twice the S/C separation and a term almost equal to $\lambda/2$, which is due to the accumulated Gouy phase. The Gouy phase is a function of the spacecraft separation, which approaches asymptotically $\pi/2$ and changes only very slowly in the far-field. The absolute values in the first line of eq. (3.171) are not accessible, because the LRI can only measure phase changes. The further lines reveal that spacecraft rotations do not introduce significant phase changes at the receive apertures, even if the waist position has an offset of $z_{\text{off}} = 2\,\text{m}$.

[19] covering 14 magnitudes of order, while machine epsilon (for double precision floating point) is in the order of 10^{-16}

In case of a fixed spacecraft ($\alpha = \beta = \gamma = 0$), the following dependency on pointing error v and h is obtained:

$$\rho_{\mathrm{RT}}(h, v, \alpha = 0, \beta = 0, \gamma = 0) \approx 400\,\mathrm{km} - 532.0\,\mathrm{nm} \\ - 8.5 \cdot \frac{10^{-4}\,\mathrm{m}}{\mathrm{rad}^2}(v^2 + h^2) + \frac{z_{\mathrm{off}}}{2} \cdot \frac{1}{\mathrm{rad}^2}(v^2 + h^2). \tag{3.172}$$

The first two terms of eq. (3.172) are the same as in the previous equation, while the last two terms have been observed already in eq. (3.160).
The results (3.171) and (3.172) verify that the phase error introduced by spacecraft rotations or beam deflections are small, which was already obtained in the separated analysis in the previous subsections. However, the model in this subsection accounts for the fact that the beams are laterally displaced w.r.t. LOS. Thus, the effect of S/C roll (angle α) is visible in eq. (3.171), but not in eq. (3.161).
All the analysis in this subsection referred to the simplified four point model depicted in fig. 3.24, which neglects potential optical bench and TMA construction errors. Also refractive index fluctuations between the spacecrafts have not been considered, but they should be small and their contribution negligible.

3.5.2 Round-Trip Optical Bench Model

Here the computation of round-trip pathlength changes in a model consisting of TMA and optical bench is described, where the distant spacecraft is neglected. This model is also used to compute the effect of optical bench construction errors, in other words, the effect of misadjustment and misalignment of components on the round-trip measurements. Various simulation results and the detailed input parameters can be found in the next section 3.6.
A simplified sketch of the setup is depicted in fig. 3.28. The laser light emitted by the master spacecraft laser with initial phase Φ travels along path a and x to the virtual plane. The phase at that point is

$$\epsilon = k(a + x) + \Phi \tag{3.173}$$

with $k = 2\pi/\lambda$. The slave spacecraft acts as a transponder, which sends the light back with the same phase, but different frequency[20]. Therefore, the phase σ can be written as

$$\sigma = \epsilon + \mathrm{offset}, \tag{3.174}$$

where the offset is some phase delay due to the propagation behind the virtual plane. This offset is assumed to be constant and therefore negligible, because the virtual plane is co-moving with the transponder. The measured phase difference at the photodiode is therefore

$$\begin{aligned}\varphi =& \sigma + k(y + b_1) - k(a + b_1) - \Phi = ka' + kx + \Phi' + ky + kb_1 - ka - kb_2 - \Phi \\ =& k(a' - a) + (\Phi' - \Phi) + k(x + y) + k(b_1 - b_2) \approx k(x + y) + k(b_1 - b_2),\end{aligned} \tag{3.175}$$

where the prime ($'$) denotes values that are delayed by the round-trip time. The first two terms are neglected in the last approximation, because they account for the laser phase or laser frequency noise (see section 3.2.2) and for a pathlength noise between beamsplitter and fiber coupler (see section 3.2.3). The contribution of these noise sources has been computed in the corresponding sections.

[20] this may sound contradictory, because the phase is the time integral of frequency. In the context of PLLs the phase is understood as the integrated frequency without the frequency offset, which is introduced in a mixer and desired from the spacecraft master oscillator.

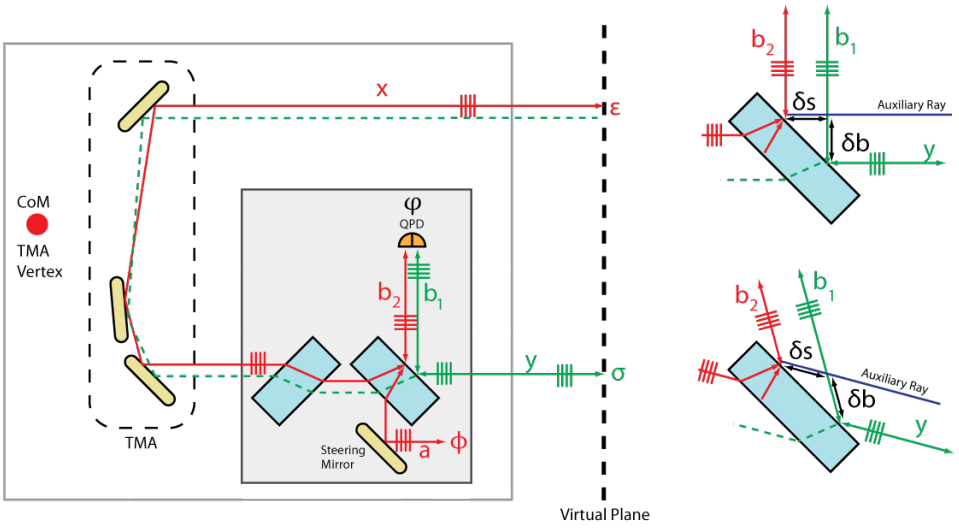

Figure 3.28: Pathlengths used in the round-trip simulation with the optical bench and TMA. The beam compressor is neglected for simplicity in this figure.

A round trip in figure 3.28 has the length $x + y + \delta s$, where δs is the length between the intersection points at the beamsplitter projected onto the beam direction coming from the aperture (see right side on the figure). The lateral offset of the ray segment y, which causes the separation between the dashed and the non-dashed path, has no influence under a plane wave approximation.
It turns out that $b_1 - b_2 = \delta b = \delta s$. This can be seen easily, if an auxiliary ray is used (fig. 3.28, right). The distances δs and δb describe the lateral displacement of two rays before and after reflection at a flat surface. It is well known that reflections at a flat surface do not change the lateral displacement of parallel beams regardless of the incidence angle[21].
Therefore, the measured phase (eq. (3.175)) is proportional to the round-trip length, which is twice the distance between center of mass or corner-cube vertex and virtual plane (property of corner-cube, cf. 3.3.2).
The shifted intersections on the beamsplitter and thus these discontinuities in the racetrack have no effect in case of flat phase fronts. The effect of curved phase fronts was not analyzed. It is therefore recommended to keep the distance between both intersection points small, e.g., by keeping the distances from aperture/steering mirror to the beamsplitter small. This minimizes the effects caused by curved phase fronts, because on small scales the phase fronts are flat (locally flat).

3.6 Simulation Results Optical Bench

3.6.1 Beam Compressor

An IfoCad simulation was written to verify the equations presented in section 3.4.1 about the beam compressor. The parameters of the simulation are given in table 3.1. The values match with those of optical components used in laboratory experiments for the GFO LRI.

[21] equivalent is the statement that the virtual image formed by a flat mirror has the same size as the object [Galen C. Duree, 2011, p.70]

Parameter	Lens 1 value	Lens 2 value
focal length f_1, f_2	81.460 mm	10.200 mm
center thickness c_1, c_2	4.000 mm	5.000 mm
substrate radius	12.700 mm	5.000 mm
type	plano-convex	plano-convex
substrate material	BK7	BK7
substrate refractive index n	1.50663	1.50663
radius of curvature r_1, r_2	41.27047 mm	-5.16767 mm
front focal distance FFD	81.460 mm	6.881 mm
back focal distance BFD	78.805 mm	10.200 mm

Table 3.1: Initial and derived parameters of the beam compressor setup.

The distance between object and image plane d_{OI} is computed by the analytical expression (eq. (3.86) to (3.90)) and is compared to the ray-tracing result. The latter approach uses several rays, which originate at the object plane (see fig. 3.15 in sec. 3.4.2). The image points and image plane are determined by finding a point location that minimizes the distance to all rays (at the back side of lens 2). Using on-axis and off-axis rays allows also the determination of the magnification factor of the beam compressor. The results for a particular value of $d_1 = 120\,\mathrm{mm}$ are tabulated in table 3.2, while the functional dependency $d_3(d_1)$ is (eq. (3.89))

$$d_3(d_1) = -0.0157 \cdot d_1 + 11.4472\,\mathrm{mm}. \tag{3.176}$$

The image plane is in the best case about 1 cm behind the second lens. Positioning of cameras, e.g. for wavefront analysis, is therefore complicated for this lens system. The ray-tracing results and analytical results coincide quite well.

Parameter	Symbol	Analytical	Ray-tracing
distance object to lens 1	d_1	120.000 mm	120.000 mm
magnification factor	m	-0.125215	-0.125212
distance lens 2 to image plane	d_3	9.595741 mm	9.595520 mm
distance object to image plane	d_{OI}	224.282163 mm	224.281950 mm

Table 3.2: Ray-tracing results and analytical results.

In a next step, a beamsplitter with thickness c_{BS}, tilt-angle α_0, and refractive index n_{BS} is placed in the setup. This causes a shift of the image plane in the direction of the ray propagation and a separation into a s- and p-direction. The new image planes are shifted by $\Delta d_3^s = m^2 \Delta d^s$ and $\Delta d_3^p = m^2 \Delta d^p$, respectively. To compensate for this effect, the distance between object and first lens has to be increased in the s-case by Δd^s and in the p-case by Δd^p. These values have been determined analytically (eq. (3.95) and (3.103)) and by ray-tracing. For the determination of Δd_1 values in the ray-tracing procedure, the object plane is shifted around, until the image points matched the value without a beamsplitter. The results for some configurations are shown in table 3.3. Additionally, the lateral shift Δy due to the beamsplitter is given there.
The last line indicates the configuration currently used in the laboratory experiments. Here, the beamsplitter causes a shift by $26\,\mu\mathrm{m}$ and $47\,\mu\mathrm{m}$ of the image plane. Assuming the average between the s- and p-case, the steering mirror should have an offset w.r.t. the nominal object plane of $(1.656 + 3.005)/2\,\mathrm{mm} \approx 2.3\,\mathrm{mm}$ along the optical axis away from the lenses. Furthermore, the optical axis is shifted laterally by $\Delta y = 1.656\,\mathrm{mm}$ at the beamsplitter.

Parameter			Analytic [mm]					Analytic–Ray-tracing [nm]			
n_{BS}	α_0	c_{BS}*	Δd^s	Δd^p	Δd_3^s	Δd_3^p	Δy**	$\delta\Delta d^s$	$\delta\Delta d^p$	$\delta\Delta d_3^s$	$\delta\Delta d_3^p$
1.2	45°	1.0	0.191	0.433	0.003	0.007	0.191	0.000	0.000	0.184	0.405
1.2	45°	6.0	1.148	2.597	0.018	0.041	1.148	0.000	0.000	1.080	2.439
2.0	45°	1.0	0.440	0.669	0.007	0.010	0.440	0.000	0.000	0.417	0.635
2.0	45°	6.0	2.639	4.014	0.041	0.063	2.639	0.000	0.000	2.486	3.775
2.0	30°	6.0	3.872	3.492	0.045	0.055	1.658	0.000	0.000	2.704	3.290
1.507	45°	5.0	1.656	3.005	0.026	0.047	1.656	0.00	0.000	1.561	2.827

Table 3.3: Verification of the analytical model by computing the difference between the analytical solution and the ray-tracing result; *units of mm; **lateral shift Δy due to beamsplitter matched ray-tracing results up to sub-nm

The analytical expression (eq. (3.95) and (3.103)) models the ray-tracing result up to nanometer for the image plane. The deviation is assumed to be due to the ray-tracing image-point fitting procedure, but was not investigated deeper.
A further comparison can be done to the Gaussian beam tracing of IfoCad. The beam parameters are transformed at each surface according to the ABCD matrix formalism. For an initial beam with waist $\omega_0 = 2.5\,\mathrm{mm}$ at the object plane and wavelength $\lambda = 1064\,\mathrm{nm}$, the q-parameter is $q \approx 18,45\,\mathrm{m} \cdot i$. The waist position of the exiting beam leaving the second lens is compared to the analytical result in table 3.4.
There is only a small constant deviation in sub-nanometer level between the analytical and q-tracing procedure. Comparing the evolution of the IfoCad q-parameter with analytical transformation leads to the conclusion that the deviations are caused by the numerical machine precision. The deviation of 0.215 nm is even present without beamsplitter, thus the analytic equations did not introduce any errors in this comparison.

Parameter			Analytic*		Difference: Analytic − q-tracing [nm]	
n_{BS}	α_0	c_{BS}*	$d_3^s + \Delta d_3^s$	$d_3^p + \Delta d_3^p$	δ_s	δ_p
No BS			9.596	9.596	0.215	0.215
1.2	45°	1.0	9.599	9.603	0.215	0.215
1.2	45°	6.0	9.614	9.636	0.215	0.215
2.0	45°	1.0	9.603	9.606	0.215	0.215
2.0	45°	6.0	9.937	9.659	0.215	0.215
2.0	30°	6.0	9.641	9.650	0.215	0.215
1.507	45°	5.0	9.622	9.643	0.215	0.215

Table 3.4: Verification of the analytical model by comparing waist positions obtained by analytic model and by IfoCad Gaussian beam tracing; *units of mm for the column(s).

According to the simulation results the analytic model of the shifts Δd^s and Δd^p seems to be correct.

3.6.2 Beam Compressor: Phase Fronts and Spot Size

Interesting for interferometry, especially for the longitudinal and DWS signal computation, is the phase front of the beams propagating through the beam compressor. Taking into account the last line from table 3.4, the difference between the waists in the s- and p-direction is

$$(\Delta d_3^p - \Delta d_3^s) = m^2(\Delta d^p - \Delta d^s) \approx 20\,\mu\mathrm{m}. \tag{3.177}$$

If we assume a photodetector at the waist of the p-direction, the radius of curvature of the phase front for the s-direction at that point is (eq. (3.113)):

$$R_s(z) = m^2(\Delta d^s - \Delta d^p)\left(1 + \frac{m^4 \cdot z_{r,\text{initial}}^2}{m^4(\Delta d^s - \Delta d^p)^2}\right) \approx 4.1\,\text{km}. \tag{3.178}$$

On a photodetector with radius $r = 1\,\text{mm}$ this results in a phase deviation of

$$\delta\rho = R_s(1 - \cos(\arcsin(1\,\text{mm}/R_s))\ ) \approx 0.12\,\text{nm}, \tag{3.179}$$

where the phase is expressed as equivalent optical pathlength. This is sufficiently small considering that the radius of curvature of a Gaussian beam, which travels 200 km, is transformed by the beam compressor to a beam with 3.1 km radius of curvature (eq. (3.110)). The phase front at two different positions is depicted in fig. 3.29. This plot indicates that the effect of phase front distortion due to astigmatism is small compared to other effects like a misplaced detector plane or offsets in the waist position.
The intensity ellipse due to the astigmatism is given by the two spot sizes (eq. (3.114)):

$$\begin{aligned}\omega_p(z) &= m \cdot 2.5\,\text{mm},\\ \omega_s(z) &= \sqrt{\frac{\lambda z_r}{\pi}\left(1 + \frac{z^2}{z_r^2}\right)} = m \cdot \omega_0 \cdot \sqrt{1 + \frac{(\Delta d^s - \Delta d^p)^2}{z_{r,\text{initial}}^2}} \approx m \cdot 2.5\,\text{mm} \cdot (1 + 2.4 \cdot 10^{-9}\,),\end{aligned} \tag{3.180}$$

where m is the beam compressor magnification factor. The spot sizes are almost equal, such that the intensity ellipse can be considered to be circular.
This very basic analysis of astigmatism is more of academic purpose. It shall provide the order of magnitude of astigmatic effects. For later simulations the Gaussian beams are propagated considering effects of general astigmatism. However, also there the effect of astigmatism did not introduce significant deviations from the expected behavior or from expected results.

3.6.3 Beam Compressor: Tolerances

So far the results presumed an accuracy of nanometer or even computer machine precision for the parameters of the beam compressor. In reality the parameters like focal length or distances are known in the best case up to micrometers. The effect of misadjustments in the system can be evaluated using eq. (3.116f.), which are given for simplicity for the thin lens derivation and for distances between principal points. With the lenses given in table 3.1 and the following parameters (see fig. 3.13):

$$\begin{aligned} d_1 &= 120\,\text{mm},\\ d_2 &= f_1 + f_2 = 91.66\,\text{mm},\\ d_3(d_1) &= 9.59574\,\text{mm} \qquad \text{(eq. (3.85))},\\ m &= -f_2/f_1 = -0.125215, \end{aligned} \tag{3.181}$$

the effect of parameter deviations on an initial ray $\vec{r} = (y, \theta)^\mathsf{T}$ can be derived:

$$\begin{aligned} y_\text{final} \approx m \cdot y + y \cdot (&-0.72 \cdot \delta d_2 + 2.26 \cdot \delta f_1 - 11.55 \cdot \delta f_2) \cdot \frac{1}{\text{m}}\\ &+ \theta \cdot (-0.12 \cdot \delta d_1 - 0.028 \cdot \delta d_2 - 7.98 \cdot \delta d_3 + 0.27 \cdot \delta f_1 + 7.07 \cdot \delta f_2), \end{aligned} \tag{3.182}$$

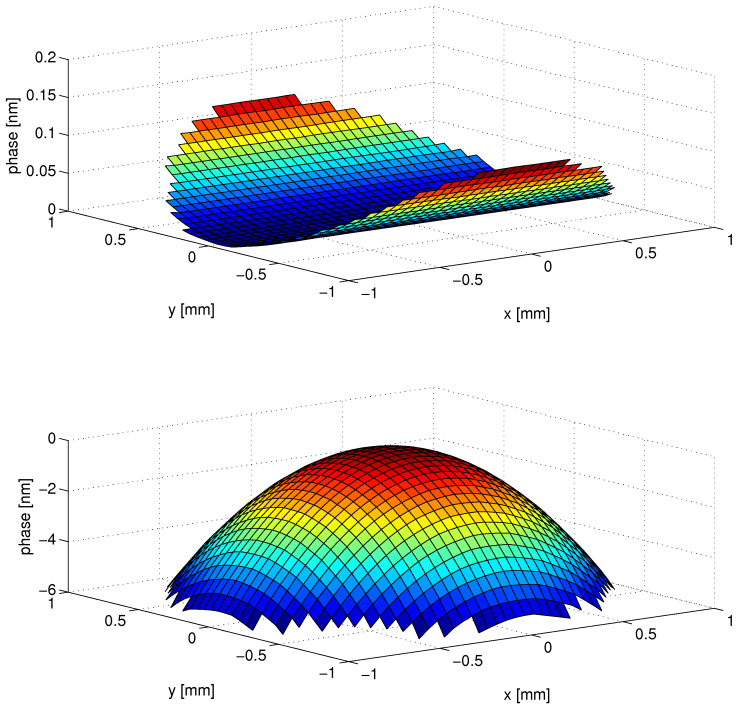

Figure 3.29: Top: Phase front at the waist in p-direction; **Bottom**: Phase front at 1 mm distance to the p-waist.

$$\theta_{\text{final}} \approx 1/m \cdot \theta + \theta \cdot (46.38 \cdot \delta d_2 - 144.42 \cdot \delta f_1 + 736.58 \cdot \delta f_2) \cdot \frac{1}{\text{m}} + y \cdot 1203.53 \cdot (\delta d_2 - \delta f_1 - \delta f_2) \cdot \frac{1}{\text{m}^2}. \tag{3.183}$$

The length units are meters and the angle θ has units of radian. From the first equation one can see that deviations in the focal length of lens 2 (δf_2) are causing ray offsets or equivalent beamwalk on the photodiode upon beam deflections θ. An initial lateral ray offset is suppressed by the magnification $|m| \approx 1/8$. Assuming an error of 10 μm for all parameters and a tilt angle $\theta = 1$ mrad, the offset on the photodiode due to the deflection would be roughly $(7.98 + 7.07) \cdot 10\,\mu\text{m} \cdot 1\,\text{mrad} \approx 150\,\text{nm}$, which is already hardly detectable. If the errors are higher, d_1 or d_3 could be tuned to minimize the coupling. However, this minimizes only the B-matrix element of the ABCD matrix. All other elements might have changed.
The same analysis can be done for a Gaussian beam with initial q-parameter

$$q_{\text{initial}} = z_0 + i\frac{\pi}{\lambda}(2.5\,\text{mm} + \Delta x)^2$$

by using equation (3.117). The formula can be expanded in Taylor series to first order for small δ-values. When products of δ are neglected, the final beam waist

position, which is the real part of the q-parameter, can be written as

$$\begin{aligned} z_{0,\text{final}} \approx\ & 1.00 \cdot \delta d_3 + 0.016 \cdot \delta d_1 - (\delta d_2 - \delta f_1 - \delta f_2) \cdot 804.0 \\ & + z_0 \cdot 0.016 + z_0 \cdot (0.18 \cdot \delta d_2 - 0.57 \cdot \delta f_1 + 2.89 \cdot \delta f_2) \cdot \frac{1}{\text{m}} \\ & + z_0^2 \cdot (\delta d_2 - \delta f_1 - \delta f_2) \cdot 2.36 \cdot \frac{1}{\text{m}^2} \\ & - \Delta x \cdot (\delta d_2 - \delta f_1 - \delta f_2) \cdot 1.28 \cdot 10^6 \cdot \frac{1}{\text{m}} \\ & - \Delta x^2 \cdot (\delta d_2 - \delta f_1 - \delta f_2) \cdot 7.72 \cdot 10^8 \cdot \frac{1}{\text{m}^2}. \end{aligned} \tag{3.184}$$

The term $\delta d_2 - \delta f_1 - \delta f_2$ is important. As one can see in the first line, a good knowledge of the focal lengths and a positioning of the lenses providing $\delta d_2 - \delta f_1 - \delta f_2 \approx 10\,\mu\text{m}$ would still lead to a shift in the waist of 8 mm. In this case an uncertainty of $10\,\mu\text{m}$ in the initial waist size would contribute additionally 0.12 mm. The initial waist position has only a small influence.
For completeness the final Rayleigh range, which is the imaginary part of the q-parameter, is given by:

$$\begin{aligned} z_{r,\text{final}} \approx\ & + 0.28\,\text{m} + 3.36 \cdot \delta d_2 - 10.46 \cdot \delta f_1 + 53.37 \cdot \delta f_2 \\ & + \Delta x \cdot 231.47 + \Delta x \cdot (2.69 \cdot \delta d_2 - 8.37 \cdot \delta f_1 + 42.70 \cdot \delta f_2) \cdot \frac{10^3}{\text{m}} \\ & + \Delta x^2 \cdot (0.46 - 1.67 \cdot \delta f_1 + 8.54 \cdot \delta f_2) \cdot \frac{10^6}{\text{m}^2}, \end{aligned} \tag{3.185}$$

where only leading terms have been considered.
The simulation results show that it is difficult to position the beam waist to better than a few millimeter with the beam compressor. Measurements of the waist position are complicated. The spot size of the local beam is only approximately $312.5\,\mu\text{m}$ at the photodiode and it is not changing rapidly. A wavefront analysis might be an option to determine the waist position if required.
The subsequent sections will show that these parameter deviations have only a minor effect on the overall LRI performance.

3.6.4 DWS Coupling Factors

The Differential Wavefront Sensing signal changes upon rotation of the steering mirror by angles $v_{\text{SM}}, h_{\text{SM}}$ and upon change of the incidence angles $v_{\text{RX}}, h_{\text{RX}}$ of the beam at the receive aperture. The angles v_{RX} and h_{RX} can be changed in an laboratory experiment by rotating the optical bench for example with a hexapod, which is a six degree of freedom rotation and translation platform. The DWS coupling factors are the derivatives of the DWS signal w.r.t. the rotation angles. They have been measured (by my colleague Daniel Schütze, AEI) in a laboratory experiment for a particular optical bench setup and are tabulated in table 3.5. Assuming an effective DWS amplification[22] of

$$\frac{m_{\text{DWS}}}{m} = 9900\,\text{rad/rad}, \tag{3.186}$$

yields with the beam compressor magnification $|m| \approx 1/8$ a DWS magnification of

$$m_{\text{DWS}} = 9900\,\text{rad/rad} \cdot m \approx 1237.5\,\text{rad/rad}, \tag{3.187}$$

where this is the ratio of phase of electric photodiode signal to the wavefront tilt directly before the photodiode. The DWS factors are in general dependent on the

[22] ratio of the phase of electric photodiode signal to the wavefront tilt before the beam compressor

Coupling	Measured in rad/rad	Theory	Fit* in rad/rad
$\partial \mathrm{DWS}_v/\partial v_{\mathrm{RX}}$	≈ 9900	m_{DWS}/m	9900*
$\partial \mathrm{DWS}_h/\partial h_{\mathrm{RX}}$	≈ 9900	m_{DWS}/m	9900*
$\partial \mathrm{DWS}_v/\partial v_{\mathrm{SM}}$	≈ 13500	$\sqrt{2}\cdot m_{\mathrm{DWS}}/m$	14000
$\partial \mathrm{DWS}_h/\partial h_{\mathrm{SM}}$	≈ 18000	$2\cdot m_{\mathrm{DWS}}/m$	19800
$\partial \mathrm{DWS}_v^{\mathrm{PM}}/\partial v_{\mathrm{SM}}$	-	$2\cdot\sqrt{2}\cdot m_{\mathrm{DWS}}/m$	28000
$\partial \mathrm{DWS}_h^{\mathrm{PM}}/\partial h_{\mathrm{SM}}$	-	$4\cdot m_{\mathrm{DWS}}/m$	39600

Table 3.5: Measured DWS coupling factors and theoretical equations. The last two lines indicate the values, which should be used for the DWS loop gain computation. *: Fit means here, that $m_{\mathrm{DWS}}/m = 9900\,\mathrm{rad/rad}$ was used to compute the remaining rows using the formula given in the *Theory*-column.

beam parameters (see eq. (3.129)). To achieve such a magnification, the local beam radius should be roughly 1.5 mm before the beam compressor. Unfortunately, the local beam size was not measured at that time, but the table 3.5 should clarify the different pre-factors. The cross terms like $\partial \mathrm{DWS}_h/\partial v$ are usually kept small, because the steering mirror or photodiode is aligned by minimizing this terms. This yields parallel v-axes for the photodiode and steering mirror.
The current phasemeter implementation in the laboratory experiments uses internally non-averaged DWS values, meaning that the factor $1/2$ *is missing in eq. (3.127). For the computation of the DWS control loop gain in the setup, the coupling factors* $\partial DWS_v^{PM}/\partial v_{SM}$ *and* $\partial DWS_h^{PM}/\partial h_{SM}$ *from table 3.5 should be used.*

3.6.5 Nominal Optical Bench Configuration

A receiver tilt with angle h corresponds to a S/C yaw rotation, while receiver tip with angle v is equivalent to a S/C pitch motion.
A simulation of the GFO LRI instrument was written in the IfoCad framework and is depticed in fig. 3.30. The parameters of the beam compressor and beamsplitter are given in section 3.6.1. The simulated photodiode has a radius of $r_{\mathrm{PD}} = 0.5\,\mathrm{mm}$ and a slit (gap) width of $d_g = 30\,\mu\mathrm{m}$.
The local beam is a Gaussian beam with waist size $w_0 = 2.5\,\mathrm{mm}$ and 15 mW power. The beam transformations are performed similar to the rules for normal Gaussian beams (eq. (3.107)), but are extended to account even for general astigmatism, although effects due to non-orthogonal astigmatism were not derived or analyzed in detail in this thesis [23].
The simulation of the received flat top beam is complicated. An accurate simulation could be done by the decomposition of the electric field at the aperture into high-order Gaussian modes and propagation of these. This feature has not been implemented in IfoCad yet. Therefore, the top hat beam is simulated with a modified Gaussian beam, which has a waist size equal to the 4 mm aperture radius. The waist position is shifted by 11.16 mm from the aperture to provide a phase front radius of curvature equal to the inter-satellite distance of $\approx 220\,\mathrm{km}$. All beam transformations are performed according to a proper general astigmatic Gaussian beam.
Only the beam intensity, when computed at the photodiode, is changed to

$$I(x,y,z) = \frac{P_0}{\pi w(z)^2} e^{-2\left(\frac{x^2+y^2}{(w(z)\cdot 1.06)^2}\right)^{20}}, \tag{3.188}$$

[23] implementation of general astigmatism in IfoCad is ongoing by Evgenia Kochkina, Albert-Einstein-Institute, Hannover

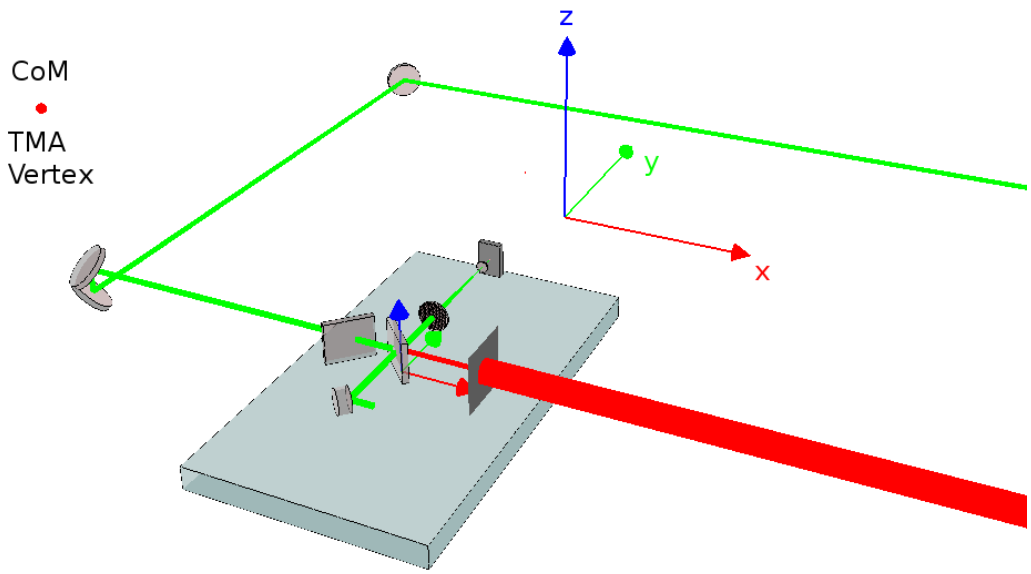

Figure 3.30: IfoCad 3d model of the setup: a virtual plane on the right side (not shown) serves as initial surface for the red beam and as the end surface for the green beam, as described in section 3.5.2.

which approximates a top hat shape due to the additional 20th power (see *received beam amplitude*, fig. 3.31 top-right plot). The factor 1.06 is an empirical small correction to obtain a total power of P_0 for the intensity function[24]. An ordinary rectangular intensity function would introduce difficulties for the adaptive numerical integrator in IfoCad, because the function is discontinuous.
Usage of the modified Gaussian beam neglects the fact that diffraction rings distort the intensity and phase front, which is a major drawback of the method. Furthermore, this beam does not satisfy the wave equation and its propagation is not described correctly therefore. However, it models the desired phase and intensity distribution at the photodiode in the theoretical undisturbed case.
The location of the steering mirror on the optical bench in this model is corrected for the transverse shift and for the shift in the image plane due the beamsplitter.
As first step, the performance of the nominal beam compressor is analyzed.
The resulting values for 8 simulation scenarios are given in table 3.6, whereas in each scenario rotations of the transmitter S/C (TX), receiver S/C (RX) and steering mirror (SM) along one direction are performed. The rows (a)-(g) contain input parameters. Simulation #1 has perfectly aligned beams along the optical axis of the beam compressor. The rows (0)-(9) show results for pure ray-tracing and provide the angles and position of the rays, when they impinging on the photodiode.
The beamwalk on the detector has a magnitude of a few nanometer and the DPS signal (not shown in table) is therefore almost zero. The receiver tip and tilt (Scenario #2 and #3) influences only the power of the top hat beam and the contrast of interference. The heterodyne efficiency (row 29ff.) is independent of the power levels and stays constant. It is therefore appropriate to evaluate the power, which mainly depends on the transmitter orientation, and the heterodyne efficiency, which mainly depends on receiver misalignment and is given by the overlap integral of both beams, separately. This can be exploited to divide the parameter space for the heterodyne signal amplitude into separate subsets, because it can be obtained from

[24]The area of the top hat deviates by the factor from $\pi w(z)^2$. The analytical solution for the area was quite long, therefore the empirical correction was used.

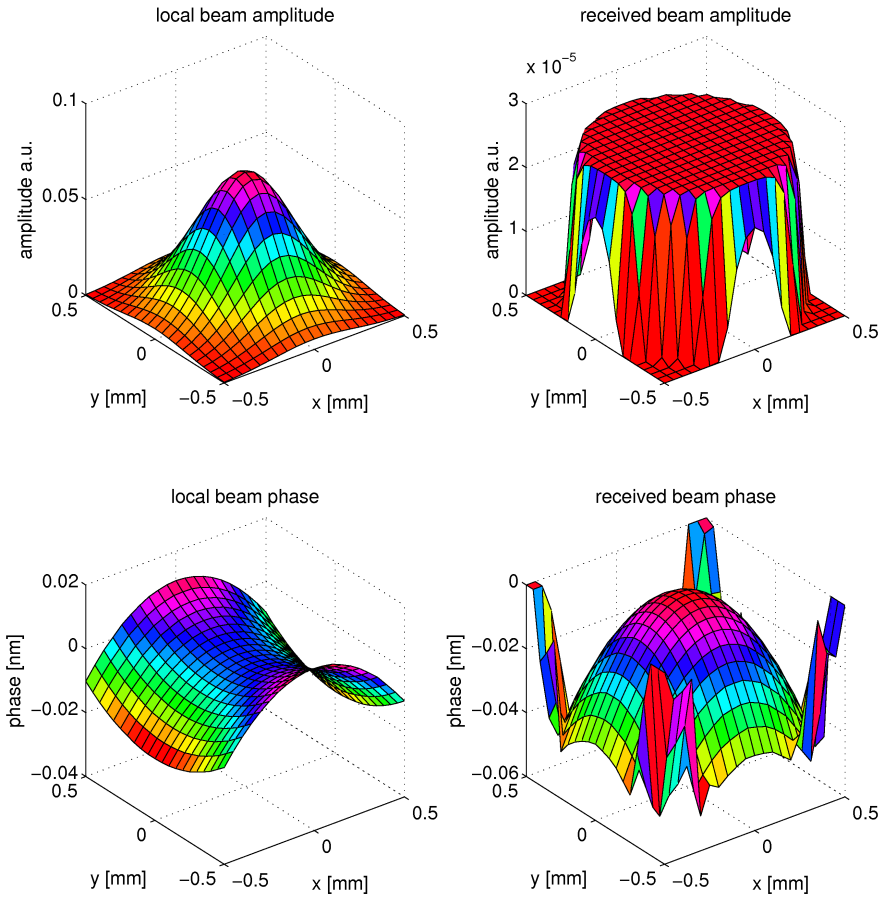

Figure 3.31: Electric field amplitude and phase at the photodetector in the nominal setup.

the power and heterodyne efficiency (eq. (3.122)).
The ray incidence angles (`TB-h, TB-v, LB-h, LB-v`) are basically magnified by the beam compressor magnification m, whereas in case of the steering mirror rotations, the geometric factors (eq. (3.138)) are applied additionally. The DWS signal (rows 13, 14) is obtained by multiplication with $m_{\mathrm{DWS}} \approx 1888$ (eq. (3.131)). In simulation #7 phase wrapping occurred, meaning that the DWS signal became larger than π and was wrapped back into the interval $[-\pi, +\pi)$.
All results are determined at the photodiode, except for the angle between incoming top hat and outgoing Gaussian beam (row 19). In case of a closed DWS control loop, this value should be close to zero.
The electric fields at the photodiode in the nominal case (scenario #1) are shown in fig. 3.31. The received beam has a phase front curvature radius of 3.1 km, while the local Gaussian beam phase front is distorted due to astigmatism.
The results from table 3.6 can also be evaluated on a grid, e.g., for tip and tilt of the receiver. In fig. 3.32 the normalized[25] contrast, which is equal to the square root of the heterodyne efficiency η, is shown for the coherent sum of all quadrants. The cross-like pattern is due to the photodiode gap and vanishes for a single element diode. This fact is non-trivial, because the heterodyne efficiency for each single quadrant has a cross-like pattern.

[25] equal beam power for local and top hat beam

Row	Parameter	Sim #1	Sim #2	Sim #3	Sim #4	Sim #5	Sim #6	Sim #7	Sim #8
a	TX-v [mrad]	0.0000	**0.1000**	0.0000	0.0000	0.0000	0.0000	0.0000	0.0000
b	TX-h [mrad]	0.0000	0.0000	**0.1000**	0.0000	0.0000	0.0000	0.0000	0.0000
c	RX-r [mrad]	0.0000	0.0000	0.0000	**0.1000**	0.0000	0.0000	0.0000	0.0000
d	RX-v [mrad]	0.0000	0.0000	0.0000	0.0000	**0.1000**	0.0000	0.0000	0.0000
e	RX-h [mrad]	0.0000	0.0000	0.0000	0.0000	0.0000	**0.1000**	0.0000	0.0000
f	SM-h [mrad]	0.0000	0.0000	0.0000	0.0000	0.0000	0.0000	**0.1000**	0.0000
g	SM-v [mrad]	0.0000	0.0000	0.0000	0.0000	0.0000	0.0000	0.0000	**0.1000**
0	LB-x [μm]	0.0000	0.0000	0.0000	0.0000	0.0000	0.0000	-0.0115	0.0000
1	LB-y [μm]	0.0000	0.0000	0.0000	0.0000	0.0000	0.0000	0.0000	0.0157
2	LB-h [mrad]	0.0000	0.0000	0.0000	0.0000	0.0000	0.0000	1.5973	0.0000
3	LB-v [mrad]	0.0000	0.0000	0.0000	0.0000	0.0000	0.0000	0.0000	1.1294
6	TB-x [μm]	0.0000	0.0000	0.0000	0.0000	0.0000	-0.0006	0.0000	0.0000
7	TB-y [μm]	0.0000	0.0000	0.0000	0.0000	-0.0006	0.0000	0.0000	0.0000
8	TB-h [mrad]	0.0000	0.0000	0.0000	0.0000	0.0000	0.7986	0.0000	0.0000
9	TB-v [mrad]	0.0000	0.0000	0.0000	0.0000	0.7986	0.0000	0.0000	0.0000
13	DWS-v [mrad]	0.0000	0.0000	0.0000	0.0000	1560.0593	0.0000	0.0000	908.5919
14	DWS-h [mrad]	0.0000	0.0000	0.0000	0.0000	0.0000	1560.0596	124.5294*	-0.1487
19	Angle-InOut [μrad]	0.0000	0.0000	0.0000	0.0000	100.0000	100.0000	200.0000	141.4214
21	TB-RoC-s [km]	3.4660	3.4660	3.4660	3.4660	7.9400	7.9400	3.4660	3.4660
22	TB-RoC-t [km]	3.4660	3.4660	3.4660	3.4660	-6.5574	-6.5574	3.4660	3.4660
23	LB-RoC-s [km]	6.0410	6.0410	6.0410	6.0410	6.0410	6.0410	-2.0677	-6.2763
24	LB-RoC-t [km]	-11.4960	-11.4960	-11.4960	-11.4960	-11.4960	-11.4960	-0.5412	-1.0328
25	DC-Power-4q [mW]	0.6316	0.6316	0.6316	0.6316	0.6316	0.6316	0.6316	0.6316
26	Contrast [%]	0.1410	0.0818	0.0818	0.1410	0.0878	0.0878	0.0059	0.0519
27	DC-Power-TB [pW]	469.6228	157.9346	157.9346	469.6228	469.6243	469.6243	469.6228	469.6228
28	DC-Power-LB [mW]	0.6316	0.6316	0.6316	0.6316	0.6316	0.6316	0.6316	0.6316
29	$\sqrt{}$HetEff-4q [%]	82.9816	82.9816	82.9816	82.9816	51.6787	51.6787	6.2077	30.0729
30	$\sqrt{}$HetEff-A [%]	82.9816	82.9816	82.9816	82.9816	72.5963	72.5958	48.3406	63.3956
31	$\sqrt{}$HetEff-B [%]	82.9816	82.9816	82.9816	82.9816	72.5963	72.5934	48.3650	63.3960

Table 3.6: Input parameters (row a-g) and some resulting values of the modeled optical bench to validate beam compressor performance; TB: flat top beam; LB: local beam; RoC: phase front radius of curvature; HetEff: heterodyne efficiency; *phase wrapping

If the steering mirror angles v_{SM} and h_{SM} are used instead of receiver tilt h_{RX} and tip v_{RX}, the axes of fig. 3.32 are scaled by a factor of 2 in h direction and by $\sqrt{2}$ in the v direction due to the geometrical factors for the steering mirror (eq. (3.138)).

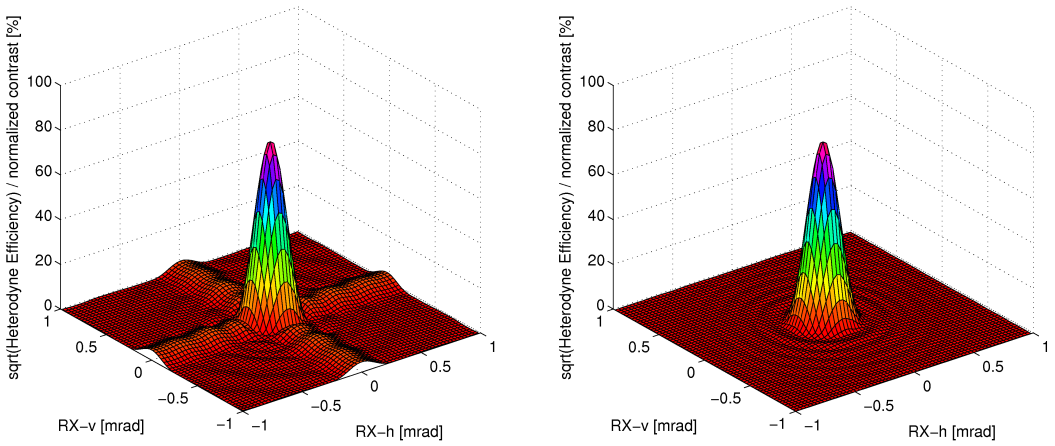

Figure 3.32: Square root of heterodyne efficiency for the coherent sum of all quadrants with 30 μm slit (left) and without slit (right) for rotations of the receiver along v (pitch) and h (yaw) direction and for nominal steering mirror position.

3.6.6 Closed-Loop DWS

The DWS control loop is emulated using a numerical equation solver (*Scaled Trust-Region Solver for Constrained Nonlinear Equations*, [Bellavia *et al.* , 2004]) to find a solution for

$$\begin{pmatrix} \mathrm{DWS}_h\ (h_{\mathrm{SM}}, v_{\mathrm{SM}}) \\ \mathrm{DWS}_v\ (h_{\mathrm{SM}}, v_{\mathrm{SM}}) \end{pmatrix} = \begin{pmatrix} 0 \\ 0 \end{pmatrix} \tag{3.189}$$

by rotating the steering mirror in v and h direction around a pivot point, which is 10 mm behind the steering mirror center. Because evaluation of the DWS is computationally expensive and the DWS is subject to phase wrapping, at first, the ray-tracing results are used to solve

$$\begin{pmatrix} \mathrm{LB}_h\ (h_{\mathrm{SM}}, v_{\mathrm{SM}}) - \mathrm{TB}_h\ (h_{\mathrm{SM}}, v_{\mathrm{SM}}) \\ \mathrm{LB}_v\ (h_{\mathrm{SM}}, v_{\mathrm{SM}}) - \mathrm{TB}_v\ (h_{\mathrm{SM}}, v_{\mathrm{SM}}) \end{pmatrix} = \begin{pmatrix} 0 \\ 0 \end{pmatrix}, \tag{3.190}$$

meaning that the incidence angles at the photodetector of the top hat ray and local beam ray are equalized. The result is used as initial guess for the DWS zeroing. A working DWS control loop yields valid round-trip pathlength measurements. In the simulation a simplified GFO LRI model with one spacecraft was used, as described in section 3.5.2.

The results of the closed DWS loop simulation are shown in table 3.8. The simulation scenario #1 is again the nominal result. In scenario #2 one can see that transmitter misalignment or translation of the receiver spacecraft perpendicular to the LOS does not change the round-trip pathlength measurement (denoted as `ROUND-LONG`). The third scenario shows the results for a translation of 10 nm along the LOS, which produces a round-trip change of 20 nm. The transmitter tilt has no influence. The independence of receiver roll (rotation along the LOS) on the round-trip is visible in scenario #4. In #5 and #6 the zero-finder rotates the mirrors by the values given in row (0) and (1) yielding zero DWS signal (rows 15,16). A small residual round-trip signal is still present, which is investigated subsequently. In all cases the angle between input and output beam (row 23) is very close to zero.

The nominal working performance of the simulated setup can be considered as sufficient, because the residual round-trip pathlength has only a magnitude of a few nanometer. The absolute numbers given in tables 3.6 and 3.8 provide a first overview and validate the expected behavior. However, such tables are unhandy, because some results change only slightly, whereas other results do not change at all. To condense the information, the functional dependency of the data is computed up to quadratic order using three evaluation points (see table 3.7). Most of the result values depend linearly or quadratically on the input parameters, which are given by the rows (a)-(h) in table 3.8. The linear and quadratic terms are called coupling factors within this thesis, because they correspond to the first and second derivatives.

Row	Parameter	Offset	Linear	Quadratic
1	DC-Power-TB/TX-v	469.623 pW	0.000 pW/mrad	-31168.8 pW/mrad^2
2	DC-Power-TB/TX-h	469.623 pW	0.000 pW/mrad	-31168.8 pW/mrad^2
3	DWS-Loop-SM-v/RX-v	0.000 mrad	0.7071 mrad/mrad	0.000 mrad/mrad^2
4	ROUND-LONG/RX-v	0 nm	-0.7071nm/mrad	3.96342 nm/mrad^2
5	DC-Power-TB/RX-v	469.623 pW	1.025e-07 pW/mrad	0.149132 pW/mrad^2
6	DWS-Loop-SM-h/RX-h	0.000 mrad	0.5 mrad/mrad	0.000 mrad/mrad^2
7	ROUND-LONG/RX-h	0 nm	0.3744 nm/mrad	5.31206 nm/mrad^2
8	ROUND-LONG/Move-X	0 nm	-2 μm/μm	-2.273e-05 nm/um^2
9	HetEff-A/RX-v	68.8594 %	0.01143 %/mrad	-0.01206 %/mrad^2
10	HetEff-B/RX-v	68.8594 %	0.01140 %/mrad	-0.01216 %/mrad^2
11	HetEff-C/RX-v	68.8594 %	-0.01143 %/mrad	-0.01206 %/mrad^2
12	HetEff-D/RX-v	68.8594 %	-0.01140 %/mrad	-0.01216 %/mrad^2

Table 3.7: Excerpt of the coupling factors for the nominal setup. A linear coupling of rotations of 1 nm/mrad = 1 μm/rad into the optical pathlength corresponds to an offset in the TMA vertex position of 1 μm.

The residual pathlength change (`ROUND-LONG`) is approximately 5 nm/mrad^2 for rotations of the receiver (row 4 and 7, table 3.7). This residual coupling is explained partially in the next subsection with angle-dependent pathlength changes in the beamsplitter. The rows (1) and (2) in table 3.7 indicate the rapid drop of intensity for transmitter misalignment, while the heterodyne efficiency (row (9)-(14)) does not change much upon receiver misalignment, because the steering mirror and DWS control loop compensates the receiver attitude jitter.

Row	Parameter	Sim #1	Sim #2	Sim #3	Sim #4	Sim #5	Sim #6	Sim #7	Sim #8
a	TX-v [mrad]	0.0000	**0.1000**	0.0000	0.0000	0.0000	0.0000	0.0000	**0.1000**
b	TX-h [mrad]	0.0000	**0.1000**	**0.1000**	0.0000	0.0000	0.0000	0.0000	**0.1000**
c	RX-r [mrad]	0.0000	0.0000	0.0000	**0.1000**	0.0000	0.0000	**0.1000**	**0.1000**
d	RX-v [mrad]	0.0000	0.0000	0.0000	0.0000	0.1000	0.0000	**0.1000**	**0.1000**
e	RX-h [mrad]	0.0000	0.0000	0.0000	0.0000	0.0000	**0.1000**	**0.1000**	**0.1000**
f	Move-X [μm]	0.0000	0.0000	**0.0100**	0.0000	0.0000	0.0000	**0.1000**	0.0000
g	Move-Y [μm]	0.0000	**0.1000**	0.0000	0.0000	0.0000	0.0000	**0.1000**	0.0000
h	Move-Z [μm]	0.0000	**0.1000**	0.0000	0.0000	0.0000	0.0000	**0.1000**	0.0000
0	**DWS-Loop-SM-h [mrad]**	0.0000	0.0000	0.0000	0.0000	0.0000	0.0500	0.0500	0.0500
1	**DWS-Loop-SM-v [mrad]**	0.0000	0.0000	0.0000	0.0000	0.0707	0.0000	0.0707	0.0707
2	LB-x [μm]	0.0000	0.0000	0.0000	0.0000	0.0000	-0.0058	-0.0058	-0.0058
3	LB-y [μm]	0.0000	0.0000	0.0000	0.0000	0.0111	0.0000	0.0111	0.0111
4	LB-h [mrad]	0.0000	0.0000	0.0000	0.0000	0.0000	0.7986	0.7986	0.7986
5	LB-v [mrad]	0.0000	0.0000	0.0000	0.0000	0.7986	0.0000	0.7986	0.7986
8	TB-x [μm]	0.0000	0.0000	0.0000	0.0000	0.0000	-0.0006	-0.0006	-0.0006
9	TB-y [μm]	0.0000	0.0000	0.0000	0.0000	-0.0006	0.0000	-0.0006	-0.0006
10	TB-h [mrad]	0.0000	0.0000	0.0000	0.0000	0.0000	0.7986	0.7986	0.7986
11	TB-v [mrad]	0.0000	0.0000	0.0000	0.0000	0.7986	0.0000	0.7986	0.7986
15	DWS-v [mrad]	0.0000	0.0000	0.0000	0.0000	0.0000	0.0000	0.0000	0.0000
16	DWS-h [mrad]	0.0000	0.0000	0.0000	0.0000	0.0000	0.0000	0.0000	0.0000
22	**ROUND-LONG [nm]**	0.0000	0.0000	-20.0000	0.0000	-0.0311	0.0906	-199.9405	0.0595
23	**Angle-InOut [μrad]**	0.0000	0.0000	0.0000	0.0000	0.0000	0.0000	0.0000	0.0000
32	TB-RoC-s [km]	3.4660	3.4660	3.4660	3.4660	14.0326	7.9964	-11.9477	-11.8588
33	TB-RoC-t [km]	3.4660	3.4660	3.4660	3.4660	-10.2233	-6.5958	-1.8300	-1.8321
34	LB-RoC-s [km]	6.0549	6.0549	6.0549	6.0270	-19.5123	-3.8172	-3.3416	-3.3419
35	LB-RoC-t [km]	-11.5463	-11.5463	-11.5463	-11.4452	-2.1129	-3.8172	-1.2079	-1.2079
36	DC-Power-4q [mW]	0.6316	0.6316	0.6316	0.6316	0.6316	0.6316	0.6316	0.6316
37	Contrast [%]	0.1410	0.0474	0.0818	0.1410	0.1410	0.1410	0.1410	0.0474
38	DC-Power-TB [pW]	469.6228	53.1135	157.9346	469.6228	469.6243	469.6243	469.6258	53.1139
39	DC-Power-LB [mW]	0.6316	0.6316	0.6316	0.6316	0.6316	0.6316	0.6316	0.6316

Table 3.8: Input parameter (row a-h) and some result values of the modeled optical bench to validate DWS closed-loop simulation and round-trip measurements; `ROUND-LONG`: round-trip pathlength; `DWS-Loop-SM`: steering mirror rotation angles determined by DWS control loop

3.6.7 Compensation Beamsplitter

In section 3.4.7 the optical pathlength changes due to a beamsplitter and the dependency on the angle of incidence are discussed. Omitting the compensation beamsplitter on the optical bench results in the following optical pathlength changes (eq. (3.142)):

$$\begin{aligned}\Delta\mathrm{OPL} = \; & 3.116\,\mathrm{mm} \pm \mathbf{1656.39\,nm/mrad} \cdot \alpha + 1.50\,\mathrm{nm/mrad}^2 \cdot \alpha + O[\alpha^3] \\ & - 0.83\,\mathrm{nm/mrad}^2 \cdot \beta^2 + O[\beta^4],\end{aligned}$$

where α is the horizontal (tilt) angle and β is the vertical (tip) angle. A compensation plate cancels the linear term in the first line, but all other contributions are doubled. In row 7 in table 3.7 a quadratic coupling of $5.31206\,\mathrm{nm/mrad}^2$ was observed in h-direction, whereas $2 \cdot 1.50\,\mathrm{nm/mrad}^2$ is predicted. For the tip direction (row 4) the observed value is $3.96342\,\mathrm{nm/mrad}^2$ and the predicted value is $2 \cdot 0.83\,\mathrm{nm/mrad}^2$. A small linear coupling term is present in both cases.
To understand the deviations, at first, the contribution of the compensation beamsplitter is removed by changing the substrate refractive index to 1.0 (row 1-4 in table 3.9). Then also the effect of the beamsplitter is ommited, again by changing the refractive index to 1.0 (row 5-8 in table 3.9). A comparison with results in table table 3.7 reveals, that the quadratic coupling factors is reduced by the expected values in each step. The linear term for tilt (row 4 in table 3.9) is in good accordance with the theoretical value of 1656.39 nm/mrad.

Row	Parameter	Offset	Linear	Quadratic
1	DWS-Loop-SM-v/RX-v	0.000 mrad	0.707107 mrad/mrad	0.000 mrad/mrad^2
2	ROUND-LONG/RX-v	0.000 nm	-0.707107 nm/mrad	3.13528 nm/mrad^2
3	DWS-Loop-SM-h/RX-h	0.000 mrad	0.5 mrad/mrad	0.000 nm/mrad^2
4	ROUND-LONG/RX-h	0.000 nm	**1656.77 nm/mrad**	3.80971 nm/mrad^2
5	DWS-Loop-SM-v/RX-v	0.000 mrad	0.707107 mrad/mrad	0.000 mrad/mrad^2
6	ROUND-LONG/RX-v	0.000 nm	-0.707107 nm/mrad	2.30696 nm/mrad^2
7	DWS-Loop-SM-h/RX-h	0.000 mrad	0.5 mrad/mrad	0.000 nm/mrad^2
8	ROUND-LONG/RX-h	0.000 nm	0.374496 nm/mrad	2.30700 nm/mrad^2
9	DWS-Loop-SM-v/RX-v	0.000 mrad	0.707107 mrad/mrad	0.000 mrad/mrad^2
10	ROUND-LONG/RX-v	0.000 nm	-0.707107 nm/mrad	0.000 nm/mrad^2
11	DWS-Loop-SM-h/RX-h	0.000 mrad	0.5 mrad/mrad	0.000 nm/mrad^2
12	ROUND-LONG/RX-h	0.000 nm	0.374480 nm/mrad	0.000 nm/mrad^2

Table 3.9: Coupling factors when compensation plate is neglected (top, row 1-4), when both beamsplitter contributions are omitted (middle, row 5-8) and if additionally the beam parameters of local and received beam are equal (bottom, row 9-12); parameter `DWS-Loop-SM-v/h` denote the rotation angles of the steering mirror determined by the DWS control loop

However, there seems to be still another contribution causing the residual quadratic couping of $2.3\,\mathrm{nm/mrad}^2$, even if the beamsplitter substrate has a refractive index of 1.0 (vacuum). Therefore, the effect of different beam wavefront shapes at the photodiode is investigated by setting both beams to the same parameter. This removes the quadratic contribution (row 10 and 12 in table 3.9). The remaining linear coupling was assumed to be due to the position of the steering mirror pivot point, which was 10 mm behind the steering mirror center. Unfortunately, this was not the case, such that the contribution remains unexplained. Also the lateral beam shift caused by the intersection point mismatch on the beamsplitter (see section 3.5.2) can be excluded as reason for the linear term, because when the refractive index of the beamsplitter is set to 1.0, the intersection points coincide and the beams overlap perfectly.

3.6.8 Sensitivity on Misalignment and Misplacement

The nominal optical bench configuration has been modeled so far. It was attempted to understand and minimize the residual coupling of $\approx 5\,\mathrm{nm/mrad}^2$ in the round trip length measurement. In a next step the influence of misalignment and misplacement of components on the different coupling factors is analyzed. Therefore, the coupling factors c_j, e.g., for receiver tilt on the round trip pathlength (`ROUND-LONG/RX-h`), are computed for the nominal component position (q_k) and for the misplaced case (q'_k). Then the Jacobian coefficients (second derivatives) are approximated using this formula:

$$\frac{c_j(q'_k) - c_j(q_k)}{q'_k - q_k}. \tag{3.191}$$

With this procedure one can not only analyze the dependency on position and orientation of components, but also on other parameters like component thickness. The varied parameters and the step sizes $q'_k - q_k$ are shown in table 3.10. The coordinate system is defined as follows: the x-axis is anti-parallel to the incoming top hat beam (normal to the receive aperture), while the z-axis is perpendicular to the optical bench platform (see figure 3.30). The y-axis supplements the triad. The steering mirror pivot point (row 18 in tabl. 3.10) is defined in a local beam coordinate frame (see figure 3.20). The spacecraft separation (row 26) changes only the power of the top hat beam in this simulation, but not the optical pathlength, because the model from section 3.5.2 is used.

Row	Parameter	Stepsize	Row	Parameter	Stepsize
1	L1/L2-thick	10 um	2	L1/L2-focal	10 um
3	CBS/BS-x,y,z	0.01 mm	4	BS-v	0.001 mrad
5	BS-h	0.01 mrad	6	CBS/BS-wedge	0.1 mrad
7	CBS/BS-thick	1 um	8	CBS/BS-n	$1 \cdot 1e$-3
9	SM-x,y,z	0.01 mm	10	SM-v,h	0.1 mrad
11	L1-x,y,z	0.3 mm	12	L1-v,h	0.5 mrad
13	L1/L2-n	$1 \cdot 1e$-3	14	L2-x,y,z	0.01 mm
15	L2-v,h	0.5 mrad	16	PD-x,y,z	0.01 mm
17	PD-v,h	1 mrad	18	SMpiv-x,y,z	1 mm
19	LB-waist	0.1 mm	20	LB-z0	10 mm
21	LB-Power	0.1 mW	22	PD-active-radius	1 um
23	PD-slit	1 um	24	Vertex-x,y,z	0.1 mm
25	AP-y, AP-z	0.01 mm	26	SC-sep	1 km
27	TB-initial-z0	0.01 mm			

Table 3.10: Setup parameter names, which have been varied for the Jacobian coefficients and the corresponding step sizes and units; L1: lens 1, L2: lens 2, CBS: compensation beamsplitter, BS: beamsplitter, SM: steering mirror, PD: quadrant photodiode, LB: local beam, TB: received top hat beam, AP: receive aperture

For simplicity and data volume reduction only the influence on the round trip pathlength (`ROUND-LONG`), beamwalk on the photodiode (`TB-x, TB-y, LB-x, LB-y`, given in a photodiode coordinate system[26]) and angle between received and outgoing beam (`Angle-InOut`) is discussed here, although the dependency for all other results has been computed as well.
The linear coupling terms are shown table 3.12. A misplacement of the TMA vertex (row 1 and 2) in lateral direction y or z by 1 mm results in a coupling 2000 nm/mrad for rotations of the receiver into the round-trip length measurement. This is in accordance with the results from the linearized coupling theory (section 3.3.4, eq. (3.82)) and underlines the importance of accurate positioning of the TMA vertex. The

[26] photodiode x-direction is in nominal case in the horizontal direction, while y-direction is perpendicular to the optical bench (vertical)

wedge angle of the beamsplitter can also introduce a coupling between receiver rotations and length measurement (row 3 and 4). In this simulation the wedge of the beamsplitter was defined at the surface facing to the compensation plate. The contribution for the beamsplitter has a different sign than for the compensation plate (cf. row 3 and 4 in table 3.12). Also the magnitude is different, because a wedge of the beamsplitter changes the incidence angle on the compensation plate, but not vice versa. The effect of a common wedge angle can be minimized by proper positioning the beamsplitter.
Also the effect of common refractive index fluctuations (row 17 and 18) cancels in the length measurement as well as in the angle difference between received beam and outgoing beam (row 29 and 29). The differential wedge angle is assumed to be in the order of 10 μrad, thus the combined effect of row (3) and (4) is small enough.
The transverse position of the lenses and the receive aperture introduce also a linear coupling between S/C rotations and pathlength measurement. However, the positioning and stability of components like lenses, beamsplitter and photodiode is assumed to be in the order of 10 μm. In this context the coupling factors seem uncritical.
Furthermore, a longitudinal displacement of lens 2 or of the photodiode introduces a small beamwalk at the photodiode (row 19-26 in table 3.12), as expected from the beam compressor tolerances analysis in section 3.6.3.
According to the assumed positioning accuracy of the components, the quadratic terms in table 3.13 seem also uncritical. The TMA vertex misplacement along the beam direction (row 11 and 12 in table 3.13), which is the insensitive axis for TMA positioning, has only a contribution of $-1.000\,\mathrm{nm/mrad^2/mm}$, while the other directions couple with 2000 nm/mrad/mm (row 1 and 2 in table 3.12).
The values for the offset changes in table 3.11 seem on the first appearance very large. However, some values like in row 11 and 12 merely state the trivial fact that a transverse shift of the photodiode by 1 mm results in a beamwalk by 1 mm.
The pathlength variations shown in row 1 and 4 for a beamsplitter wedge is not measurable, because it is a static offset and the wedge is supposed not to change significantly during operation. Fluctuations of the temperature will influence the refractive index and the thickness of the beamsplitter, such that rows 2,3,8,9 are of interest for further analysis. In this thesis the dependency of refractive index or of the thickness variation on temperature was not investigated.
Noteworthy are row 7 and 10 in table 3.11, because they state a change of the measured pathlength when the longitudinal position of the lens 1 or 2 changes. Although this distance is a common path for the local and top hat beam, a shift in the lens position modifies the wavefronts for each beam in a different way due to the different beam parameter. These terms vanish if identical beam parameter for the local and top hat are used. Further investigation with proper top hat beams (using higher-order Gaussian modes) should reveal, if this effect is to be expected in real measurements.
One can conclude that the largest influence on the length measurement is given by the TMA vertex positioning and that most of the other parameter seem uncritical. The positioning of the lenses w.r.t. to the photodiode is important to suppress the beamwalk on the photodiode.

Row	Parameter	Value
1	ROUND-LONG/CBS-wedge	−5984.025 nm/mrad
2	ROUND-LONG/CBS-n	5661.832 nm/1e-3
3	ROUND-LONG/BS-n	5661.832 nm/1e-3
4	ROUND-LONG/BS-wedge	1731.369 nm/mrad
5	ROUND-LONG/CBS-h	1657.894 nm/mrad
6	ROUND-LONG/BS-h	1656.498 nm/mrad
7	ROUND-LONG/L2-y	732.861 nm/mm
8	ROUND-LONG/CBS-thick	623.287 nm/um
9	ROUND-LONG/BS-thick	623.287 nm/um
10	ROUND-LONG/L1-y	−247.021 nm/mm
11	LB-x/PD-x	−1000.000 um/mm
12	TB-y/PD-z	−1000.000 um/mm
13	LB-x/L2-x	940.690 um/mm
14	LB-y/L2-z	940.690 um/mm
15	LB-x/L1-x	179.862 um/mm
16	TB-y/L1-z	179.862 um/mm
17	TB-x/AP-y	125.215 um/mm
18	TB-y/AP-z	−125.215 um/mm
19	TB-x/BS-y	−125.215 um/mm
20	TB-x/BS-x	−125.215 um/mm
21	LB-x/SM-x	−125.215 um/mm
22	LB-x/SM-y	−125.215 um/mm
23	TB-y/BS-v	−12.404 um/mrad

Table 3.11: Offset coupling factors for the optical bench setup parameters sorted in descending order of the absolute value

Row	Parameter	Value
1	ROUND-LONG/RX-h/Vertex-y	−2000.000 nm/mrad/mm
2	ROUND-LONG/RX-v/Vertex-z	2000.000 nm/mrad/mm
3	ROUND-LONG/RX-h/CBS-wedge	−81.761 nm/mrad/mrad
4	ROUND-LONG/RX-h/BS-wedge	64.585 nm/mrad/mrad
5	ROUND-LONG/RX-v/L2-z	47.831 nm/mrad/mm
6	ROUND-LONG/RX-h/L2-x	47.808 nm/mrad/mm
7	ROUND-LONG/RX-h/L1-x	−36.011 nm/mrad/mm
8	ROUND-LONG/RX-v/L1-z	−35.907 nm/mrad/mm
9	ROUND-LONG/RX-h/BS-h	11.959 nm/mrad/mrad
10	ROUND-LONG/RX-v/BS-v	8.679 nm/mrad/mrad
11	ROUND-LONG/RX-h/CBS-h	−3.006 nm/mrad/mrad
12	ROUND-LONG/RX-v/CBS-v	−2.342 nm/mrad/mrad
13	ROUND-LONG/RX-h/BS-x	−1.954 nm/mrad/mm
14	ROUND-LONG/RX-h/BS-y	−1.953 nm/mrad/mm
15	ROUND-LONG/RX-v/AP-z	−1.952 nm/mrad/mm
16	ROUND-LONG/RX-h/AP-y	1.952 nm/mrad/mm
17	ROUND-LONG/RX-h/BS-n	1.598 nm/mrad/1e-3
18	ROUND-LONG/RX-h/CBS-n	−1.598 nm/mrad/1e-3
19	TB-y/RX-v/PD-y	7.986 um/mrad/mm
20	TB-x/RX-h/PD-y	7.986 um/mrad/mm
21	LB-x/RX-h/PD-y	7.986 um/mrad/mm
22	LB-y/RX-v/PD-y	7.986 um/mrad/mm
23	LB-x/RX-h/L2-y	−7.958 um/mrad/mm
24	TB-x/RX-h/L2-y	−7.958 um/mrad/mm
25	TB-y/RX-v/L2-y	−7.958 um/mrad/mm
26	LB-y/RX-v/L2-y	−7.957 um/mrad/mm
27	LB-x,y/RX-h/L1-x	3.387 um/mrad/mm
28	Angle-InOut/RX-h/BS-wedge	1.350 urad/mrad/mrad
29	Angle-InOut/RX-h/CBS-wedge	−1.350 urad/mrad/mrad

Table 3.12: Linear Jacobian coupling factors sorted in descending order of the absolute value.

Row	Parameter	Value
1	ROUND-LONG/RX-h/L1-y	−8.325 nm/mrad^2/mm
2	ROUND-LONG/RX-v/L1-y	−8.323 nm/mrad^2/mm
3	ROUND-LONG/RX-v/L1-z	−5.521 nm/mrad^2/mm
4	ROUND-LONG/RX-h/L1-x	−4.980 nm/mrad^2/mm
5	ROUND-LONG/RX-v/L1-x	−4.406 nm/mrad^2/mm
6	ROUND-LONG/RX-h/L1-z	−2.205 nm/mrad^2/mm
7	ROUND-LONG/RX-h/L2-y	−1.785 nm/mrad^2/mm
8	ROUND-LONG/RX-v/L2-y	−1.774 nm/mrad^2/mm
9	ROUND-LONG/RX-v/LB-waist	−1.209 nm/mrad^2/mm
10	ROUND-LONG/RX-h/LB-waist	−1.208 nm/mrad^2/mm
11	ROUND-LONG/RX-h/Vertex-x	−1.000 nm/mrad^2/mm
12	ROUND-LONG/RX-v/Vertex-x	−1.000 nm/mrad^2/mm
13	LB-x/RX-h/L1-x	−0.821 um/mrad^2/mm
14	TB-y/RX-v/L1-z	−0.818 um/mrad^2/mm
15	TB-x/RX-h/L1-x	−0.818 um/mrad^2/mm
16	LB-y/RX-v/L1-z	−0.816 um/mrad^2/mm
17	TB-y/RX-v/L2-z	0.745 um/mrad^2/mm
18	TB-x/RX-h/L2-x	0.745 um/mrad^2/mm
19	LB-y/RX-v/L2-z	0.743 um/mrad^2/mm
20	LB-x/RX-h/L2-x	0.691 um/mrad^2/mm
21	Angle-InOut/RX-v/PD-z	−2.783 urad/mrad^2/mm
22	Angle-InOut/RX-v/L2-z	2.571 urad/mrad^2/mm
23	Angle-InOut/RX-h/L1-z	2.385 urad/mrad^2/mm
24	Angle-InOut/RX-h/PD-z	−2.114 urad/mrad^2/mm
25	Angle-InOut/RX-h/L2-x	−2.041 urad/mrad^2/mm
26	Angle-InOut/RX-v/L1-x	1.592 urad/mrad^2/mm
27	Angle-InOut/RX-v/L2-x	−1.506 urad/mrad^2/mm
28	Angle-InOut/RX-r/L2-x	−1.386 urad/mrad^2/mm
29	Angle-InOut/RX-v/PD-x	1.141 urad/mrad^2/mm

Table 3.13: Quadratic Jacobian coupling factors sorted in descending order of the absolute value.

3.6.9 Steering Mirror induced Pathlength Changes

In section 3.2.3 off-racetrack pathlength fluctuations are discussed. The pathlength a_1 in fig. 3.4, from the steering mirror to the beamsplitter, is present in the final measurement of the phase (eq. (3.51)) and changes upon steering mirror rotation. We estimate here the coupling of steering mirror rotations into the pathlength. Assuming just a tilted flat plate in a distance s_{nom} (see fig. 3.33), the pathlength dependency on tip v and tilt h is

$$s(v) = \frac{s_{\text{nom}}}{\cos(v)} \approx s_{\text{nom}} + s_{\text{nom}} \frac{v^2}{2} \tag{3.192}$$

$$\begin{aligned} s(h) = s' + z &= \frac{s_{\text{nom}}}{\cos(h)} + \frac{\sin(h) \cdot \sin(\alpha_0) \cdot s_{\text{nom}}}{\sin(\pi/2 - h - \alpha_0)} \\ &\approx s_{\text{nom}} \cdot \left(1 + h \cdot \tan(\alpha_0) + \frac{h^2}{2}(1 + 2 \cdot \tan(\alpha_0))\right). \end{aligned} \tag{3.193}$$

The angles v and h are not the steering mirror rotation angles, but the ray deflection angles and therefore equal to S/C rotation yaw and pitch, when the DWS loop is closed.

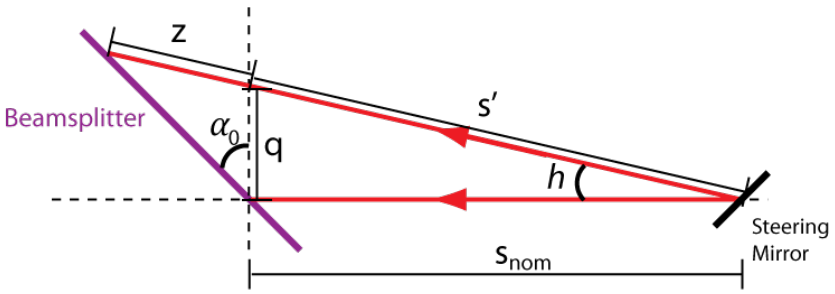

Figure 3.33: Simplified model for optical pathlength changes between beamsplitter and steering mirror.

For a distance of $s_{\text{nom}} = 7\,\text{cm}$ between steering mirror and beamsplitter, which is tilted by $\alpha_0 = 45°$, the evaluation yields

$$s(v) \approx 70\,\text{mm} + 35\,\text{nm/mrad}^2 \cdot v^2 \tag{3.194}$$

$$s(h) \approx 70\,\text{mm} + 70\,\mu\text{m/mrad} \cdot h + 105\,\text{nm/mrad}^2 \cdot h^2. \tag{3.195}$$

These results approximate the IfoCad results given in table 3.14. The deviations can be explained with the refractive index of the beamsplitter substrate, which was neglected in this derivation. The refractive index of the substrate introduces an offset as well as an angle-dependent coupling, as described in section 3.4.7.
With these coupling factors and data on the spacecraft jitter in yaw and pitch, one can estimate the contribution of spacecraft rotations on the final length measurement precision, as it is done in section 3.2.3.

Row	Parameter	Offset	Linear	Quadratic
1	OptPath-a1/RX-v	75.529 mm	0 nm/mrad	27.633 nm/mrad^2
2	OptPath-a1/RX-h	75.529 mm	69408.10 nm/mrad	97.983 nm/mrad^2

Table 3.14: Coupling factors for optical pathlength a_1 upon spacecraft rotation.

3.6.10 Monte Carlo Simulation

In the previous subsection 3.6.8 the Jacobian coefficients are derived, which describe the dependency of the measured signals on changes of individual optical bench parameters. In each step a single parameter is varied, while all other parameters have their nominal value. In a Monte Carlo simulation all parameters are chosen randomly at the same time. With this approach one can simulate the tolerances of each component and errors in the positioning on the OB.
In total 2200 optical benches with different parameter sets are simulated. The input parameters are shown in table 3.15. The center and mean value μ corresponds to the nominal parameter. The probability distribution is a truncated Gaussian distribution ([Wanner, 2010, clipped normal distribution, p. 172]), where σ is the interval size. The parameters are chosen randomly from the interval $\mu - \sigma ... \ \mu + \sigma$, whereas values close to μ are more likely than values close to the interval limits (Gaussian distribution).
The parameter 1 (`db`) is the distance between the receive aperture and the beamsplitter. The offset between TMA vertex and center of rotation is 4 mm along the insensitive axis (parameter 55), whereas a large uncertainty of 10 mm is assumed. The tolerances in the sensitive axes are set to 250 μm (parameter 56 and 57). According to the linearized coupling theory (sec. 3.3.4), the expected round-trip pathlength change upon rotation is $2 \cdot 250$ nm/mrad.

No	Parameter	Value: $\mu \pm \sigma$	No	Parameter	Value: $\mu \pm \sigma$
1	db	70 ± 1 mm	2	L1-thick	4000 ± 10 um
3	L1-focal	81460 ± 10 um	4	L2-thick	5000 ± 10 um
5	L2-focal	10200 ± 10 um	6	BS-x	0 ± 0.01 mm
7	BS-y	0 ± 0.01 mm	8	BS-z	0 ± 0.01 mm
9	BS-v	0 ± 0.1 mrad	10	BS-h	0 ± 0.1 mrad
11	BS-wedge	0 ± 10 urad	12	BS-thick	5000 ± 10 um
13	BS-n	$(150663 \pm 1) \cdot 10^{-5}$	14	SM-x	0 ± 0.01 mm
15	SM-y	0 ± 0.01 mm	16	SM-z	0 ± 0.01 mm
17	SM-v	0 ± 0.1 mrad	18	SM-h	0 ± 0.1 mrad
19	L1-x	0 ± 0.05 mm	20	L1-y	0 ± 0.05 mm
21	L1-z	0 ± 0.05 mm	22	L1-v	0 ± 1 mrad
23	L1-h	0 ± 1 mrad	24	L1-n	$(150663 \pm 1) \cdot 10^{-5}$
25	L2-x	0 ± 0.05 mm	26	L2-y	0 ± 0.05 mm
27	L2-z	0 ± 0.05 mm	28	L2-v	0 ± 1 mrad
29	L2-h	0 ± 1 mrad	30	L2-n	$(150663 \pm 1) \cdot 10^{-5}$
31	PD-x	0 ± 0.01 mm	32	PD-y	0 ± 0.01 mm
33	PD-z	0 ± 0.01 mm	34	PD-v	0 ± 1 mrad
35	PD-h	0 ± 1 mrad	36	SMpiv-x	-10 ± 1 mm
37	SMpiv-y	0 ± 1 mm	38	SMpiv-z	0 ± 1 mm
39	LB-waist	2.5 ± 0.1 mm	40	LB-z0	0 ± 100 mm
41	LB-Power	15 ± 0.1 mW	42	PD-active-radius	500 ± 10 um
43	PD-slit	30 ± 2 um	44	CBS-x	0 ± 0.1 mm
45	CBS-y	0 ± 0.1 mm	46	CBS-z	0 ± 0.1 mm
47	CBS-v	0 ± 0.1 mrad	48	CBS-h	0 ± 0.1 mrad
49	CBS-wedge	0 ± 10 urad	50	CBS-thick	5000 ± 10 um
51	CBS-n	$(150663 \pm 1) \cdot 10^{-5}$	52	AP-y	0 ± 0.01 mm
53	AP-z	0 ± 0.01 mm	54	SC-sep	220 ± 30 km
55	Vertex-x	4 ± 10 mm	56	Vertex-y	0 ± 0.25 mm
57	Vertex-z	0 ± 0.25 mm	58	BIAS-ROLL	0 ± 10 mrad
59	BIAS-YAW	0 ± 3 mrad	60	BIAS-PITCH	0 ± 3 mrad

Table 3.15: Input parameters with center value and interval size for the truncated Gaussian distribution; L1: lens 1, L2: lens 2, CBS: compensation beamsplitter, BS: beamsplitter, SM: steering mirror, SPpiv: SM pivot point, PD: quadrant photodiode, LB: local beam, TB: received top hat beam, AP: receive aperture.

In addition to previous simulations, an initial misalignment between LRI and S/C

frame (parameter 58-60) is introduced. This permanent rotation in yaw, pitch and roll direction might be caused by the vibrations during the S/C launch.
The linear coupling factors for the round-trip length measurement are shown in fig. 3.34. The maximum value is approximately 520 nm/nrad, whereas 500 nm/nrad is expected from the linearized coupling theory. Thus, approximately 20 nm/nrad are caused by effects like the initial LRI frame misalignment or by a combination of different misalignments and misplacements. The quadratic terms are depicted in fig. 3.35.

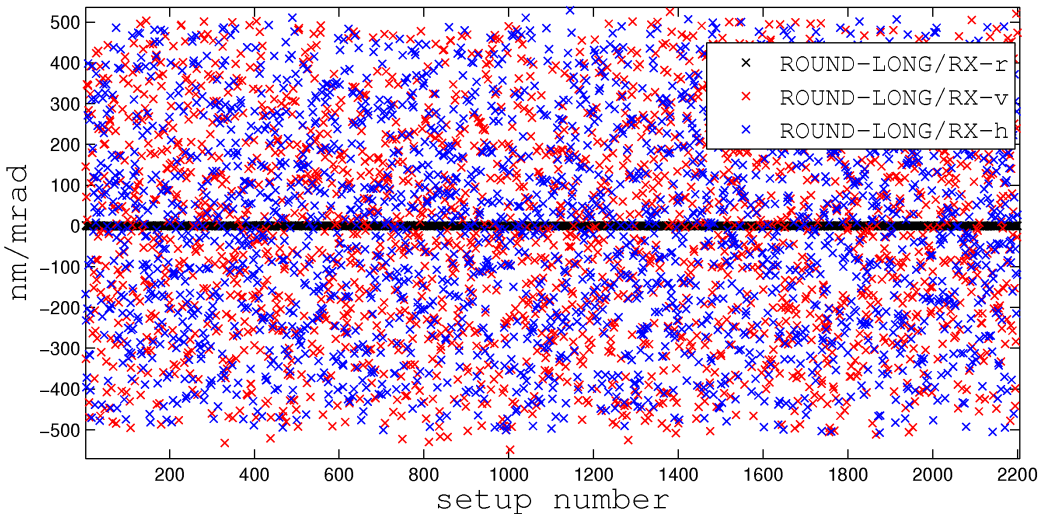

Figure 3.34: Linear coupling factors of rotations for roll (`RX-r`), pitch (`RX-v`) and yaw (`RX-h`).

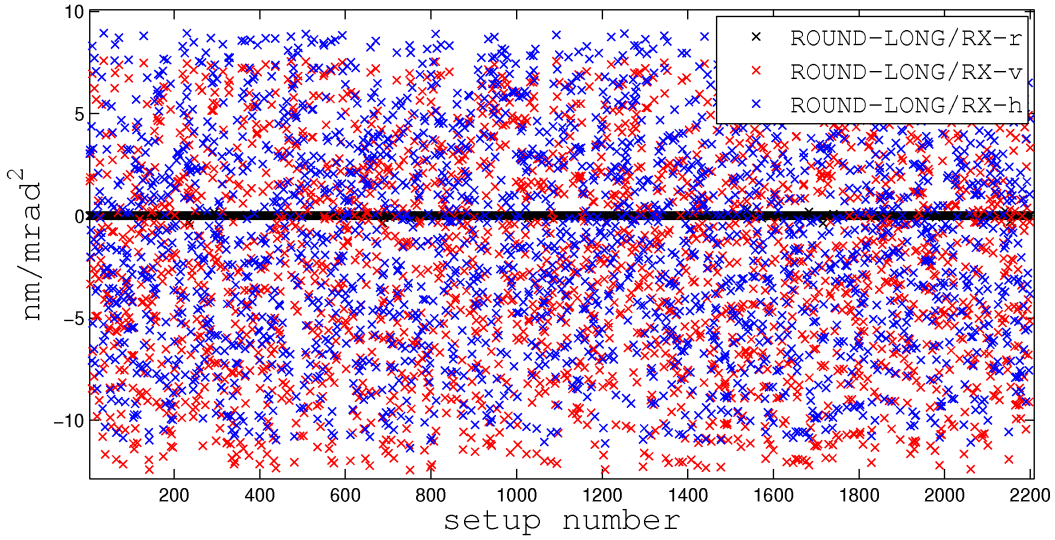

Figure 3.35: Quadratic coupling factors of rotations for roll (`RX-r`), pitch (`RX-v`) and yaw (`RX-h`).

The offset angle between received and outgoing beam is shown in fig. 3.36. The corresponding linear and quadratic terms are below 1.0 μrad/mrad and below 1.2 μrad/mrad^2. Further analysis showed, that the offset angle (up to 18 μrad) is highly correlated with the wedge angles of the beamsplitter and compensation plate. In this simulation an uncorrelated wedge of 10 μrad for both components is assumed, such that the differential wedge is up to 20 μrad. This tolerance could be tightened by a factor of two, so that the final angle is below 9 μrad.

This Monte Carlo simulation revealed the importance of the differential wedge of CBS and BS for the (anti-)parallelism of outgoing and incoming beam. The TMA vertex offset in the insensitive axis seems to be uncritical for the final performance. The contribution of TMA vertex offsets in the sensitive axes are the dominating effects for the coupling between rotations and length measurement. Other contributions, e.g., due to a combination of different misplacements and misadjustments, produce a coupling of about 20 nm/mrad.

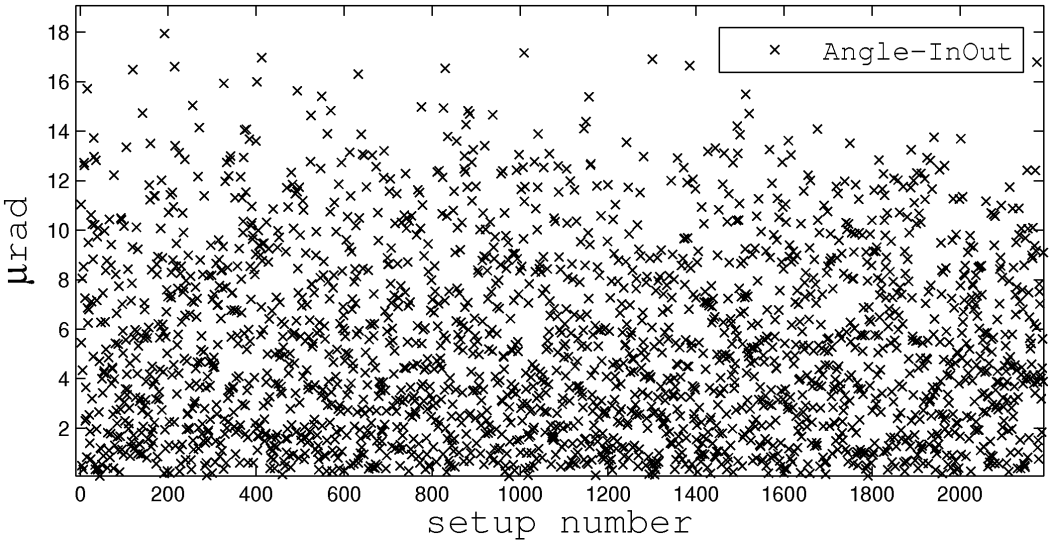

Figure 3.36: Offset angle between received light and outgoing beam direction on the OB.

3.7 Summary, Conclusion and Outlook

In the second part of this thesis an overview about the optical bench simulations for the GRACE Follow-On Laser Ranging Interferometer was given. In the beginning the overall LRI working principle was presented, whereas some noise sources like laser frequency noise and off-racetrack pathlength noise were discussed in more detail. The basic properties of corner-cubes, and in particular the application for the Triple Mirror Assembly of the LRI, were explained. The Optical Bench and single components were introduced. Effects due to the astigmatism of the beamsplitter were derived analytically and were compared to numerical IfoCad simulations in later sections. This analysis provided also the correction for the position of the steering mirror, which is required when light propagates through the beamsplitter. This information is of interest for the construction of the optical bench.
Then phase errors, caused by spacecraft rotations or steering mirror motion, in a full racetrack configuration were treated. The results showed only a small and uncritical coupling into the length measurement. Also the power drop on the receiver upon transmitter misalignment and the propagation direction of the received beam were explained. In the end various simulation results concerning the beam compressor and the whole optical bench verified the expected behavior. Small residual coupling factors were investigated and could be explained with the (quadratic) angle-dependent optical pathlength changes in the beamsplitter or with the wavefront overlap.
The overall setup seems to be robust, such that small misalignment and misplacement of components have only a minor effect on the final length measurement.
However, one should always keep in mind that these simulations use idealized models. The light fields are treated as Gaussian beams without any wavefront distortion, which might be caused by flatness imperfections of the optical components. The

coatings of the components were neglected as well. In laboratory experiments various other factors (e.g. temperature, air fluctuations, electric noise) play a role. Various discussed effects and couplings are probably too small to be observed in laboratory experiments, but they deepen the understanding of the optical LRI system.
In the future the simulations could be modified to use high-order Gaussian beams to simulate the top hat beam more accurately. Also consideration of coatings and polarization effects might be envisaged.

Appendix A

Lissajous Orbit Coefficients for $N = 3$

The non-zero coefficients are:

$$\omega_{20} = \frac{3\left(c_4\left(-3k^4+8k^2-8\right)-4c_3k^2\left(k^2(x_{2020}-2x_{2000}+4x_{2000}+2x_{2020}+2y_{2020}k)\right)\right)}{8k^2((3c_2-4)k+4\lambda)}, \tag{A.1}$$

$$\omega_{02} = -\frac{3\left(4c_3\left(k^2(x_{0202}-2x_{0200})+4x_{0200}+2x_{0202}+k(2y_{0202}+z_{1111}+2z_{111(-1)})\right)+c_4\left(k^2-12\right)\right)}{8((3c_2-4)k+4\lambda)}, \tag{A.2}$$

$$y_{1210} = \frac{3\left(c_4\left(-26c_2+2k^2-13\lambda^2+11\right)+4c_3s_4\right)}{16\lambda((3c_2-4)k+4\lambda)}, \tag{A.3}$$

$$y_{3010} = \frac{3\left(\frac{2s_1(k-\lambda)}{(3c_2-4)k+4\lambda}+4c_3k^2(4x_{2000}+2x_{2020}+y_{2020}k)-4c_4\left(k^2-2\right)\right)}{16k^3\lambda}, \tag{A.4}$$

$$y_{3030} = -\frac{3\left(k\left(2c_2+9\lambda^2+1\right)\left(4c_3k(x_{2020}k-y_{2020})+c_4\left(k^2+4\right)\right)-8\lambda\alpha\right)}{64k^3\left(-20c_2^2+c_2\left(9\lambda^2+10\right)-18\lambda^2+10\right)}, \tag{A.5}$$

$$\alpha = \left(3k^2(2c_3x_{2020}+c_4)-3c_3y_{2020}k^3+2c_4\right), \tag{A.6}$$

$$x_{3030} = \frac{6c_3k^2\left(8c_2x_{2020}+8c_2y_{2020}k-15x_{2020}\lambda^2+x_{2020}+12y_{2020}\lambda-8y_{2020}k\right)-\frac{1}{8}c_4\beta}{32k^3\left(-20c_2^2+c_2\left(9\lambda^2+10\right)-18\lambda^2+10\right)}, \tag{A.7}$$

$$\beta = \left(414c_2^2+c_2\left(207\lambda^2+127\right)-108k^2+540\lambda^2+8\right) \tag{A.8}$$

$$y_{1212}\frac{3\left(4c_3\gamma+c_4((8-11c_2)k+6\lambda)\right)}{64\left(\left(11c_2^2+17c_2-28\right)k-18(c_2-2)\lambda\right)}, \tag{A.9}$$

$$\gamma = \left(x_{0202}(11c_2k-8k+6\lambda)+y_{0202}\left(4c_2-6\lambda^2+2\right)-3z_{1111}\left(2c_2+\lambda^2+1\right)\right), \tag{A.10}$$

$$x_{1212} - \frac{3\left(c_4\left(-10c_2+33\lambda^2+1\right)+4c_3s_3\right)}{64\left(\left(11c_2^2+17c_2-28\right)k-18(c_2-2)\lambda\right)}, \tag{A.11}$$

$$z_{0303} = \frac{3(c_4-4c_3x_{0202})}{8\left(c_2-9\lambda^2\right)}, \tag{A.12}$$

$$z_{2121} = -\frac{3\left(4c_3k(x_{2020}k-z_{1111})+c_4\left(k^2+4\right)\right)}{8k^2\left(c_2-9\lambda^2\right)}, \tag{A.13}$$

$$d_{02} = \frac{3(c_4(-3(c_2-2)k-17\lambda)+2c_3s_2)}{4((3c_2-4)k+4\lambda)}, \tag{A.14}$$

$$d_{20} = \frac{3\left(\frac{2\lambda s_1}{(3c_2-4)k+4\lambda}+8c_3x_{2000}k^2+4c_3x_{2020}k^2-4c_3z_{1111}k-8c_3z_{111(-1)}k-c_4k^2+12c_4\right)}{8k^2}, \tag{A.15}$$

with additional abbreviations:

$$s_1 = 4c_3k^2\left(k^2(x_{2020} - 2x_{2000}) + 4x_{2000} + 2x_{2020} + 2y_{2020}k\right) + c_4\left(3k^4 - 8k^2 + 8\right), \quad \text{(A.16)}$$

$$s_2 = 6c_2x_{0202}k + 2c_2(2y_{0202} + z_{1111} + 2z_{111(-1)}) + 2\lambda(6x_{2000} + 5x_{0202}) - \quad \text{(A.17)}$$

$$4k(2x_{2000} + x_{0202}) + \lambda^2(2y_{0202} + z_{1111} + 2z_{111(-1)}) + 2y_{0202} + z_{1111} + 2z_{111(-1)}, \quad \text{(A.18)}$$

$$s_3 = 8c_2x_{0202} + 8c_2y_{0202}k - 8c_2z_{1111}k - 15x_{0202}\lambda^2 + x_{0202} + 12y_{0202}\lambda$$
$$- 8y_{0202}k - 18z_{1111}\lambda + 8z_{1111}k, \quad \text{(A.19)}$$

$$s_4 = 2x_{2000}\left(6c_2 - 2k^2 + 3\lambda^2 - 1\right) + x_{0202}\left(2c_2 + 2k^2 + \lambda^2 - 3\right) + \quad \text{(A.20)}$$

$$3c_2k(y_{0202} + z_{1111} + 2z_{111(-1)}) - 2k(z_{1111} + 2z_{111(-1)}) + 2\lambda(z_{1111} + 2z_{111(-1)}) \quad \text{(A.21)}$$

Appendix B

Halo Orbit Coefficients for $N = 3$

The non-zero coefficients are:

$$\omega_{20} = \frac{3\left(c_4\left(-3k^4+8k^2-8\right)-4c_3k^2\left(k^2(x_{2020}-2x_{2000}+4x_{2000}+2x_{2020}+2y_{2020}k)\right)\right)}{8k^2((3c_2-4)k+4\lambda)}, \tag{B.1}$$

$$\omega_{02} = -\frac{3\left(4c_3\left(k^2(x_{0202}-2x_{0200})+4x_{0200}+2x_{0202}+k(2y_{0202}+z_{1111}+2z_{111(-1)})\right)+c_4\left(k^2-12\right)\right)}{8((3c_2-4)k+4\lambda)}, \tag{B.2}$$

$$y_{1210} = \frac{3\left(c_4\left(-26c_2+2k^2-13\lambda^2+11\right)+4c_3s_4\right)}{16\lambda((3c_2-4)k+4\lambda)}, \tag{B.3}$$

$$y_{3010} = \frac{3\left(\frac{2s_1(k-\lambda)}{(3c_2-4)k+4\lambda}+4c_3k^2(4x_{2000}+2x_{2020}+y_{2020}k)-4c_4\left(k^2-2\right)\right)}{16k^3\lambda}, \tag{B.4}$$

$$y_{3030} = -\frac{3\left(k\left(2c_2+9\lambda^2+1\right)\left(4c_3k(x_{2020}k-y_{2020})+c_4\left(k^2+4\right)\right)-8\lambda\alpha\right)}{64k^3\left(-20c_2^2+c_2\left(9\lambda^2+10\right)-18\lambda^2+10\right)}, \tag{B.5}$$

$$\alpha = \left(3k^2(2c_3x_{2020}+c_4)-3c_3y_{2020}k^3+2c_4\right), \tag{B.6}$$

$$x_{3030} = \frac{6c_3k^2\left(8c_2x_{2020}+8c_2y_{2020}k-15x_{2020}\lambda^2+x_{2020}+12y_{2020}\lambda-8y_{2020}k\right)-\frac{1}{8}c_4\beta}{32k^3\left(-20c_2^2+c_2\left(9\lambda^2+10\right)-18\lambda^2+10\right)}, \tag{B.7}$$

$$\beta = \left(414c_2^2+c_2\left(207\lambda^2+127\right)-108k^2+540\lambda^2+8\right) \tag{B.8}$$

$$y_{1212} = \frac{3\left(4c_3\gamma+c_4((8-11c_2)k+6\lambda)\right)}{64\left(\left(11c_2^2+17c_2-28\right)k-18(c_2-2)\lambda\right)}, \tag{B.9}$$

$$\gamma = \left(x_{0202}(11c_2k-8k+6\lambda)+y_{0202}\left(4c_2-6\lambda^2+2\right)-3z_{1111}\left(2c_2+\lambda^2+1\right)\right), \tag{B.10}$$

$$x_{1212} = -\frac{3\left(c_4\left(-10c_2+33\lambda^2+1\right)+4c_3s_3\right)}{64\left(\left(11c_2^2+17c_2-28\right)k-18(c_2-2)\lambda\right)}, \tag{B.11}$$

$$z_{0303} = \frac{3(c_4-4c_3x_{0202})}{8\left(c_2-9\lambda^2\right)}, \tag{B.12}$$

$$z_{2121} = -\frac{3\left(4c_3k(x_{2020}k-z_{1111})+c_4\left(k^2+4\right)\right)}{8k^2\left(c_2-9\lambda^2\right)}, \tag{B.13}$$

$$d_{02} = \frac{3(c_4(-3(c_2-2)k-17\lambda)+2c_3s_2)}{4((3c_2-4)k+4\lambda)}, \tag{B.14}$$

$$d_{20} = \frac{3\left(\frac{2\lambda s_1}{(3c_2-4)k+4\lambda}+8c_3x_{2000}k^2+4c_3x_{2020}k^2-4c_3z_{1111}k-8c_3z_{111(-1)}k-c_4k^2+12c_4\right)}{8k^2}, \tag{B.15}$$

where the following additional abbreviations were used:

$$s_1 = 4c_3k^2\left(k^2(x_{2020} - 2x_{2000}) + 4x_{2000} + 2x_{2020} + 2y_{2020}k\right) + c_4\left(3k^4 - 8k^2 + 8\right), \quad \text{(B.16)}$$

$$s_2 = 6c_2x_{0202}k + 2c_2(2y_{0202} + z_{1111} + 2z_{111(-1)}) + 2\lambda(6x_{2000} + 5x_{0202}) - \quad \text{(B.17)}$$

$$4k(2x_{2000} + x_{0202}) + \lambda^2(2y_{0202} + z_{1111} + 2z_{111(-1)}) + 2y_{0202} + z_{1111} + 2z_{111(-1)}, \quad \text{(B.18)}$$

$$s_3 = 8c_2x_{0202} + 8c_2y_{0202}k - 8c_2z_{1111}k - 15x_{0202}\lambda^2 + x_{0202} + \quad \text{(B.19)}$$

$$12y_{0202}\lambda - 8y_{0202}k - 18z_{1111}\lambda + 8z_{1111}k, \quad \text{(B.20)}$$

$$s_4 = 2x_{2000}\left(6c_2 - 2k^2 + 3\lambda^2 - 1\right) + x_{0202}\left(2c_2 + 2k^2 + \lambda^2 - 3\right) + \quad \text{(B.21)}$$

$$3c_2k(y_{0202} + z_{1111} + 2z_{111(-1)}) - 2k(z_{1111} + 2z_{111(-1)}) + 2\lambda(z_{1111} + 2z_{111(-1)}) \quad \text{(B.22)}$$

Appendix C

In this *Mathematica* notebook the DWS amplification factor for two beams with flat phase front and Gaussian intensity profile is derived. The result is dependend on the photodiode radius and on the two widths of the two beams (which does not need to be equal). It is assumed that the beams are centered on the photodiode and the slit of the quadrant photodiode is neglected.

General Phasefront and Intensity

We start with a very general definition of a rotation matrix:

```
RMUVW[u_, v_, w_] :=
 RotationMatrix[w, {0, 0, 1}].RotationMatrix[v, {0, 1, 0}].RotationMatrix[u, {1, 0, 0}]
```

Then we define a spherical phasefront with radii of curvature Rx and Ry, and with tilt α and tip β. The evaluation point is given in cartesian coordinates x,y on the photodiode, whereby x=0,y=0 is the photodiode center.

```
SphericalWavefront[x_, y_, α_, β_, Rx_, Ry_] :=
 (RMUVW[β, α, 0].{x, y, -(Sqrt[1 - x^2 / Rx^2 - y^2 / Ry^2] - 1) * Rx}).({0, 0, 1})
```

We plot the phasefront: The x,y axes denote the position on the photodiode, while the z-direction is the phase (in units of millimeter)

```
Plot3D[SphericalWavefront[x, y, 0.0, 0.003, 200, 200], {x, -10, 10},
 {y, -10, 10}, PlotRange → {{-10, 10}, {-10, 10}, {-1, 1}}, AxesLabel → {x, y, z}]
```

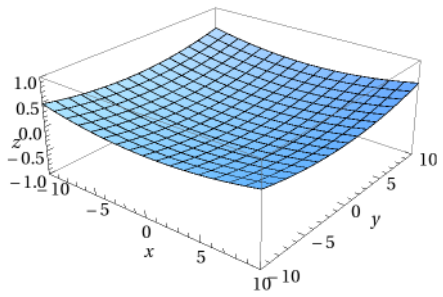

Generate a Gaussian amplitude with tip α and tilt β and with width w0, evaluation point on the photodiode is given in cartesian coordinates x,y

```
AmplGaussian[x_, y_, α_, β_, w0_] :=
 (RMUVW[β, α, 0].{x, y, Exp[-(x^2 + y^2) / w0^2]}).({0, 0, 1})
```

Plot the Gaussian amplitude: the x,y is the position on the photodiode, z-direction denots the amplitude in arbitrary units

```
Plot3D[AmplGaussian[x, y, 0, 0.03, 0.3], {x, -0.5, 0.5},
 {y, -0.5, 0.5}, PlotRange → Full, AxesLabel → {x, y, z}]
```

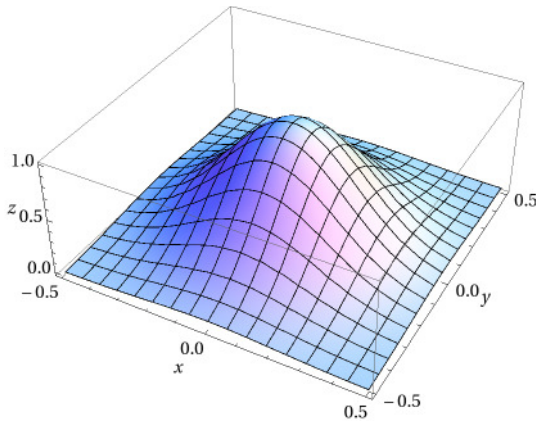

Simplified Phasefront and Amplitude

Now we simplify the spherical phasefront to a flat phasefront (the radii of curvature go to infinity) and we linearize the tilt α and tip β. In addition we switch the evaluation point to polar coordinates r, θ instead of cartesian x,y and we convert the phase to units of radian

```
SimplPhaseFront[r_, θ_, α_, β_] := 2 * Pi / λ *
  Evaluate[Limit[FullSimplify[Normal[Series[SphericalWavefront[x, y, αx, βx, Rx, Ry] /.
            {x → r * Sin[θ], y → r * Cos[θ]}, {αx, 0, 1}, {βx, 0, 1}]]] /.
       {Rx → Ry}, {Ry → Infinity}][[1]] /. {βx → β, αx → α}]
```

```
SimplPhaseFront[r, θ, α, β]
```

$$\frac{2\,\pi\,r\,(\beta\,\text{Cos}[\theta]-\alpha\,\text{Sin}[\theta])}{\lambda}$$

The same for the amplitude:

```
SimplAmplitude[r_, θ_, α_, β_, w0_] :=
 Evaluate[Simplify[Normal[Series[AmplGaussian[x, y, a, b, w0] /.
       {x -> r * Sin[θ], y -> r * Cos[θ]}, {a, 0, 1}, {b, 0, 1}]]] /. {a → α, b → β}]
```

```
SimplAmplitude[r, θ, α, β, w0]
```

$$e^{-\frac{r^2}{w0^2}}+r\,\beta\,\text{Cos}[\theta]-r\,\alpha\,\text{Sin}[\theta]$$

Complex Amplitudes of the Photodiode

We further simplify the problem. We assume that the tip and tilt directions are independent and (due to the symmetry) the DWS amplification factors are equal for both directions. Thus, we consider only the tilt. To get the DWS amplification factor we compute the complex amplitude for the top and for the bottom half of the photodiode.

The real part of the complex amplitude is the spatial integral of "Ampl1*Ampl2*Cos[PhaseDifference]", while the imaginary part is "Ampl1*Ampl2*Sin[PhaseDifference]". In addition we assume that the PhaseDifference is small, such that Cos[PhaseDifference] == 1, and Sin[PhaseDifference] = PhaseDifference. The integration is performed in polar coordinates, therefore a factor r is in the integrand. The domain of integration is the top or bottom half of the photodiode.

PDr is the photodiode radius.

```
CoeffRealTop :=
 Evaluate[Integrate[r * SimplAmplitude[r, θ, α1, 0, w1] * SimplAmplitude[r, θ, α2, 0, w2],
   {r, 0, PDr}, {θ, 0, Pi}]]

CoeffRealBottom :=
 Evaluate[Integrate[r * SimplAmplitude[r, θ, α1, 0, w1] * SimplAmplitude[r, θ, α2, 0, w2],
   {r, 0, PDr}, {θ, Pi, 2 * Pi}]]

CoeffImagTop :=
 Evaluate[Integrate[r * SimplAmplitude[r, θ, α1, 0, w1] * SimplAmplitude[r, θ, α2, 0, w2] *
    (SimplPhaseFront[r, θ, α1, 0] - SimplPhaseFront[r, θ, α2, 0]), {r, 0, PDr}, {θ, 0, Pi}]]

CoeffImagBottom :=
 Evaluate[Integrate[r * SimplAmplitude[r, θ, α1, 0, w1] * SimplAmplitude[r, θ, α2, 0, w2] *
    (SimplPhaseFront[r, θ, α1, 0] - SimplPhaseFront[r, θ, α2, 0]), {r, 0, PDr}, {θ, Pi, 2 * Pi}]]
```

DWS amplifcation factor

The DWS amplification (or signal) is the the phase difference between the top and bottom complex amplitude coefficient, in complex notation simply: ArcTan[c_top / c_bottom]. If we use a small angle approximation, ArcTan is the identity and we can write "ArcTan[c_top / c_bottom] =Ampl[c_top]/Ampl[c_bottom]*Phase[c_top]-Phase[c_bottom]". In the IfoCAD code a factor 1/2 is apparent, since IfoCAD computes the phase for each segment. If the top & bottom half has two segments and the phases are added, the difference needs to be divided by 2.

We assume that the amplitudes on the top and bottom half of the photodiode are almost equal, therefore we can compute the DWS amplification factor approximately as "Phase[c_top]-Phase[c_bottom] = Imag[c_top]/Real[c_top] -Imag[c_bottom]/Real[c_bottom]":

```
Res := Simplify[Normal[Series[
    (CoeffImagBottom / CoeffRealBottom - CoeffImagTop / CoeffRealTop), {α1, 0, 1}, {α2, 0, 1}]]]
```

```
Res
```

$$-\left(4\,(\alpha 1-\alpha 2)\left(2\,\mathrm{PDr}\,\sqrt{w1^2+w2^2}-e^{\mathrm{PDr}^2\left(\frac{1}{w1^2}+\frac{1}{w2^2}\right)}\sqrt{\pi}\;w1\;w2\;\mathrm{Erf}\left[\frac{\mathrm{PDr}\,\sqrt{w1^2+w2^2}}{w1\;w2}\right]\right)\right)\Big/$$
$$\left(\left(-1+e^{\mathrm{PDr}^2\left(\frac{1}{w1^2}+\frac{1}{w2^2}\right)}\right)\sqrt{w1^2+w2^2}\;\lambda\right)$$

Validation

Check the result for two large flat top beams, this should yield the well-known DWS formula: 16/3*(a1-a2)*PDr/ λ

```
Limit[Limit[Res, {w1 → Infinity}], {w2 → Infinity}]
```

$$\left\{\frac{16\;\mathrm{PDr}\;(\alpha 1-\alpha 2)}{3\;\lambda}\right\}$$

The overlap of one flat top with a Gaussian beam yields:

```
Limit[Res, {w1 → Infinity}]
```

$$\left\{\frac{4\;(\alpha 1-\alpha 2)\left(-2\;\mathrm{PDr}+e^{\frac{\mathrm{PDr}^2}{w2^2}}\sqrt{\pi}\;w2\;\mathrm{Erf}\left[\frac{\mathrm{PDr}}{w2}\right]\right)}{\left(-1+e^{\frac{\mathrm{PDr}^2}{w2^2}}\right)\lambda}\right\}$$

The result for the GRACE-Follow On Laser Ranging Interferometer should be roughly 1880

```
Res /. {λ → 1.064*^-3, w1 → 500, w2 → 2.5 / 8, PDr → 0.5}
```

```
1888.41 (α1 - α2)
```

Appendix D:

Analysis of polarization effects in corner-cubes for GRACE-FO interferometry

1 Introduction

In this appendix, first published as Technical Note in January 2012, we analyze polarization effects of three mirrors aligned in a corner-cube configuration considering different mirror materials. Various paper exist on polarization effects of corner-cube retroreflectors ([1], [2], [3] or [4]). Unfortunately the authors usually use local beam coordinate frames, which are aligned with corner-cube faces, while we are interested in space-fixed polarization states. This complicates the comparison of results.

For this analysis an IfoCad version was extended to allow polarization raytracing. We use an extended Jones-Matrix formalism as described in [4] to compute the output polarization vector for different mirror materials. The complex reflectivity and transmittance coefficients for each mirror are computed from well-known Fresnel equations.

2 Setup

We assume an optical bench with normal vector in +x direction. The initial beam direction is +z. After three reflections at the mirror surfaces of the corner-cube, the outgoing beam is anti-parallel to the incoming beam. This property is independent of corner-cube attitude. Also the geometrical pathlength of a beam is invariant under rotations of the corner-cube around the intersection point of all three mirror planes (called 'vertex'). Further information on properties of corner-cubes can be found in [5].

In the GRACE-FO mission a Triple Mirror Assembly (TMA) will be used, which is mainly a corner-cube, where unused mirror surface areas are removed. With other words, the TMA consists of three separated mirrors, where all mirror planes are mutually perpendicular. The position of the mirror center and the normal vectors of the mirror planes define the vertex position.

In [6] the following mirror configuration is given, which we used in our simulations[1].

$$\vec{c}_1 = \begin{pmatrix} 24.000 \\ -300.000 \\ -333.941 \end{pmatrix} \text{mm}, \qquad \vec{c}_2 = \begin{pmatrix} -24.000 \\ -266.058 \\ -300.000 \end{pmatrix} \text{mm}, \qquad \vec{c}_3 = \begin{pmatrix} -24.000 \\ 300.000 \\ -300.000 \end{pmatrix} \text{mm}$$

$$\vec{n}_1 = \begin{pmatrix} -1/\sqrt{2} \\ 0.5 \\ -0.5 \end{pmatrix}, \qquad \vec{n}_2 = \begin{pmatrix} 1/\sqrt{2} \\ 0.5 \\ -0.5 \end{pmatrix}, \qquad \vec{n}_3 = \begin{pmatrix} 0 \\ -1/\sqrt{2} \\ -1/\sqrt{2} \end{pmatrix}$$

The body-diagonal of the corner-cube given by $\vec{n}_d = (\vec{n}_1 + \vec{n}_2 + \vec{n}_2)/3$, which is here not parallel to the input beam direction. This case is referred as non-normal incidence in the literature. In nominal case the beam is reflected at the centers of each mirror. The separation between in- and outgoing beam is 600 mm. The origin of the coordinate system coincides with the vertex of the TMA. The setup is illustrated in figure 1.

The angle of incidence (AOI) at each mirrors is dependent on the orientation of the corner-cube. In nominal case, the AOIs at M1, M2 and M3 are $60.0°, 60.0°, 45.0°$, respectively. The linear

[1] reversed normal vectors were used, because normal vectors point outwards in ifocad

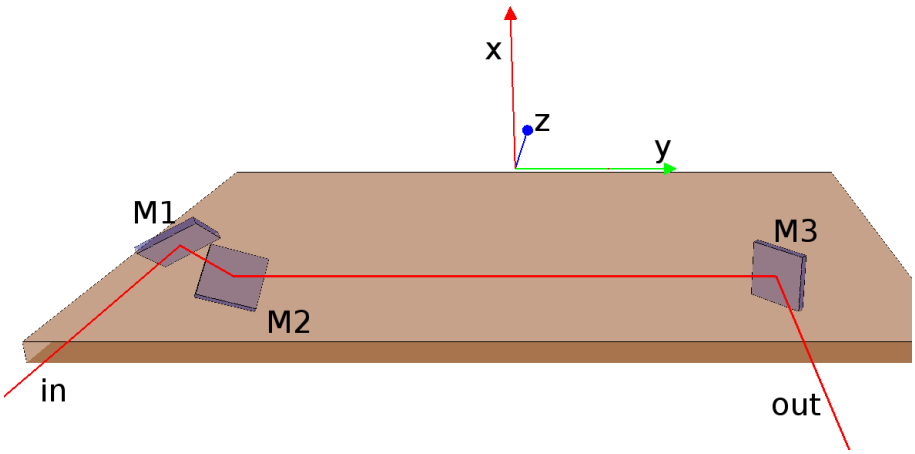

Figure 1: Setup

polarization types p (parallel) and s (perpendicular, german "senkrecht") are defined with respect to the optical bench and for an input beam with wave vector[2] $\vec{k} = \begin{pmatrix} 0 \\ 0 \\ +1 \end{pmatrix}$ given by $\vec{P}_s = \begin{pmatrix} 1 \\ 0 \\ 0 \end{pmatrix}$ and $\vec{P}_p = \begin{pmatrix} 0 \\ 1 \\ 0 \end{pmatrix}$. The first two components of the polarization vector correspond to the Jones vector, if the propagation direction is along the z-direction.

3 Material constants

At each mirror we assume direct reflection at a single thick layer of metal. The (real) refractive index and the extinction coefficient for considered metals are shown in figure 2.

The laser wavelength is assumed to be 1064 nm. The following configurations were simulated:

Material	real refractive index	extinction coefficient
Gold (Au)	0.28519	7.3536
Silver (Ag)	0.23424	7.2143
Aluminum (Al)	1.37628	10.245
Non-Absorbing (NA)	1.4000	0.000

4 Polarization Matrices

The polarization matrix $\hat{\mathbb{P}}$ describes the change of a polarization vector $\vec{P}_{\text{in}}$ upon reflection (or transmission), furthermore it transforms the wave vector:

$$\hat{\mathbb{P}}\vec{P}_{\text{in}} = \vec{P}_{\text{out}} \quad , \quad \hat{\mathbb{P}}\vec{k}_{\text{in}} = \vec{k}_{\text{out}}.$$

The polarization matrix of an optical system like a corner-cube is the product of single polarization matrices $\hat{\mathbb{P}} = \hat{\mathbb{P}}_3 \cdot \hat{\mathbb{P}}_2 \cdot \hat{\mathbb{P}}_1$ ([4]). A polarization matrix is only valid for one particular wave vector $\vec{k}$, but it is independent of the input polarization vector.

The polarization matrices for each scenario are:

$$\hat{\mathbb{P}}_{\text{Au}} = \begin{pmatrix} 0.96368 \cdot e^{56.49310°\,i} & 0.02344 \cdot e^{53.24253°\,i} & 0.00000 \\ 0.02328 \cdot e^{-115.98516°\,i} & 0.96556 \cdot e^{52.52696°\,i} & 0.00000 \\ 0.00000 & 0.00000 & 1.00000 \cdot e^{-180.00000°\,i} \end{pmatrix}$$

[2] wave vectors are always normalized in this document

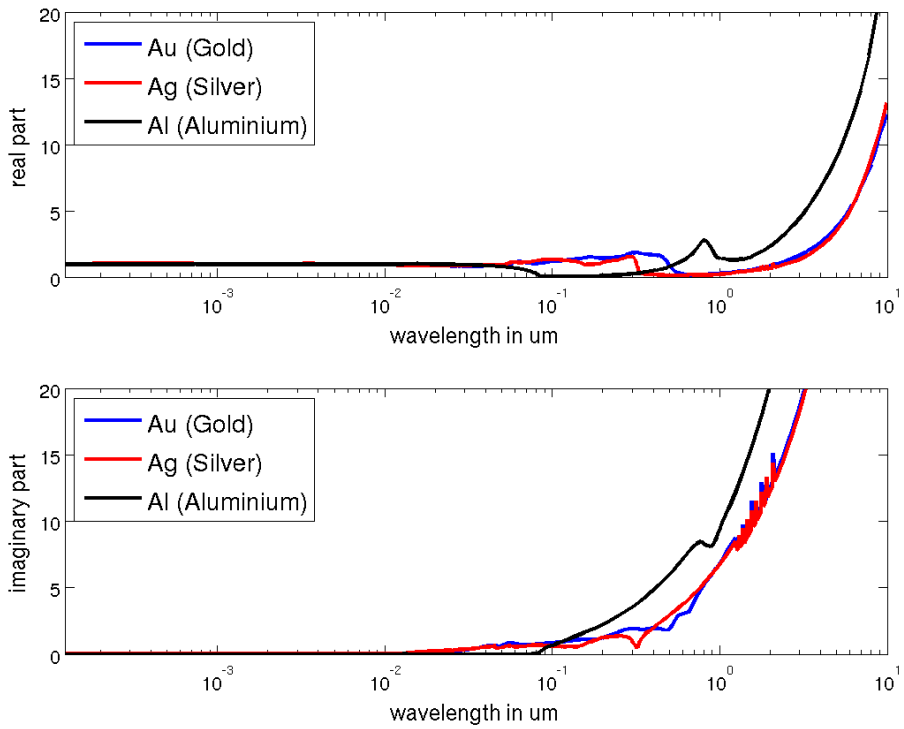

Figure 2: real and imaginary part of refractive index for different materials, source: http://refractiveindex.info

$$\hat{\mathbb{P}}_{\mathrm{Ag}} = \begin{pmatrix} 0.96892 \cdot e^{57.56275^\circ i} & 0.02441 \cdot e^{53.50263^\circ i} & 0.00000 \\ 0.02427 \cdot e^{-115.52158^\circ i} & 0.97050 \cdot e^{53.54087^\circ i} & 0.00000 \\ 0.00000 & 0.00000 & 1.00000 \cdot e^{-180.00000^\circ i} \end{pmatrix}$$

$$\hat{\mathbb{P}}_{\mathrm{Al}} = \begin{pmatrix} 0.91920 \cdot e^{36.34309^\circ i} & 0.00441 \cdot e^{47.96650^\circ i} & 0.00000 \\ 0.00437 \cdot e^{-127.79751^\circ i} & 0.92397 \cdot e^{34.00669^\circ i} & 0.00000 \\ 0.00000 & 0.00000 & 1.00000 \cdot e^{-180.00000^\circ i} \end{pmatrix}$$

$$\hat{\mathbb{P}}_{\mathrm{NA}} = \begin{pmatrix} 0.00973 \cdot e^{180.00000^\circ i} & 0.00872 \cdot e^{180.00000^\circ i} & 0.00000 \\ 0.00243 \cdot e^{0.00000^\circ i} & 0.00125 \cdot e^{0.00000^\circ i} & 0.00000 \\ 0.00000 & 0.00000 & 1.00000 \cdot e^{180.00000^\circ i} \end{pmatrix}$$

The first column of the polarization matrices corresponds to the outgoing polarization for a s-polarized input. The second column for the p-polarized case. The electric field amplitude of the outgoing beam for s-polarized input light can be plotted easily, as shown in fig. 3 for aluminum. The polarization vector $(0.91920 \cdot e^{36.34309^\circ i}, 0.00437 \cdot e^{-127.79751^\circ i}, 0)^T$ depicted on the figure is elliptical left-circulating[3]. Please note, that the x-y-amplitude scale is unequal and hence the ellipticity is exaggerated on this plot.

5 Polarization change

In fig. 4 the outgoing polarization ellipses for p- and s-polarized inputs are illustrated. The numerical values can be found in table 1 and 2. The amount of depolarization (transfer of power from one linear polarization into the orthogonal polarization) is for both kinds of input similar. However, the retardation is for the p-input almost 0° leading to linear polarization. Also the overall reflectivity is higher for p-light.

[3]two different conventions exist on definition of direction of rotation

An interesting result is obtained for the Non-Absorbing scenario. For p-input the outgoing beam is s-polarized. For s-polarized input the outgoing beam is also s-polarized, but with a phase shift of 180° as stated in [5]. Due to the low reflectivity in this case, this scenario is more of academic nature and for validation of the method.

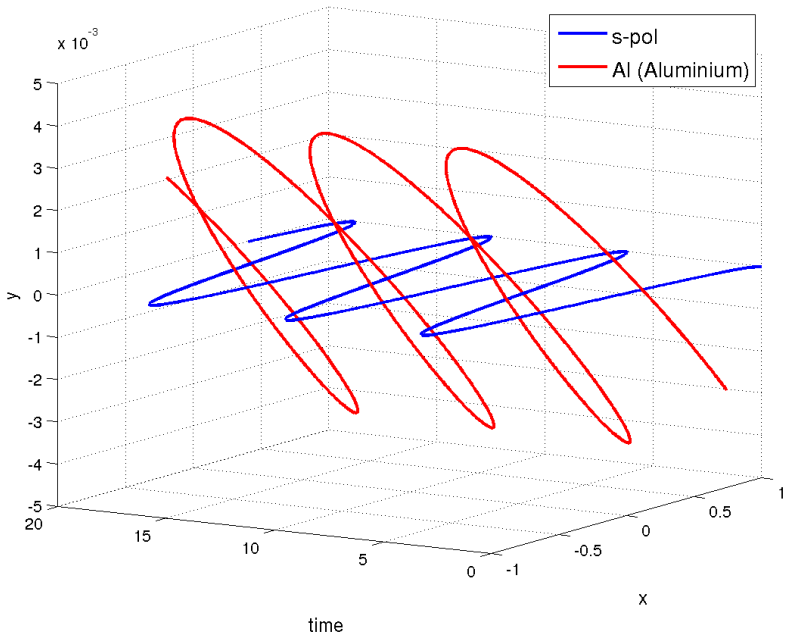

Figure 3: Electric field amplitude of outgoing beam for s-polarized input. The outgoing beam is left-circulating. The axes scaling is unequal.

6 Polarization induced phase changes

The geometrical pathlength of a beam passing through a corner-cube is **independent** of rotations around the corner cube vertex. However, the phase of the light will change due to attitude dependent polarization effects. If the corner cube or TMA is rotated, the phase and amplitude terms in the polarization matrices will change, resulting in an overall change of phase and amplitude. Assuming an interferometric length measurement, the phase change can be expressed as equivalent optical pathlength change.

In this section we estimate coupling factors of rotations into the optical pathlength due to polarization effects. Therefore the TMA is rotated around the vertex and around the X, Y and Z axis independently from $-1\,\mathrm{mrad}$ to $+1\,\mathrm{mrad}$. The time series of rotation angles and changes in AOIs are depicted in fig. 5. The w-rotation corresponds to a roll-rotation of the spacecraft and does not change the incidence angles (the wave vector of in- and outgoing beam is parallel to z-axis).

The phase change of silver is shown in fig. 6 for different input and detection (output) polarization states. One should notice that the phase for crossed polarizations (s-input and p-detection or vice versa) is more sensitive on rotations, but the outgoing beam power is very low in these cases, as stated in the previous section. All coupling factors are summarized in table 3. The amplitude is almost constant during rotations and hence not further investigated here.

References

[1] M.A. Player *Polarization Properties of a Cube-Corner Reflector* 1988: Journal of Modern Optics, Vol. 35

[2] J. Liu, R.M.A. Azzam *Polarization properties of corner-cube retroreflectors: theory and experiment* 1996: Applied Optics Vol. 36

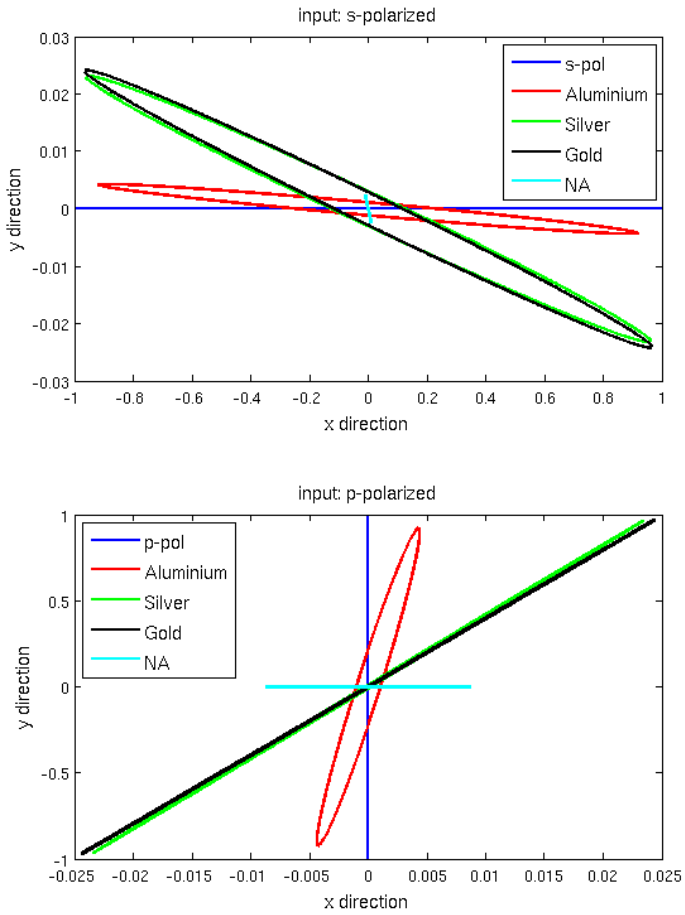

Figure 4: Outgoing beam amplitudes for s- and p-polarized input beams.

[3] Marija Scholl *Ray trace through corner-cube retroreflector with complex reflection coefficients* 1995: Applied Optics Vol. 12

[4] G. Yun, K. Crabtree, R.A. Chipman *Three-dimensional ray-tracing calculus I: definition and diattenuation* 2011: Applied Optics, Vol. 50

[5] GR-AEI-TN-1002 *The GRACE-C Interferometer* internal document

[6] STI: GRACE FO LRI *Optical Desing and Tolerances* internal document

	Aluminum	Silver	Gold	Non-Absorbing
In-Power	1.000	1.000000	1.000000	1.000000
Power-Out-s	0.844923	0.938803	0.928690	0.000095
Power-Out-p	0.000019	0.000589	0.000542	0.000006
Ellipse Major Axis Power	0.844941	0.939384	0.929223	0.000101
Ellipse Minor Axis Power	0.000001	0.000009	0.000009	0.000000
|Ellipticity Angle|	0.06°	0.18°	0.18°	0.00°
Phase Difference s-p	−164.18 °	−173.09 °	−172.47 °	−180.00 °
Rotation Angle of Ellipse	−0.26 °	−1.42 °	−1.37 °	−14.02 °
Polarization Type	weakly elliptical left-circulating			linear

Table 1: Polarization parameter of outgoing beam for s-input.

	Aluminum	Silver	Gold	Non-Absorbing
In-Power	1.000000	1.000000	1.000000	1.000000
Power-Out-s	0.000019	0.000596	0.000550	0.000076
Power-Out-p	0.853715	0.941864	0.932305	0.000002
Ellipse Major Axis Power	0.853734	0.942460	0.932854	0.000078
Ellipse Minor Axis Power	0.000001	0.000000	0.000000	0.000000
|Ellipticity Angle|	0.06°	0.00°	0.00°	0.00°
Phase Difference s-p	−13.94 °	0.04 °	−0.71 °	−180.00 °
Rotation Angle of Ellipse	−0.27 °	−1.44 °	−1.39 °	−98.16 °
Polarization Type	weakly elliptical right-circulating	almost linear		linear

Table 2: Polarization parameter of outgoing beam for p-input.

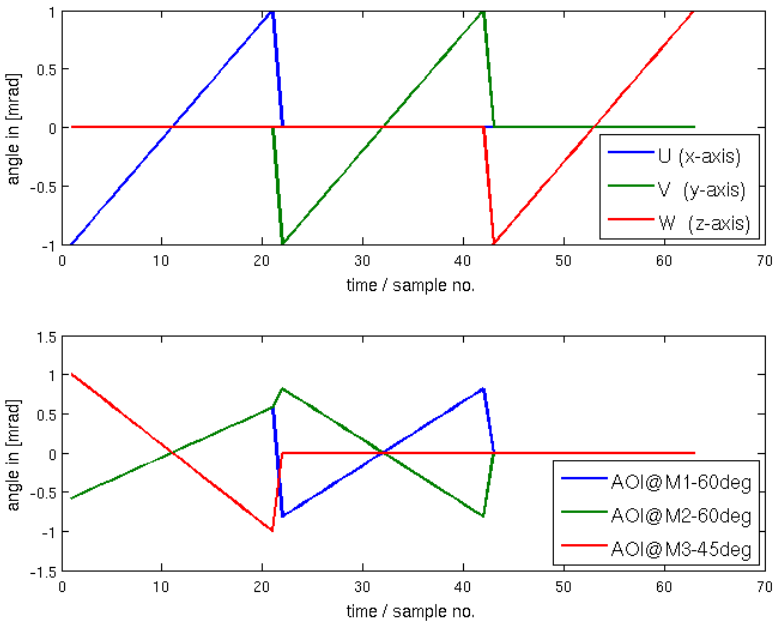

Figure 5: Rotation angles of TMA (top) and change in angle of incidence on each mirror.

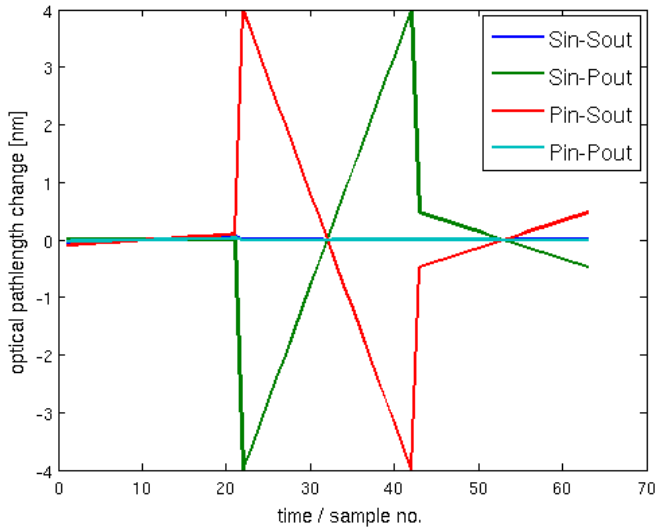

Figure 6: Phase change expressed as pathlength variation for silver.

	Aluminum				Silver		
In-Out	U	V	W		U	V	W
s-s	0.00316	< 0.0001	< 0.0001		0.0714	-0.0008	0.0008
p-p	0.0053	< 0.0001	< 0.0001		0.0251	0.0008	-0.0008
s-p	-0.0038	11.3736	-1.4478		-0.0014	3.9921	-0.4709
p-s	0.0382	-11.3739	1.4481		0.0953	-3.9927	0.4714
	Gold				Non-Absorbing		
In-Out	U	V	W		U	V	W
s-s	0.0703	-0.0008	0.0008		0.0000	0.0000	0.0000
p-p	0.0247	0.0008	-0.0008		0.0000	0.0000	0.0000
s-p	-0.0015	4.0679	-0.4812		0.0000	0.0000	0.0000
p-s	0.0935	-4.0685	0.4818		0.0000	0.0000	0.0000

Table 3: coupling factors in units of nm/mrad due to attitude dependent polarization effects

Appendix E

Time-dependent offset frequency

In this section we evaluate the effect of a time-dependent offset frequency on the phase-derived range measurement. The current plan for GRACE Follow-On LRI foresees a constant offset frequency, however future missions might require a variable offset frequency to keep the beatnote within a certain band, e.g. when pendulum orbits with higher Doppler rates are used. We assume a relative velocity $v_r(t)$ between the spacecrafts given by

$$v_r(t) = v_{\max} \cdot \sin\left(\frac{2\pi}{T}t\right), \tag{E.1}$$

where $v_{\max} = 8\,\mathrm{m/s}$ is the maximal relative velocity and $T = 5666\,\mathrm{s}$ is the orbital period. Thus the biased inter-satellite distance can be written as

$$\rho_{\mathrm{real}}(t) = \int_0^t v_r(t')\ dt'. \tag{E.2}$$

The phase provided by the phasemeter was defined as (eq. (3.9))

$$\Psi(t) = 2\pi \int_0^t f_{\mathrm{PD}}^{\mathrm{master}}(t') - f'_{\mathrm{off}}\ dt' \approx 2\pi \int_0^t f_{\mathrm{off}} - 2v_r(t')\left(\frac{1}{\lambda} + \frac{f_{\mathrm{off}}}{2c}\right) - f'_{\mathrm{off}}\ dt'. \tag{E.3}$$

As in section 3.1.2, we assume that the offset frequency subtracted on the master spacecraft f'_{off} is equal to the offset frequency used in the PLL on the slave spacecraft f_{off}, but time dependent according to

$$f_{\mathrm{off}}(t) = f'_{\mathrm{off}}(t) = f_a \cdot \sin\left(\frac{2\pi}{T}t + \varphi\right) + f_0, \tag{E.4}$$

where $f_0 = 7.5\,\mathrm{MHz}$ is an offset frequency and $f_a = 10\,\mathrm{MHz}$ is the amplitude of the frequency modulation. Choosing the phase offset $\varphi = 0\,\mathrm{rad}$ provides a beatnote on the master spacecraft within 2...15 MHz.
Furthermore, we account for a time offset δt, such that the measured phase can be written as:

$$\Psi(t) \approx 2\pi \int_0^t f_{\mathrm{off}}(t) - 2v_r(t')\left(\frac{1}{\lambda} + \frac{f_{\mathrm{off}}(t)}{2c}\right) - f_{\mathrm{off}}(t+\delta t)\ dt'. \tag{E.5}$$

The difference between phase-derived and real range is then

$$\delta\rho(t) := \frac{-1}{2 \cdot k}\Psi(t) - \rho_{\mathrm{real}}(t), \tag{E.6}$$

where the approximated wave number $k = 2\pi/\lambda$ is used to relate the phase to a length measurement. With straight forward algebraic manipulation one obtains for $\delta t = 0$:

$$\delta\rho(t) = \text{offset} - \frac{f_0 \cdot T \cdot v_{\max} \cdot \lambda}{4 \cdot c \cdot \pi} \cos\left(\frac{2\pi}{T}t\right) - \frac{f_a \cdot T \cdot v_{\max} \cdot \lambda}{16 \cdot c \cdot \pi} \sin\left(\frac{4\pi}{T}t + \varphi\right) \quad \text{(E.7)}$$

$$\approx \text{offset} - 96\,\mu\text{m} \cdot \cos\left(\frac{2\pi}{T}t\right) - 32\,\mu\text{m} \cdot \sin\left(\frac{4\pi}{T}t\right) \quad \text{(E.8)}$$

Two sinusoidal signals, so-called tones, with orbital and twice the orbital frequency are present in the phase-derived range. If the Doppler shift velocity is expanded to higher orders (in eq. (3.7)) also higher harmonics would appear. The tones are caused by the fact that the wave number is assumed to be constant in the computation of the range. However, the phase-derived length measurement can be corrected for these tones in post-processing.
Another difficulty might be caused by time-jitter, which is assumed here to be the delay between real offset frequency of the PLL on the slave S/C and the subtracted offset frequency on the master S/C. The first order series expansion yields:

$$\frac{\partial\delta\rho(t)}{\partial\delta t} = \text{offset}(t) - f_a \cdot \lambda \cdot \frac{\sin\left(\frac{2\pi}{T}t + \varphi\right) - \sin(\varphi)}{4\pi}\delta t + \mathcal{O}(\delta t^2) \quad \text{(E.9)}$$

$$= \text{offset}(t) - 0.84\,\text{m/s} \cdot (\sin(2 \cdot \pi \cdot t/T + \varphi) - \sin(\varphi)) \cdot \delta t + \mathcal{O}(\delta t^2). \quad \text{(E.10)}$$

As one can see, the coupling into the phase-derived length is 0.84 m/s and might require a time-jitter at ns/$\sqrt{\text{Hz}}$ level to produce a length fluctuation at nm/$\sqrt{\text{Hz}}$ level. However, current plans suggest a constant offset frequency, such that these difficulties are obsolete.

Appendix F:

A note on TMA mirror misalignments for the GRACE Follow-On Laser Ranging Interferometer (GFO LRI)

1 Introduction

In this document we analyze the effect of TMA mirror misalignments in the GFO LRI on the beam parallelism and on the coupling coefficients of rotations into (optical) pathlength. The analysis is based on analytical raytracing, omitting any polarization effects of corner-cubes, refractive index changes or spatial extension of laser light.

The analysis was realized in `Mathematica`.

2 Analytical Raytracing

Here we derive some basic ideas of analytical raytracing, which are applied in the next subsections. Throughout this document computations are performed in the Euclidean space $\mathbb{R}^3$, meaning that vectors have three components and matrices, which are denoted with a hat $\widehat{M}$, have the dimension 3×3.

We define a laser beam as a straight line, parameterized by some parameter l, a beam direction $\vec{d}$ and a beam origin at position $\vec{p}$:

$$\vec{b}(l) := \vec{p} + l \cdot \vec{d}. \tag{1}$$

A mirror is defined in this document as a plane, given by a mirror center $\vec{c}$ and a mirror normal vector $\vec{n}$. We note that a plane can be parameterized with $M(\vec{c}, \vec{n}, \vec{x}) = 0$ (*Hesse normal form* of a plane), where the function M is given by

$$M(\vec{c}, \vec{n}, \vec{x}) := \vec{n} \cdot \vec{x} - \vec{c} \cdot \vec{x}, \tag{2}$$

with $\vec{x} = (x, y, z)^\mathsf{T}$. When a light ray is reflected at a mirror it changes the direction according to

$$\vec{d}_{\text{out}} = \hat{D}(\vec{n}) \cdot \vec{d}_{\text{in}}, \tag{3}$$

with

$$\hat{D}(\vec{n}) := -\widehat{R}(180°, \vec{n}), \tag{4}$$

where $\widehat{R}(180°, \vec{n})$ is a rotation matrix for a rotation around the axis $\vec{n}$ by 180°. The intersection (reflection) point of a ray at a mirror can be computed by solving

$$M(\vec{c}, \vec{n}, \vec{b}(l)) = M(\vec{c}, \vec{n}, \vec{p} + l \cdot \vec{d}) = 0 \tag{5}$$

for the parameter l:

$$l_s = L(\vec{c}, \vec{n}, \vec{p}, \vec{d}) := \frac{(\vec{c} - \vec{p}) \cdot \vec{n}}{\vec{n} \cdot \vec{d}}. \tag{6}$$

The intersection point is then $\vec{b}(l_s)$. All these functions can be easily implemented in an algebraic manipulation program.

3 The Nominal Setup

We analyze the propagation of a light ray through a hollow corner-cube retro-reflector consisting of three mirrors M_1, M_2 and M_3 given by the following mirror centers $\vec{c}_i$ and the mirror normal vector $\vec{n}_i$ [4]:

$$\vec{c}_1 := \begin{pmatrix} 300.0 \\ 300.0 \\ -24.0 \end{pmatrix} \text{mm}, \qquad \vec{c}_2 := \begin{pmatrix} 300.0 \\ -266.0588745 \\ -24.0 \end{pmatrix} \text{mm}, \qquad \vec{c}_3 := \begin{pmatrix} 333.9411255 \\ -300.0 \\ 24 \end{pmatrix} \text{mm}, \tag{7}$$

$$\vec{n}_1 := \begin{pmatrix} 1/\sqrt{2} \\ -1/\sqrt{2} \\ 0 \end{pmatrix}, \qquad \vec{n}_2 := \begin{pmatrix} 0.5 \\ 0.5 \\ 1/\sqrt{2} \end{pmatrix}, \qquad \vec{n}_3 := \begin{pmatrix} 0.5 \\ 0.5 \\ -1/\sqrt{2} \end{pmatrix}. \tag{8}$$

The setup is depicted in fig. 1. The nominal vertex $\vec{V}_{\text{nom}}$ of the TMA, in other words the intersection point of all three mirror planes, can be computed by the well-known formula

$$\vec{V}_{\text{nom}}(\vec{c}_1, \vec{n}_1, \vec{c}_2, \vec{n}_2, \vec{c}_3, \vec{n}_3) := \frac{(\vec{c}_1 \cdot \vec{n}_1) \cdot (\vec{n}_1 \times \vec{n}_3) + (\vec{c}_2 \cdot \vec{n}_2) \cdot (\vec{n}_3 \times \vec{n}_1) + (\vec{c}_3 \cdot \vec{n}_3) \cdot (\vec{n}_1 \times \vec{n}_2)}{|\vec{n}_1 \vec{n}_2 \vec{n}_3|}, \tag{9}$$

where $|\vec{n}_1 \vec{n}_2 \vec{n}_3|$ is the determinant of a matrix created by writing $\vec{n}_i$ side-by-side [1]. We note that the nominal vertex for this particular setup is at the origin $(0, 0, 0)^\mathsf{T}$mm.

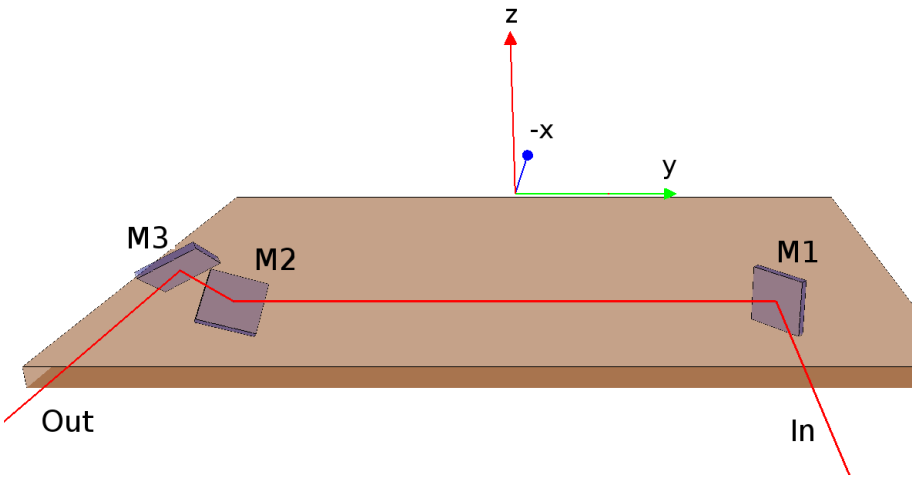

Figure 1: Ray propagation through a hollow corner-cube.

We define the initial ray at a position $\vec{b}_0$ as

$$\vec{b}_0(l) := \vec{p}_0 + l \cdot \vec{d}_0 = \begin{pmatrix} x_0 \\ 300.0 + y_0 \\ -24.0 + z_0 \end{pmatrix} \text{mm} + l \cdot \begin{pmatrix} -1 \\ 0 \\ 0 \end{pmatrix}, \tag{10}$$

where $x_0 > 300.0\,\text{mm}$ is a variable for the distance between the corner-cube and the origin of the ray. The paramters y_0, z_0 describe a lateral displacement of the initial ray w.r.t. the nominal optical axis. The initial ray $\vec{b}_0$ is reflected at M_1 into a ray called $\vec{b}_1$, which is reflected at M_2 into a ray $\vec{b}_2$, which is again reflected at M_3 into the final ray $\vec{b}_3$. The angle of incidence on M_1 is 45° and at M_2 and M_3 it is 60°.

In addition we assume a virtual plane, which is normal to the direction of the initial ray $\vec{b}_0$ and intersects with the origin of the initial ray. The final ray $\vec{b}_3$ intersects with the virtual plane and is terminated at that point. In total we obtain four ray segments. The first ray length l_0 can be computed using eq. (6):

$$l_0 = L(\vec{c}_1, \vec{n}_1, \vec{p}_0, \vec{d}_0). \tag{11}$$

Then one can write ray $\vec{b}_1$ as

$$\vec{b}_1(l) = \vec{p}_1 + l\vec{d}_1 = \vec{b}_0(l_0) + l \cdot \widehat{D}(\vec{n}_1) \cdot \vec{d}_0. \tag{12}$$

The ray segment length l_1 can be computed again using eq. (6). Iteratively, one can derive all beams until $\vec{b}_3$. The final beam $\vec{b}_3$ is a function of all mirrors. Its direction can be written as

$$\vec{d}_3 = \widehat{D}(\vec{n}_3) \cdot \widehat{D}(\vec{n}_2) \cdot \widehat{D}(\vec{n}_1) \cdot \vec{d}_0, \tag{13}$$

where $\vec{d}_0$ is simply $(-1, 0, 0)^\mathsf{T}$. Since the nominal setup assumes a perfect retro-reflector, the final direction is anti-parallel to the incoming beam:

$$\vec{d}_3 = \begin{pmatrix} 1 \\ 0 \\ 0 \end{pmatrix}, \tag{14}$$

which follows directly from the fact that

$$\widehat{D}(\vec{n}_3) \cdot \widehat{D}(\vec{n}_2) \cdot \widehat{D}(\vec{n}_1) = -\widehat{\mathbb{1}} \tag{15}$$

for three mutually orthogonal (and normalized) vectors $\vec{n}_1,\ \vec{n}_2,\ \vec{n}_3$, when computed using eq. (4).

The final beam intersects with the virtual plane at

$$\vec{b}_3(l_3) = \begin{pmatrix} x_0 \\ -300.0 - y_0 \\ 24.0 - z_0 \end{pmatrix}, \tag{16}$$

showing that the corner-cube produces a lateral displacement of 620 mm (when $y_0 = z_0 = 0$). The (optical) pathlength ρ through the setup is the sum of all segments,

$$\rho(\vec{c}_1, \vec{n}_1, \vec{c}_2, \vec{n}_2, \vec{c}_3, \vec{n}_3) = l_0(\vec{c}_1, \vec{n}_1) + l_1(l_0, \vec{c}_2, \vec{n}_2) + l_2(l_1, \vec{c}_3, \vec{n}_3) + l_3, \tag{17}$$

and simplifies in the nominal setup to $2 \cdot x_0$ (twice the distance virtual plane-vertex). With eq. (17) a lengthy analytical expression for the pathlength can be computed in finite time.

4 TMA Rotations

We now introduce the rotation angles u for roll, v for pitch and w for yaw and the rotation matrix

$$\widehat{R}(u, v, w) = \widehat{R}\left(u, (1, 0, 0)^\mathsf{T}\right) \cdot \widehat{R}\left(v, (0, 1, 0)^\mathsf{T}\right) \cdot \widehat{R}\left(w, (0, 0, 1)^\mathsf{T}\right), \tag{18}$$

which is composed of elementary rotation matrices for rotations around the x, y and z direction. Since the angles u, v, w are small, the rotation matrices commute and the order of rotations does not matter. The TMA mirrors shall rotate around a point $\vec{\delta} = (\delta x, \delta y, \delta z)^\mathsf{T}$ and not around the origin (or nominal TMA vertex). The transformation of each mirror can be written as

$$\vec{n}_i(u, v, w) = \widehat{R}(u, v, w) \cdot \vec{n}_i, \tag{19}$$

$$\vec{c}_i(u, v, w) = \widehat{R}(u, v, w) \cdot (\vec{c}_i - \vec{\delta}) + \vec{\delta}. \tag{20}$$

Since rotations of all three normal vectors maintain the orthogonality of the vectors, the final beam direction is invariant under TMA rotations:

$$\vec{d}_3 = \widehat{D}(\vec{n}_3(u, v, w)\ ) \cdot \widehat{D}(\vec{n}_2(u, v, w)\ ) \cdot \widehat{D}(\vec{n}_1(u, v, w)\ ) \cdot \vec{d}_0 = \begin{pmatrix} 1 \\ 0 \\ 0 \end{pmatrix}. \tag{21}$$

The optical pathlength ρ is a lengthy expression, therefore we expand it in a series up to second order in $u,\ v,\ w$ and obtain (see also [3])

$$\begin{aligned} &\rho(\ \vec{c}_1(u, v, w),\ \vec{n}_1(u, v, w),\ \vec{c}_2(u, v, w),\ \vec{n}_2(u, v, w),\ \vec{c}_3(u, v, w),\ \vec{n}_3(u, v, w)\ ) \\ &\approx 2 \cdot x_0 + \begin{pmatrix} 0 \\ 2 \cdot \delta z \\ -2 \cdot \delta y \end{pmatrix} \cdot \begin{pmatrix} u \\ v \\ w \end{pmatrix} + \begin{pmatrix} 0 \\ -\delta x \\ -\delta x \end{pmatrix} \cdot \begin{pmatrix} u^2 \\ v^2 \\ w^2 \end{pmatrix}. \end{aligned} \tag{22}$$

The first term is again twice the distance between virtual plane and vertex. We should note that interferometrically one can only measure changes of x_0. The second term contains the linear coupling and the third term the quadratic coupling of rotations into the pathlength. The offset between point of rotation and vertex $(\delta x, \delta y, \delta z)$ should be kept small to minimize coupling of spacecraft rotations into optical pathlength.

5 TMA mirror misalignments

To incorporate TMA mirror misalignments we transform eq. (7) and (8) to a local TMA frame, which has the same origin as the spacecraft frame (the nominal TMA vertex $\vec{V}_{\mathrm{nom}} = (0,0,0)^{\mathsf{T}}$), but is aligned with the normal vectors of the TMA. The mirror centers become

$$\begin{aligned}
\vec{c}_{1,\mathrm{loc}} &:= \widehat{R}^{-1}_{\mathrm{TMA}\to\mathrm{SC}} \cdot (\vec{c}_1 - \vec{V}_{\mathrm{nom}}) + \vec{V}_{\mathrm{nom}} = \begin{pmatrix} 0 \\ 316.970563 \\ 283.029437 \end{pmatrix} \mathrm{mm}, \\
\vec{c}_{2,\mathrm{loc}} &:= \widehat{R}^{-1}_{\mathrm{TMA}\to\mathrm{SC}} \cdot (\vec{c}_2 - \vec{V}_{\mathrm{nom}}) + \vec{V}_{\mathrm{nom}} = \begin{pmatrix} 400.264069 \\ 33.941125 \\ 0 \end{pmatrix} \mathrm{mm}, \\
\vec{c}_{3,\mathrm{loc}} &:= \widehat{R}^{-1}_{\mathrm{TMA}\to\mathrm{SC}} \cdot (\vec{c}_3 - \vec{V}_{\mathrm{nom}}) + \vec{V}_{\mathrm{nom}} = \begin{pmatrix} 448.264069 \\ 0 \\ 33.941125 \end{pmatrix} \mathrm{mm}, \qquad (23)
\end{aligned}$$

$$(24)$$

and the normal vectors transform to

$$\begin{aligned}
\vec{n}_{1,\mathrm{loc}} &:= \widehat{R}^{-1}_{\mathrm{TMA}\to\mathrm{SC}} \cdot \vec{n}_1 = \begin{pmatrix} 1 \\ 0 \\ 0 \end{pmatrix}, \\
\vec{n}_{2,\mathrm{loc}} &:= \widehat{R}^{-1}_{\mathrm{TMA}\to\mathrm{SC}} \cdot \vec{n}_2 = \begin{pmatrix} 0 \\ 0 \\ 1 \end{pmatrix}, \\
\vec{n}_{3,\mathrm{loc}} &:= \widehat{R}^{-1}_{\mathrm{TMA}\to\mathrm{SC}} \cdot \vec{n}_3 = \begin{pmatrix} 0 \\ 1 \\ 0 \end{pmatrix}. \qquad (25)
\end{aligned}$$

The rotation matrix is given by

$$\widehat{R}^{-1}_{\mathrm{TMA}\to\mathrm{SC}} := \begin{pmatrix} \leftarrow & \vec{n}_1 & \rightarrow \\ \leftarrow & \vec{n}_3 & \rightarrow \\ \leftarrow & \vec{n}_2 & \rightarrow \end{pmatrix} = \widehat{R}(-\alpha, \vec{q}), \qquad (26)$$

where the order of vectors was swapped to obtain a right-handed system and a matrix determinant of $+1$. The rotation axis $\vec{q}$ is the eigenvector of $\widehat{R}^{-1}_{\mathrm{TMA}\to\mathrm{SC}}$ to the eigenvalue 1, while the angle of rotation can be computed using the trace of the matrix:

$$\mathrm{tr}\left(\widehat{R}^{-1}_{\mathrm{TMA}\to\mathrm{SC}}\right) = 1 + 2 \cdot \cos(-\alpha). \qquad (27)$$

We introduce for each mirror a small tip and tilt misalignment denoted by angles α_i and β_i, such that

$$\begin{aligned}
\vec{n}^{\,e}_{1,\mathrm{loc}} &:= \begin{pmatrix} 1 \\ \alpha_1 \\ \beta_1 \end{pmatrix}, \\
\vec{n}^{\,e}_{2,\mathrm{loc}} &:= \begin{pmatrix} \alpha_2 \\ \beta_2 \\ 1 \end{pmatrix}, \\
\vec{n}^{\,e}_{3,\mathrm{loc}} &:= \begin{pmatrix} \alpha_3 \\ 1 \\ \beta_3 \end{pmatrix}. \qquad (28)
\end{aligned}$$

Finally, we transform the error-prone normal vectors back to the spacecraft frame according to

$$\vec{n}^{\,e}_i := \widehat{R}_{\mathrm{TMA}\to\mathrm{SC}} \cdot \vec{n}^{\,e}_{i,\mathrm{loc}} = \widehat{R}(+\alpha, \vec{q}) \cdot \vec{n}^{\,e}_{i,\mathrm{loc}}. \qquad (29)$$

We should note that there exists now a *true* vertex (see eq. (9))

$$\vec{V}_{\text{true}}(\vec{c}_1,\vec{n}_1^e,\vec{c}_2,\vec{n}_2^e,\vec{c}_3,\vec{n}_3^e) \overset{\text{linearized}}{\approx} \begin{pmatrix} \begin{pmatrix}224.132\\200.132\\224.132\end{pmatrix}\cdot\vec{\alpha}+\begin{pmatrix}200.132\\16.9706\\16.9706\end{pmatrix}\vec{\beta} \\ \begin{pmatrix}-224.132\\200.132\\200.132\end{pmatrix}\cdot\vec{\alpha}+\begin{pmatrix}-200.132\\16.9706\\16.9706\end{pmatrix}\vec{\beta} \\ \begin{pmatrix}0.\\283.029\\-316.971\end{pmatrix}\cdot\vec{\alpha}+\begin{pmatrix}0.\\24.0\\-24.0\end{pmatrix}\vec{\beta} \end{pmatrix} \text{mm}, \tag{30}$$

with $\vec{\alpha}=(\alpha_1,\alpha_2,\alpha_3)^\mathsf{T}$ and $\vec{\beta}=(\beta_1,\beta_2,\beta_3)^\mathsf{T}$ being the mirror misalignments in radian. The true vertex is accessible, e.g. by measuring the mirror planes physically with a coordinate measurement machine, while the nominal vertex $\vec{V}_{\text{nom}}$ is purely virtual and not a good reference point anymore.

As we will see subsequently the relative angles γ_1, γ_2 and γ_3 between the mirror planes are a helpful quantity:

$$\vec{\gamma}=\begin{pmatrix}\gamma_1\\\gamma_2\\\gamma_3\end{pmatrix}=\begin{pmatrix}\alpha_1+\alpha_3\\\alpha_2+\beta_1\\\beta_2+\beta_3\end{pmatrix}=\begin{pmatrix}\measuredangle(\vec{n}_1^e,\vec{n}_3^e)\\\measuredangle(\vec{n}_1^e,\vec{n}_2^e)\\\measuredangle(\vec{n}_2^e,\vec{n}_3^e)\end{pmatrix}. \tag{31}$$

5.1 Beam Parallelism

We combine eq. (29) and eq. (20) to obtain the error-prone mirror normal vectors upon spacecraft rotations

$$\vec{n}_i^e(u,v,w)=\widehat{R}(u,v,w)\cdot\vec{n}_i^e \tag{32}$$

and evaluate the final beam direction

$$\vec{d_3}=\widehat{D}(\vec{n}_3^e(u,v,w)\ )\cdot\widehat{D}(\vec{n}_2^e(u,v,w)\ )\cdot\widehat{D}(\vec{n}_1^e(u,v,w)\ )\cdot\vec{d_0}$$

$$\overset{\text{linearized}}{\approx}$$

$$\begin{pmatrix}1\\0\\0\end{pmatrix}+\begin{pmatrix}0&0&0\\-1.414&-1.414&0\\1.0&-1.0&1.414\end{pmatrix}\vec{\gamma} \tag{33}$$

$$+\begin{pmatrix}0&0&0\\-1.0\cdot u+1.0\cdot v&1.0\cdot u-1.0\cdot v&-1.414\cdot u-1.414\cdot v\\-1.414\cdot u+1.0\cdot w&-1.414\cdot u-1.0\cdot w&-1.414\cdot w\end{pmatrix}\vec{\gamma}, \tag{34}$$

where one can see that in case of no misalignments ($\vec{\gamma}=0$) the outgoing beamdirection is $(1,0,0)^\mathsf{T}$. This equation provides the dependency of the outgoing beam direction w.r.t. the misalignment angles. The last term shows, that the beam direction can depend on the spacecraft orientation $u,\ v,\ w$, although the effect is very small, since γ_i has a magnitude of μrad and $u,\ v,\ w$ of mrad. The static misalignment (second term) has coefficients of the order ≈ 1, meaning that a mirror misalignment of 1 μrad causes a beam deflection of approximately 1 μrad.

The static misalignment matrix was verified by raytracing.

5.1.1 Application to TMA requirements

We assume a requirement of $\delta = 15\,\mu$rad total beam deflection due to a TMA. In addition we assume that the two close-by mirrors M_2 and M_3 are aligned with an error below $\gamma_3 = 5\,\mu$rad. The total static beam deflection δ is approximately given by

$$\delta=\sqrt{(-1.141\cdot\gamma_1-1.141\cdot\gamma_2)^2+(1.0\cdot\gamma_1-1.0\cdot\gamma_2+1.414\cdot\gamma_3)^2}, \tag{35}$$

which parameterizes an ellipse when our assumptions are plugged in (see fig. 2). The errors for γ_1 and γ_2 should be within this ellipse to obtain a total beam deflection with less than 15 μrad.

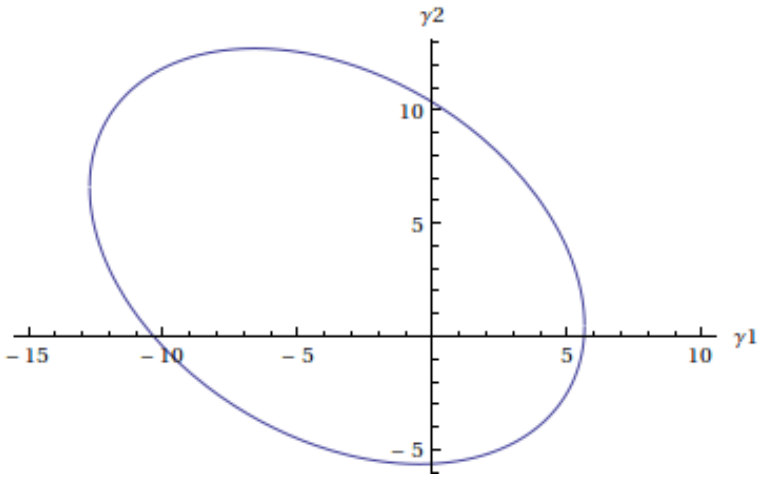

Figure 2: Error ellipse for TMA misalignment angles γ_1 and γ_2 in μrad for the particular assumptions given in the text.

5.1.2 Results by Yoder

In a paper by Yoder [2] the beam deflections due to corner-cube errors are analyzed. One result is that if the misalignment angles $|\gamma_i|$ are below θ, the final beam deflection is below $3.26 \cdot \theta$. In the derivation given in this document, one can show that the total error is maximal $3.41 \cdot \theta$, when $\gamma_1 = -\gamma_2 = \gamma_3 = \theta$ is used. The cause of this discrepancy was not investigated.

5.2 Pathlength

For rotations around the true vertex we compute the following pathlength coupling

$$\rho\left(\ \vec{c}_1(u,v,w),\ \vec{n}_1^e(u,v,w),\ \vec{c}_2(u,v,w),\ \vec{n}_2^e(u,v,w),\ \vec{c}_3(u,v,w),\ \vec{n}_3^e(u,v,w)\ \right) \tag{36}$$

$$\approx 2 \cdot x_0 + \begin{pmatrix} 1.414 \cdot y_0 + 1.0 \cdot z_0 \\ 1.414 \cdot y_0 - 1.0 \cdot z_0 \\ 1.414 \cdot z_0 \end{pmatrix} \cdot \vec{\gamma} \tag{37}$$

$$+ u \cdot \begin{pmatrix} 266.1\,\mathrm{mm} + (y_0 - \delta y) + 1.414(z_0 - \delta z) \\ -333.9\,\mathrm{mm} - (y_0 - \delta y) + 1.414(z_0 - \delta z) \\ 424.3\,\mathrm{mm} + 1.414(y_0 - \delta y) \end{pmatrix} \cdot \vec{\gamma} \tag{38}$$

$$+ v \cdot \left(2 \cdot \delta z + \begin{pmatrix} -300.0\,\mathrm{mm} - y_0 + \delta x \\ 300.0\,\mathrm{mm} + y_0 - \delta x \\ 424.3\,\mathrm{mm} + 1.414(y_0 + \delta x) \end{pmatrix} \cdot \vec{\gamma} \right) \tag{39}$$

$$+ w \cdot \left(-2 \cdot \delta y + \begin{pmatrix} -24.0\,\mathrm{mm} - z_0 + 1.414\delta x \\ -24.0\,\mathrm{mm} + z_0 + 1.414\delta x \\ 33.94\,\mathrm{mm} + 1.414 z_0 \end{pmatrix} \cdot \vec{\gamma} \right), \tag{40}$$

where $\rho, x_0, y_0, z_0, \delta x, \delta y, \delta z$ are in millimeter and the angles $\vec{\gamma}, u, v, w$ are in radian.

6 Point of Minimal Coupling

The point of minimal coupling (POMC) is the point, where the partial derivatives of the optical pathlength ρ w.r.t. the spacecraft rotation angles u, v, w are minimal. We derive the coupling coefficients for a rotation around the true vertex:

$$\begin{pmatrix} \partial\rho/\partial u \\ \partial\rho/\partial v \\ \partial\rho/\partial w \end{pmatrix} = \begin{pmatrix} 266.059 & -333.941 & 424.264 \\ -300.0 & +300.0 & 424.264 \\ 24 & -24 & -33.9411 \end{pmatrix} \cdot 1\,\mathrm{mm} \cdot \vec{\gamma}$$
$$+ \begin{pmatrix} 0 & -\gamma_1 + \gamma_2 - 1.414\gamma_3 & -1.414\gamma_1 - 1.414\gamma_2 \\ \gamma_1 - \gamma_2 + 1.414\gamma_3 & 0 & 2 \\ 1.414\gamma_1 + 1.414\gamma_2 & -2 & 0 \end{pmatrix} \cdot \begin{pmatrix} \delta x \\ \delta y \\ \delta z \end{pmatrix}, \tag{41}$$

where we assumed no lateral beam offset ($y_0 = z_0 = 0$) and where $\delta x, \delta y, \delta z$ is an offset in the point of rotation from the true vertex. As one can see, the coupling is very small for mirror misalignments in the range of μrad. Therefore one can say that for the assumed TMA mirror misalignments the POMC is at the true vertex (which was computed w.r.t. the nominal vertex in eq. (30)).

If higher accuracy is required, one can use the Moore-Penrose pseudo-inverse to solve eq. (41) for $\delta x, \delta y, \delta z$. The pseudo inverse is required, since the system is singular (one has a line of zero coupling for the uv rotations and another line for uw rotations). The pseudo-inverse provides a solution, which minimizes

$$\left| \begin{pmatrix} \partial\rho/\partial u \\ \partial\rho/\partial v \\ \partial\rho/\partial w \end{pmatrix} \right|^2 \tag{42}$$

w.r.t. $\delta x, \delta y$ and δz. The solution can be linearized to

$$\begin{pmatrix} \delta x \\ \delta y \\ \delta z \end{pmatrix} \approx \begin{pmatrix} 0\,\mathrm{mm} \\ 12\,\mathrm{mm} \cdot (-\gamma_1 + \gamma_2) + 16.97\,\mathrm{mm} \cdot \gamma_3 \\ 150\,\mathrm{mm} \cdot (-\gamma_1 + \gamma_2) + 212.132\,\mathrm{mm} \cdot \gamma_3 \end{pmatrix}. \tag{43}$$

References

[1] http://mathworld.wolfram.com/Plane-PlaneIntersection.html

[2] P.R. Yoder, Jr. *Study of Light Deviation Errors in Triple Mirrors and Tetrahedral Prisms*

[3] Vitali Müller (Master thesis): *Interferometer simulations for the GRACE Follow-On mission*

[4] GR-AEI-TN-1002 *The GRACE-C Interferometer* internal document

Bibliography

Alda, Javier. 2003. *"Laser and Gaussian Beam Propagation and Transformation"*. Article. Encyclopedia of Optical Engeneering.

ANU. 2012. *http://grace.anu.edu.au/technology-development/freq-stabilisation.php*. website. Australian National University.

Arnaud, J. A., & Kogelnik, H. 1969. "Gaussian Light Beams with General Astigmatism". *Appl. Opt.*, **8**(8), 1687–1693.

Baune, Christopher. 2009. *Design, implementation and characterization of a telescope simulator for the LISA optical bench*. Bachelor Thesis. Albert-Einstein-Institute, University Hanover.

Bellavia, Stefania, Macconi, Maria, & Morini, Benedetta. 2004. STRSCNE: A Scaled Trust-Region Solver for Constrained Nonlinear Equations. *Computational Optimization and Applications*, **28**, 31–50. 10.1023/B:COAP.0000018878.95983.4e.

Benenson, W., Harris, J.W., Stöcker, H., & Lutz, H. 2002. *Handbook of Physics*. Prentice-Hall series in educational innovation. Springer.

Bik, J., Visser, P., & Jennrich, O. 2007. LISA satellite formation control. *Advances in Space Research*, **40**(1), 25–34.

Bowler, G. 1976. *Gravitation and relativity*. International series in natural philosophy. Pergamon Press.

Boy, Jean-Paul, Hinderer, Jacques, & Linage, Caroline. 2012. Retrieval of Large-Scale Hydrological Signals in Africa from GRACE Time-Variable Gravity Fields. *Pure and Applied Geophysics*, **169**, 1373–1390.

Canalias, E., Gomez, G., Marcote, M., & Masdemont, J. J. 2004. *Assessment of mission design including utilisation of libration points and weak stability boundaries*. Tech. rept. 03-4103a. European Space Agency, the Advanced Concepts Team. Available on line at www.esa.int/act.

Case, K., Kruizinga, G., & Wu, S.-C. 2010. *GRACE Level 1B Data Product User Handbook*. Tech. rept. Jet Propulsion Laboratory, California Institute of Technology.

Chipman, Russell A., Shamir, Joseph, Caulfield, H. John, & Zhou, Qi-Bo. 1988. Wavefront correcting properties of corner-cube arrays. *Appl. Opt.*, **27**(15), 3203–3209.

Clarke, Arthur C. 1947. Stationary Orbits. *Journal of the British Astronimical Association*, **57**, 232–237.

Coleman, T., & Li, Y. 1996. A Reflective Newton Method for Minimizing a Quadratic Function Subject to Bounds on Some of the Variables. *SIAM Journal on Optimization*, **6**(4), 1040–1058.

Conklin, J.W., Buchman, S., Aguero, V., Alfauwaz, A., Aljadaan, A., *et al.* . 2011. LAGRANGE: LAser GRavitational-wave ANtenna at GEo-lunar Lagrange points. *ARXIV:1111.5264*.

Davis, A., Mewaldt, R., Stone, E., & Smith, C. 2004. Solar and Interplanetary Data From the Advanced Composition Explorer. *Space Weather*, **2**(7), S07003.

DECIGO-Team. 2009. DECIGO: The Japanese space gravitational wave antenna. *Journal of Physics: Conference Series*, **154**(1), 012040.

Dhurandhar, S.V., Rajesh Nayak, K., Koshti, S., & Vinet, J.-Y. 2005. Fundamentals of the LISA stable flight formation. *Class.Quant.Grav.*, **22**, 481–488.

Dunham, David W., & Farquhar, Robert W. 2002. *Assessment of mission design including utilisation of libration points and weak stability boundaries*. Tech. rept. 03-4103b. Johns Hopkins University – Applied Physics Laboratory. Available on line at www.esa.int/act.

Faller, J. E., Bender, P. L., Hall, J. L., Hils, D., & Vincent, M. A. 1985. Space Antenna for Gravitational Wave Astronomy. *In: in proceedins, colloquium on kilometric optical arrays in space, 23-25 October 1984, CARGESE, CORSICA, FRANCE*. JILA Pub. 3012.

Farquhar, Robert W., & Kamel, Ahmed A. 1973. Quasi-periodic orbits about the translunar libration point. *Celestial Mechanics and Dynamical Astronomy*, **7**, 458–473. 10.1007/BF01227511.

Farquhar, R.W. 1968. *The control and use of libration-point satellites*. Dept. of Aeronautics and Astronautics, Stanford University.

Folkner, W.M., deVine, G., Klipstein, W.M., McKenzie, K., Spero, R., Thompson, R., & Yu, N. 2011. Laser Frequency Stabilization for GRACE-2. *In: ESTF*.

Freise, Andreas, & Strain, Kenneth A. 2010. Interferometer Techniques for Gravitational-Wave Detection. *Living Reviews in Relativity*, **13**(1).

Galen C. Duree, J. 2011. *Optics For Dummies*. Wiley.

Gill, P.E., Murray, W., & Wright, M.H. 1981. *Practical optimization*. Academic Press.

Gómez, G. 2001. *Dynamics and Mission Design Near Libration Points*. World Scientific Monograph Series in Mathematics, no. v. 1. World Scientific.

Gómez, Gerard, Masdemont, Josep, & Simó, Carles. 1998. Quasihalo orbits associated with libration points. *Journal of the Astronautical Sciences*, **46**(2), 135–176.

Grote, H, Heinzel, G, Freise, A, Gossler, S, Willke, B, Lück, H, Ward, H, Casey, M, Strain, K A, Robertson, D, Hough, J, & Danzmann, K. 2002. The automatic alignment system of GEO 600. *Classical and Quantum Gravity*, **19**(7), 1849.

Gómez, G., Masdemont, J., & Simó, C. 1997. Lissajous Orbits Around Halo Orbits. *AAS*, **95**, 117–134.

Halliday, David, Resnick, Robert, & Walker, Jearl. 2010. *Fundamentals of Physics, Part 4, 9th Edition*.

Hechenblaikner, Gerald. 2010. Measurement of the absolute wavefront curvature radius in a heterodyne interferometer. *J. Opt. Soc. Am. A*, **27**(9), 2078–2083.

Heinzel, G., Rüdiger, A., Schilling, R., & Hannover, T. 2002. Spectrum and spectral density estimation by the Discrete Fourier transform (DFT), including a comprehensive list of window functions and some new flat-top windows. *Max Plank Institute*, **12**, 122.

Heinzel, Gerhard. 2012. *Ifocad: A framework of C subroutines to plan and optimize the geometry of laser interferometers*. Software Documentation. Albert-Einstein-Institute, University Hanover.

Hellings, Ronald W. 1996. Gravitational wave detectors in space. *Contemporary Physics*, **37**(6), 457–469.

Hobbs, P.C.D. 2011. *Building Electro-Optical Systems: Making It all Work*. Wiley Series in Pure and Applied Optics. Wiley.

Hodgson, N., & Weber, H. 1997. *Optical Resonators: Fundamentals, Advanced Concepts, and Applications*. Springer.

Horwath, M., Lemoine, J.-M., Biancale, R., & Bourgogne, S. 2011. Improved GRACE science results after adjustment of geometric biases in the Level-1B K-band ranging data. *Journal of Geodesy*, **85**, 23–38. 10.1007/s00190-010-0414-2.

Howell, K. C., & Pernicka, H. J. 1988. Numerical determination of Lissajous trajectories in the restricted three-body problem. *Celestial Mechanics*, **41**, 107–124.

Howell, KC, & Barden, BT. 1999. Trajectory design and stationkeeping for multiple spacecraft in formation near the Sun-Earth L1 point. *Pages 4–8 of: IAF 50th International Astronautical Congress*.

Hughes, S.P. 2002. Preliminary optimal orbit design for the Laser Interferometer Space Antenna(LISA). *Advances in the Astronautical Sciences*.

Ilk, K. H., Flury, J., Rummel, R., Schwintzer, P., Bosch, W., Haas, C., Schroeter, J., Stammer, D., Zahel, W., Miller, H., Dietrich, R., Huybrechts, P., Schmeling, H., Wolf, D., Goetze, H. J., Riegger, J., Bardossy, A., Guentner, A., & Gruber, T. 2005 (01). *Mass transport and mass distribution in the Earth system*. Proposal for a German priority research program, 2nd edition. GOCE-Projektbuero TU Muenchen, GeoForschungsZentrum Potsdam.

James, J.D. Mireles. 2006. *Celestial Mechanics*. Lecture Notes. http://www.math.rutgers.edu/ jmireles/.

Jha, A.K. 2009. *A Textbook Of Applied Physics*. I.K. International Publishing House Pvt. Limited.

Jorba, Angel, & Masdemont, Josep. 1999. Nonlinear dynamics in an extended neighbourhood of the translunar equilibrium point. *Pages 430–434 of: Hamiltonian Systems with Three or More Degrees of Freedom*. Springer.

Kim, Hwi, & Lee, Byoungho. 2007. Optimal design of retroreflection corner-cube sheets by geometric optics analysis. *Optical Engineering*, **46**(9), 094002+.

Kim, Jeongrae. 2000. *Simulation Study of A Low-Low Satellite-Satellite Tracking Mission*. Dissertation. University of Texas.

Kochkina, E., Heinzel, G., Wanner, G., Müller, V., Mahrdt, C., Sheard, B., Schuster, S., & Danzmann, K. 2013 (Jan.). Simulating and Optimizing Laser Interferometers. Astronomical Society of the Pacific Conference Series, vol. 467.

Kolemen, E., Kasdin, N. J., & Gurfil, P. 2007 (Feb). Quasi-Periodic Orbits of the Restricted Three-Body Problem Made Easy. *Pages 68–77 of: New Trends in Astrodynamics and Applications III*. American Institute of Physics Conference Series, vol. 886.

Lau, K.S., Zhou-Ping, X., & Yau, S.T. 2008. *Third International Congress of Chinese Mathematicians*. Ams/IP Studies in Advanced Mathematics, no. v. 2. Amer Mathematical Society.

Li, G., ZHAOHUA, YI, Heinzel, G., Rüdiger, A., Jennrich, O., Wang, L., Xia, Y., Zeng, F., & Zhao, H. 2008. Methods for orbit optimization for the LISA gravitational wave observatory. *International Journal of Modern Physics D*, **17**(07), 1021–1042.

LISA. 1993. *Proposal for Laser-Interferometric Gravitational Wave Detector in Sapce*. ESA proposal. MPQ fuer Quantenoptik, Garching, Muenchen.

LISA. 2000. *LISA System and Technology Study Report*. Internal Report ESA-SCI(2000)11. ESA.

LISA. 2011. *LISA Assessment Study Report (Yellow Book)*. ESA/SRE(2011)3. ESA.

Liu, Jian, & Azzam, R. M. A. 1997. Polarization properties of corner-cube retroreflectors: theory and experiment. *Appl. Opt.*, **36**(7), 1553–1559.

Mayer, J. R. 1993. Polarization optics design for a laser tracking triangulation instrument based on dual-axis scanning and a retroreflective target. *Optical Engineering*, **32**(12), 3316–3326.

Meschede, D. 2008. *Optics, Light and Lasers: The Practical Approach to Modern Aspects of Photonics and Laser Physics*. Physics textbook. John Wiley & Sons.

Mickens, R.E. 1981. *An Introduction to Nonlinear Oscillations*. Cambridge University Press.

Misner, C.W., Thorne, K.S., & Wheeler, J.A. 1973. *Gravitation*. Physics Series, no. pt. 3. W. H. Freeman.

Montenbruck, Oliver, & Gill, Eberhard. 2000. *"Satellite orbits: Models, methods, and applications"*. Berlin: Springer.

Morrison, Euan, Meers, Brian J., Robertson, David I., & Ward, Henry. 1994. Automatic alignment of optical interferometers. *Appl. Opt.*, **33**(22), 5041–5049.

NASA. 2012 (August). *Gravitational-Wave Mission Concept Study Final Report*. Report: http://pcos.gsfc.nasa.gov/physpag/GW_Study_Rev3_Aug2012-Final.pdf. NASA.

Nayfeh, A.H. 2008. *Perturbation Methods*. Physics textbook. Wiley.

NGO-Yellowbook. 2011. *NGO assessment study report (Yellow Book), ESA/SRE(2011)19, December 2011.*

Peck, Edson R. 1948. Theory of the Corner-Cube Interferometer. *J. Opt. Soc. Am.*, **38**(12), 1015–1015.

Peck, Edson R. 1962. Polarization Properties of Corner Reflectors and Cavities. *J. Opt. Soc. Am.*, **52**(3), 253–253.

Rausch, Raoul R. 2005. *Earth to Halo orbit transfer trajectories.* MSc. thesis. Purdue University.

Richardson, D. L. 1980. Analytic construction of periodic orbits about the collinear points. *Celestial Mechanics*, **22**(Oct.), 241–253.

Richardson, David L. 1980b. Halo Orbit Formulation for the ISEE-3 Mission. *Journal of Guidance Control and Dynamics*, **3**, 543–548.

Saleh, Bahaa, & Teich, Malvin Carl. 1991. *Fundamentals of Photonics.*

Scholl, Marija S. 1995. Ray trace through a corner-cube retroreflector with complex reflection coefficients. *J. Opt. Soc. Am. A*, **12**(7), 1589–1592.

Schütze, D., Stede, G., Müller, V., Gerberding, O., Mahrdt, C., Sheard, B., Heinzel, G., & Danzmann, K. 2013 (Jan.). LISA-like Laser Ranging for GRACE Follow-on. Astronomical Society of the Pacific Conference Series, vol. 467.

Segre, Sergio E., & Zanza, Vincenzo. 2003. Mueller calculus of polarization change in the cube-corner retroreflector. *J. Opt. Soc. Am. A*, **20**(9), 1804–1811.

Sheard, B., & Heinzel, G. 2011. *The GRACE-C interferometer.* Internal Technical Note, v.5, Date: 2011.02.20. Albert-Einstein-Institute.

Sheard, B., Heinzel, G., Danzmann, K., Shaddock, D., Klipstein, W., & Folkner, W. 2012. Intersatellite laser ranging instrument for the GRACE follow-on mission. *Journal of Geodesy*, 1–13. 10.1007/s00190-012-0566-3.

Sommerfeld, Martin. 2010. *Development of a calibrated quadrant photodiode pair (CQP).* Diploma thesis. Albert-Einstein-Institute, University Hanover.

Stede, Gunnar. 2011. *Interferometrische Charakterisierung von Retroreflektoren für satellitengestützte Erdschwerefeldbestimmung.* Diploma thesis (german). Albert-Einstein-Institute, University Hanover.

Steel, W.H. 1983. *Interferometry.* Cambridge Studies in Modern Optics. Cambridge University Press.

Thompson, R., Folkner, W.M., de Vine, G., Klipstein, W.M., McKenzie, K., Spero, R., Yu, N., Stephens, M., Leitch, J., Pierce, R., Lam, T.T.-Y., & Shaddock, D.A. 2011 (may). A flight-like optical reference cavity for GRACE follow-on laser frequency stabilization. *Pages 1 –3 of: Frequency Control and the European Frequency and Time Forum (FCS), 2011 Joint Conference of the IEEE International.*

Thurman, Robert, & Worfolk, Patrick A. 1996. *The Geometry of Halo Orbits in the Circular Restricted Three-Body Problem.* Tech. rept.

Tinto, Massimo, & Dhurandhar, Sanjeev V. 2005. Time-Delay Interferometry. *Living Reviews in Relativity*, **8**(4).

Troebs, M., Barke, S., Moebius, J., Engelbrecht, M., Kracht, D., d'Arcio, L., Heinzel, G., & Danzmann, K. 2009. Lasers for LISA: Overview and phase characteristics. *Journal of Physics: Conference Series*, **154**(1), 012016.

Turner, M.J.L. 2009. *Rocket and Spacecraft Propulsion.* Springer Praxis books in astronautical engineering. Springer.

Vallado, David A., & McClain, Wayne D. 2007. *"Fundamentals of astrodynamics and applications".* 3. ed. edn. Space technology library, vol. 21. Hawthorne, Calif.: Microcosm Press [u.a.].

Velicogna, I. 2009. Increasing rates of ice mass loss from the Greenland and Antarctic ice sheets revealed by GRACE. *Geophysical Research Letters*, 19503.

Wang, Furun. 2000. *"GRACE CG offset determination by magnetic torquers during in-flight phase"*. CSR-TM-00-01. Center for Space Research, The University of Texas at Austin.

Wanner, Gudrun. 2010. *Complex optical systems in space: numerical modelling of the heterodyne interferometry of LISA Pathfinder and LISA*. PhD thesis. Albert-Einstein-Institute, University Hanover.

Wanner, Gudrun, Heinzel, Gerhard, Kochkina, Evgenia, Mahrdt, Christoph, Sheard, Benjamin S., Schuster, Soenke, & Danzmann, Karsten. 2012. Methods for simulating the readout of lengths and angles in laser interferometers with Gaussian beams. *Optics Communications*, **285**(24), 4831 – 4839.

Wertz, J.R., & Larson, W.J. 1999. *Space Mission Analysis and Design*. Space Technology Library. Springer.

Wie, B. 1998. *Space Vehicle Dynamics and Control*. AIAA Education Series. American Institute of Aeronautics and Astronautics.

Zazzera, F.B., Topputo, F., & Massari, M. 2004. *Assessment of mission design including utilisation of libration points and weak stability boundaries*. Tech. rept. 03-4103b. European Space Agency, the Advanced Concepts Team. Available on line at www.esa.int/act.